UNIVERSITÀ DI PARMA

UNIVERSITA' DEGLI STUDI DI PARMA

DOTTORATO DI RICERCA IN
" *Scienza e Tecnologia dei Materiali*"
CICLO XXXVII

Synthesis and Development of "Green" Chalcogenides Inks via High-Energy Ball Milling for the Realization of Ultra-Low-Cost Thin Film Solar Cells

Coordinatore:

Chiar.mo Prof. Enrico Dalcanale

Tutore:

Dott. Andrea Zappettini

Co-Tutore:

Dott. Davide Delmonte

Dottoranda: Elena Del Canale

Anni Accademici 2021/2022 – 2023/2024

A Daniele,

amata stella

che ha reso chiaro questo difficile cammino

ABSTRACT

New technological solutions for green energy and optoelectronics are needed to surpass current methodologies and performance benchmarks, demanding an extra effort from researchers in the field of material science for the synthesis, characterization, and prototyping of more performant materials and devices.

This PhD thesis demonstrates how mechanochemistry (MC) can be smartly applied in this field, particularly exploiting high energy ball milling methodologies. This simple and cost-effective technique allows direct control of materials reactivity and the synthesis of stable/metastable inorganic solids through solid-state reactions of the constituent elements or compounds. MC leverages the non-equilibrium thermodynamic regime, enabling the process to occur around ambient conditions while exchanging extreme local energy to the reactants. Moreover, it is possible to obtain large amounts of pure products without using toxic reactants and solvents.

Specifically, this thesis presents the application of MC to Cu(In,Ga)(S,Se) (CIGSSe) chalcogenides, well-known as efficient absorbers ($\alpha > 10^4\ cm^{-1}$) for thin film solar cells. Through MC, pure phases can be obtained by finely varying the cationic (In/Ga) and anionic (S/Se) ratios of the solid solution, allowing the tuning of the optical bandgap from 1.02 eV ($CuInSe_2$) to 2.5 eV ($CuGaS_2$) to match the solar spectrum.

A bottom-top process is presented that stabilizes a PV ink from mechanochemically synthesized low bandgap chalcogenides ($CuInS_2$ and $CuInSe_2$) for liquid-phase deposition. The process was optimized to obtain a stable suspension in n-butanol with the correct crystallographic structure and composition. A high temperature selenization treatment demonstrated effectiveness in improving the crystallinity and conductivity of the $CuInSe_2$ films. The addition of ethanolamine as a complexing agent inside the $CuInSe_2$ ink further enhanced these properties, achieving a resistivity of $k\Omega \cdot cm$. The photovoltaic cell demonstrated promising performance with a V_{OC} of 331 mV and a J_{SC} of 1.8 mA/cm^2.

For high bandgap chalcogenides ($CuInGaS_2$ and $CuGaSSe_2$), mechanochemical synthesis and refinement were successful in obtaining a pure phase. The refinement conditions allowed fine control of the particle size of CIGS, resulting in a semi-transparent ink with over 70% transparency in the spectral region between 750 and 1300 nm. A prototype device on a transparent FTO substrate showed a photovoltaic response.

Additionally, the use of high energy ball milling processed $CuInSe_2$ as a hole transport layer in carbon-based Formamidinium Lead Iodide hybrid-perovskite solar cells was explored. Devices assembled with different concentrations and layers of CISe ink maintained efficiency over 24 hours, with some cells outperforming reference cells after aging, suggesting a possible stabilizing effect on perovskite cells.

The second part of the thesis focused on the mechanochemical synthesis of the FE-PV compound SbSI and its post-deposition treatments using Pulsed Electron Deposition (PED). The solid-state reaction of SbSI was successfully applied using mechanochemical synthesis from its constituent elements. A collaboration with the *Universitat Politècnica de Catalunya*, Barcelona, studied oriented recrystallization using a high-pressure furnace. XRD and SEM analyses confirmed notable recrystallization and preferential orientation of crystallites, addressing sublimation issues and promoting crystallization with a specific orientation. This research represents a significant milestone in developing functional SbSI FE-PV devices.

SUMMARY

1 INTRODUCTION: ANALYSIS OF THE GLOBAL ENERGY MARKET, PHOTOVOLTAIC INDUSTRY, AND GEOPOLITICAL LANDSCAPE

The escalating climate crisis, triggered by the relentless exploitation of fossil fuels, has propelled the world toward an inevitable energy revolution.

Over the past century, fossil fuels, including coal, oil, and natural gas, have held a preeminent position as humanity's primary energy sources. However, the combustion of these fuels releases a combination of greenhouse gases (GHGs), predominantly carbon dioxide (CO_2), methane (CH_4), and nitrous oxide (N_2O), into the Earth's atmosphere.

Such GHGs exacerbate the greenhouse effect, which is a natural phenomenon in which solar radiation penetrates the atmosphere and reaches the Earth's surface, where a portion of the solar energy is reflected, and the remaining part is absorbed and then converted into heat. The presence of GHGs in the atmosphere helps to retain a fraction of this heat, preventing its complete escape back into space and creating a more hospitable environment for the development and sustenance of life. However, if the levels of GHGs are too high, they result in an abnormal increase in global temperatures, thereby contributing to climate change, one of the most pressing challenges facing humanity today.

Other human activities are responsible for this: forests, crucial for absorbing and converting into oxygen carbon dioxide, are being cut down, releasing stored carbon back into the atmosphere. Livestock farming contributes to the release of large quantities of methane from the digestion of food from animals. Additionally, the use of nitrogen-based fertilizer and fluorinated gases (F-gases) in various products (e.g., aerosol sprays, refrigerators, and air conditioners) contribute to increasing greenhouse gas concentrations. However, the primary concern lies in the burning of fossil fuels for energy: in 2022, global GHG emissions were predominantly composed of CO_2, which accounted for 71.6% and resulted from the combustion of fossil fuels. CH_4 contributed 21% of the total emissions, while the remaining share consisted of N_2O (4.8%) and F-gases (2.6%).[1]

This, in fact, has caused global temperatures to rise, leading to a range of negative impacts on the environment and human societies. Rapid and widespread changes in the atmosphere, ocean, cryosphere, and biosphere have occurred due to human-caused climate change, affecting weather and climate extreme events worldwide. This has led to widespread adverse impacts on nature and people, with vulnerable communities being disproportionately affected. Human influence has indisputably provoked a warming of the atmosphere, ocean, and land, causing a significant rise in global mean sea levels and increasing the frequency and intensity of extreme weather events such as heatwaves, heavy precipitation, droughts, and tropical cyclones. Approximately 3.3 to 3.6 billion people live in highly vulnerable contexts and are consequently exposed to acute food insecurity and reduced water security, particularly in regions such as Africa, Asia, Central and South America.[2] In these macro-regions, agricultural productivity growth has slowed. Climate change has also caused substantial and increasingly irreversible losses in various ecosystems, driving local species extinctions and mass mortality events. Moreover, ocean warming and acidification have adversely affected food production from fisheries and shellfish aquaculture.

The Intergovernmental Panel on Climate Change (IPCC) reported that the global temperature has already increased by approximately 1.1°C since the preindustrial era and that limiting global warming to 1.5°C above preindustrial levels is mandatory to stop this devastating and catastrophic impact on mankind: the consequences of failing to mitigate climate change are severe. However, achieving this goal would require rapid, far-reaching, and unprecedented changes in all aspects of society.[3]

1.1 The Data

As such, the world's appetite for energy remains insatiable: by 2023, the demand for energy continued to surge across various nations, fueled by increasing wealth and growing populations.

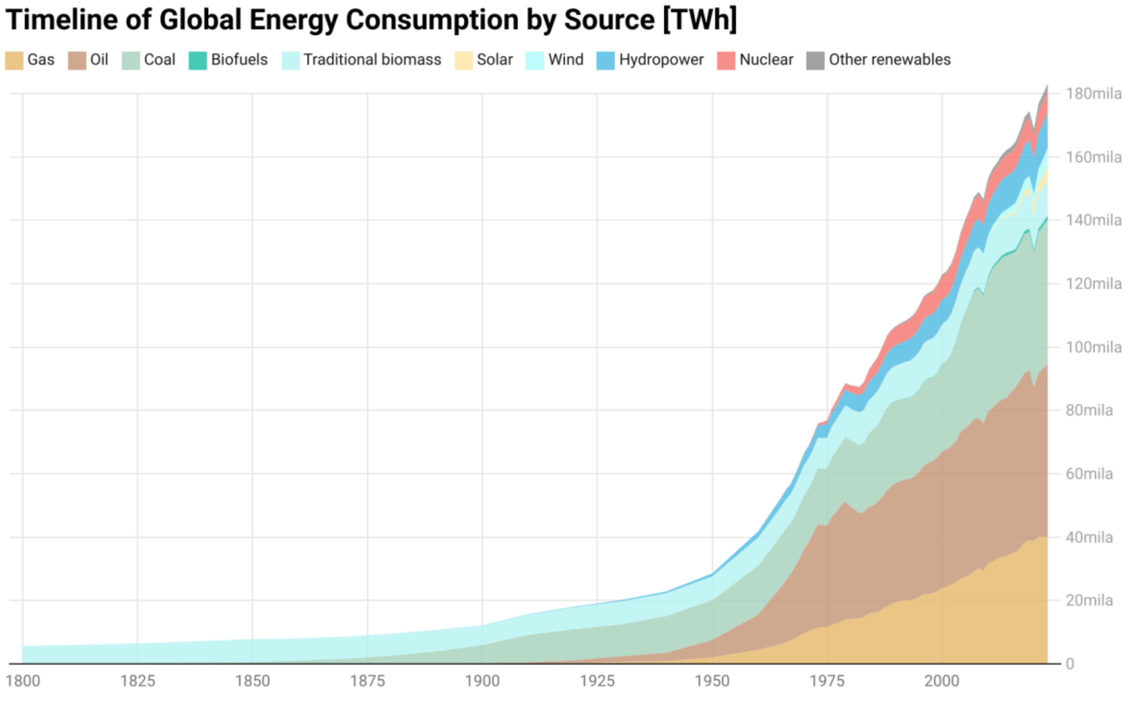

Fonte: © Energy Institute 2024 • Creato con Datawrapper

Figure 1: Timeline evolution of global energy consumption from 1800 to 2023, categorized by various energy sources. It highlights the shifting dynamics, the growth of the energy demand and the increasing diversification of energy sources over time.[4]

The year 2023 marked a year of unprecedented production and consumption of energy, with most markets reverting to their pre-COVID-19 levels and long-term trends as supply chain disruptions subsided. Notably, oil consumption experienced a robust rebound, which was driven primarily by China's relaxation of its zero-COVID lockdown policies. Despite the stagnant demand for natural gas, crude oil consumption surpassed 100 million barrels per day for the first time in history, and coal demand surpassed the previous year's record. Renewable energy consumption increased at a rate six times faster than total primary energy, while electricity (secondary energy) demand grew 25% faster than total primary energy consumption. "Primary energy" refers to energy sources that are found in nature and have not undergone any conversion or transformation processes.

Specifically, Figure 1 illustrates that global energy consumption has consistently risen nearly every year from 1800 to 2023, reaching approximately 620 EJ (or 172,000 TWh) in 2023, with a growth rate of +2% from the previous year (Figure 2).

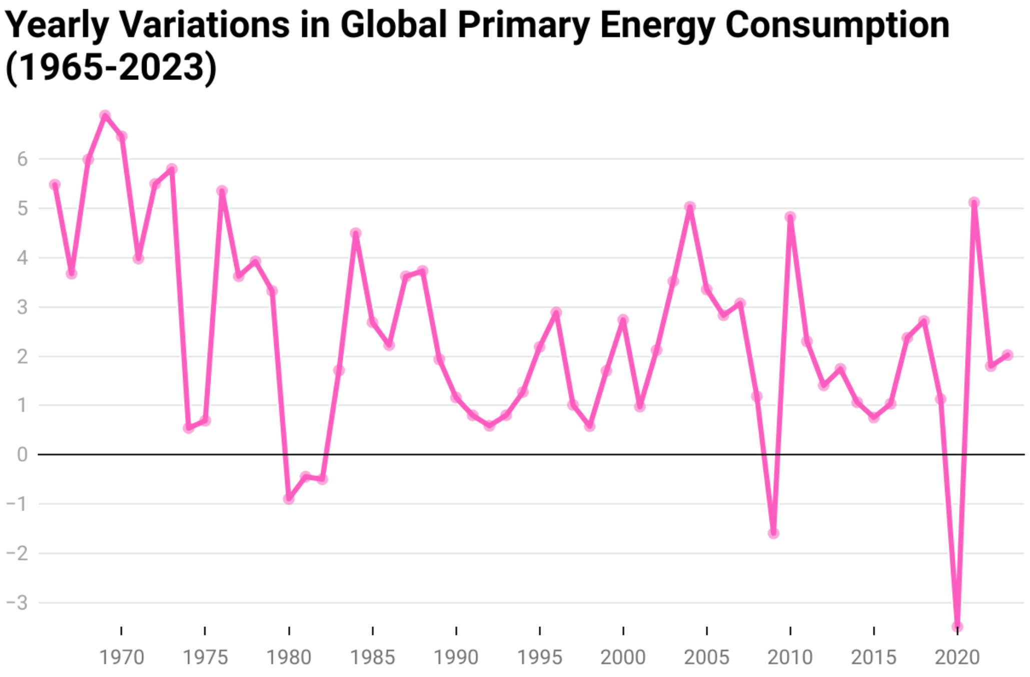

Yearly Variations in Global Primary Energy Consumption (1965-2023)

Source: © Energy Institute 2024 • Created with Datawrapper

Figure 2: Annual Variation in Global Primary Energy Consumption (1965-2023). Notably, there are three significant drops in consumption, occurring in 1974, 2010, and 2020. These declines can be attributed to major global events: the 1974 drop is linked to the oil crisis, the 2010 drop is associated with the global financial crisis, and the 2020 drop is a result of the COVID-19 pandemic.[4]

This growth rate exceeded its ten-year average by 0.6% and surpassed its 2019 pre-COVID-19 level by more than 5%. However, the addition of energy from low-carbon sources has not been sufficient to meet the growth in total global energy demand. This indicates that the use of fossil fuels has continued to rise, setting a new record in 2023, primarily driven by increasing oil consumption.

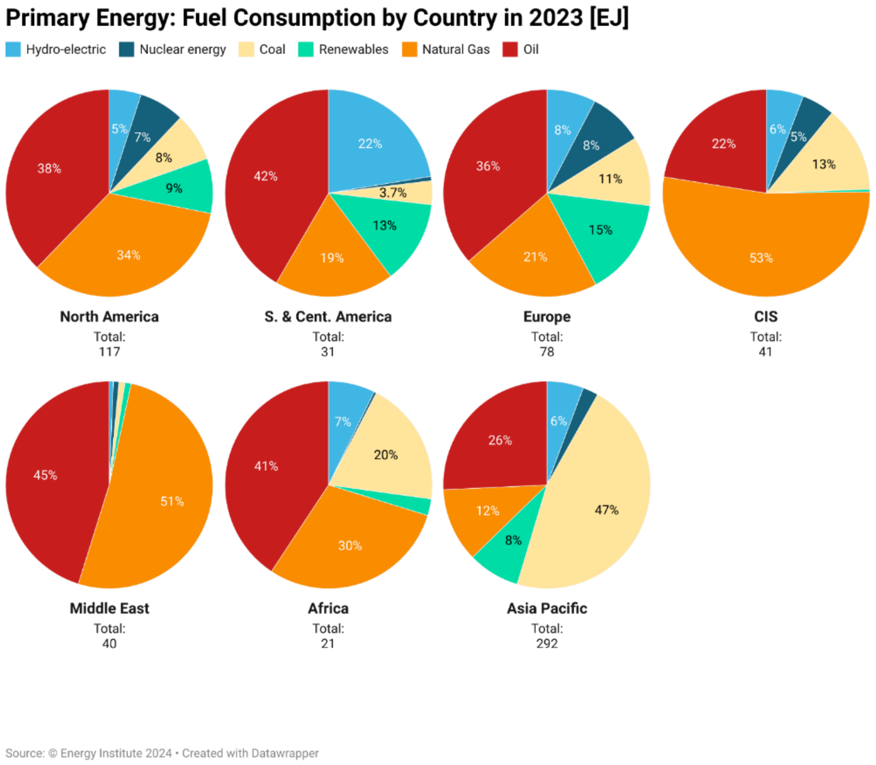

Figure 3: Distribution of fuel consumption across different regions of the world: North America, Central and South America, Europe, Commonwealth of Independent States (CIS), Middle East, Africa, and Asia Pacific.

The exception to this trend is the Commonwealth of Independent States (CIS) and the Middle East states, where natural gas is the dominant energy source. In detail, as presented in Figure 3, oil consumption in North America is predominant (38%), closely followed by natural gas (34%). In Central and South America, oil is also the primary fuel (42%), with significant use of hydroelectric sources (22%). Europe's fuel consumption is led by oil (36%), with substantial use of natural gas (21%) and renewable energies (15%), making it the region with the highest utilization of renewables. In the CIS states, natural gas consumption surpasses other fuels (53%), with oil still being widely used (22%). The Middle East is dominated by natural gas (51%) and oil (45%). In Africa, oil consumption is predominant (41%), with natural gas (30%) and coal (20%) also being widely used. In the Asia Pacific region, coal is the primary fuel (47%), followed by oil (26%).[4]

Although the demand for natural gas, a relatively less carbon-intensive fossil fuel, remained unchanged, the escalated use of more carbon-intensive oil and coal led to another negative record: energy-related greenhouse gas emissions, which breached 40 $GtCO_2$ for the first time ever. The most important source of CO_2 energy-related emissions remains fossil fuel combustion, accounting for approximately 87% of the total. If CO_2 emissions were maintained close to recent levels, the carbon budget estimated by the Intergovernmental Panel on Climate Change (IPCC) to be consistent with a high probability of limiting average global temperature increases to 2°C would be exhausted by the early 2040s.

However, there is a changing composition of energy demand over the outlook, which is characterized by three main trends: a gradual and slight decline in the role of hydrocarbons, rapid growth in renewable energy, and increasing electrification of the world, supported by low-carbon hydrogen in processes and activities that are hard to electrify. In fact, renewable energy sources accounted for 14.6% of total primary energy consumption in 2023, a 0.4% increase from the previous year. In addition to nuclear energy, they represented more than 18% of total primary energy consumption. Renewable energy is largely made up of wind, solar power and bioenergy and includes geothermal power. Projections show that the share of renewables in global primary energy increased from approximately 10% in 2019 to between 35% and 65% by 2050, driven by the improved cost competitiveness of renewables, together with the increasing prevalence of policies encouraging a shift to low-carbon energy and enormous investments, with a very rapid increase of approximately 50% since 2019, reaching approximately $1.9 trillion in 2023.

This growth has been driven by wind and solar energy. In particular, the capacity of solar photovoltaics (PV) experienced rapid growth in 2023, surpassing the previous year's record, with +32.2% of installed capacity worldwide. Although growth is occurring on a global scale, Asia is experiencing the most impressive growth, dominating the market with a 61.6% share of the international total, with China accounting for 69.8% of that share. Europe follows with a share of 21.1%. Notably, the highest growth rate is observed in South and Central America, with a 39.4% increase compared to the previous year (Table 1).[4]

Country	Growth Rate in 2023 (%)	Share 2023 (%)
North America	20.8	11
South and Central America	39.4	3.8
Europe	23.1	21.1
CIS	24.2	0.3
Middle East	32.6	1.3
Africa	6.1	0.9
Asia Pacific	38.2	61.6

Table 1: Annual Installed Photovoltaic Growth Rate and Market Share in 2023 by region.[4]

Europe's Photovoltaic Dilemma: Addressing the Gap with China through Technological Diversification

China's dominance in the photovoltaic (PV) market, particularly with silicon technology, is a testament to its strategic investments and aggressive expansion in the renewable energy sector.

In 2023, solar energy accounted for more than 70% (346 GW) of the renewables' capacity additions, with China contributing to approximately a quarter of this growth.[5] On the other hand, Europe has installed just over 56 GW of solar energy, representing only 16% of the total amount of solar capacity added (Figure 4).

China sets up as the global leader in renewable energy. The country is projected to account for nearly 60% of the new renewable capacity expected to come online worldwide by 2028.

Despite the phase-out of national subsidies in 2020 and 2021, the deployment of onshore wind and solar PV systems in China is accelerating.

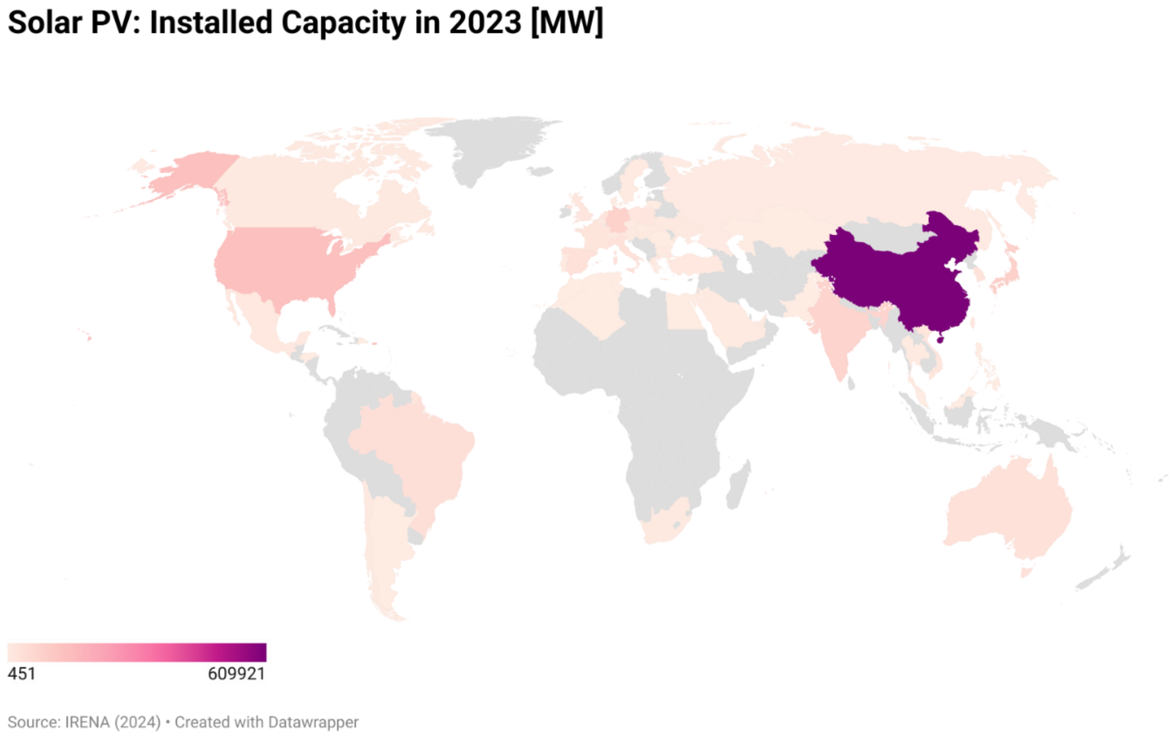
Solar PV: Installed Capacity in 2023 [MW]

Source: IRENA (2024) • Created with Datawrapper

Figure 4: Map of the installed photovoltaic (PV) capacity for each country around the world. Countries shaded in grey indicate that data was not available. The map provides a visual representation of the global distribution.

Several factors contribute to China's dominance. Massive investment, with over $130 billion allocated this year alone, has allowed China to hold more than 80% of the world's polysilicon, wafer, cell, and module manufacturing capacity through 2026.[6] China's share of the Asia Pacific region's production is staggering at 69.8%, with a 43% global share.[7] This is the highest rate, followed by the 9.8% share of the USA and the 5.08% share of Germany. Additionally, the cost competitiveness of Chinese-made modules, which are 50% cheaper than those produced in Europe and 65% cheaper than those produced in the US, presents a significant barrier for other regions to compete effectively. Strong and supportive government policies and incentives have further supported the rapid growth of China's solar industry, boosting both domestic production and global exports. This results in China being able to produce 2.2 times the module capacity that is installed worldwide (Figure 5).

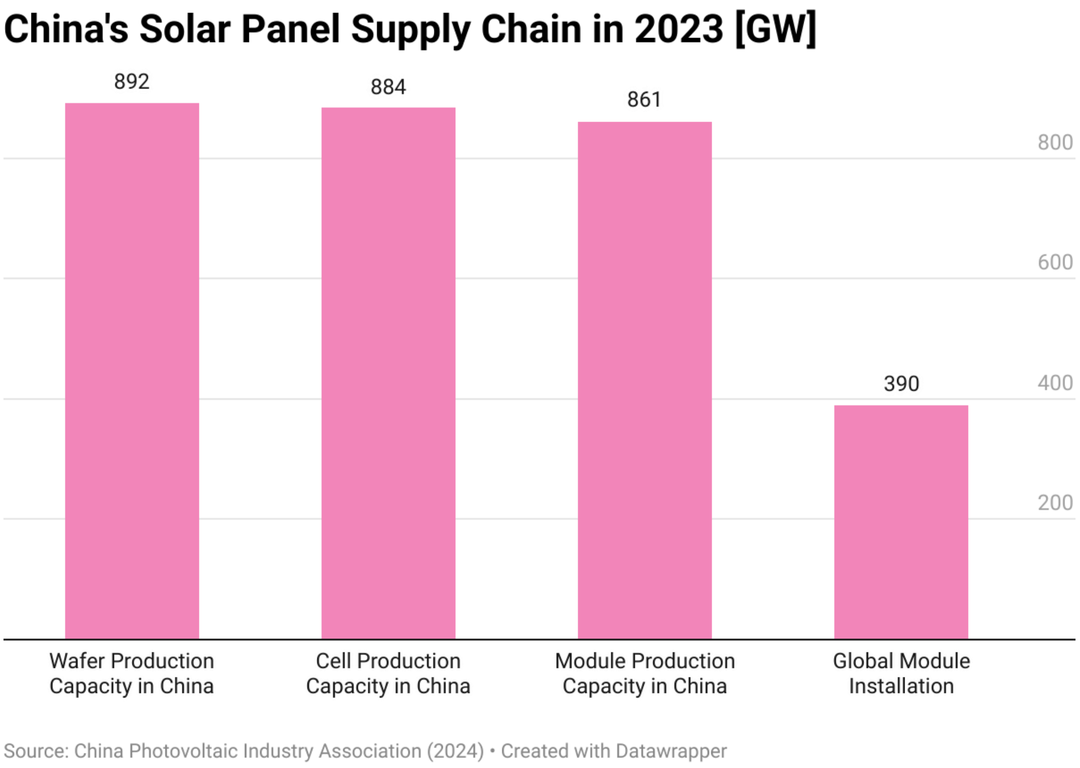

Figure 5: Solar panel supply chain in China as of 2023. China currently produces 2.2 times the globally installed PV capacity.[8]

The projections from Climate Energy Finance show that China will achieve its national 2030 target for wind and solar PV installations this year, six years ahead of schedule.[9] China's role is pivotal in meeting the global goal of tripling renewable energy capacity, as the country is expected to install more than half of the new capacity required globally by 2030.

Europe's struggle to compete is evident in its limited production capacity and higher production costs. Despite the efforts, Europe has not been able to compete China's production capacity. In 2023, Europe contributed only 2% of the total PV module production, whereas China contributed 86%.[10] The higher cost of producing solar modules in Europe makes it difficult for European manufacturers to compete with Chinese products. This cost disparity, a dependence on Chinese supply and the absence of control in the raw materials mining and purification, are impossible challenges for Europe to overcome. Even with plans for module capacity expansion in the U.S. and India, which announced more than 200 GW of planned module capacity since 2022, driven by initiatives such as the Inflation Reduction Act (IRA) in the U.S. and the Production Linked Incentive (PLI) in India, overseas markets still cannot eliminate their dependence on China for wafers and cells in the next three years.[4]

The Inefficacy of Protectionist Measures in European Solar Panel Production: Prioritizing Innovation and Deployment for Enhanced Resilience

European solar panel manufacturers are advocating for financial assistance from European governments, proposing measures such as import tariffs, subsidies for domestic production, and the purchase of excess inventories. However, a critical examination of such protectionist policies reveals their inefficacy and potential for adverse effects. In 2013, the European Union imposed tariffs on Chinese solar panels following industry complaints of unfair competition. This intervention not only failed to stimulate significant growth in European manufacturing capacity but also impeded solar deployment, thereby undermining climate goals.

Similarly, the proposal to subsidize the domestic production of 'made in Europe' solar panels is flawed. This approach is driven by ongoing negotiations in Brussels, which target 40% of Europe's demand for various clean technologies to be met by domestic production by 2030. However, this blanket strategy overlooks the unique value chains, existing competencies, and global market dynamics of different technologies. The global solar market is currently oversupplied, and minimal climate benefits are gained from subsidizing additional production. Furthermore, Europe lacks a competitive advantage in terms of full manufacturing processes, with the majority of solar jobs located in the installation sector rather than manufacturing.

While concerns about excessive dependency on foreign suppliers are legitimate, particularly in light of Europe's reliance on Russian natural gas, neither tariffs on Chinese solar panel imports nor indiscriminate subsidies to European manufacturers offer a viable solution. Instead, the EU should explore more nuanced strategies to bolster resilience. One such approach could be the establishment of a strategic stockpile of solar panels, a strategy that the EU has overlooked for years but is beginning to reconsider, for example, critical raw materials. This could be achieved by requiring large European deployers to maintain a certain share of their market as reserves. This would ensure a margin of flexibility in the event of an abrupt halt to supplies from China. Additionally, the EU should intensify efforts in solar panel recycling, which is not only important for environmental reasons but also serves as a future source of raw materials needed for panel manufacturing.

Beyond the solar sector, fostering resilience requires a holistic, economy-wide approach that focuses on areas where Europe can realistically develop its own economic advantages and firms that are not overly reliant on subsidies. Pursuing China's dominance in the mass-produced, oversupplied silicon technology markets is unlikely to yield success.

By diversifying its focus to invest in innovative PV technologies, rather than domestic content, Europe can reduce its dependence on Chinese supply and carve out a niche in the global solar market. This strategic shift could not only enhance Europe's competitiveness but also drive technological advancements in the renewable energy sector. Even within the rapidly evolving solar sector, there is substantial scope for innovative new products, materials and technologies.

1.2 Photovoltaic Materials and Technology State of the Art

PV energy is based on the production of electricity through the photoelectric effect, using sunlight as the primary direct source. On average, the sun irradiates 1367 W/m^2 at the Earth's atmospheric boundaries, with an effective power of approximately 174,300 TW. Of this value, about 30% is reflected back or absorbed by the atmosphere, and a portion falls on the oceans; however, the potential power that can be captured on land remains enormous, in the order of several tens of thousands of TW (to give an idea, consider that the average power of a large power plant is around 1 GW). The amount of solar energy that reaches the Earth's surface is therefore enormous, about ten thousand times greater than all the energy used by humanity as a whole. The availability of an unlimited source, as well as the costs, longevity, and stability of the devices, allow this technology to maintain a monopoly on the renewable energy market, even though only a tiny fraction is currently exploited.

In recent years, research in this field has sought to honor the promise of further room for improvement in terms of cost, optimization, and Power Conversion Efficiency (PCE), the most important parameter of a solar cell: this indicates how effectively the cell converts sunlight into electrical energy, expressed as a percentage of the total incident solar radiation power.

1.2.1 The Evolution of Photovoltaic Technology: An Overview of the Three Generations and the Photovoltaic Landscape

1.2.1.1 1st generation devices

The first-generation devices are the most widely used commercially, making up about 97% of the PV market in 2023.[10] These are the so-called crystalline silicon (c-Si) based solar cells.

In 2023, mono-crystalline silicon cells account for around 97% of the global annual production.[10] The production of mono-crystalline silicon cells begins with the purification of metallurgical-grade silicon, which is extracted from silicon dioxide found in sand or quartz. The purified silicon is then melted, and a single crystal is grown using the Czochralski method, where a seed crystal is dipped into the molten silicon and slowly pulled up while rotating, forming a large, cylindrical ingot. This ingot is sliced into thin wafers using a wire saw, and the wafers are treated to remove any damage and contaminants. After the deposition, doping is performed to create p-type and n-type regions, forming the p-n junction necessary for the solar cell to function. To complete the device, an antireflection coating is applied to minimize sunlight reflection, and metal contacts are added to the front and back surfaces. This structure results in a uniform, dark appearance and high efficiency, with a PCE of around 20%. The laboratory-scale record of mono-Si cells is currently 26.8% (Figure 6). The high cost, related to this complex manufacturing process, limits them mainly to the space-constrained applications, where extremely high efficiency is needed.

Poly-crystalline silicon solar cells have a market share of around 0.8% of c-Si production.[10] The difference with mono-crystalline silicon is that, once the Si is purified, it is melted and cast into large blocks or ingots using a process called directional solidification. During this process, the molten silicon is cooled and solidified in a controlled manner, resulting in a poly-crystalline ingot composed of multiple small crystals, which gives it a distinctive blue, speckled appearance. These cells are typically cut into square wafers, reducing waste during manufacturing. Poly-crystalline cells are generally less efficient than mono-crystalline cells, with efficiencies ranging from 15% to 19%, and a laboratory-scale efficiency of 24.4% (Figure 6). However, their production cost is significantly cheaper compared to mono-crystalline cells. This makes them a more cost-effective option for many applications, such as in residential and commercial solar installations.

Both c-Si types are known for their durability and stability, with lifespans of 25–30 years or more.

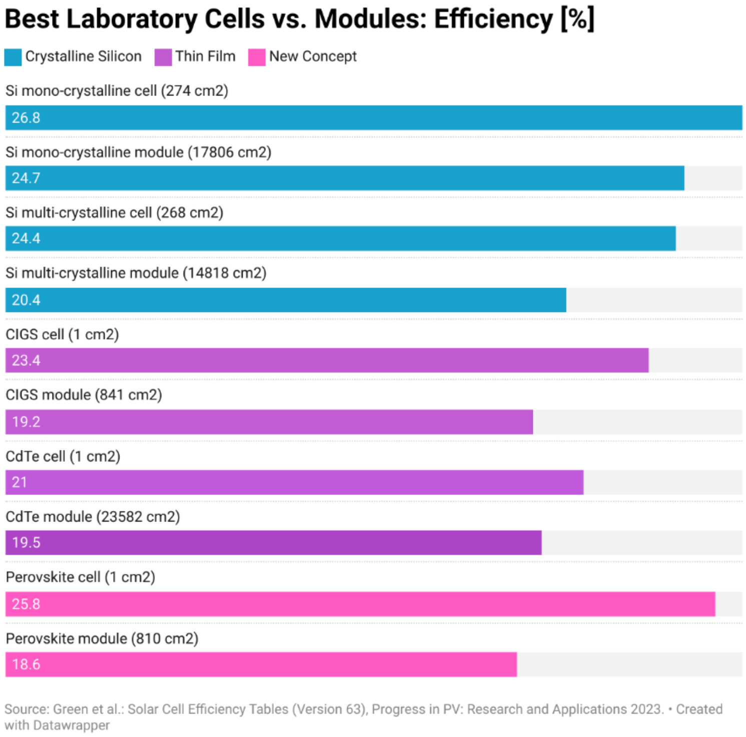

Source: Green et al.: Solar Cell Efficiency Tables (Version 63), Progress in PV: Research and Applications 2023. • Created with Datawrapper

Figure 6: Comparison of Laboratory Cell Efficiencies and Module Efficiencies by Photovoltaic Generation. It includes only the most widely adopted technologies for each generation.[10]

However, the silicon PV technology is almost saturated, both from the efficiency and the cost reduction point of view. Talking about efficiencies, this is due to a combination of practical material/devices limitations (grading, anti-reflective coats), which the main topic on the ongoing research in this field, and fundamental physical limits. In fact, silicon does not have optimal absorption in the near UV region of the solar spectrum, which allows only a limited portion of the radiation to be converted efficiently. Moreover, theoretical simulations estimate that in the single p-n junction devices, such as the silicon one, there is an upper limit of conversion efficiency of 32% due to recombination of carriers and thermal losses for these solar cells, the so-called “Shockley-Queisser limit”.

From the cost point of view, it is not even possible to further reduce production costs today. In fact, silicon is currently one of most abundant and cheapest raw materials; the main costs of the devices are represented by the glass and the polymers used to incapsulate and from the metal grids, which cannot be replaced in the actual technology.

This is why, since the 1970s, second-generation devices based on thin film technology have also been introduced on the market.

1.2.1.2 2nd generation devices

Second-generation devices are characterized by the use of various semiconductor materials that form layers of 1-4 µm deposited on inexpensive materials (glass, polymers, metals, etc.) and can be assembled on flexible and lightweight structures. The most widely used technologies are based on:

1. Amorphous Silicon (a-Si): Amorphous silicon is deposited onto the substrate using techniques such as plasma-enhanced chemical vapor deposition (PECVD).[11] During this process, silane gas (SiH_4) is introduced into a vacuum chamber, where it is decomposed by a plasma to form a thin layer of amorphous silicon. Unlike crystalline silicon, amorphous silicon has a disordered atomic structure, making it more prone to defects and impurities. For this reason, hydrogen is often added to passivate defects and dangling bonds, improving the material's electronic properties and stability. After deposition, the material is doped to create p-type and n-type regions, which form the essential p-n junction for the solar cell's functionality. Just like single-junction c-Si devices, an antireflection coating is then applied to reduce sunlight reflection, and metal contacts are added to both the front and back surfaces.

   The efficiency of a-Si solar cells typically ranges from 7% to 10%, with the highest reported efficiency being 12.69%.[12] These cells are significantly cheaper compared to c-Si technology, but their PCE is still too low for them to be widely adopted in the market, and they can suffer from degradation over time, affecting their long-term performance.

2. Cadmium Telluride (CdTe): These cells are the most widely used second-generation devices on the market, holding over 90% share of these devices on the market. They are known for their high absorption coefficient, which allows them to absorb a significant portion of the solar spectrum with a very thin layer of material. The CdTe cells are prepared by depositing the semiconductor layer onto the substrate using various techniques such as close-space sublimation, electrodeposition, or sputtering. During this process, cadmium and tellurium are heated and vaporized, then deposited as a thin film on the substrate. The CdTe layer is subsequently treated with cadmium chloride ($CdCl_2$) to improve its electrical properties and grain structure. A buffer layer, often made of cadmium sulfide (CdS), is deposited on top of the CdTe layer to form the p-n junction. Finally, a back contact, typically made of a conductive material like copper or graphite, is applied.

   CdTe solar cells have achieved efficiencies of up to 22% in laboratory settings (Figure 6) and are commercially viable with efficiencies up to 19%.[13] However, the use of toxic materials like cadmium in CdTe solar cells raises environmental and health concerns, requiring careful handling and disposal.

3. Copper Indium Gallium Selenide (CIGS): CIGS solar cells use a solid solution of copper (C), indium (I), gallium (G), and selenium (S). These cells are known for their high absorption coefficient and flexibility in element composition within the solid solution, which allows for tuning the band gap to optimize solar energy conversion. For cell preparation, the CIGS thin film is typically deposited onto a molybdenum substrate using vacuum techniques such as co-evaporation, sputtering, or electrodeposition. Then, a buffer layer, often made of CdS, is deposited on top of the CIGS layer to form the p-n junction. Finally, a transparent conductive oxide (TCO) layer, such as zinc oxide, is applied to the front surface to facilitate electrical contact.

   CIGS solar cells have achieved efficiencies of up to 23.4% in laboratory settings (Figure 6) and are commercially viable with efficiencies typically around up to 22%.[14] However, they contain rare and expensive elements, such as gallium and indium. Also, the techniques used for thin-film deposition are typically expensive. Since the costs of the core elements cannot be reduced at present, it is mandatory to develop cheaper techniques and cell structures.

4. Copper Zinc Tin Sulfide (CZTS): CZTS solar cells use a compound semiconductor made of copper (C), zinc (Z), tin (T), and sulfide (S). These cells are considered an alternative to CIGS cells, as they do not contain rare and expensive elements like indium and gallium. The architecture of the cell is basically the same, but CZTS can be deposited using co-evaporation, sputtering, or solution-based methods, reducing the costs.

   CZTS solar cells have shown promise but are still in the development stage, with efficiencies typically lower than CIGS cells.

Regardless of the semiconductor involved, this technology has offered and continues to offer prospects for cost reduction at equal efficiency with those of the previous generation, but in year 2023 it contributed with about 2.5% to the total PV-market.[10] While it was necessary to develop alternative technologies to try to reduce the silicon production costs, and the thin-film technology is a good alternative, we still have the same physical limitations of absorption and Shockley-Queisser limits, as the second-generation devices are made with a single-junction, similar to the first-generation ones.

1.2.1.3 3rd generation devices

To exceed this limit once again, the so-called third generation of photovoltaics is historically introduced, which includes various frontier technologies. The main representative and competitive technologies of this category are:

- Quantum Dot-based solar cells: Quantum dot solar cells represent an innovative approach to photovoltaic technology, utilizing nano-scaled semiconductor particles known as quantum dots. These particles have unique optical and electronic properties due to quantum confinement effects, which allow them to absorb a broader range of the solar spectrum compared to traditional solar cells. Quantum dots can be tuned to absorb specific wavelengths of light by adjusting their size and composition, making them highly versatile for solar energy conversion.

The primary advantage of quantum dot solar cells is their potential for high efficiency. By capturing a wider range of sunlight, these cells can theoretically achieve efficiencies exceeding the Shockley-Queisser limit of single-junction solar cells. Additionally, quantum dot solar cells can be manufactured using low-cost, solution-based processing techniques, such as spin-coating or printing, which makes them suitable for large-scale production.

However, quantum dot solar cells face several challenges that need to be addressed for their widespread adoption. One of the main issues is stability. Quantum dots are sensitive to environmental factors like oxygen and moisture, which can lead to degradation and reduced performance over time. Another concern is the use of toxic elements like lead and cadmium in many high-performing quantum dot materials, which raise environmental and health concerns.

- Organic photovoltaic devices (OPV): OPV solar technologies utilize organic materials, such as polymers and small molecules, to convert sunlight into electricity. Unlike traditional silicon-based solar cells, OPV cells are made from carbon-based materials that are lightweight, more flexible, and can be processed using low-cost, large-scale manufacturing techniques like printing or coating. This makes OPV cells particularly suitable for applications where flexibility and low weight are important, such as in wearable electronics, building-integrated photovoltaics (BIPV), and portable devices.

  One of the key advantages of OPV cells is their potential for low-cost production. The materials used in OPV cells are abundant and relatively inexpensive, and the manufacturing processes are simpler and less energy-intensive compared to those for inorganic solar cells. Additionally, OPV cells can be made semi-transparent, making them ideal for integration into windows and other transparent surfaces.

However, OPV cells currently face challenges in terms of efficiency and stability. The power conversion efficiencies of OPV cells are generally lower than those of inorganic solar cells, typically ranging from 5% to 15%.[15] Furthermore, the organic materials used in OPV cells can degrade over time when exposed to light, heat, and oxygen, which affects their long-term performance.

- Hybrid Perovskite Solar Cells (PSCs): Hybrid Perovskite solar cells represent a cutting-edge technology which combines the advantages of organic and inorganic materials to convert sunlight into electricity. These cells are based on a class of materials known as perovskites, which have a crystal structure characterized by the general formula ABX_3, where A and B are cations and X is an anion. In hybrid perovskites, the A cation is typically an organic molecule, such as methylammonium ($CH_3NH_3^+$), while the B cation is usually a metal like lead (Pb^{2+}) or tin (Sn^{2+}), and the X anion is often a halide like iodide (I^-) or bromide (Br^-).

One of the key advantages of hybrid perovskite solar cells is their high PCE. These cells have achieved efficiencies exceeding 25% in laboratory settings,[16] rivaling the performance of traditional silicon-based solar cells. This high efficiency is attributed to the unique properties of perovskite materials, including strong light absorption, high charge carrier mobility, defect tolerance and long carrier diffusion lengths.

Hybrid perovskite solar cells are also attractive due to their potential for low-cost production. The materials used in these cells are relatively abundant and inexpensive, and the manufacturing processes, such as solution processing and printing techniques, are simpler and less energy-intensive compared to those for silicon solar cells. Additionally, perovskite materials can be deposited on flexible substrates, making them suitable for applications where flexibility and low weight are important, such as in wearable electronics and BIPV.

However, hybrid perovskite solar cells face several challenges that need to be addressed for their widespread adoption. One of the main issues is stability. Perovskite materials are sensitive to moisture, heat, and light, which sooner or later lead to degradation and reduced performance over time. Another drawback is the use of toxic elements like lead in many high-performing perovskite materials, which raises environmental and health concerns.

Ongoing research and development efforts are focused on improving the stability, efficiency, and environmental friendliness of hybrid perovskite solar cells. Advances in material science, device architecture, and manufacturing techniques are expected to enhance the performance and durability of these cells, making them more competitive with traditional solar technologies and expanding their range of applications.

- Multi-junction solar cells

Multi-junction solar cells are engineered to surpass the efficiency limitations of single-junction cells by layering multiple semiconductor materials, each with a unique band gap. This design enables the cell to harness a wider part of the solar spectrum, significantly boosting the overall efficiency. Each layer captures a specific range of photon energies, with the top layer absorbing high-energy photons and the bottom layer capturing lower-energy photons. These layers are electrically connected in series, combining the current generated by each layer.

Common multi-junction cells consist of three or more layers, often incorporating expensive materials like gallium indium phosphide (GaInP), gallium arsenide (GaAs), gallium nitride (GaN) and germanium (Ge). Since typically these materials are grown with extremely expensive vacuum techniques (for example, Metalorganic Chemical Vapor Deposition (MOCVD) or Molecular Beam Epitaxy (MBE)), [17] these cells are typically employed in high-efficiency applications, such as space satellites and concentrated photovoltaic (CPV) systems, where maximizing power output is essential. Multi-junction solar cells have achieved efficiencies reaching 39.46% in laboratory settings[18] and are commercially viable with efficiencies typically around 30% to 40%.[19]

Although multi-junction cells offer superior efficiency, they are more complex and costly to produce compared to single-junction cells. For this reason, one of the biggest challenges is obtaining multi-junction cells from pre-existing optimized technologies, for example, combining as different layers the commercial silicon cells, the thin-film CIGS technology or also the hybrid-perovskite one, caring to better match the optical and mechanical properties of this. Ongoing research focuses on reducing production costs and enhancing performance, aiming to make these advanced solar cells more accessible for a broader range of applications.

1.3 Aim of this thesis

In this PhD thesis, I have conducted an in-depth study of two distinct classes of PV materials: the chalcogenides belonging to the series $Cu(In_{1-x}Ga_x)(S_ySe_{1-y})_2$ (CIGSSe) and a chalcohalide SbSI. Given the extensive introduction of the solar community background in the previous chapter, it is evident that one focus of the research in the solar PV field must be on exploring various alternative technologies to silicon. To make these alternatives viable in the industrial landscape, it is imperative to reduce manufacturing and production costs.

In light of this objective, I have emphasized the use of low-cost synthesis and deposition techniques wherever feasible. Specifically, I have investigated several chalcogenides within the CIGSSe class, synthesizing them in the solid state using a green, low-cost, and scalable technique known as high-energy ball milling. This method avoids the use of toxic solvents, making it an environmentally friendly option.

My research has concentrated on various solid solutions for different purposes. I have explored low bandgap solutions such as $CuInSe_2$ (1.1 eV)[20] and $CuInS_2$ (1.45 eV),[21] which are suitable for standalone thin-film solar cells. Additionally, I have aimed to increase the bandgap of these materials by manipulating their composition, synthesizing $CuInGaS_2$ and $CuGaSSe_2$ directly.[22] I have also employed mechanochemistry to reduce the size of these materials to the sub-micrometer scale, mimicking the properties and advantages of quantum dots. This approach allows for their use as top cells in multi-junction devices.

To maintain low production costs, I have utilized physical deposition techniques from the liquid phase, such as drop casting, spin coating, and doctor blade. These methods involve redispersing the solid-state synthesized materials in common organic solvents, a technique that, to the best of my knowledge, has not been reported in the literature at the time of this thesis. The resulting suspensions have shown promise in interfacing with perovskites, paving the way for the potential realization of multi-junction perovskite-CIGSSe systems.

Furthermore, I have synthesized the chalcohalide SbSI using high-energy ball milling for the first time in literature. The aim is to use SbSI as a PV absorber in standard thin-film devices, as well as a key material in the development of ferro-photovoltaic cells, a conceptual and emerging technology. For the deposition of the thin film, two approaches were explored: (i) liquid-phase deposition, similar to the method used for CIGSSe, and (ii) a vacuum technique known as pulsed electron deposition (PED), which utilizes a target made from SbSI synthesized via high-energy ball milling.

The overarching goal of my thesis is to demonstrate that there is still significant progress to be made and numerous opportunities to be explored in the research of alternative materials and technologies. Through my work, I aim to contribute to a small but meaningful advancement in this field.

2 MATERIALS, TECHNOLOGIES AND METHODS

This chapter deals with materials, technologies, and methods that I have used in the context of this thesis. Herein, it is reported a detailed overview about the properties of materials and the different technologies which are related to this research , together with a discussion on the basic principles on theory and functioning of photovoltaic cells, the physics behind and other details on experimental setups, and characterization techniques employed to achieve the scientific objectives.

2.1 Materials

2.1.1 $Cu(In_{1-x}Ga_x)(S_ySe_{1-y})_2$ chalcogenides

Crystal Structure of Copper-Based I-III-VI_2 Compounds

Copper-based I-III-VI_2 chalcogenides, such as $CuInSe_2$ **(CISe)**, $CuGaSe_2$ **(CGSe)**, $CuInS_2$ **(CIS)**, Cu(In,Ga)Se_2 **(CIGS)**, and CuIn(Se,S)$_2$ **(CISSe)** solid solutions, exhibit either a tetragonal chalcopyrite structure (space group $I42d$) or a cubic sphalerite symmetry (space group $F43m$). Additionally, these compounds can exhibit CuAu (CA)-type, CuPt-type, and ordered vacancy compound (OVC) structures (Figure 7); these are generally less interesting for PV applications due to their complex crystal structure, which makes them difficult to grow as high-quality thin films.

Additionally, their electronic properties are less suitable for efficient light absorption and charge carrier generation compared to the chalcopyrite phase. These phases may also suffer from stability issues, leading to material degradation over time. Furthermore, the overall efficiency of solar cells is generally lower, and the manufacturing processes are more complex and costly, as these phases are typically obtained under high pressure/high temperature conditions.[23]

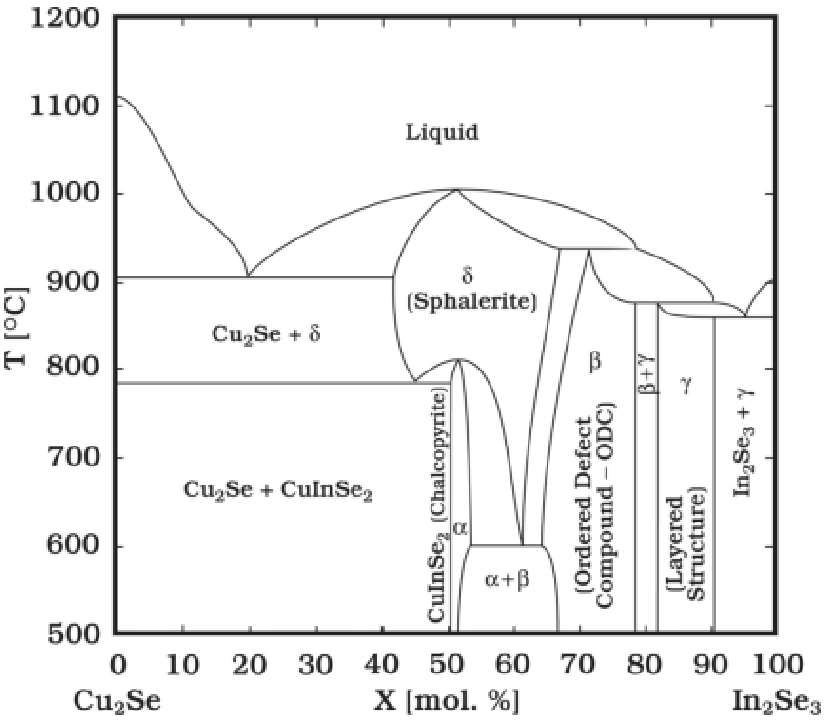

Figure 7: Phase diagram along the Cu_2Se-In_2Se_3 pseudo binary section of the Cu-In-Se chemical system.[24]

The phase with much more photovoltaic interest is the chalcopyrite. In this structure, generically ABC_2, the lattice is body-centered tetragonal (space group $I\bar{4}2d$) with four atoms per unit cell. Each A and B atom is tetrahedrally coordinated to four C atoms, while each C atom is tetrahedrally coordinated to two A atoms and two B atoms in an ordered manner. The chalcopyrite structure can be viewed as a superstructure of the zinc blende (sphalerite) structure, arising from an ordered substitution of zinc blende metal atoms of valence Z (Figure 8). This ordered substitution doubles the unit cell size in the z-direction. If A and B atoms are randomly distributed, the sphalerite structure results.

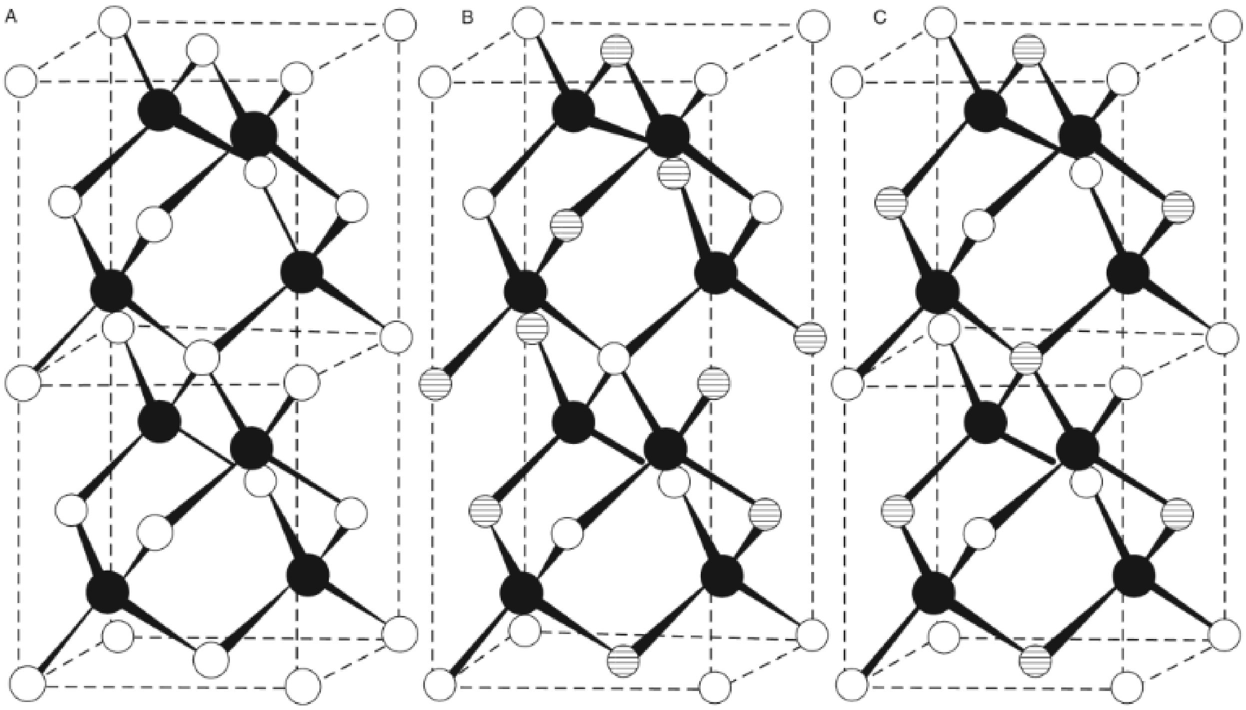

Figure 8: Crystal Structure of CuInSe$_2$ (A) Sphalerite or Zinc blende (○ Zn atom (Cu or In) and ● se atom), (B) Chalcopyrite (○ Cu, ◍ In, and ● Se), and CuAu (CA) (○ Cu, ◍ In, and ● Se).[25]

The precise location of C atoms in the chalcopyrite structure depends on the strengths of A-C and B-C interactions. Robins' atomic pressure theory suggests stronger bonding of C atoms with their two nearest neighbors due to A-atom d-electron conduction to the bonding. As a consequence, the C-atoms being shifted from their ideal positions by a small amount, characteristic of the chalcopyrite structure and it is usually quantified by [2-(c-a)].[25]

The atomic positions in the chalcopyrite structure are as follows:

- A-atom: (0,0,0), (1/2,0,1/4), (1/2,1/2,1/2), (0,1/2,3/4)
- B-atom: (1/2,1/2,0), (0,1/2,1/4), (0,0,1/2), (1/2,0,3/4)
- C-atom: (3/4,1/4+2,1/8), (1/4,3/4-2,1/8), (1/4-2,1/4,3/8), (3/4+2,3/4,3/8)
- Vacancy: (3/4,1/4-2,5/8), (1/4,3/4+2,5/8), (1/4+2,1/4,7/8), (3/4-2,3/4,7/8)

The primary intensity peaks are (112), (204, 220), and (116, 312). The (112) peak is typically the highest intensity peak, followed by (204, 220) and then (116, 312). These peak intensities depend on growth conditions such as substrate temperature and the ratio between the element compositions. Characteristic chalcopyrite peaks, such as (101), (103), (211), (213), (105), and (301), are often observed but can be difficult to distinguish from noise in X-ray diffraction (XRD) patterns due to their low intensities, particularly in thin films.

The chalcopyrite structure is converted into the CA structure by transforming alternating (100) A cation planes by a/2 in a <100> direction, as shown in Figure 8. In the OVC structure, the ($2V_{Cu}+ In_{Cu}$*) defect pair plays a major role in reconstructing the crystal structure. However, the chalcopyrite structure is tolerant to small shifts due to atom substitutions, making it ideal for creating a wide range of solid solutions.

Optoelectronic Properties

The great advantage of films made from these copper-based solid solutions is that the optical bandgap, typically direct, can be modulated by varying the cationic ratio In/Ga (x) and the anionic ratio S/Se (y), ranging from 1.04 eV (CISe)[27] to 2.5 eV (CGS). The bandgap values for other common chalcopyrites are reported in Table 2.

The band structure characteristics of the ternary or multinary (TMCC) Cu-chalcogenides differ from those of conventional II–VI compounds. The valence band maximum is higher, and the bandgap is narrower than II–VI compounds. Therefore, the electrons in the valence band of TMCC are easily removed, and TMCC tends to be a p-type semiconductor. This common characteristic of TMCC as well as their typically very high absorption coefficient ($>10^4$ cm^{-1})[26] makes this class of chalcogenides suitable to be employed as absorber materials in thin-film solar cells.

Material	Bandgap [eV]	Efficiency [%]	Reference
$CuInSe_2$	1.04	14.5	J.A.M. Abushama *et al.*, 1993[27]
$Cu(In,Ga)Se_2$	1.09	22.8	K. Rui *et al*, 2016[28]
$CuGaSe_2$	1.68	11.0	S. Ishizuka *et al*, 2013[29]
$CuInS_2$	1.5	11.4	K. Siemer *et al*, 2001[30]
$Cu(In,Ga)S_2$	1.57	15.5	H. Hiroi *et al*, 2016[31]
$CuGaS_2$	2.5	1	K. Tanaka *et al*, 1989[32]

Table 2: Bandgap and efficiencies of solar cells made from various chalcopyrites.

Wada et al. showed that the VBMs of the I–III–VI_2 chalcopyrite compounds consist of the antibonding orbitals of (I nd + VI n'p) and the CBMs consist of the antibonding orbitals of (III n's + VI n'p). The electronic structure of I–III–VI_2 chalcopyrite compounds can be better understood depicting the schematic molecular orbital diagrams of $(I–VI_4)^{7-}$ and $(III–VI_4)^{5-}$ clusters.[33]

Using CISe as an example, *W. Takahiro et al.* reproduced in Figure 9 the schematic molecular orbital diagrams of $CuSe_4^{7-}$ and $InSe_4^{5-}$ clusters.[34] The orbital of the VBM (HOMO) consists of the antibonding orbital of Cu 3d and Se 4p, and the orbital of the CBM (LUMO) consists of the antibonding orbital of In 5s and Se 4p. The bandgap of CISe is the difference between the VBM and CBM energy levels. Therefore, the CBM level changes significantly by substituting a group III element, such as In with Ga, but not the VBM, which is affected by the substitution of a group I element, such as substituting Cu with Ag.

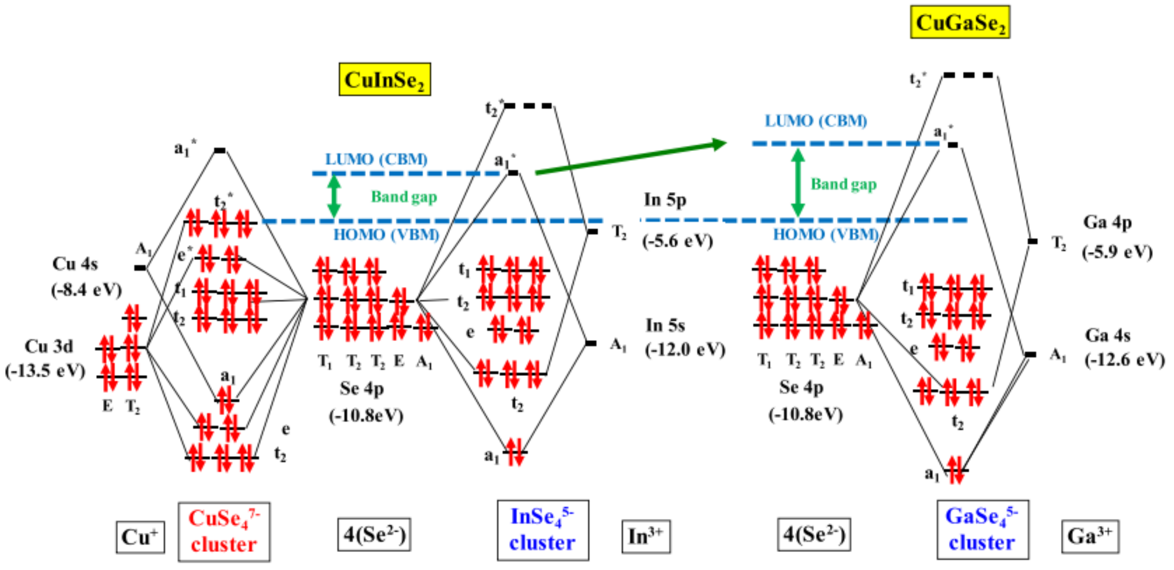

Figure 9: Schematic molecular orbital diagrams of $CuSe_4{}^{7-}$, $InSe_4{}^{5-}$ and $GaSe_4{}^{5-}$.

For this reason, the VBM level of the $Cu(Ga_xIn_{1-x})Se_2$ solid solution system does not change significantly when the In/Ga ratio is changed, while the CBM does. Indeed, both VBM and CBM levels change significantly by substituting a group VI element, such as Se with S (Figure 10).

All these compounds may exhibit p, n, or intrinsic-type conduction, depending on the composition inside the solid solution. Typically, a Cu percentage greater than 25% or an excess of the chalcogen ion leads to strong p-type conductivity, while the contrary means intrinsic or n-type conductivity. The Cu vacancies are considered responsible for this behavior, as they act as acceptors and capture an electron from the valence band, leaving behind a mobile hole in the valence band and thus resulting in p-type conduction. For the same reason, indium/gallium deficiencies induce n-type conductivity, as they act as donors.[35]

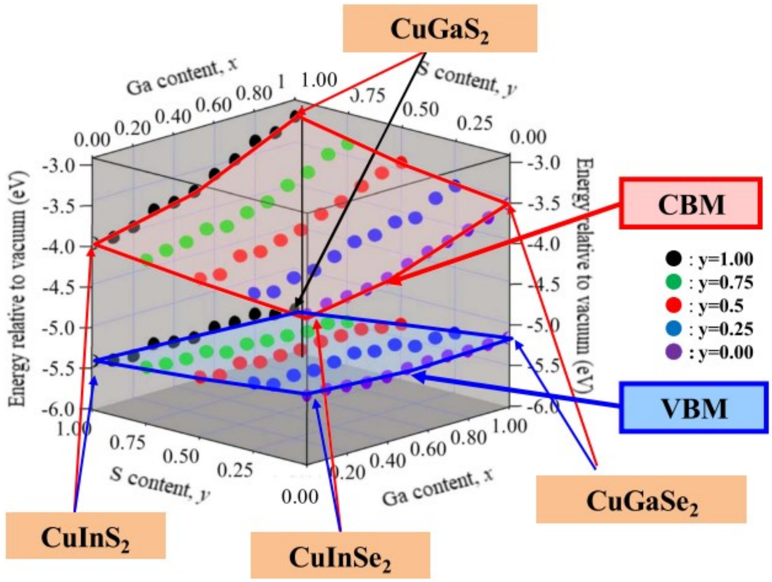

Figure 10: Energy levels of the VBM and CBM from the vacuum level of the $Cu(Ga_xIn_{1-x})(S_ySe_{1-y})_2$ chalcopyrite system as a function of Ga content (x), and S content (y).[34]

State of the art

Chalcogenides of the class $Cu(Ga_xIn_{1-x})(S_xSe_{1-x})_2$ are currently obtained through complex and costly vacuum deposition processes such as co-evaporation,[36,37,38] sequential sputtering,[39,40,41] Pulsed Laser Deposition,[42,43,44] and Low Temperature - Pulsed Electron Deposition.[45,46] These processes address the thermodynamic stability issues arising from the intricate phase diagram of the compound and ensure the formation of the chalcopyrite phase over other non-PV stoichiometries. All these techniques allow the production of thin films with a high level of purity and good morphological quality for PV applications, but with current technology, cost reduction is challenging. CIS[47] and CIGSe[48] has also been synthetized via high energy ball milling, but no other solid solutions have been reportedly obtained with this method. In addition to the high cost of vacuum systems maintenance, sputtering, PLD, and LT-PED techniques use bulk polycrystalline solid targets as chalcogenides' source; but, since the incongruent melting and phase diagram, it is difficult to obtain these targets at low cost. Up to date, they are primarily obtained through melt growth techniques such as the Czochralski method, the Bridgman method, or Hot Isostatic Pressing (HIP).[49]

To overcome the limitations of vacuum techniques and target synthesis, less costly solution-based methods have been progressively studied. These methods involve the use of a solution of metallic elements that will form the film. The main techniques include coating (spray, spin, dip), which involves the direct deposition of the product onto a substrate through various coating mechanisms. These techniques have the advantage of being practical and simple but require significant use of solvents,[50] mainly toxic (e.g. hydrazine).[51] These deposition methods often do not allow to create a film of sufficient quality for direct PV application: typically, suboptimal homogeneity and bad adhesion are obtained, as well as the formation of a significant number of defects both at the macroscopic and the microscopic level which limits efficiency. Therefore, post-treatments such as thermal annealing in a controlled atmosphere are often necessary to achieve recrystallization, greater homogeneity, and grain coalescence. Despite this, the huge economic and processing advantages of such a kind of methods are paving the way to new research activity on the optimization of these liquid deposition methods and/or on the identification of new or feasible materials suitable for such applications.

2.1.2 Antimony sulphoiodide (SbSI)

Ternary chalcohalides of the group AVBVICVII (where AV = Bi, Sb, As; BVI = S, Se, Te, O; CVII = I, Br, Cl, F) have gained significant attention due to their unique properties, making them suitable for a variety of applications. Examples include ionizing radiation detectors based on BiSI,[52] BiOI sonocatalysts,[53] BiOCl catalysts,[54] $Sn_7Br_{10}S_2$ for laser technologies,[55] and microwave oscillators such as BiSCl, BiSBr, BiSI, BiSeI, BiSeBr, and BiSeCl.[56]

Among these compounds, antimony sulphoiodide (SbSI) stands out as the most well-known representative. SbSI possesses a strongly anisotropic crystal structure characterized by double chains $[(SbSI)\infty]_2$, which consist of two chains related by a twofold screw axis and linked together by short and strong Sb–S bonds. Weak van der Waals-type bonds bind these double chains, resulting in the low mechanical strength of SbSI crystals, which often exhibit a needle-like shape (Figure 11).

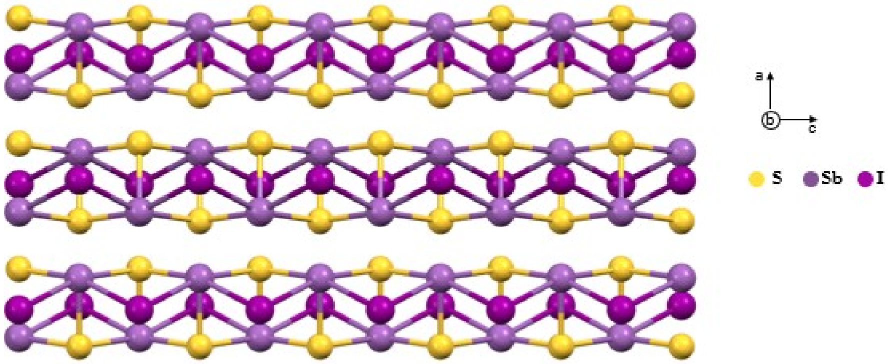

Figure 11: Crystal Structure of antimony sulphoiodide.

SbSI exhibits a ferroelectric phase $Pna2_1$ below 298 K, an antiferroelectric phase in the temperature range from 298 K to 410 K, and a paraelectric phase Pnam above 410 K.[57] The crystal structure of SbSI above room temperature is disordered so that the assignment of a definite space group is an approximation. The best approximation is the antiferroelectric space group $P2_12_12_1$, which features an alternating arrangement of polar double chains $[(SbSI)\infty]_2$ parallel to the [001] axis. In both the ferroelectric and antiferroelectric phases, the double chains are polar due to alternating shorter and longer Sb-S and Sb-I bonds. The asymmetry of the (S,I)-Sb-(S',I') arrangement results in the polarity of the double chains, which are all oriented in the same direction in the ferroelectric phase. In the antiferroelectric phase, the arrangement of the polar double chains becomes antiparallel (up and down). Only above 410 K do the double chains become non-polar, and the crystal structure adopts the paraelectric space group Pnam. Thus, SbSI undergoes a sequence of ferro- and non-ferroelectric phase transitions: $Pna2_1$ - $P2_12_12_1$ - Pnam.

The origin of the ferroelectric distortion is the small displacements of Sb with respect to S and I atoms, resulting in the formation of a net dipole moment per unit cell. This effect in

SbSI has been known since 1962.[58] However, spectroscopic studies, including far-infrared, Raman, neutron, and microwave analyses,[59] have shown that the simple displacive soft-mode picture is insufficient to fully describe the phase transition and ferroelectricity in SbSI. *A. Audzijonis et al.*,[60] in 1998, proposed a model for which ferroelectricity and phase transitions in SbSI are closely related to its electronic structure and phonon interactions. The changes in the electronic structure, pressure, electric field, or thermal fluctuations alter the form of the soft-mode potential, so the temperature of the ferroelectric phase transition, and its order.

This unique structure endows SbSI to an astonishing set of properties: since ferroelectric polarization is temperature-dependent, all ferroelectric materials are also pyroelectric. Additionally, the switching of dipoles into ferroelectric materials causes a field-dependent volume change, making all ferroelectrics and pyroelectrics also piezoelectric. Consequently, ferroelectric materials exhibit a variety of interesting properties that depend on the applied electric field, temperature, strain, and other parameters, such as electromechanical, electrocaloric, and non-linear optical properties.

However, the most intriguing feature of SbSI, in the context of this thesis, is also its semiconducting and photovoltaic behavior, which, when combined with its ferroelectricity, makes SbSI a so-called ferro-photovoltaic (FE-PV) material. The FE-PV effect generates a steady PV response (photocurrent or photovoltage) along the polarization direction in ferroelectric materials. While ferroelectrics are often thought of as insulators, this is not a strict requirement. In fact, a material can exhibit both semiconducting and ferroelectric properties. Semiconducting ferroelectrics possess a band gap which may lead to mild electrical conductivity and a crystal structure that supports spontaneous polarization. This combination of properties is possible because the ferroelectric polarization can influence the band structure and the movement of charge carriers within the material. These materials are of great interest for applications in photovoltaics,[61] sensors,[62] and memory devices,[63] as they allow for unique functionalities like switching polarization states and controlling charge carrier movement simultaneously. This interplay between the electronic structure and the crystal lattice enables novel phenomena, such as the ferroelectric photovoltaic effect, where the polarization helps in separating photo-excited charge carriers, enhancing photovoltaic performance.

Various attempts to design FE-PV devices based on materials like BFO, BCFMO, and YbFO[64] have been reported. The peculiarity of these devices is the ability to switch the photocurrent direction by changing the spontaneous polarization direction of a ferroelectric material with an external electric field.

For these applications, SbSI is one of the most intriguing materials due to pretty low coercive field (E_C=100 V/cm at 0°C) and high saturation polarization (P_s=25µC/cm^2) of the ferroelectric state (T_C = 298 K),[65] high charge mobility,[66] and an indirect optical bandgap of 1.86 eV.[67]

Currently, SbSI crystals are reported to be prepared by the vertical Bridgman technique,[68] by the sintering of antimony trisulfide (Sb_2S_3) and antimony triiodide (SbI_3),[69] by hydrothermal processes,[70] by Chemical Vapor Deposition,[71] or by sonochemical synthesis routes.[72] All these methods require high temperatures and/or high pressures, highlighting the need for innovative techniques which can consent to produce this material under milder conditions.

2.2 Technologies

2.2.1 The Theory behind a solar cell

2.2.1.1 Photoelectric Effect and Semiconductor Physics

A photovoltaic cell is a device that converts solar radiation directly into electrical energy through the photoelectric effect. The photoelectric effect, discovered by the German physicist Hertz in the late 19th century and later interpreted by Einstein (for which he was awarded the Nobel Prize in Physics in 1905), is a physical phenomenon initially observed in certain metals. When these metals are exposed to light radiation, they emit electrons with kinetic energy proportional to the frequency of the incident radiation. In a semiconductor, the fundamental brick for photovoltaics, the absorption of radiation can promote an electron from a bound state to a "free" state, thereby generating an outgoing current and consequently producing electrical energy.

From a theoretical point of view, this effect is described by the so-called band theory of solids; according to this theory, when isolated atoms combine to form a crystal, the structure of the energy levels of the innermost electrons and their corresponding wave functions are not appreciably changed, causing these electrons to remain bound to individual atoms. However, the levels of the outermost shell are drastically modified by the presence of neighboring atoms: the coupling of the wave functions of the electrons leads to the formation of a dense band of energy levels corresponding to delocalized electronic states. An electron occupying one of these levels is therefore not bound to a single atom but is shared by several atoms in the crystal. Such electrons belonging to this band, called valence band, are thus not confined to individual atoms and can contribute to electrical conduction. Above the valence band, other bands of higher energy are formed, separated or not, by a forbidden energy interval called the 'energy gap' (or 'band gap'). The allowed energy band immediately above the valence band is called the conduction band.

The valence electrons can be treated as a gas of Fermi particles that can move freely within a solid, each with its effective mass. At absolute zero, they will distribute according to the Fermi-Dirac distribution, filling the allowed electronic states starting from the lowest energy level. The highest energy level that becomes occupied is called the Fermi level. The structure of these bands and the number of electrons in the valence band determine the electrical properties of crystalline solids, which can be categorized into conductors, insulators, and semiconductors:

- Conductors: The valence band and the conduction band overlap; in these materials, the Fermi level falls within the band. This implies that electrons have the possibility to move to nearby energy levels, resulting in high mobility. At temperatures above 0K, some electrons will occupy higher levels in the band, but many will remain available.
- Insulators: At 0K, the valence band is completely filled, and the conduction band is empty; the two bands are separated by an energy gap (> 5 eV), and the Fermi energy falls within the region between the two bands. At higher temperatures, if the energy gap is much larger than the thermal excitation kT, the probability of an electron being excited into the conduction band is negligible. The conduction band will therefore remain practically empty even at elevated temperatures.
- Semiconductors: The band structure is similar to that of insulators, with the difference that the energy gap between the two bands is smaller (<5 eV). This implies that, even at low temperatures, although there are few electrons in the conduction band, they have a very high number of available states, resulting in non-zero conductivity. As the temperature increases, the number of electrons available in the conduction band increases exponentially, thereby increasing the conductivity of the material.

When a light flux impinges on the crystal lattice of a semiconductor, the electrons in the material that receive photons with energy equal to the band gap value (E_g) can overcome it and transition from the valence band to the conduction band. If the photon energy $E = h\nu$

is greater than E_g, the struck electron will reach a more external zone on the conduction band but will then return to the minimum level of the band by dissipating the excess energy (thermalization phenomenon). If the energy is lower, no absorption occurs, and the semiconductor is said to be transparent in this spectral region.

It is important to distinguish between direct and indirect band gap semiconductors, which arises from the dissimilarity in the dispersion relation of these materials (Figure 12).

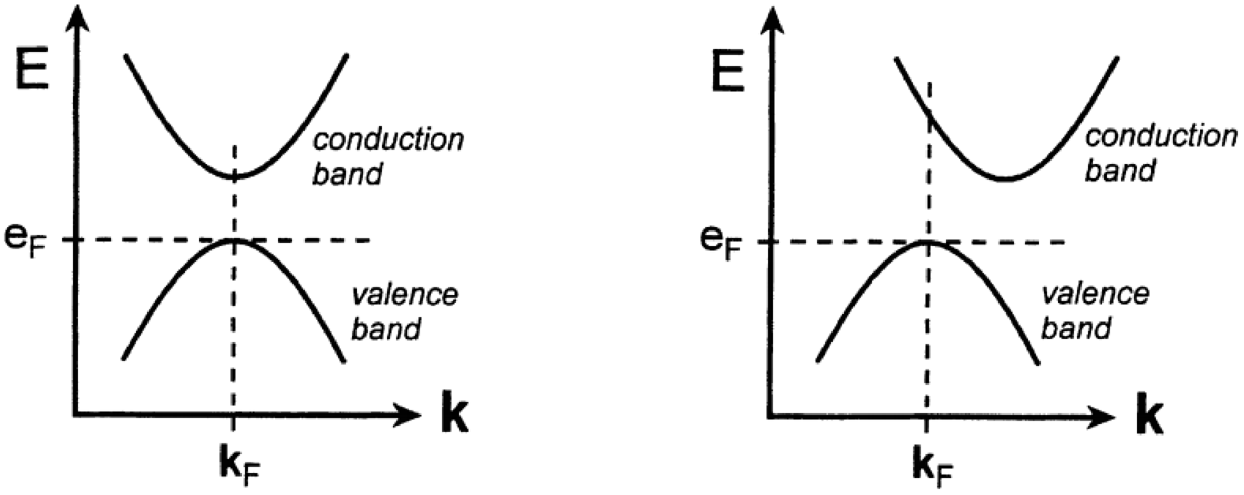

Figure 12: Semiconductors with direct (left) and indirect (right) band gaps. The figure shows the Fermi energy, which is the energy of the highest occupied level by electrons at absolute zero; the corresponding wave vector is called the Fermi wave vector.[73]

If one observes the graph of energy as a function of the wave vector of the lattice electrons, it is noted that in some cases, the position of the energy minimum of the conduction band is aligned with the maximum of the valence band. In this case, it is referred to as a direct band gap, for which, if a photon is absorbed, its energy represents the difference in the initial and final energy states of the material itself. In the case of an indirect band gap, the minimum and maximum of the two bands correspond to different values of ~k. It is still possible to excite an electron from the valence band, considering that the necessary change in ~k to reach the conduction band can be induced by a phonon, which has lower energy than a photon but considerably higher momentum. It is fundamental to recognize that in this case, due to the involvement of two different particles, the probability of radiation absorption is lower compared to direct band gap semiconductors.

2.2.1.2 Electrons and Holes: Recombination Phenomena

The process underlying the absorption of light is the excitation of an electron from the valence band to the conduction band. The excited electron leaves a vacancy in the valence band, known as a hole, which is associated with a positive charge (equal in magnitude but opposite to that of the electron) and can be considered a real particle. In hole transport mechanics, the hole is occupied by neighboring electrons in a cascading motion that continuously generates new holes moving effectively in the opposite spatial direction. However, if a free electron encounters a hole during its motion, a recombination phenomenon occurs, leading to the emission of a photon.

In semiconductors, radiative phenomena of absorption and emission, where there is no change in the wave vector ~k, are linked to these processes of electron and hole generation and recombination and are highly dependent on the band diagram of the material.

In particular, one of the most important is the band-to-band recombination, the predominant process in the presence of a direct band gap. This occurs when an electron in the conduction band decays into the valence band, dissipating energy. In the case of an indirect band gap, it is necessary for a phonon to be emitted as well, making this process rather improbable.

There are also non-radiative processes, among which we distinguish:

- Auger Recombination: Transitions that occur through the direct recombination of electrons and holes; the excess recombination energy is transferred to a third carrier that is excited to a higher level within the same band, which in turn transfers its energy to a phonon to return to its original state. This mechanism is rather rare in intrinsic semiconductors and becomes significant only for materials with very high doping percentages, characterized by an extremely high number of carriers in the conduction band.

- Band-Impurity Recombination (Shockley-Read-Hall): The trapping of charge carriers by impurities in the crystal; this corresponds to the transition of an electron from levels very close to the conduction band, introduced into the gap by such impurities, which act as recombination centers, to other levels. The energy produced in this process is transferred through phonons. This mechanism predominates in indirect band gap semiconductors.

  Within this process, we can distinguish four active mechanisms based on the level at which the transition occurs (Figure 13):

  1. Thermal emission of electrons (A): Electrons on the impurity levels transition to the conduction band.
  2. Capture of electrons (B): An electron recombines with an empty level in the gap.
  3. Thermal emission of holes (C): Electrons in the valence band are excited to the levels in the gap, generating a hole.
  4. Capture of holes (D): A hole in the valence band is captured by a recombination center.

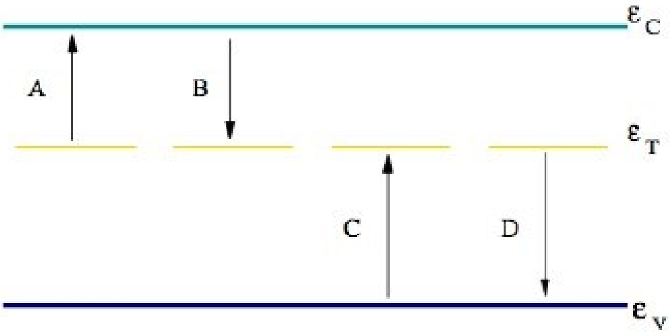

Figure 13: Band-impurity recombination.[74]

Typically, recombinations are closely related to defects, as the presence of an impurity usually creates a distortion in the lattice periodicity, introducing additional energy levels within the energy gap. These energy levels can act as intermediate states that facilitate the recombination of electrons and holes, thereby reducing the overall efficiency of the devices.

Defects are generally classified into two categories: shallow and deep. Shallow defects are typically caused by highly soluble impurities, such as dopants, which are intentionally introduced to modify the electrical properties of the material. These impurities create energy levels close to the conduction or valence band edges, allowing for the controlled modification of the material's conductivity. Shallow defects are essential for creating p-type and n-type semiconductors, which are the building blocks of a solar cell, as described in the next chapter.

On the contrary, deep defects are caused by more severe lattice distortions, such as vacancies, interstitial defects, and antisites. Defects are highly prevalent on the surface of the crystal, which is the most defective part due to its exposure to the environment and the termination of the lattice structure. Deep defects induce significant local distortions in the lattice, creating both traps and recombination sites. Traps can capture and temporarily immobilize charge carriers, while recombination sites facilitate the annihilation of electron-hole pairs, leading to a strong reduction of charge carriers. The presence of deep defects has a strong correlation with carrier lifetime, the average time a charge carrier remains free before recombining, which is a critical parameter for PV. In fact, deep defects can significantly reduce carrier lifetime by providing efficient pathways for recombination.

Understanding and managing defects is crucial for optimizing the performance of semiconductor devices. Techniques such as passivation, which involves coating the surface with a material that reduces the density of surface defects, can help mitigate the effects of deep defects.

2.2.1.3 The p–n Junction

The concentration of electrons and holes in a semiconductor (under non-illuminated conditions) can be controlled by introducing substitutional impurities into the crystal. This process, known as doping, can be intentional or unintentional and is determined by the spontaneous presence (intrinsic semiconductor) or artificial introduction (extrinsic semiconductor) of atoms to increase the concentration of holes (acceptor atoms) or electrons (donor atoms) within the material. If holes are the majority carriers, the semiconductor is said to be of p-type; conversely, if electrons dominate, the semiconductor is said to be of n-type. While in intrinsic semiconductors the Fermi level lies in the mid-point of the bandgap, in extrinsic semiconductors the Fermi level is not equidistant from the conduction and valence bands due to unequal numbers of electrons and holes. In the case of silicon (4+), n-type-doping is achieved adding group V elements (P, Sb etc.) to donate free electrons, increasing the number of electrons in the conduction band. Thus, the Fermi level lies close to the conduction band. In p-type Si, adding group III elements (B, Al, etc.) create holes in the valence band, increasing the number of holes. Therefore, the Fermi level lies close to the valence band.

The added carriers are mobile charges, so when two materials, one of p-type and one of n-type, are brought into contact, a very high concentration gradient of carriers is created, immediately giving rise to diffusion currents of holes from the p-region to the n-region and electrons in the opposite direction, until a new charge equilibrium condition is reached (Figure 14).

This forms the so-called "depletion layer." In the depleted region, there are also unbalanced fixed charges, i.e., donor atoms that have given up an electron and acceptors that have acquired one; for this reason, the depletion region is also called the space charge region (the p and n regions, being overall neutral, are instead called quasi-neutral regions).

The presence of oppositely charged ions causes a very intense electric field to form in this region, which opposes the diffusion current I_D; this diffusive motion, which cannot extend for thermodynamic reasons, will quickly decay, bringing the system to equilibrium when the diffusion current I_D and the drift current I_S, due to the electric field pushing the minority carriers to cross the junction, balance out, making the total current zero.

At the edges of the depletion region, a static electric field and therefore a potential difference V_0 will be created, which hinders the motion of holes towards the n-region and electrons towards the p-region.

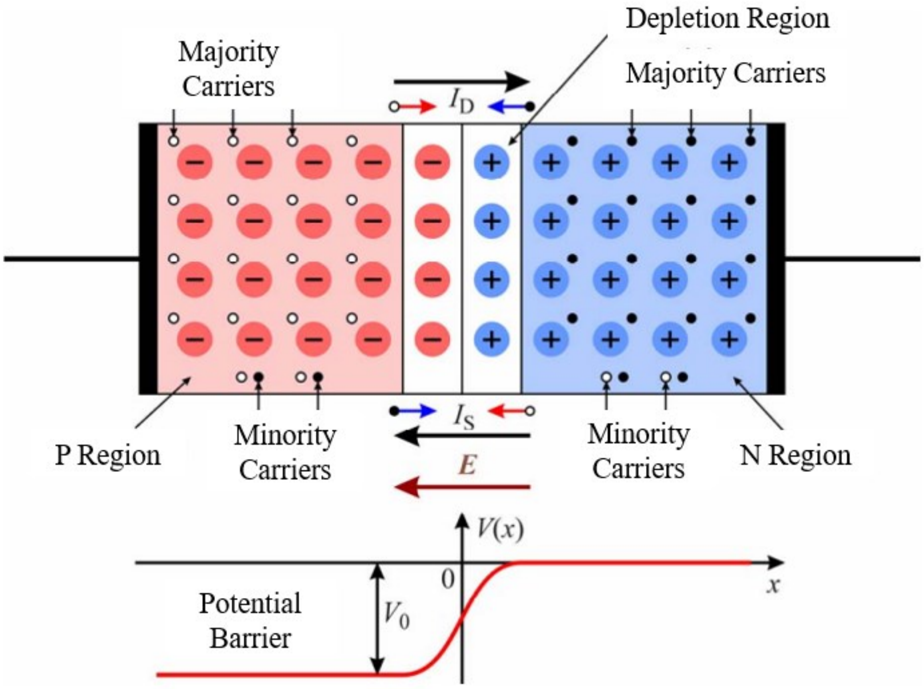

Figure 14: Schematic representation of a p-n junction.

Dimensionally, the depletion layer W is inversely proportional to the N_A and N_D density of carriers in the p-type and in the n-type semiconductor respectively:

$$W = \sqrt{\frac{2\varepsilon}{q}\Delta V\left(\frac{1}{N_D}+\frac{1}{N_A}\right)}$$

Equation 1

Where ε is the material dielectric constant and q is the elemental charge.

For the realization of a solar device, it will be necessary to insert a p-n junction within a circuit, wiring the ends of the system with ohmic contacts to avoid a rectifying effect or Schottky barrier effect between the contact metal and the semiconductor. The terminal connected to the p-region is called the anode, while the one connected to the n-region is called the cathode. This two-terminal electronic device, called a junction diode, is characterized by a strongly non-linear current-voltage relationship (Figure 15). It is also possible to bias a junction diode by connecting it to a voltage DC source V_D. If the positive pole is applied to the n-region and the negative pole to the p-region, the junction is said to be forward-biased; in this case, the voltage source forces the potential barrier V_0 to have a lower value than the equilibrium value, favoring the diffusion motion of holes from the p-region, where they are majority carriers and therefore present in large quantities, to the n-region, where they are minority carriers. Similarly, this occurs for electrons in the opposite direction. Once they have crossed the junction and become minority carriers, the carriers continue their diffusion motion, moving further away from the transition region. In the vicinity of the junction, the system is therefore in a state of non-equilibrium: there will be recombination processes between majority and minority carriers until a new equilibrium state is reached. In this case, the forward current I_F ($I_{Forward}$) increases exponentially with increasing V_D.

In the reverse bias condition, the potential barrier is instead forced to a higher value than the equilibrium value, with the effect of further separating electrons and holes, causing an expansion of the depletion region. A weak reverse current I_R ($I_{Reverse}$) circulates, which is six to ten orders of magnitude lower than the forward current I_F.

2.2.1.4 Characteristic Parameters of a Solar Cell

For a junction diode, the I-V relationship can be expressed as:

$$I = I_{SC} - I_{o1}\left(e^{\frac{qV}{kT}} - 1\right) - I_{o2}\left(e^{\frac{qV}{2kT}} - 1\right)$$

Equation 2

where I_{SC} (*short circuit current*) corresponds to the maximum current that flows through the cell in short circuit condition (V = 0) and is due to the generation and collection of electron-hole pairs when the junction is illuminated; I_{o1} and I_{o2} represent the dark saturation currents due to recombinations that occur in the quasi-neutral regions and the space charge region, respectively.

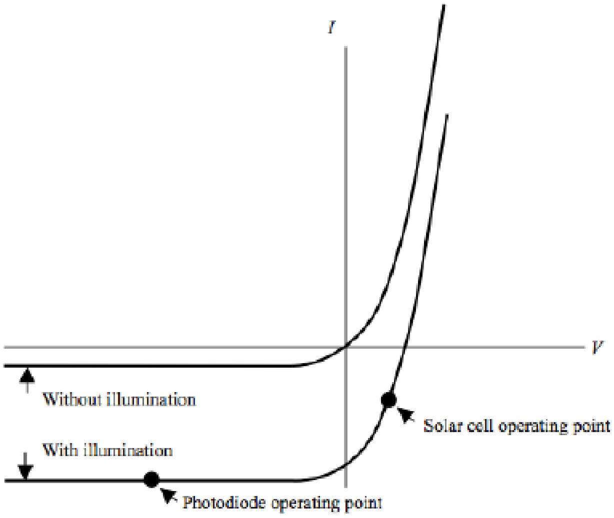

Figure 15: I-V characteristic of a p-n junction under conditions of absence and presence of illumination.[75]

Figure 15 represents the I-V characteristic of a junction diode under different conditions. It is noted that, under reverse bias conditions (V < 0), there is a saturation current that increases due to the optical generation of electron-hole pairs. Under forward bias conditions, there is always a reverse current, which is normally much lower than the diffusion current.

The operating point for a solar cell is therefore calculated such that the current exits from the positive terminal of the junction (p-part), through the external circuit, to the negative terminal (n-part). Typically, for the representation of the I-V curve of a solar cell, it is sufficient to show the fourth quadrant, where the operating point is located. It is possible to approximate a solar cell with an equivalent electrical circuit, consisting of an ideal current generator in parallel with a diode in reverse bias (Figure 16).

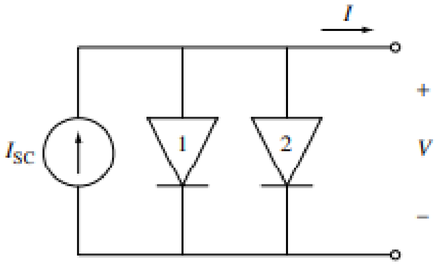

Figure 16: Equivalent circuit for an ideal solar cell.[76]

The current-voltage characteristic of a standard silicon cell is shown in Figure 17.

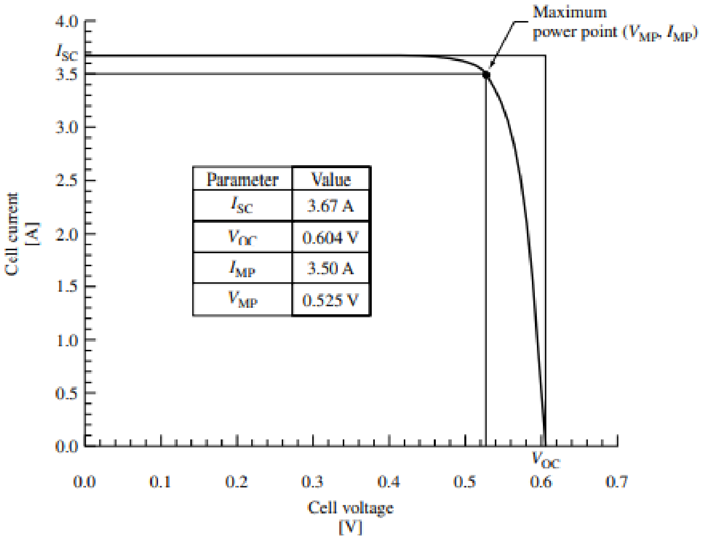

Parameter	Value
I_{SC}	3.67 A
V_{OC}	0.604 V
I_{MP}	3.50 A
V_{MP}	0.525 V

Figure 17: I-V characteristic of a standard silicon cell.[76]

The most important figures of merit for a solar cell are:

- I_{SC} (short circuit current): Obtained by setting V=0 in Equation 2, i.e., is the current that flows through the cell when the voltage across it is zero, effectively short-circuiting the cell. It represents the maximum current the solar cell can generate under given illumination conditions and is directly proportional to the intensity of the incident light.
- V_{OC} (open circuit voltage): Obtained by setting I = 0, it results in:

$$V_{OC} = \frac{Kt}{q} \ln\left(\frac{I_{SC} + I_{01}}{I_{01}}\right) \approx \frac{Kt}{q} \ln\left(\frac{I_{SC}}{I_{01}}\right)$$

Equation 3

since typically $I_{SC} \gg I_{01}$. It is the value of forward voltage that compensates for the built-in potential of the p-n junction and is achieved when the driving force of the photogenerated current is nullified, resulting in a measured current intensity of zero.

- P_{MP} (maximum power point): The point of maximum power produced by the cell; calculated as the product of $I = I_{MP}$ and $V = V_{MP}$. As seen in Figure *17*, this point defines a rectangle whose area, given by $P_{MP} = I_{MP} \cdot V_{MP}$, represents the operating condition for a cell with maximum power yield.
- FF (fill factor): This parameter quantifies the maximum power that can be developed by the cell by measuring the "sharpness" of the I-V curve, and it is represented as the ratio between the maximum power square and the product $I_{SC} \cdot V_{OC}$. It is calculated as:

$$FF = \frac{I_{MP} V_{MP}}{I_{SC} V_{OC}}$$

Equation 4

For highly efficient cells, this parameter should be close to 1.

- Ψ (efficiency): Represents the fundamental parameter for a solar cell, i.e., the solar conversion efficiency. It is calculated as:

$$\eta = \frac{P_{MP}}{P_{in}} = \frac{FF I_{SC} V_{OC}}{P_{in}}$$

Equation 5

where P_{in} is the power of the incident solar radiation.

There are some physical constraints which determine the existence of a theoretical upper limit to the efficiency that can be achieved by a single-junction device:

1. The primary limiting effect is the inability to convert photons with energy lower than the bandgap E_g of the absorber. Additionally, there is the inability to utilize photons with energy greater than the bandgap E_g of the absorber; the excess energy of these photons is quickly converted into heat through thermalization processes, which limits the efficiency to approximately 50%.
2. Discrepancy between the value of V_{MP} and E_g. In fact, to create a pair of carriers, an energy at least equal to E_g is necessary; in any case, however, $V_{MP} < E_g$. For silicon, for example, the ratio $\frac{V_{MP}}{E_g}$ is approximately 60%, limiting the total efficiency to approximately 33%.

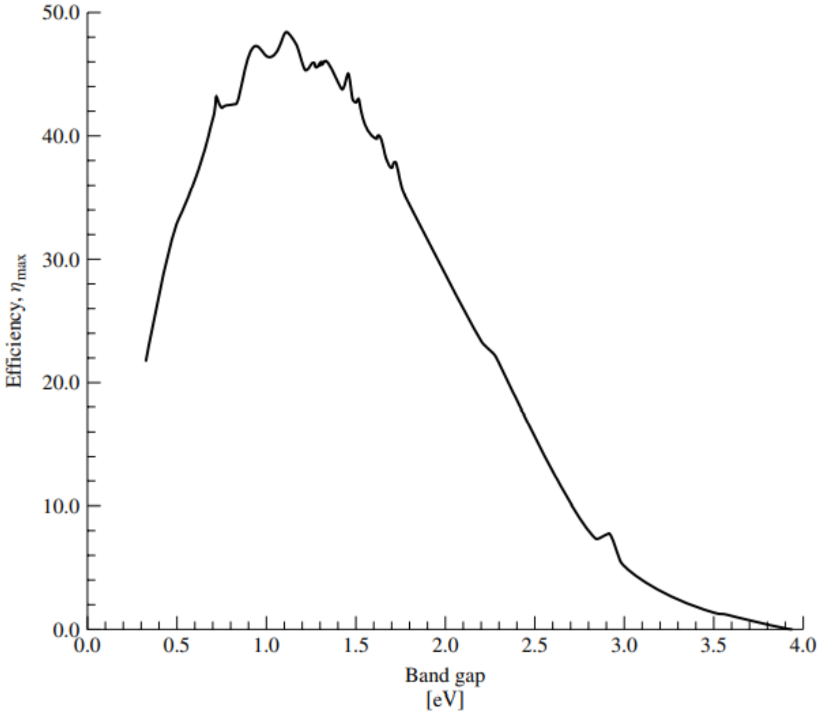

Figure 18: Ideal efficiency limit of a single-junction cell as a function of the band gap calculated by Shockley and Queisser.[77]

This theoretical efficiency limit is resumed in the so called “Shockley-Queisser limit” (Figure 18);[77] the maximum theoretical conversion efficiency of the solar spectrum occurs for a homojunction consisting of a semiconductor with a band gap of 1.34 eV and corresponds to

33%. In the case of silicon, the band gap has a value of 1.1 eV, and the efficiency is limited to 32%.

Efficiency is also conditioned by the operating temperature of the cell: typically, it is found that η decreases with increasing temperature, due to the increase in saturation currents and the resistance of the material to the passage of the photogenerated current.

The Real Junction: Parasitic Resistances

Equation 2 neglects the parasitic resistances typically found in a real cell. In particular, these are summarized as:

- $\boldsymbol{R_{sh}}$ (Shunt Resistance): Represents the losses due to leakage currents in the cell.
- $\boldsymbol{R_S}$ (Series Resistance): Represents the sum of the resistances due to both the material and the contact resistance between the cathode, semiconductor, buffer layer, and anode.

If we include these resistances in the model of Equation 2, the I-V characteristic becomes:

$$I = I'_{SC} - I_{o1}\left(e^{\frac{q(V+IR_S)}{kT}} - 1\right) - I_{o2}\left(e^{\frac{q(V+IR_S)}{2kT}} - 1\right) - \frac{V + IR_S}{R_{sh}}$$

Equation 6

where I'_{SC} is the short circuit current in the absence of parasitic resistances.

Figure 19 shows the effects of these resistances; in particular, it is noted that the shunt resistance R_{sh} does not affect the current I_{SC} but reduces V_{OC}; the exact opposite occurs in the case of series resistance. To obtain the equation of the real diode, it is necessary to rewrite Equation 6 as:

$$I = I'_{SC} - I_o\left(e^{\frac{q(V+IR_S)}{A_0kT}} - 1\right) - \frac{V + IR_S}{R_{sh}}$$

Equation 7

where A_0 is the ideality factor of the diode and assumes values between 1 and 2; if $A_0 \approx 1$, then the recombination processes in the quasi-neutral regions dominate in the diode, while if $A_0 \rightarrow 2$, then recombination in the depletion region dominates.

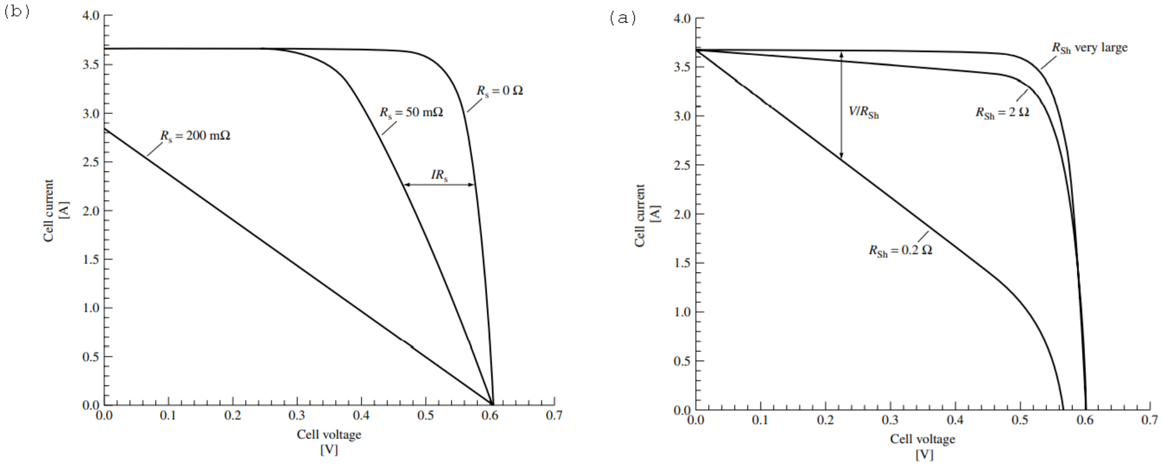

Figure 19: Detrimental Effect on the I-V characteristic of a solar cell of (a) increasing series resistance ($R_S = 0, 50, 200\ \Omega$) and (b) decreasing shunt resistance ($R_{Sh} \rightarrow \infty, 2, 0.2\ \Omega$).[76]

How to obtain Efficient Solar Cells?

Using the figures of merit described above, it can be concluded that to realize an efficient solar cell, it is necessary that:

1. I_{SC} and V_{OC} are high.
2. *FF* as close as possible to 1.
3. The photogenerated current is maximized, minimizing shading effects due to the presence of electrical contacts or wiring; the loss of absorbed light due to the reflectance of the material must be minimized, and the junction must have sufficient optical thickness to absorb most of the photons with $E > E_g$, reducing transmittance to a minimum.

From the definition of V_{OC}, it is clear that by reducing the saturation current, this voltage increases and consequently the *FF*. Therefore, for the realization of a high-performance cell, it is substantially required that recombinations throughout the device are minimized and that the absorption of photons with energy $E > E_g$ is maximized.

2.2.2 Single Junction Thin-Film Solar Cells

This paragraph will present the thin-film stand-alone architecture used in the context of this thesis. Specifically, Figure 20 illustrates the typical structure of a substrate-configuration thin-film solar cell with a CIGSSe absorber layer, deposited on soda-lime glass, which serves as the substrate. This type of glass, containing sodium, allows for the diffusion of the alkali metal into the absorber layer at the typical deposition temperatures of chalcogenides. This diffusion helps to reduce recombination and promotes grain boundary passivation, thereby lowering the series resistance of the system. It may also be necessary to introduce a higher percentage of Na into the material to further improve its electrical properties. This can be achieved through an additional deposition between the substrate and the absorber, again facilitating diffusion with temperature.

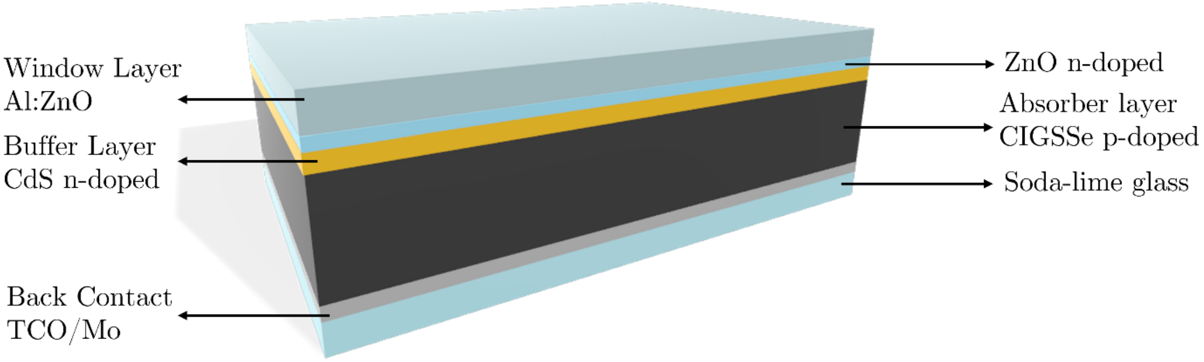

Figure 20: Structure of a solar cell with a CIGSSe absorber layer (not to scale).[78]

On top of the glass, a layer of a metallic conductor, typically a few hundred nanometers thick, is deposited to act as an ohmic back contact (commonly Mo or Transparent Conductive Oxides as FTO, ITO, etc.). This layer allows for the capture of photogenerated electron-hole pairs. Next, the p-type absorber layer, which is the chalcogenide, is deposited. Due to its extremely high absorption, this layer can be very thin, ranging from 1 to 3 µm or even less for certain purposes. The p-n junction is formed by depositing a buffer layer of approximately 50 nm of cadmium sulfide (CdS), an n-type semiconductor with a higher bandgap, using chemical bath deposition (CBD). This buffer layer helps to neutralize the formation of electrically active defects so avoiding or reducing the lowering of the device's performance.

To minimize carrier recombination at the p-n interface, which reduces the cell's efficiency, a Cu-deficient absorber ($< 25\%$) is often used. In Cu-deficient compounds, copper vacancies form a periodic structure on the surface, creating an Ordered Defect Compound (ODC).[79] The ODC has a wider bandgap compared to the chalcopyrite itself; specifically, the valence band is lower than that of the bulk, preventing holes from reaching the interface with the n-layer and thus limiting recombination.

The n-type region is then extended by sputtering two transparent conducting oxide (TCO) window layers: undoped zinc oxide (UZO) and aluminum-doped zinc oxide (AZO, Al 2%). The AZO layer serves as the transparent front contact for the solar cell.[80]

This substrate configuration is more commonly used due to its advantages in high-temperature processing, but CIGSSe-based solar cells can also be designed in a superstrate configuration, in which the layers are deposited onto a transparent substrate (e.g., glass) in the reverse order: transparent front contact, buffer layer, CIGSSe absorber layer, and finally the back contact. Light enters through the transparent substrate and front contact before reaching the CIGS absorber layer; this offers potential benefits in manufacturing simplicity and cost reduction, but it may also present challenges in maintaining the quality of the CIGSSe layer. Moreover, it can prevent oxygen contamination at the interface between CIGSSe and buffer layer.[81]

In thin-film solar cells, the alignment of the band gaps of the different layers is crucial for efficient charge separation and minimizing recombination. Proper band gap alignment ensures that a wide range of photon energies can be absorbed, maximizing both the open-circuit voltage and short-circuit current. Additionally, it facilitates efficient charge transfer between the absorber and buffer layers, reducing interface defects and enhancing the overall stability and performance of the solar cell.

Moreover, band gap alignment plays a critical role in charge selectivity and selective transport. By aligning the energy levels of the conduction and valence bands, the solar cell can effectively separate electrons and holes, directing electrons to the n-type region and holes to the p-type region. This selective transport minimizes the chances of electrons and holes recombining before they can be extracted as useful electrical energy, thereby improving the overall efficiency of the solar cell.

2.2.3 Multi-Junction and Tandem Solar Cells

Third-generation photovoltaics aim to meet the demand for increasingly efficient and cost-effective energy conversion technology by improving existing and commercially available devices. Practically, this involves leveraging second-generation thin film technology, sharing the goal of using non-toxic and highly available materials. One idea to enhance the efficiency of such devices is to create an optical and/or mechanical coupling of thin-film cells with different bandgaps, resulting in a multi-junction cell with a theoretical efficiency limit of up to 86.6%.[82]

Currently, practical applications are limited due to the high cost, low scalability and material incompatibility of the needed processes. Among the possible cell combinations, only two technologies have produced market-viable devices. The first is based on amorphous silicon, which, despite its low cost, has low efficiency and is mainly used in consumer electronics. The second is based on III-V semiconductor multi-junction cells, which have achieved a record efficiency of 46% (with junctions GaInP/GaAs, GaInAsP/GaInAs),[83] making them the standard for high-efficiency applications, especially in space environments.

Other materials, such as crystalline silicon, CdTe, CIGS, and perovskites, are valid alternatives but are currently limited to laboratory demonstrators.[84]

2.2.3.1 Efficiency Losses

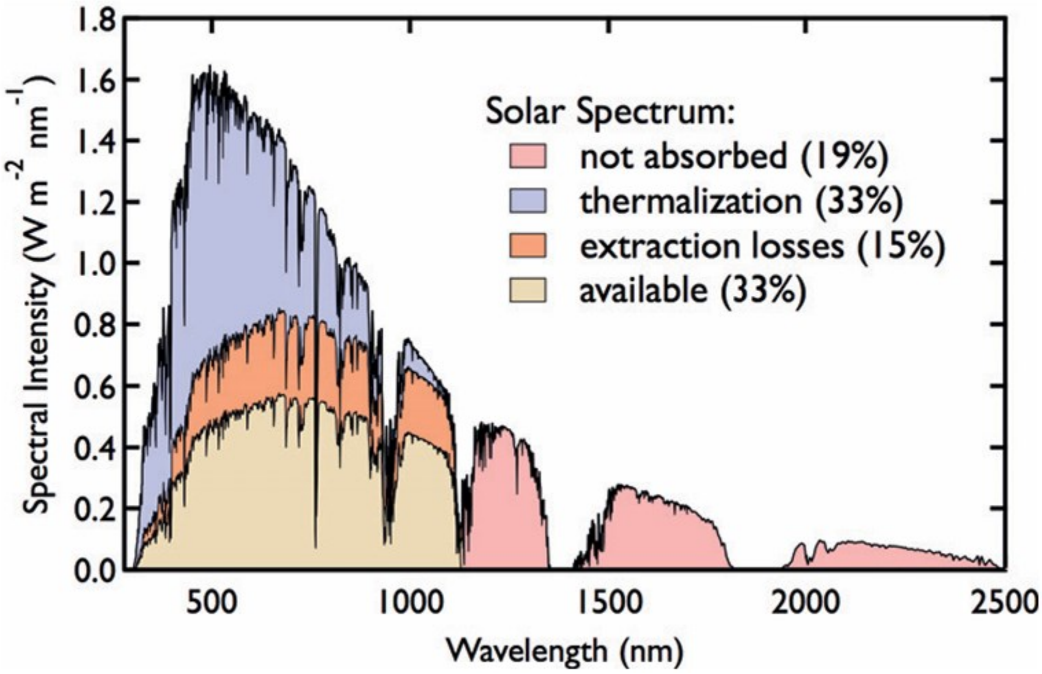

Figure 21: Efficiency loss mechanisms in a solar cell.[85]

Third-generation photovoltaics aim to reduce the efficiency losses characteristic of standard cells, primarily due to the mechanisms shown in

Figure 21.

The most significant losses ($\approx 55\%$) occur due to the non-absorption of photons with energy $h\nu < E_g$ and the thermalization of electron-hole pairs generated by the absorption of photons with energy $h\nu > E_g$. Other losses can occur at the junction and contacts, due to reflection, electrical gradients, the presence of contacts, and thermal losses due to their resistance. Recombination losses account for approximately 8.5% and are primarily due to radiative phenomena.

Currently, three different approaches have been proposed to mitigate these losses:

1. Increasing the number of energy levels.

2. Capturing excited carriers before thermalization.
3. Generating multiple electron-hole pairs with a single high-energy photon or a pair of carriers with energy higher than the bandgap with a single lower-energy photon.

The implementation of strategy (1) leads to the development of tandem solar cells, which have surpassed the Shockley-Queisser limit of silicon.

2.2.3.2 Multi-junction Cells

Multi-junction solar cells are constructed by stacking multiple semiconductors with different optical bandgaps in decreasing order: i.e., the top cell must have the highest bandgap to absorb high-frequency photons and allow lower-energy photons to reach the underlying layers. This approach, first suggested by Jackson in 1955,[86] automatically separates different wavelengths of the solar spectrum and achieves selective photon absorption.

2.2.3.2.1 Classification of Tandem Solar Cells

Tandem solar cells are classified into types A and B based on the number of transparent conductive electrodes (TCEs) and the number of contact terminals, ranging from 2 to 4 (Figure 22).

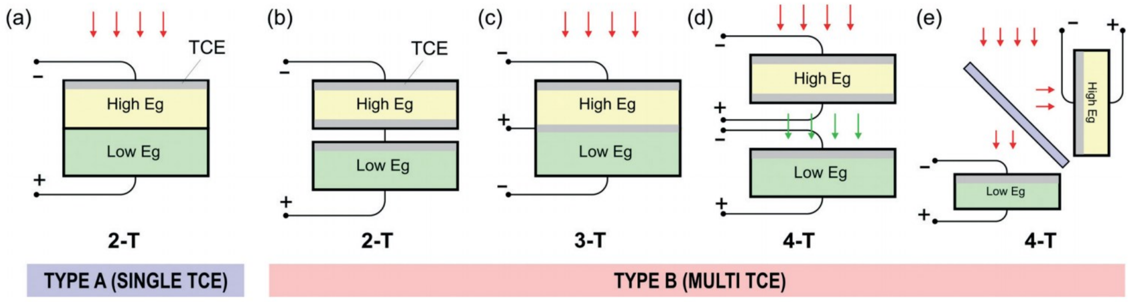

Figure 22: Types of tandem cells based on the number of TCEs and terminals.[87]

Type A cells are monolithic series-interconnected cells grown on a single substrate (one TCE), implying the presence of two terminals (2-T). This configuration is used almost exclusively in commercial products due to its simplicity. Type B cells, including 2-terminal mechanical stacking, 3-terminal (3-T), and 4-terminal (4-T) cells, allow for the independent realization of individual devices, simplifying production and characterization.

2.2.3.2.2 Theoretical Efficiency Limits of Tandem Solar Cells

To understand how the performance of tandem cells varies with different configurations, a simplified and idealized Schottky-Queisser (SQ) limit can be considered (Figure 23).

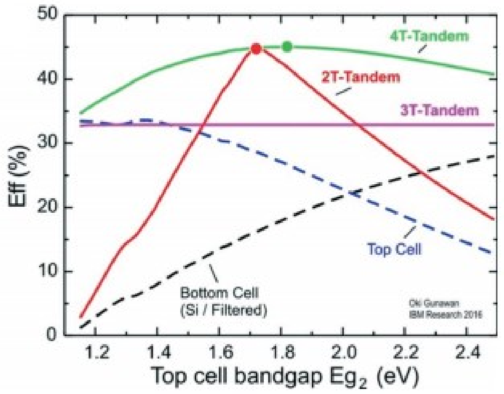

Figure 23: Efficiency as a function of the top cell bandgap calculated with an SQ limit approximation for different tandem configurations.[87]

1. **4-T Tandem**: The cells operate independently, so the efficiency is simply the sum of each cell's efficiency, reaching values of approximately 45%.
2. **3-T Tandem**: The cells operate in parallel, with a common terminal. Efficiency is almost constant, independent of the top cell choice.
3. **2-T Tandem**: The cells can be realized through mechanical or monolithic coupling. The total current is limited by the cell with the lower current, and the voltage is

summed in series. The efficiency shows a considerable dependence on the bandgap E_{g2}, with optimal performance at $E_{g2} = 1.72$ eV.

2.2.3.2.3 Materials for the Absorber Layer in a Tandem Solar Cell

The realization of a 2-T tandem cell requires two stringent conditions on the materials for both the top and bottom layers:

1. The currents generated by each cell must be matched, which can be achieved by selecting materials with appropriate optical bandgaps.
2. There must be process compatibility in the realization of the different layers, meaning the bottom cell and the p-n junction must withstand the temperatures required for the top cell's realization. A solution to this problem could be the independent realization of the two devices, i.e., the use of 4-terminal tandem cells.

Another possibility to consider is the insertion of intermediate layers to minimize series resistance and any parasitic optical absorptions. These materials should have a high bandgap, an appropriate refractive index, and a high carrier density.[88] Despite numerous studies on these compounds, top cells based on chalcopyrites have not yet come close to their theoretical potential. The bandgaps of CIGSSe-based materials range from 1.04 eV for $CuInSe_2$ to 2.5 eV for $CuGaS_2$, covering a wide portion of the spectrum and offering more matching possibilities with various substrates. The main problem with using these materials is the difficulty in developing a high-efficiency, high-bandgap top cell that is effectively transparent, due to the extremely high optical absorption of these materials and the difficulty in obtaining a nanostructured phase due to the stability of the crystallographic structure, conferred by very strong metal/chalcogen covalent bonds. Additionally, high-quality films typically require very high processing temperatures (400-600 °C). In the case of a 4-T tandem, this is not a problem, but if a monolithic structure is desired, the bottom cell material must be carefully chosen. Silicon, which is intrinsically stable at this temperature range, is currently one of the most valid solutions to overcome this problem, mainly because it is also very high efficient cheap and standard technological reference and thanks to the low band gap can behave as ideal bottom cell of a tandem system.

2.2.4 Hybrid – Perovskite Solar Cells

Hybrid-Perovskite solar cells (PSCs) utilizing organo-lead halide perovskite absorbers have garnered significant attention due to their exceptional qualities, such as high absorption coefficients, direct bandgaps, high charge carrier mobility, and long diffusion lengths. Methylammonium lead iodide ($CH_3NH_3PbI_3$)[89] and formamidinium lead iodide ($CH(NH_2)_2PbI_3$)[90] are two of the most notable light-harvesting perovskites with a direct bandgap of 1.55 eV and 1.49eV,[91] making them an ideal light absorber in PSCs. Perovskite films can be prepared using either one-step or two-step sequential deposition methods. Various solar cell architectures, including perovskite-sensitized solar cells, mesoporous PSCs, and planar n-i-p or p-i-n heterojunction solar cells,[92] have been developed to enhance solar cell efficiency.[93]

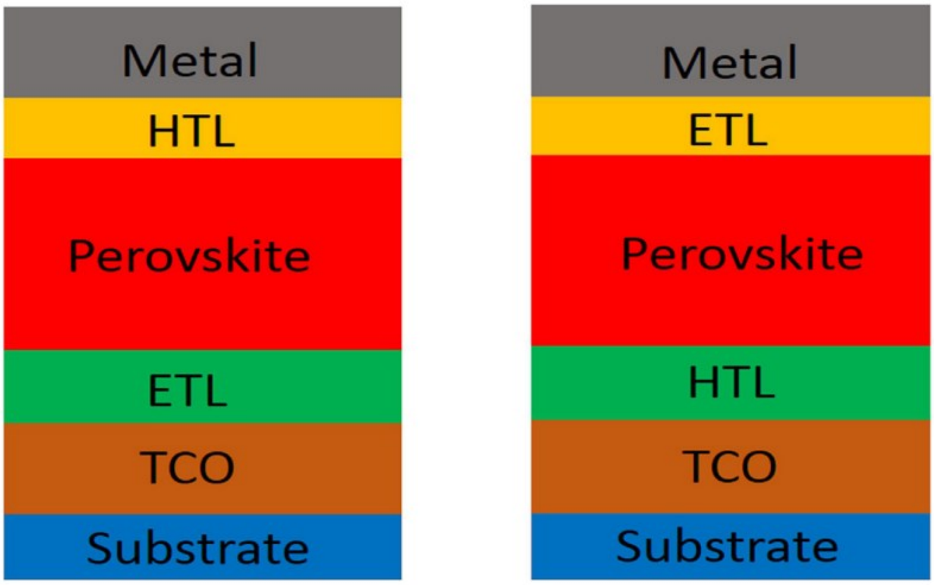

Figure 24: Planar n-i-p (left) or p-i-n (right) perovskite heterojunction solar cells.[92]

These junctions consist of three layers: a p-type layer, an intrinsic (i-type) layer, and an n-type layer (Figure 24). When light (photons) strikes the solar cell, it is primarily absorbed by the intrinsic layer. Photons with energy greater than the bandgap of the material excite electrons from the valence band to the conduction band, creating electron-hole pairs. The electric field created by the p-i-n junction drives the separation of the electron-hole pairs. Electrons are attracted to the n-type layer, acting as an electron transport layer (ETL), while holes are attracted to the p-type layer, acting as a hole transport layer (HTL). Electrons move through the n-type layer to the external circuit, while holes move through the p-type layer to the external circuit. This allows to obtain selectivity in the direction of the carriers and an efficient charge separation, reducing the recombination inside the layers.

In PSCs, the perovskite typically serves as the intrinsic layer due to its high absorption coefficient, direct bandgap, and long diffusion lengths. Notably, the organic small molecule 2,2′,7,7′-tetrakis-(N,N-di-p-methoxyphenylamine)-9,9′-spirobifluorene (spiro-OMeTAD) is widely used as a HTM in high-performance PSCs with mesoporous or planar n-i-p architectures. Other organic small molecules and polymers, such as poly(3-hexylthiophene) (P3HT) and polytriarylamine (PTAA), also employed as HTMs in PSCs.[94]

Despite the high efficiency achieved with these HTMs, their relatively high cost and complicated synthetic procedures limit large-scale production. Additionally, most of these HTMs require lithium salt doping, such as lithium bis(trifluoromethylsulfonyl)imide (Li-TFSI),[95] to improve hole mobility and performance. However, the hygroscopic nature of Li-TFSI can cause decomposition of perovskite and reduce device stability. Therefore, developing other HTMs with low cost and high stability is necessary.

It has already been demonstrated that copper-based inorganic semiconductor CIGSSe nanocrystals can act as a new HTM in PSCs.[96] In particular, $CuInS_2$ quantum dots were applied as an HTM in conventional PSCs to replace the organic hole conductor spiro-OMeTAD.[97] CIGSSe offers a wide range of bandgaps, covering a significant portion of the solar spectrum. The high optical absorption and stability of CIGSSe make it an excellent complement to perovskite materials, also expanding their photo response. It can also help overcome the stability issues associated with perovskites, as CIGSSe is known for its robustness and long-term performance.

2.2.5 Novel concepts of thin-film photovoltaic devices: Ferro-Photovoltaic cells

Ferroelectric-photovoltaic (FE-PV) devices have been studied for several decades with various ferroelectric oxides. Although the PV effect in ferroelectrics was discovered over five decades ago, it garnered negligible attention due to the small photoresponses obtained.

A FE-PV solar cell is a novel concept of PV device that utilizes the unique properties of ferroelectricity to emancipate the photovoltaic effect of the absorber. Contrarily, conventional PV cells, which rely on the p-n junction to separate photogenerated charge carriers, FE-PV cells leverage the residual net polarization arising from the polar crystal structure of a ferroelectric material to achieve hole-electron separation in a unique physical phase: thus, the internal field can separate photogenerated charge carriers without the need for a p-n junction. The PV response in ferroelectric materials is mainly due to the bulk PV effect,[98,99] which produces a photovoltage within the bulk of the material, rather than at an interface or junction. Additionally, secondary factors such as domain wall theory,[100] the Schottky-junction effect,[98,101] changes in injection barriers, and the depolarization electric field also contribute to this response.[98,102] The spontaneous polarization in ferroelectrics is a modulable property, meaning that the photovoltaic response can be controlled by modulating the polarization. This offers a way to optimize the performance of the solar cell. Noteworthy, the intrinsic drawback of ferroelectric material is its general dielectric behavior which determines low extraction currents, high values of the optical band gap and consequently very low efficiencies.[103] Recently, however, FE-PV have breathed new life and interest into third-generation solar cells with the discovery of exceptionally large photo-responses in compounds like $Pb(Zr,Ti)O_3$ (PZT), $BiFeO_3$ (BFO), and Bi_2FeCrO_6 (BFCO),[103] together with other promising results obtained with alternative compounds, such as SbSI.[104] Two typical architectures (vertical or lateral configurations), used for FE-PV devices are illustrated in Figure 25.

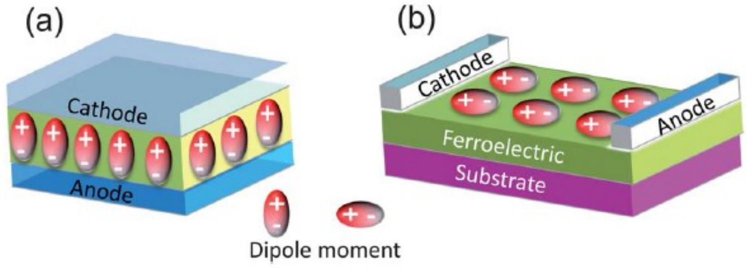

Figure 25: (a) Vertical and (b) lateral FE-PV device architectures.[105]

Given that FE-PV devices have largely remained an academic curiosity rather than finding practical application up to now, the study of these FE-PV architectures remains a truly novel concept that is yet to be investigated.

2.3 Methods

In this chapter, the main synthesis, deposition, and characterization techniques used in this thesis are described, with a particular focus on the basic working principle of the synthesis techniques (high energy ball milling) and deposition techniques (LT-PED) which have been employed in an original manner compared to the current state of the art.

2.3.1 Mechanochemistry via High Energy Ball Milling Method

Mechanochemical synthesis (MC) exploits a solid-state reaction activated by the transfer of mechanical energy and heat through the impact, rolling, sliding and grinding of appropriately sized and hard milling spheres against a mixture of precursor powders. The great advantage of mechanochemical synthesis lies in its ability to operate under ambient pressure and temperature conditions without the need for solvents or toxic chemical components. The simplicity of the milling mechanism ensures a very low process cost and a very high reaction yield. Being mediated by local non-equilibrium thermodynamics, this synthesis method enables the obtainment of metastable phases or the activation of solid-state reactions of components with incompatible physical characteristics (reactions between low-melting and high-melting compounds, or materials with very different melting temperatures and vapor pressures), making it a technique with unique potential for the synthesis of chalcogenides, which are the subject of this thesis.

2.3.1.1 Theoretical Models of Mechanochemistry

The theory of the MC reaction is governed by complex processes, which are introduced below.

- Hot Spot Theory: This was the first MC theory developed in 1985.[106] According to this model, the solid-state synthesis is regulated by the friction processes of the surfaces. During deformation, there is an increase in temperature in the affected area (over 1000K) in a short time interval ($10^{-4} \div 10^{-3}$ s), which initiates the reaction and the propagation of cracks. The local temperature was calculated by considering both the heat propagation mechanisms in the affected material and by comparing the temperatures required to obtain specific gaseous decomposition products.[107]

- Magma Plasma Model: This model was developed in 1967.[108] It predicts that, during the impacts between the different components, a large amount of energy (up to 10^4 K) is released, which is responsible for the formation of a special plasma state characterized by the emission of excited fragments of solid substances and electrons, which are extremely reactive (Figure 26).

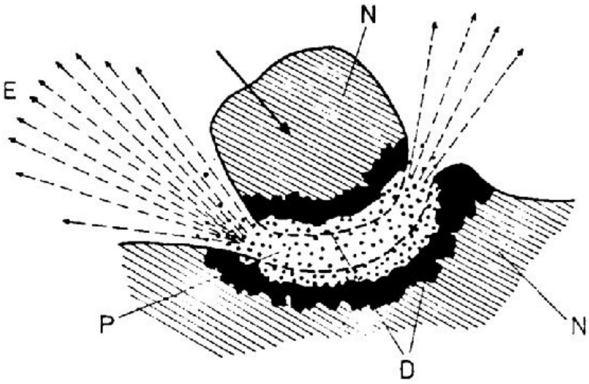

Figure 26: Magma Plasma Model. E: exo-electrons - N: Non-deformed solid - D: Highly deformed surface layer - P: Plasma.[109]

The variety of emissions allows the description of different excitation processes; each of these determines the chemical activation of the material and is characterized by a specific relaxation time, inversely proportional to the energy of the process. Processes with long lifetimes, such as defects and dislocations, have been studied at the thermodynamic level: they depend on the free energy of Gibbs of a mechanically excited solid with respect to the ground state, which defines which process guides the chemical activation.

2.3.1.2 Mechanical Activation

Mechanical activation (MA) is the process that increases the chemical reactivity of a substance without changing its composition but by stably altering its solid structure. This process depends on three factors: disorder, mobility, and structural relaxation; each activated state has a relaxation time, but if this time is significantly shorter than the time required for the reaction, then that particular state will not contribute to the process. Conversely, excited states with long relaxation times directly intervene in the reaction and can be subdivided into primary and secondary processes:

- Primary Processes: These lead to an increase in the free energy of the reactants, favoring the advancement of the chemical reaction; examples are the increase in the internal and surface energy of the particles and increase of the surface area.
- Secondary Processes: These occur on the activated solid during or after milling, such as recrystallization, adsorption and aggregation.

Therefore, MA can be seen as a multi-step process involving changes in the energetic parameters and the amount of accumulated energy in solids at each step. These steps are mainly four: (1)accumulation of defects, (2), amorphization, (3) formation of metastable polymorphous forms and (4) chemical reactions, and are collectively referred to as MA. In particular, various types of defects (

Figure 27) play crucial roles in MC.

The thermodynamics and kinetics that govern the mechanochemical process will be discussed in detail below.

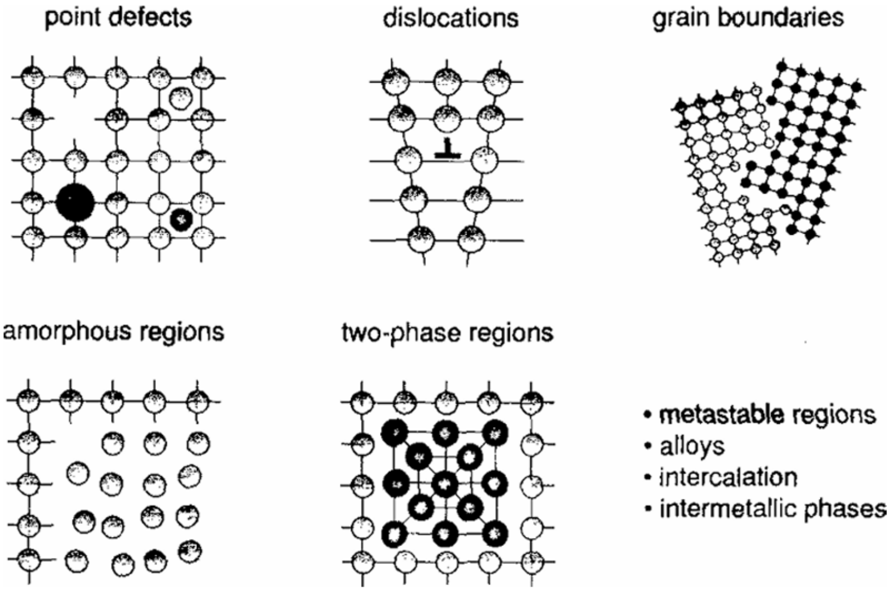

Figure 27: Defects created by mechanical activation of solids.[110]

2.3.1.3 Thermodynamics in Mechanochemistry

Interactions among solids, such as in MC, involve the depletion of initial substances and the generation of final substances, governed by physicochemical rules. These transformations can be described using core thermodynamic equations:[110]

$$\Delta G_{reac} = \Delta H - T\,\Delta S$$

Equation 8

where ΔH is the enthalpy of the reaction, T is the temperature, and ΔS is the entropy; if the crystalline structure remains largely unchanged, the latter term is negligible. ΔG determines the nature of the reaction: if $\Delta G > 0$, the reaction proceeds towards the products, while if $\Delta G < 0$, it proceeds towards the reactants; if the system is at equilibrium, then:

$$\Delta G_{reac} = \Delta G^0_{reac} + RTln(\frac{a_{AB}}{a_A a_B})$$

Equation 9

where two reactants (a_A and a_B) and one product (a_{AB}) and their respective chemical activities are considered. If we consider a reaction where the reactants are only solid crystals, at ambient temperature and pressure, then the second term in Equation 9 is zero.

Understanding the relationship between the state of a solid before and after mechanical activation requires available data to describe these states. Unlike gases and liquids, solid particles cannot be characterized by just a few thermodynamic factors. Even at absolute zero temperature, activated solids possess a finite zero-point entropy due to the disorder of lattice components. The inner thermodynamic equilibrium is first achieved above the melting temperature. The state at any lower temperature depends significantly on preliminary treatment, such as the type, intensity, and duration of mechanical stress. The resulting type and concentration of defects (

Figure 27) determine the thermodynamic state.

Standing this, a new definition of activated solid, from Hüttig's definition, needs to be taken into account. Following his theory, the mechanically activated solid state as a thermodynamically and structurally unstable arrangement at temperatures exceeding the melting point. He characterized the activated state of solid by "residual" Gibbs energy:

$$\Delta G = G_T^* - G_T$$

Equation 10

where T is the temperature, G_T^* is the energy of the activated solid state, and G_T is that of the non-activated state. This can be simplified as follows:

$$\Delta G = \Delta G_1^* + \Delta G_2^*$$

Equation 11

where ΔG_1^* is the residual surface energy and ΔG_2^* the lattice defect formation energy.

It holds for the surface energy in thermodynamics

$$\Delta G_1^* = \sigma \Delta S$$

Equation 12

where σ is specific surface energy and ΔS in the change of overall surface of a solid. It was estimated for mechanical activation of ionic crystals that the surface energy ΔG_1 corresponds approximatelly to 10% of overall Gibbs energy ΔG.

2.3.1.4 Kinetics of Mechanochemical Reactions

Literature reports several attempts to apply solid-state heterogeneous kinetics to MC systems,[111] but few similarities exist with classical kinetics. MC's unique characteristics, such as impulse character, spatial non-uniformity, and changing interaction conditions, complicate the kinetic descriptions, making a general approach almost impossible.

The evolving conditions of a solid-state reaction can be exemplified by changes in surface area (Figure 28). Initially, surface area grows as solids fragment into crystallites (I). Later stages involve plastic deformation and secondary particle formation (II), with the surface area remaining constant due to mechanochemical equilibrium. Chemical reactions occur within these secondary aggregates, potentially leading to crystallization or repeated amorphization (III). The relations between the duration of stages depend on the amount of mechanical energy loading. If it is low, the process can stop at stage II; at high energies, stages II and III occur.

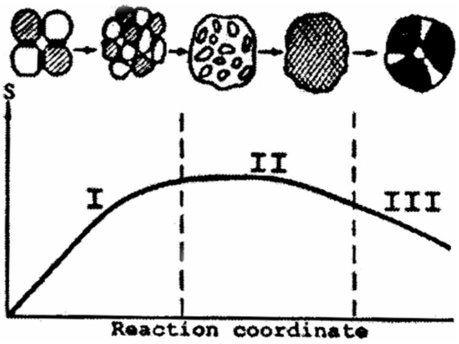

Figure 28: The change of specific surface area (S) during a mechanochemical reaction.[111]

MA and dispersion are statistical processes, therefore in this context chemical interactions can be approached using collision theory. In fact, the reaction rate in a mill estimated as:

$$v = K_m x S_n$$

Equation 13

where K_m is a constant, describing the probability of reaction to occur at a given mechanical action, x is the collision probability between particles and milling body, and S_n is the contact area between A and B components during mechanical action. Dispersion increases S_n, and new surface area formation can be described by:

$$S = S_m(1 - e^{-kt})$$

Equation 14

where S is the specific surface area after milling time t, S_m is the maximum specific surface area. Constant k is the rate constant governing new surface formation.

A similar equation can be used to describe the contact area S_n, which is proportional to the total surface of particles:

$$S_n = S_{nm}(1 - e^{-kt})$$

Equation 15

As the reaction proceeds, the amount of initial reactants decreases, reducing the probability for reagent particles to meet each other. Similar to the law of mass action, the interaction rate can be written as:

$$\frac{d\alpha}{dt} = K_m x S_n (1 - \alpha)(1 - \varepsilon\alpha)$$

Equation 16

where α and $\varepsilon\alpha$ are transformation degrees for substances A and B, and $\varepsilon = n/m$ is a mixture composition coefficient, where n is a stoichiometric coefficient representing the ratio of A and B moles in the product, and m is a real molar ratio of A and B in the initial mixture.

Integrating Equation 16 taking into account Equation 15 yields to the following equation:

$$\frac{1}{\varepsilon-1}=ln\frac{1-\alpha}{1-\varepsilon\alpha}=K\left[t-\frac{1}{k}(1-e^{-kt})\right]$$

Equation 17

Where

$$K=K_m x S_{nm}$$

Equation 18

At stoichiometric component ratio $n=m,\ \varepsilon=1$, the integration gives the equation:

$$\frac{\alpha}{1-\alpha}=K\left[t-\frac{1}{k}(1-e^{-kt})\right]$$

Equation 19

In the case when specific surface area is linearly dependent on milling time (i.e., $S_t=kt$), Equation 16 transforms into

$$\frac{\alpha}{1-\alpha}=Kt^2$$

Equation 20

In the case when specific surface area of the mixture is not changed during the milling, i.e., $S_t=const$ (it occurs when the initial substances are taken in highly disperse state or when a stationary state is achieved at which the substances are not milled but only are subjected to plastic flow), the integration of Equation 16 gives an equation similar to that describing by bimolecular reaction:

$$\frac{\alpha}{1-\alpha}=Kt$$

Equation 21

These models point out a fundamental concept in MC kinetic, namely that the rate of reaction is linked to specific surface area changes over time. However, these models do not account for the far-from-equilibrium nature of MC, nor do relate chemical reactivity to mechanical deformation or connect overall kinetics with mechanical processing methods, therefore excluding to describe different effects and complex reactions that can be observed in MC.

For example, they well-represent only simple reactions such the decomposition of pyrite FeS_2 into iron sulfide and sulfur, but they fail to describe the formation of non-equilibrium phases by milling oxidic compounds such the transformations of litharge - massicot and massicot - litharge that are reported for milling of PbO. Also, it excludes describing important effects that are observed in the growth mechanism of new phases with nanodimension crystal or in the MC reduction reaction of sulfides by a metal.

However, since MC processes can be described in terms of discrete consecutive stages, the experimental data are usually fitted with simplified mathematical models, e.g., with the logistic growth function in the case of PbO milling and with the Avrami-Erofeev equation for nanostructure formation.

What connects all the experimental models used to characterize the kinetics of various mechanochemical processes in ball milling is the observation that the kinetics of mechanically activated transformations are governed more by the total number of collisions than by time.

A useful theoretical framework widely used to understand and analyze the complexities of reaction kinetics in MC systems is the concept of "two kinetics" elaborated by *Lyakhov et al.*,[112] which addresses the dual nature of processes influencing the reaction rates during mechanical activation. It distinguishes between two main classes of factors influencing mechanochemical reactions: extensive factors and dynamic factors.

Extensive factors include characteristics such as specific surface area, particle size distribution, and the shape of particles. These factors are not limited by the reaction time and can persist throughout the process. On the other hand, dynamic factors include energy storage, stress relaxation, local temperature, and pressure. These factors have relaxation times comparable to the reaction time and can significantly affect the reaction kinetics.

The key to understanding the concept of two kinetics lies in the relaxation times of these factors. Short-lived states, with relaxation times less than the characteristic reaction time ($\tau_{ch} = 1/k$), may not significantly influence the reactivity of activated solids. In contrast, long-lived states, with relaxation times much longer than the characteristic reaction time

($\tau_i >> \tau_{ch}$), can be considered constant during the reaction and are crucial for mechanical activation studies. These concepts are taken into account in the "two kinetics" equation:

$$\frac{d\alpha}{dt} = k(T, p_i^e, \dots, p_k^e, p_{k+1} + 1, \dots, p_n) \cdot f(\alpha)$$

Equation 22

where a is the degree of transformation of the reactants, k is the kinetic constant of the reaction, p are the activation parameters of the reaction, specifically $p_i^e, \dots, p_k^e$ are the short-lived parameters, $p_{k+1}, \dots, p_n$ are the constant parameters, while $f(a)$ is a conversion function of the reactants into products. What is clear from this analysis is that activating the reaction itself is likely to be far more effective than focusing on the precursors of the reaction.

Just by considering this separation of two relatively independent kinetics, it is easy to understand all the complexity of reacting of mechanically activated compounds: still, there is an open-call to study a theoretical model that could help to gain a deeper understanding of these kinetic behaviors and enhance the efficacy of MC methods.

2.3.1.5 Planetary Ball Milling and Synthesis Parameters

Planetary Ball Milling (high energy ball milling with a planetary mill) consists of milling the material using jars placed in rotational motion around the central axis of the mill and simultaneously in a faster rotational motion around their own axis, in a manner similar to a planetary system. Inside these jars, the powdered reactants and a certain quantity of milling spheres are inserted.

This system exploits two competing centrifugal forces, which allow for the induction of different types of stress, including compression, friction, and collisions between spheres and powder, powder and powder, and powder and the wall. The effectiveness of these impacts is extremely dependent on the rotational speed of the mill and the density, size, and mass of the powders and spheres; the spheres can adopt three different types of motion distinguished based on the centrifugal force of rotation and the force of gravity:

- Cascade Movement: At low rotational speeds, gravity exerts a stronger influence than centrifugal force on the spheres. As a result, the balls tend to stay in contact with each other, rolling over one another, rather than being thrown outward against the mill's walls. This means that the impacts that occur when the balls collide with each other or with the material being milled are less forceful and less effective in promoting mechanical activation.
- Cataract Movement: Increasing the rotational speed causes the spheres to slightly detach and tend to "fall" on each other, optimizing the impacts; this is the best condition for inducing the mechanical activation of the reaction.
- Centrifugal Movement: Beyond a certain speed, the spheres remain adherent to the surface of the jar due to the high centrifugal force. This significantly worsens the efficiency of the impacts but maximizes the quality of the refinement.

The outcome of a ball milling process depends on various external parameters: evaluating each of them allows for the obtainment of products with a high degree of reproducibility. In the case of planetary ball milling, the reaction is mainly influenced by:

1. Reactants: It is necessary to insert into the jar a mixture of the reactant powders that is as homogeneous as possible so that, during the impacts, the local stoichiometry is approximately invariant and it is precisely the desired one for obtaining the goal products ; typically, the reactants are pre-mixed by hand in a mortar, often aiding the process with an appropriate non-reactive and volatile solvent (usually alcohols) to ensure better homogenization of the powders

2. Material of the Jars and Spheres: The jars and spheres should be made of the same material to avoid as much as possible erosions during the impact, sliding, and rubbing processes between them. The choice of material must be appropriate: in particular, it must have greater hardness than the reactants; the type of material will influence the energy exchanged during the impacts with the powders and therefore the reaction process. The materials commonly used for jars and spheres are steel, tungsten carbide, agate, alumina, zirconia, and silicon nitride.

3. Number and Size of the Spheres: A large number of spheres makes the motion more disordered, favoring a high impact statistic and greater efficiency in energy transfer; a larger size of the spheres is more effective on initially large crystallites, while a smaller size is more suitable for milling small particles. Typically, the spheres are produced in sizes ranging from 1 mm to 2 cm in diameter, but this can vary depending on the material.

4. Filling of the Jars: There must be sufficient space to allow the movement of powders and spheres; the volume should not exceed 50% of the available volume. This helps to reduce the chaos of the process and limit the deterioration of the milling means.

5. Working Atmosphere: In some processes, the use of an atmosphere with the presence of oxygen can favor the formation of impurity phases through oxidation; it may therefore be useful to work in an inert atmosphere of argon or nitrogen. In other cases, the choice of a particular atmosphere can favor the formation of specific compounds, making the gas itself to be part of the process as an oxidizing/reducing agent.

6. Temperature and Pressure: The temperature and pressure are typically those of the ambient laboratory and are not varied during the process, although at the local level, the temperatures can reach very high values; due to this, the average temperature of the jars slightly increases with the processing time, which is why the ball milling process typically includes pauses that favor the cooling of the system. The local pressure stimulated during impact can reach up to 6 GPa, while inside the jar, which is usually sealed with gaskets that prevent exchange with the external atmosphere, the pressure is almost invariant.

Keeping in mind these previous considerations which have to be addressed in order to identify the most suitable conditions for the synthesis, there are there fundamental parameters which regulate the MC reaction and must be carefully taken into account:

1. Time (Time): Long milling times favor the reduction of particle size and increase the possibility of obtaining nanocrystallization and/or amorphization of the powder;

on the other hand, at equal energy of the process, long times favor the increase in the statistical weight of the quantity of impurity phase due to the wear and erosion of the jars and spheres with consequent contamination of the product. As described in the previous paragraph, it is precisely the kinetic processes that have a strong dependence on time, so the extension of the synthesis times favors such mechanisms compared to purely thermodynamic ones. The milling time can be spaced out with pauses (pause parameter) of adjustable duration.

2. Ball-to-Powder Ratio (BPR): A higher sphere-to-powder ratio allows to increas the number of impacts per unit mass of powder vs. time. Increasing the BPR causes various events: an increase in the reaction rate, with an increase in temperature and amorphization of the product, a variation in the composition of the final powders, and a reduction in particle size. This parameter therefore plays a key role in the regulation of the crystallinity and morphology of the final product.
3. Velocity of Milling (RPM): The rotational speed around the main axis of the mill, usually measured in rounds per minute. The rotation occurs in a clockwise direction but can be periodically reversed using the “Reverse” function, allowing for more uniform particle size distribution of the final products. Increasing the rotational speed generally allows to increase the kinetic energy of the spheres and simultaneously brings to the enhancement of the inner temperature of the jars, causing secondary phenomena such as decomposition, the production of metastable phases, and the inclusion of any impurities in the reactant. Additionally, it allows for a further increase in the reaction rate. In some cases, high rotational speeds can lead to significant recrystallization of the product.

During a ball milling process, it may sometimes be useful to add a solvent to achieve what is known as LAG - Liquid Assisted Grinding; the solvent is adsorbed onto the surface of the particles, reducing their surface energy and thus improving the milling process, favoring the reduction of final agglomerates or the amorphization of the product. Mainly, under equal kinetic and thermodynamic conditions, the presence of LAG results in a higher degree of homogeneity and better refinement of the powder product. Another important consequence of the LAG treatment is the possibility to stabilize/metastabilize a suspension of the refined powder in the solvent. Rarely, LAG is applied to perform MC reactions, due to the too low energy exchange.

MC has already proven to be an effective, safe, and economical technique for the synthesis of semiconductors. Within the scope of this thesis, the mechanochemical process for the synthesis of unconventional chalcogenides has become a standardized process, revealing an extraordinary capability for complete control in the realization of CIGSSe solid solutions, exploring various cationic/anionic substitution ratios, and their morphology, particle size, and degree of crystallinity, characteristics that will be analyzed using the techniques described in the following chapter.

The tools used for MC in this thesis are the Planetary Ball Milling Pulverisette 7 - Classic Line and, above all, the Pulverisette 7 - Premium Line (Figure 29), whose technical specifications are indicated in Table 3.

Figure 29: Planetary Ball Mill Pulverisette 7 - Premium Line, produced by Fritsch.

In particular, the Pulverisette 7 Premium Line system used in the context of this thesis is equipped with:

- Pressure-sealed jars of agate and zirconia with a capacity of 45 ml
- Agate spheres of 5 and 10 mm, zirconia spheres of 3, 5, 10 mm

- Inert gas: nitrogen, argon, anhydrous ammonia

Specification	Value
Number of jars	2
Jar capacity	20, 45, 80 ml
Sphere size	0.1 - 20 mm
Milling	Dry/wet with the possibility of controlled atmosphere (1-20 atm) (Sealed jars)
Maximum jar rotation speed	2200 rpm
Maximum main disc rotation speed	100 - 1100 rpm
Centrifugal acceleration	95g

Table 3: Pulverisette 7 - Premium Line Mill technical specifications

2.3.1.6 Target Preparation

The targets usable as source material for vacuum depositions were realized by mimicking the method described by Delmonte et al.,[47] but adapting the P-T conditions of thermal treatment and sintering to obtain a compact and crystalline target of SbSI.

2.3.2 Deposition Techniques

2.3.2.1 Liquid Phase Methods

Liquid phase deposition of suspensions of nanoparticles is a versatile and widely used technique for creating thin films with controlled properties. This method involves dispersing nanoparticles in a liquid medium to form a stable suspension, which is then deposited onto a substrate using various techniques. Within the context of this thesis, it will be demonstrated that is possible to obtain stable suspensions of sub-micrometrical particles both of CIGSSe and SbSI taking advantage of the LAG process performed by high energy ball milling apparatus.

Drop-casting is one of the simplest liquid phase methods, where a drop of the suspension is placed onto the substrate and then properly dried, forming a thin film. This technique is straightforward and requires minimal equipment (Micropipette Eppendorf Research® plus, 1 channel, 20 – 200 μL for the deposition, and occasionally (for less volatile solvents) a hot plate for drying treatment, but may result in non-uniform morphology and uncontrolled film thickness.[113] Spin coating, on the other hand, involves depositing the suspension onto a spinning substrate, which spreads the liquid evenly across the surface due to centrifugal force. This method allows for the creation of highly uniform films with controlled thickness, but it doesn't allow to achieve a highly dense films and the layer is often affected by high porosity and a elevate number of grain boundaries.[113] In this thesis, a WS-400-6NPP-LITE-WS-650-23 Laurell Spin Coater equipped with a Eppendorf Research® plus, 1 channel, 20 ÷ 200 μL Micropipette. Doctor blading is another effective technique, where a blade is used to spread the suspension across the substrate at a controlled speed and thickness. Here, a ZUA 2000 universal applicator from Zehntner was used. This method is particularly useful for depositing large-area films and can be easily scaled up for industrial applications. In this thesis it will be demonstrated that for the CIGSSe suspensions is the optimal deposition method to obtain controlled and dense thin films.

Before the deposition via liquid phase methods, all the substrates were pre-treated with a cleaning process that involves several steps of ultrasonic bath for 10 minutes, at 37 Hz frequency, 40°C, in various solvents in sequence: water, isopropanol, acetone. After drying with nitrogen, they were placed in a UV-Ozone cleaner (PSD Standard Novascan UV-Ozone Cleaner) for 20 minutes. A UV-Ozone cleaner treatment has reported several effects on molybdenum and FTO substrates. The primary effect is the removal of organic contaminants from the substrate surface. UV-Ozone treatment generates highly reactive ozone and atomic oxygen, which oxidize and decompose organic residues, leaving a cleaner surface. This process enhances the surface wettability by increasing the hydrophilicity of the substrate, which is crucial for improving the adhesion and uniformity of the films deposited via liquid phase methods. Additionally, the treatment can modify the surface chemistry by introducing hydroxyl groups, which can facilitate chemical bonding with deposited materials.[114]

Chemical Bath Deposition

A cadmium sulfide buffer layer with thickness 90 nm is deposited with Chemical Bath Deposition; the samples are kept in a beaker containing double-distilled water, ammonia (NH_3) and a $CdSO_4$ solution (0.1M), at 60°C for 5 minutes, after which thiourea ($CS(NH_2)_2$) is added 2 minutes later. The beaker with sample and mixture were then kept in the bath at 60 °C and washed with double-distilled water.[115]

2.3.2.2 Vacuum Methods

Pulsed Electron Deposition

Pulsed electron deposition (PED) uses a high-energy beam to achieve stoichiometric material transfer from a single target. However, using an electron beam instead of a laser beam offers several advantages: lower cost, higher efficiency and rate of deposition, smaller deviations in the stoichiometry of the deposited material, and simpler handling.

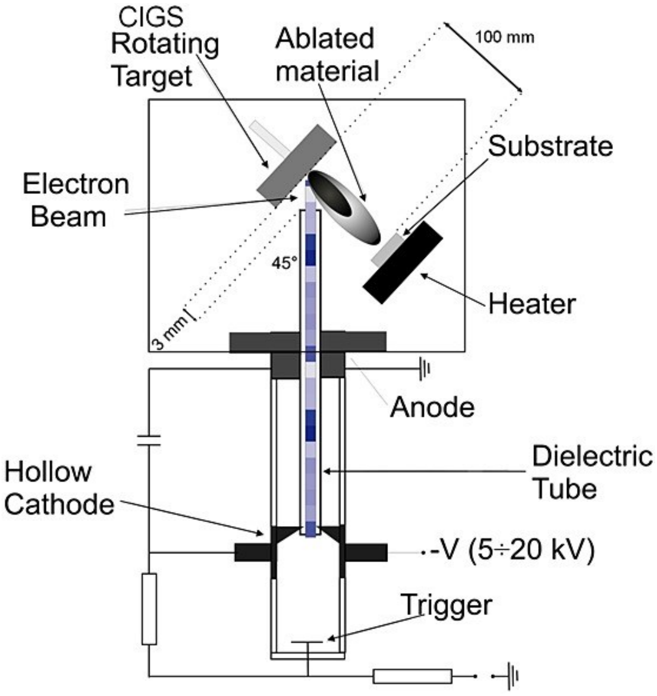

Figure 30: The LT-PED setup used at IMEM-CNR.[45]

The Low Temperature (LT)- PED setup installed at IMEM-CNR and shown in Figure 30, provides a good overview of the general principle behind PED: electrons are emitted from the electron gun at high energies (5÷20 keV) and guided toward the target by a dielectric tube. The acceleration voltage and pulse rate of the electron beam can be varied according to the particular material and to the deposition requirements.

When high-energy electrons hit the target surface, a plasma plume is formed, consisting of two components: a plasma plume of ablated material (ablation plume) and a plasma plume of evaporated material (evaporation plume), characterized by different angular distribution. Ablation is the mechanism which enables the stoichiometric transfer of the target's elements onto the substrate and is the desired process in PED. It occurs due to higher energy electrons (kinetic energies $\geq$ 10 keV), which cause vaporization of the target material outside of thermodynamic equilibrium as their energy is dissipated within a small volume. Evaporation from the target occurs at thermodynamic equilibrium and results in non-stoichiometric material transfer, making it an undesirable component in PED. It is caused by lower energy electrons (kinetic energies $\leq$ 1 keV), which gradually heat the target surface during deposition, forming a melt from which incongruent evaporation occurs. The evaporation plume is off-stoichiometric since the more volatile elements will be present at higher concentrations.

A thin film deposited via PED grown at room temperature typically shows an amorphous structure, so an annealing in mild temperature and pressure is typically needed to recrystallize the material. Otherwise, the substrate can be heated directly in the vacuum chamber to obtain directly a crystalline film and at the same time to force partial or complete growth orientation of the crystallites.

In this thesis, films were grown via PED using a high vacuum chamber kept at 10^{-7} mbar on standby, equipped with a PEBS-20 commercial source (supplied by Neocera Inc., Beltsville, MD, USA).

RF- Sputtering

The architecture of the window layers used in the single junction devices are a 100 nm layer of undoped zinc oxide (i-ZnO), used to cover the CdS buffer layer to limit the effects of shunting paths, and an 800 nm layer of aluminum-doped zinc oxide (Al-ZnO) was used as the final transparent front contact. Both layers were deposited by RF-sputtering at room temperature, using commercial 5 cm diameter targets from Testbourne Ltd. The targets underwent a cleaning process before deposition, which was performed at a pressure of 5×10^{-3} mbar of Ar gas at room temperature. The sheet resistances of the i-ZnO and Al-ZnO layers were found to be $\geq 2 \times 10^{6}$ Ω/sq and 10-22 Ω/sq, respectively, with a transmittance of ~85% (±3%). The top undoped ZnO (UZO) and Al-doped ZnO (AZO) layers were deposited via RF magnetron sputtering (Angstrom Sciences) at room temperature (RT) and 120 W in an Ar atmosphere (5.0×10^{-1} Pa).

2.3.3 Characterization techniques

This chapter outlines the primary instruments, techniques, and parameters employed to characterize both the high energy ball milling powders and the thin films and solar devices discussed in this work.

2.3.3.1 Structural and morphological analysis

Powder X-Ray Diffraction (PXRD)

In this study, PXRD was used to verify the structural properties of both the powders obtained via high energy ball milling and thin films. Additionally, it served as a screening method to evaluate the crystalline texture and the mean crystallite size. The recorded patterns were compared with calculated reference diffraction patterns of the expected phases using Match! Software equipped with PDF ICCD 2000 structure database.[116]

Two powder X-ray diffraction instruments were used for measurements: Thermo Electron ARL Xtra for preliminary screening and a Rigaku Smartlab XE diffractometer equipped with an Euler cradle for high-resolution measurements. The Thermo Electron ARL X'tra powder diffractometer was set at 20 kV and 30 mA to obtain the specified radiation, equipped with a Si(Li) solid-state detector. Each sample was placed on a stationary zero-background sample holder and scanned over a variable 2ϑ range, typically of 10°-65°, with variable step size. Rigaku Smartlab XE diffractometer was used in Bragg-Brentano geometry with Cu $K\alpha$ wavelength. A Ni filter was used to suppress the $K\beta$ contribution. 5.0° soller slits were located both on the incident and diffracted beam and data were collected using a HyPix3000 detector operating in 1D mode.

Raman Spectroscopy

In this study, Raman Spectroscopy was used to study the structural properties of the powders obtained via high energy ball milling.

Raman measurements were recorded using a micro-Raman apparatus (Horiba Jobin–Yvon Labram) equipped with a confocal microscope (Olympus BH-4) with 4, 10, 50, ULWD 50 and 100 objectives (lateral spatial resolutions of approximately 25, 10, 2, 2 and 1µm). The spectrometer is fitted with two lasers emitting at 633 nm and at 532 nm, an edge filter, a 256×1024 pixel CCD detector, a grating, and a density filter wheel. The spectrometer is calibrated at the silicon Raman peak of 520.6 cm−1 before each measurement. The apparatus was equipped with a Linkam cryostate (-190÷ RT) cooled with liquid nitrogen.

Scanning Electron Microscopy and Energy-Dispersive X-Ray Spectroscopy (SEM-EDX)

In this study, SEM analysis was used to verify the morphological properties of both the powders obtained via high energy ball milling and the thin films deposited via liquid phase techniques or via PED, while Focused Ion Beam cross-sectioning technique was used to investigate morphology and thickness of the thin films. EDX was indeed performed to qualitatively verify the elements ratio in the samples.

During this PhD activity, a Zeiss Auriga Compact Scanning Electron Microscopy equipped with a Field Emission Gun (Schottky-type) source (FEG-SEM) was used for routine analyses. The FEG source focuses the electron beam better to obtain higher resolution compared to a common SEM. This instrument can reach a resolution of 1.2 nm at 15 kV; the voltage is modulable in the range between 100 V and 30 kV. The operating currents can vary between 4 pA and 100 nA, while magnification can start at 12X and reach, in ideal conditions, 900 kX. However, the electron beam is usually set to work between 5 and 20 kV and within the magnification range between 500X and 100 kX. InLens and Everhart-Thornley detectors were used (for higher and lower resolution, respectively). The instrument was equipped with an Oxford Energy Dispersive X-Ray Spectrometer detector for compositional microanalysis and with a Zeiss Auriga Compact Focused Ion Beam system for cross-sectionial samples preparation.

2.3.3.2 Electrical Measurements

The vertical and planar resistance of the absorber layer films, and the current density-voltage (I-V) characteristics of the complete solar cells were collected by using a Keithley 2614B Sourcemeter and an AAB solar simulator (ABET SUN 2000) under Standard Test Conditions (AM1.5G, 25°C).

Sourcemeter and solar simulator are both controlled by dedicated software developed using LabView, which allows for the automation of data acquisition and the control of measurement parameters.

Resistivity, transport and mobility measurements were collected by performing Hall effect measurements in Van Der Pauw geometry and Seebeck effect measurements.

2.3.3.3 Optical Measurements

UV-VIS-NIR Spectroscopy

UV-VIS-NIR spectroscopy was employed to study the optical properties of the thin films, measuring optical transmission and absorption. In particular, a JASCO V-770 spectrophotometer was used, with halogen and deuterium lamps as sources, changed at 900 nm and a photomultiplier and a Peltier cooled PbS, as detectors. The scanning range was kept between 300 and 1200 nm, with a scan speed of 400nm/min. In particular, the UV-VIS spectrophotometer can directly measure transmittance, i.e., the amount of light transmitted by the sample through the ratio between the intensity of the incident light I_0 and that of the transmitted light I. The relationship between absorbance (Abs) and transmittance (T) is described by the following equation:

$$Abs = 2 - \log\frac{I}{I_0} \cdot 100 = 2 - \log(T)$$

Equation 23

The diffuse reflectance of the thin films was performed with the same apparatus, JASCO V-770 spectrophotometer, equipped with an integrating sphere and operating in diffuse reflectance mode in the range between 400 and 1200 nm.

The sum of the components gives the total reflectance, which relates to other spectrophotometric quantities according to an energy conservation relation:

$$Abs + R + T = 1$$

Equation 24

Absorbance measurements on a semiconductor allow to experimentally retrieve the value of its optical bandgap *Eg*. From the spectrum, the absorption threshold of the material incomes when the energy of the radiation is sufficient to excite an electron from the valence band to the conduction band. This calculation is performed using the empirical Tauc relation:

$$\alpha h\nu = A\left(h\nu - E_g\right)^n$$

Equation 25

where α is the absorption coefficient and A is the absorption constant. The exponent n is related to the possible electronic transitions, and it is equal to 2 for allowed indirect transitions, to 3 for forbidden indirect transitions, to 1/2 for allowed direct transitions, and to 3/2 for forbidden direct transitions. For negligible reflectance values, the absorption coefficient can be calculated directly from the absorbance Abs as $a = 2.303Abs/t$, where t is the thickness of the absorbing layer. By plotting $(ah\nu)^2$ vs. $h\nu$, a typically constant curve at low energies and a linear curve at higher energies are obtained. The intercept of this curve with the x-axis provides the empirical value of the bandgap.

This relation can also be used starting from a diffuse reflectance spectrum, converting Reflectance values in absorbance using the Kubelka-Munk function:[117]

$$F(R) = \frac{(1-R)^2}{2R}$$

Equation 26

By plotting $F(R)$ vs. $h\nu$, a similar curve to the previous case is obtained.

3 RESULTS AND DISCUSSION

3.1 $Cu(In_{1-x}Ga_x)(S_ySe_{1-y})_2$ chalcogenides

3.1.1 High Energy Ball Milling Mechanosynthesis

The mechanochemical syntheses of $CuInSe_2$ (CISe), $CuInS_2$ (CIS) and of the solid solutions $Cu(In_{1-x}Ga_x)S_2$ (CIGS) and $CuGa(S_\gamma Se_{1-\gamma})_2$ (CGSSe) were performed exploiting binary sulfides and selenides of the desired cations as reactants, carrying out the following solid-state chemical reactions:

Reaction 1. $Cu_2Se + In_2Se_3 \rightarrow 2CuInSe_2$

Reaction 2. $Cu_2S + In_2S_3 \rightarrow 2CuInS_2$

Reaction 3. $Cu_2S + (1-x)In_2S_3 + xGa_2S_3 \rightarrow 2Cu(In_{1-x}Ga_x)S_2$

Reaction 4. $yCu_2S + (1-y)Cu_2Se + (1-y)Ga_2Se_3 + yGa_2S_3 \rightarrow 2CuGa(S_\gamma Se_{1-\gamma})_2$

To identify the most suitable anionic and cationic ratios in point 3. and 4., for the application purpose of this research, the theoretical bandgap of these materials was analyzed as a function of the compositional fractions x and y using the model proposed by Bär et al.[118] This model employs a linear approximation between the bandgaps of each end-member of the solid solutions, corrected by a characteristic material constant called the optical bowing constant. Specifically, it was found that:

1. $E_g^{CIGS}(x) = xE_g^{CGS} + (1-x)E_g^{CIS}(x) - b^{CIGS} * x(1-x)$ Equation 27
2. $E_g^{CGSSe}(y) = yE_g^{CGS} + (1-y)E_g^{CGSe} - b^{CGSSe} * y(1-y)$ Equation 28

where $b^{CIGS}(eV) \approx 0.21$ and $b^{CGSSe}(eV) \approx 0$. The bandgap value which maximizes the power conversion efficiency (PCE) of a tandem cell on commercial Si is calculated to range between 1.7 and 1.9 eV. For these reasons we select to focus on those compositions of solid solutions series which return a bandgap close to a mean value of 1.8 eV. Precisely, this is achieved by x = 0.4 and y = 0.2, as shown in Figure 31.

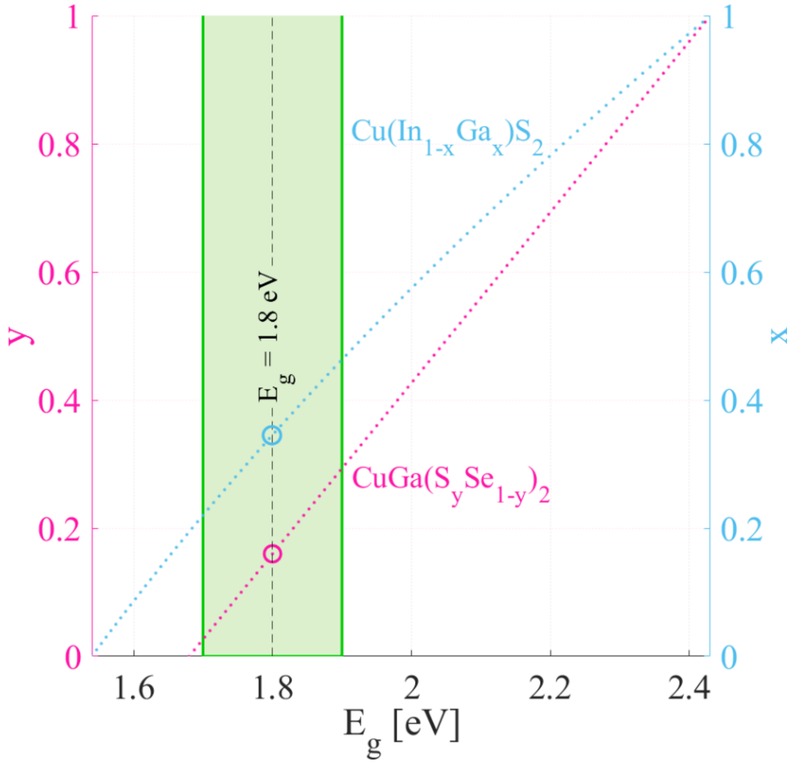

Figure 31: Calculation of the bandgap of CIGS (in red) and CGSSe (in blue) as a function of the percentage of substitutional species inserted into the structure. The ideal range of values for top-cell absorbers interfaced with Si bottom-cells is identified by the green-shaded areas.

The syntheses were initially performed working with the Fristch Pulversiette 7 Classic Line high energy milling apparatus (see paragraph 2.3.1.5) using mechanochemical (MC) parameters and conditions similar to those used to stabilize the ternary sulfur chalcopyrite $CuInS_2$, as reported by *Delmonte et al.*.[47] In particular, the process was performed in dry milling conditions (without the use of any solvent) and in ambient atmosphere, applying a thermodynamic process characterized by intermediate ball-to-powder ratio (BPR) values, short times, and high revolutions per minute (RPM). The reactants used for the synthesis of CISe, CIS, CIGS and CGSSe allowed the use of agate jars (SiO_2), which have a hardness of approximately 6.5-7 Mohs,[119] higher than that of typical sulfides/selenides (< 4 Mohs),[120] reducing the risk of erosion of the grinding media during the process.

Specifically, the best MC parameters (Protocol 1) for sulfur-based compositions resulted to be:

- RPM: 650
- BPR: 17 - Balls: 10 mm
- Time: 120 min, Pause: 0 min, Reverse: Off
- Atmosphere: Air, RP

The reactions' product appeared as a black opaque powder, providing an initial but qualitative confirmation about the successful formation of the desired phase (the initial mixture is usually brownish orange).

Quantitative analysis was performed using powder X-ray diffraction (PXRD), as shown in Figure 32. The disappearance of all the peaks related to reactants and the formation of a single phase compatible with the typical tetragonal structure of chalcopyrite were evident for reactions 2, 3, and 4. However, for CISe, this MC protocol was found to be unsuitable, as traces of reactants and spurious phases were detected in the PXRD pattern (Figure 32(a)), pointing out that the reaction is not complete with the protocol chosen.

Contrarily, sulfur-based compounds showed the formation of a pure chalcopyrite phase without byproducts. Particularly, Figure 32(b) shows the obtainment of the predicted CIS tetragonal structure. Figure 32(c) shows CIGS as the only product of reaction 2, exhibiting a shift towards higher angles compared to the CIS pattern, thus indicating the introduction of a constitutional percentage of Ga substituting In in the structure and slight modifications of the cell parameters due to the different atomic sizes of the two cations. This did not alter the spatial symmetry of the cell (space group I-42d).

The reflections were correctly located between those calculated for the end-members CIS and CGS, with the new peak center position that seems to be proportional to the ratio

In:Ga=3:2. These considerations were analogous to that of CGSSe (Figure 32 (d)), where along with an optimal reaction yield, the full width at half maximum (FWHM) compared to that of CIS suggested greater crystallinity of the product.

However, compared to a material produced with other techniques, the peak width of the PXRD pattern of the MC synthetized chalcogenides, which depends on the microstructure, was significantly larger, indicating a very fine average size of individual crystallites.

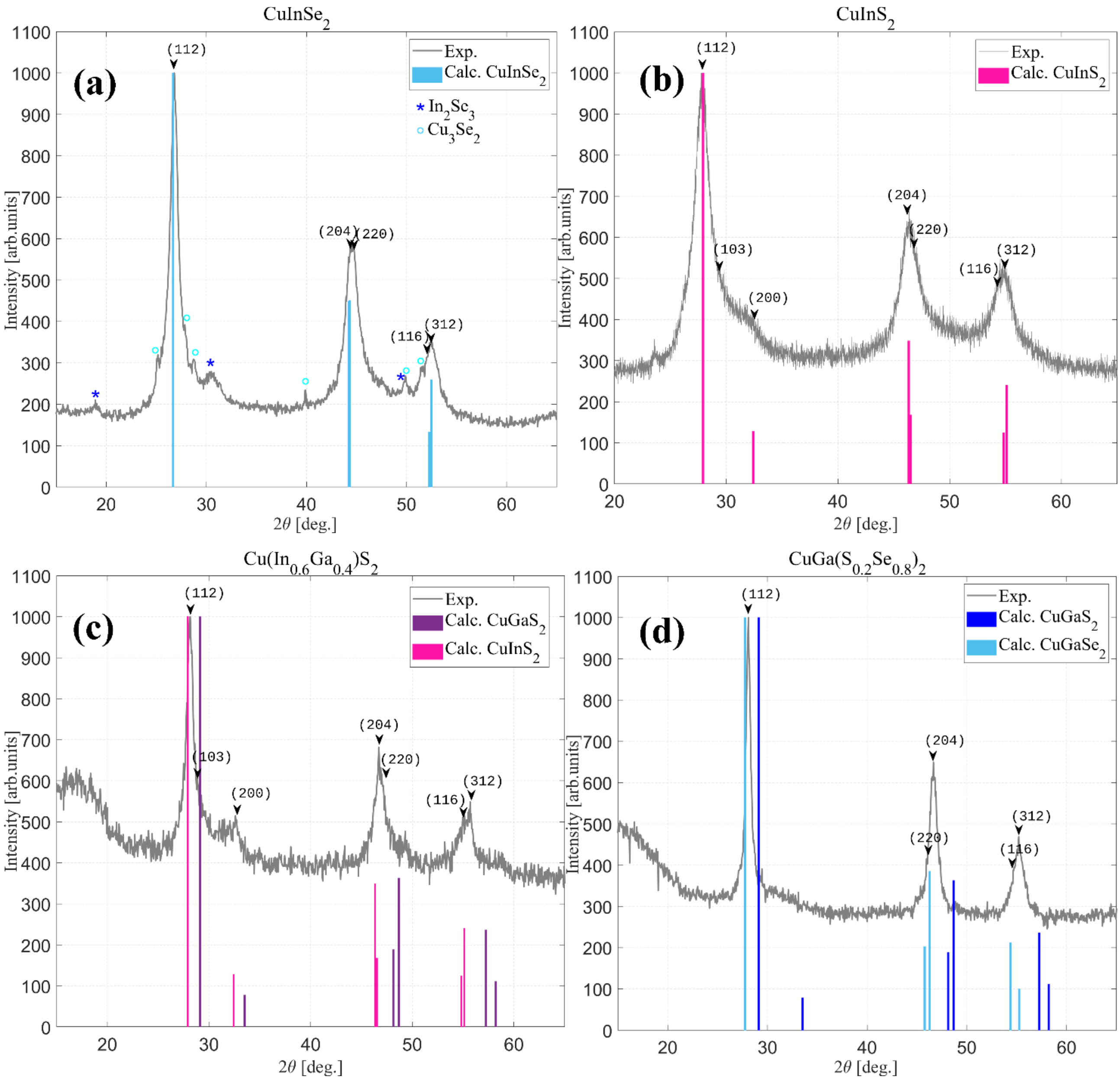

Figure 32: XRD patterns of the powders obtained from the reactions 1(a), 2(b), 3(c) and 4(d), using SiO_2 jars @650 RPM, 17 BPR, 120 min (Protocol 1).

Notably, selenium-based mechanochemical products have been usually found to exhibit greater crystallinity compared to those containing only sulfur. Indeed, selenides are usually far less stable than their parent sulfides. This means that, in the same energy condition, the reactivity of Selenides is higher, giving rise to faster and more complete reactions which result in more crystalline products.

A second MC protocol (Protocol 2) was found to be effective for the completement of the CISe reaction (Figure 33), using longer milling time with respect to the first protocol to complete the reaction, but with lower energies, to avoid degradation of the phase:

- RPM: 550
- BPR: 17 - Balls: 10 mm
- Time: 180 min, Pause: 0 min, Reverse: Off
- Atmosphere: Air, RP

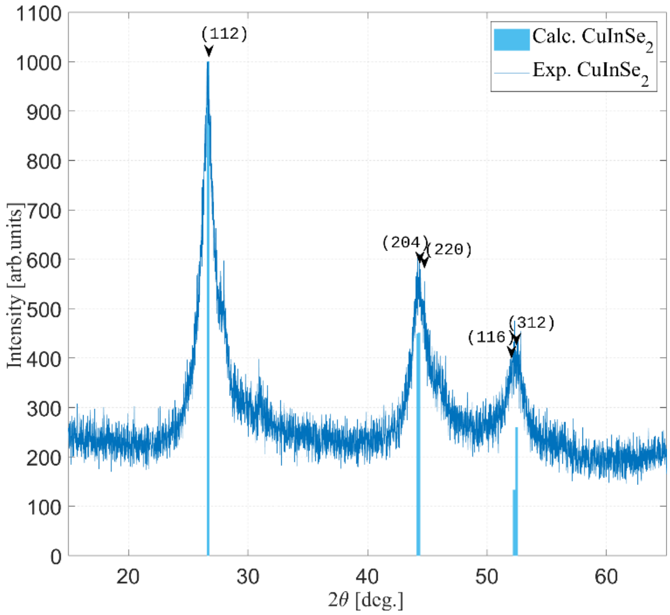

Figure 33: XRD patterns of the powders obtained for reaction 1, using SiO_2 jars @550 RPM, 17 BPR, 180 min (protocol 2).

3.1.1.1 High Energy Ball Milling Mechanosynthesis in controlled atmosphere

These results prove the effectiveness of MC in the synthesis of this class of materials, further important improvements are needed whether, as in this case, we are dealing with semiconductive compounds production for PV applications. The major issue is the way the process is performed. The reported experiments were conducted in ambient atmosphere, so in the presence of oxygen. It is known that for chalcogenides the introduction of substitutional S/Se-O be is highly detrimental to the semiconductive properties causing a transition from p-type character to n-type doping.[121] For these reasons it was decided to conduct the MC process in the ball milling apparatus Fritsch Pulverisette 7 “Premium Line”. In this apparatus (described in paragraph 2.3.1.5) which allows to perform ball milling in closed jars where it is then possible to control di atmosphere up to 5 bar of pressure.

Hence, in this stage of the experimental part, the reactants were introduced in a nitrogen-controlled atmosphere at a pressure of 4 bar and the MC synthesis was performed keeping the same RPM with respect to the previous experiments (respectively 650 for sulfur-based compounds and 550 for pure selenide) and extending duration from 2 to 3 hours. In addition, it was decided to increase the frequency of the impacts by enhancing the BPR parameter from 17 to 24, in order to evaluate the effects that on the granulometry of the product. Moreover, we increased also the exchanged kinetic energy during the process not by increasing the RPM parameter but replacing the grinding medium (jars and spheres) of agate with zirconia (ZrO_2). The use of ZrO_2 instead of agate allows in principle to reduce the wear of jars and balls thanks to its higher hardness (7.5 Mohs).[119]

Noteworthy, MC synthesis in controlled atmosphere was investigated imposing intentional copper sub-stoichiometry for all four compositions, specifically, $Cu_{0.9}In_{1.1}Se_2$, $Cu_{0.9}In_{1.1}S_2$, $Cu_{0.9}(In_{0.66}Ga_{0.44})S_2$ and $Cu_{0.9}Ga_{1.1}(S_{0.2}Se_{0.8})$. This is needed for the realization of the best performant p-n junction such a kind of chalcogenides based thin film solar cells, for the reasons that will be discussed in the subsection 2.2.2.

Definitely, the set MC parameters (Protocol 3) for these experiments were:

- ZrO_2 sealed jars
- Balls 10 mm
- RPM 650 (CIS, CIGS, CGSSe) – RPM 550 (CISe)
- BPR 24
- Time 3h - No pause - Reverse Off
- Atmosphere: N_2, 4 bar

The products of this MC process were then analyzed by PXRD.

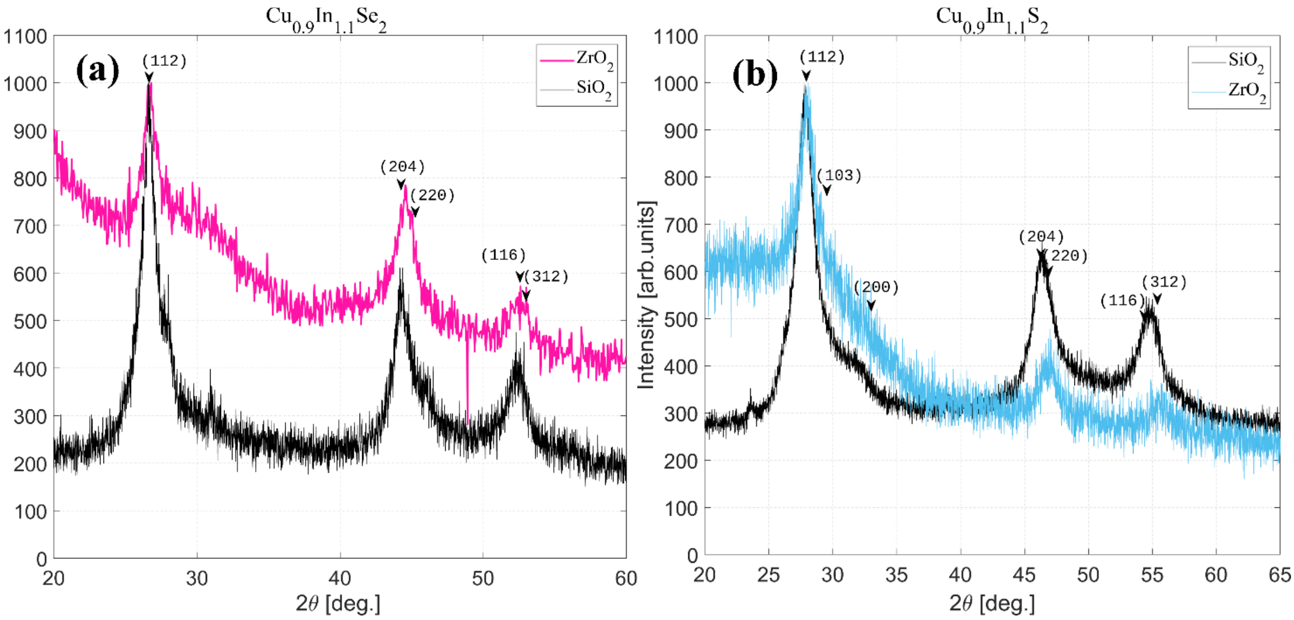

Figure 34: XRD analysis of CISe (a, pink curve) synthesized in ZrO_2 jars @550 RPM, 24 BPR, 180 min and under controlled nitrogen atmosphere and CIS (b, blue curve) synthesized in ZrO_2 jars @650 RPM, 24 BPR, 180 min and under controlled nitrogen atmosphere; to be compared with the XRD of the same compounds obtained in SiO_2 jars (black curves).

From the XRD analysis of CISe and CIS compounds, shown in Figure 34(a) and (b) respectively, it is evident that the increase in process energy, due to the change to zirconia jars and spheres, result in a significant reduction in the grain size of the powder compared to the previous experiment carried out in agate and air environment. It is important to underline the nanocrystalline population of the chalcopyrite phase emerges from an amorphous-like broad peak, indicating an inhomogeneous distribution of the grains, rather low degree of crystallinity and sub-micrometric granulometry.

For the more complex quaternary solid solutions, such as CIGS (Figure 35(a)) and CGSSe (Figure 35(b)), only a slight increase in the FWHM of the XRD peaks can be observed, meaning a small reduction in the grains' mean size.

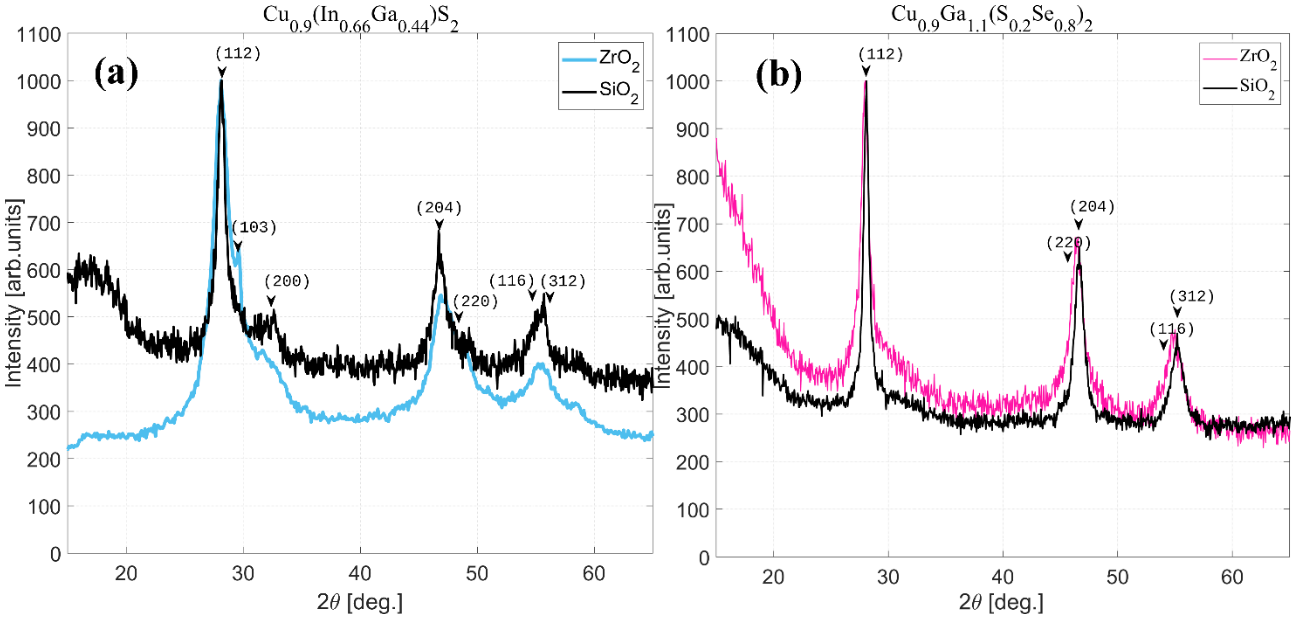

Figure 35: XRD pattern for (a) CIGS and (b) CGSSe synthesized in ZrO_2 jars @650 RPM, 24 BPR, 180 min and under controlled nitrogen atmosphere, to be compared with the XRD of the same compounds obtained in SiO_2 jars (black curves).

Additionally, EDX spectroscopy was conducted on the powders, as shown in Table 4, which yielded results consistent with the predicted compositional ratios and confirmed that any impurity phases, if present, are below the detection threshold of the instrument (i.e. 1% of atomic composition percentage).

Element	CISe calculated	CISe experimental	Element	CIS calculated	CIS experimental
Cu	22.5%	23.1%	Cu	22.5%	22.2%
In	27.5%	25.1%	In	27.5%	26.7%
Se	50.0%	51.8%	S	50.0%	51.1%
Element	CIGS calculated	CIGS experimental	Element	CGSSe calculated	CGSSe experimental
Cu	22.5%	22.9%	Cu	22.5%	20.0%
In	16.5%	16.4%	Ga	27.5%	25.7%
Ga	11.0%	11.6%	S	10.0%	11.2%
S	50.0%	49.1%	Se	40.0%	43.1%

Table 4: EDX analysis of CISe, CIS, CIGS and CGSSe powders.

The structural and compositional analyses demonstrated an effective reduction of the crystallinity which mainly observed for the end members of the solid solution, i.e. CIS and CISe compounds. SEM analyses allowed to confirm particles' sizes inhomogeneous distribution ranging from a few tens of nm up to crystallites on the order of 1000 nm. In particular, the CISe grains (Figure 37) appear to be less amorphous, with more defined edges indicative of a crystalline structure, compared to those of CIS (Figure 36).

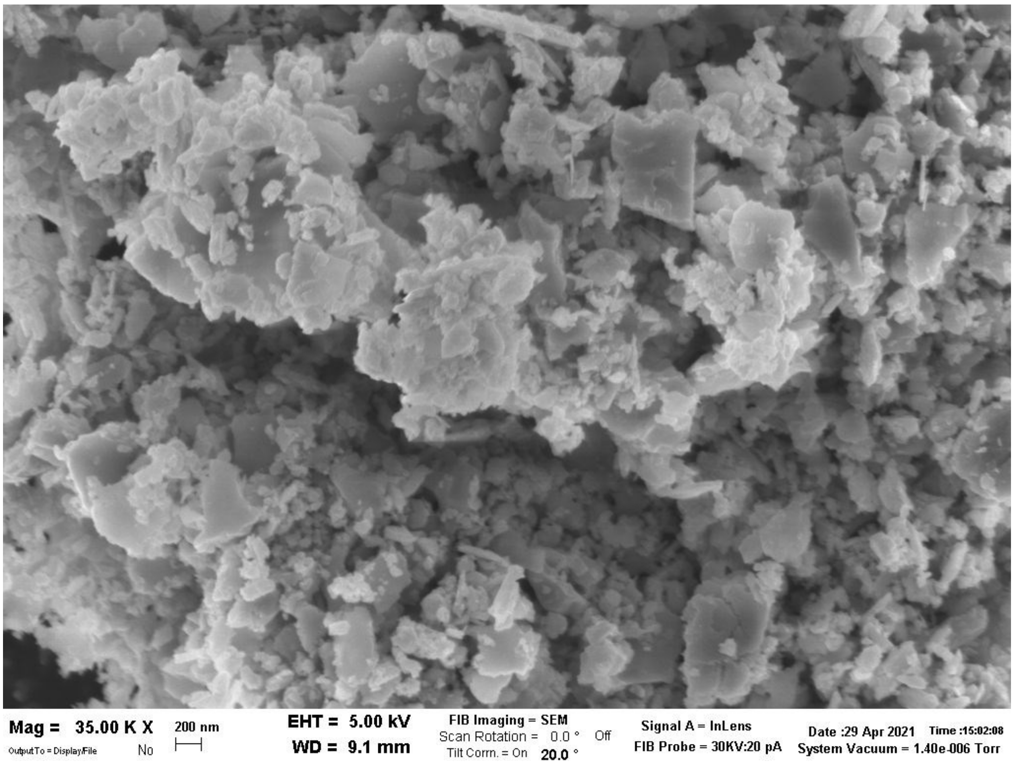

Figure 36: SEM image of CIS synthesized in ZrO_2 jars @650 RPM, 24 BPR, 180 min

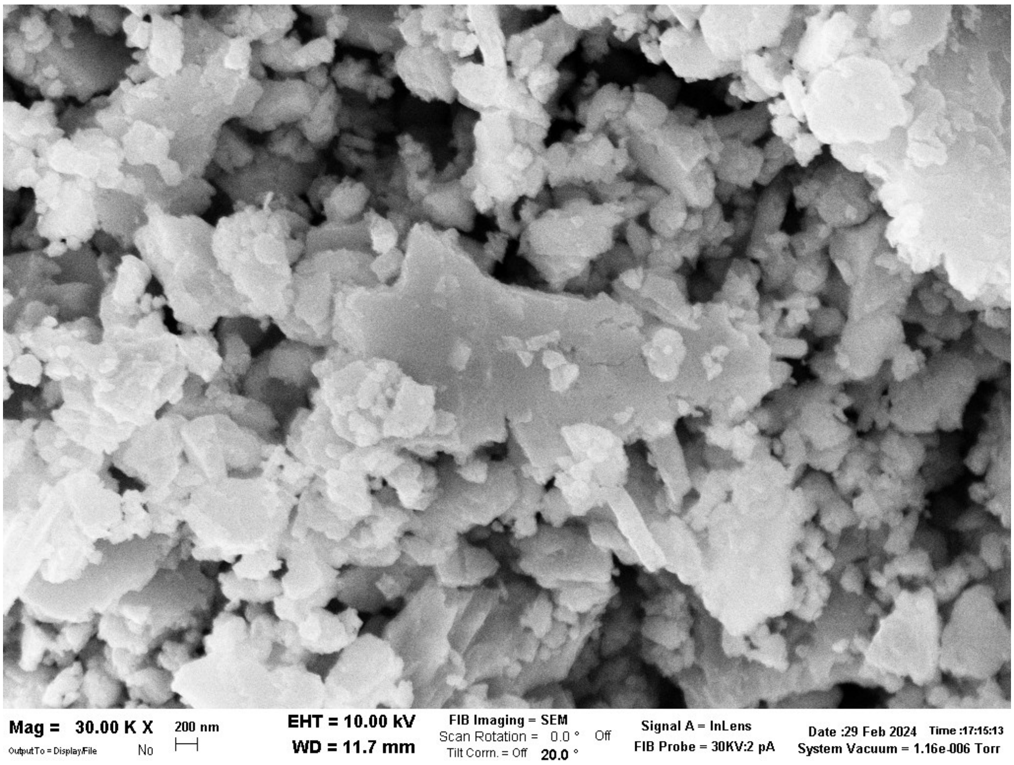

Figure 37: SEM image of CISe synthesized in ZrO_2 jars @550 RPM, 24 BPR, 180 min

In conclusion, the compounds CISe, CIS, CIGS and CGSSe with the desired compositions were successfully synthesized via MC during this thesis. Specifically, the high BPR synthesis regime performed in ZrO_2 sealed jars under nitrogen-controlled atmosphere proved to be the most functional for initiating the MC reaction. However, while the greater kinetic energy exchanged under the same MC conditions with respect to the agate case allows for better activation of the MC reaction, a higher degree of defectiveness is induced into the products. In some applications, as will be discussed in paragraph 3.1.2.2, this is functional for modifying the optical absorption properties of the material in the creation of semi-transparent thin-film absorbers. On the other hand, for the conventional stand-alone solar cell application, it is more important to reduce the degree of defectiveness to avoid deteriorating the optical and electrical properties of the material and achieve the best possible performances.

For these reasons, in the following chapter the MC reactions will be carried out exploiting (1) agate grinding media for low bandgap CIS and CISe (stand-alone applications), and (2) zirconia grinding media for high bandgap CIGS and CGSSe solid solutions (tandem cell applications).

As mentioned before, it is difficult to induce significant changes in the crystallinity of the product by tweaking with the MC parameters and this aspect is crucial in order to reduce and uniform the crystallites size so that a proper suspension can be (meta-)stabilized in suitable solvents for liquid-phase deposition processes. Therefore, an additional ball milling process was studied, at lower energies in both cases, taking advantage from kinetics rather than thermodynamics. The result of this experimental research is reported in the next paragraph.

3.1.2 High Energy Ball Milling Refinement

As described in subsection 2.3.1, it is feasible to perform liquid-assisted grinding (LAG) processes to reduce and homogenize the size of the crystalline grains of chalcogenides. The effects of this treatment (called refinement) were comprehensively studied starting on the powders obtained via MC reactions. In particular, two distinct applications of these materials were considered: stand-alone cells based on low-gap chalcogenides (CISe and CIS), which will require a film with (1) high absorption of the solar radiation, (2) compactness and high density, (3) thickness of at least1 µm (to prevent the depletion region from having the same dimensions as the film, leading to a layer fully depleted of carriers). Additionally, top cells for tandem devices based on high-gap chalcogenides (CIGS and CGSSe) were considered, which require a semi-transparent absorber layer to allow the radiation absorbed by the bottom cell to pass through.

This led to the exploration of two different regimes:

1. For stand-alone cell application, a low-energy regime of the milling refinement it was employed, i.e. using agate jars, with the main objective of uniforming the size of the powders retaining a larger crystallite size.
2. For tandem cell application, a high-energy regime in ZrO_2 jars was used, aiming not only to uniform the size of the powders but also to reduce their size at the submicrometric scale in order to modify the absorption and thus the energy gap of the material. This is crucial because this family of chalcogenides possesses a very high absorption coefficient ($> 10^4\ cm^{-1}$), which gives to the material usually black color and full absorption of at least the visible part of the solar spectrum. A key ingredient in the realization of a tandem device top cell is indeed the identification of a material which may let part of light pass through the absorber and get converted by the bottom cell, so it is important to obtain in this case semitransparency of the selected chalcogenide.

3.1.2.1 Low energy Refinement: Ink for stand-alone solar cells applications

The refinements presented in this section were sequentially performed on the CISe and CIS powders synthesized in SiO_2 jars under nitrogen atmosphere in Pulverisette 7 PL apparatus, with the optimized parameters reported in the paragraph 3.1.1 (High Energy Ball Milling Mechanosynthesis) for CISe and CIS synthesis in agate mechanicals media. Preliminary tests of refinements and ink stability were performed varying in particular two milling parameters: RPM (between 350-500) and time (between 6 and 24h), while BPR was set to 50, using 5 mm agate spheres and selecting as LAG medium 4 ml of 2-propanol as the process solvent due to its pretty intermediate boiling point and volatility (if compared to other standard solvents such as ethanol and acetone).

At the end of the refinement process, a suspension of powders in isopropanol with variable stability was obtained. For short time and low velocities, the powder particles precipitated within 1÷ 8 hours. While a longer refinement (approx. 1 day) and higher RPM (500) leads to a more enduring and homogeneous suspension with stability that surpasses 24 hours. Such suspension appeared black, dense, and uniform in color (Figure 38(a)). Given their resemblance to pigmented varnish, the CIS and CISe suspensions will be referred to as "Black chalcogenides varnish/ink" in this thesis. The varnish can be readily applied to a glass slide using a Pasteur pipette. In a few minutes, the solvent completely evaporates, leaving a pretty homogeneous, opaque layer on the glass slide (Figure 38(b)).

Figure 38: Picture of (a) Black Chalcogenide ink and (b) a glass slide on which the CISe ink was deposited with a brush.

The XRD analysis performed on the CISe MC powders refined in the indicated conditions shows broader peaks which means reduction in the crystalline grain size.

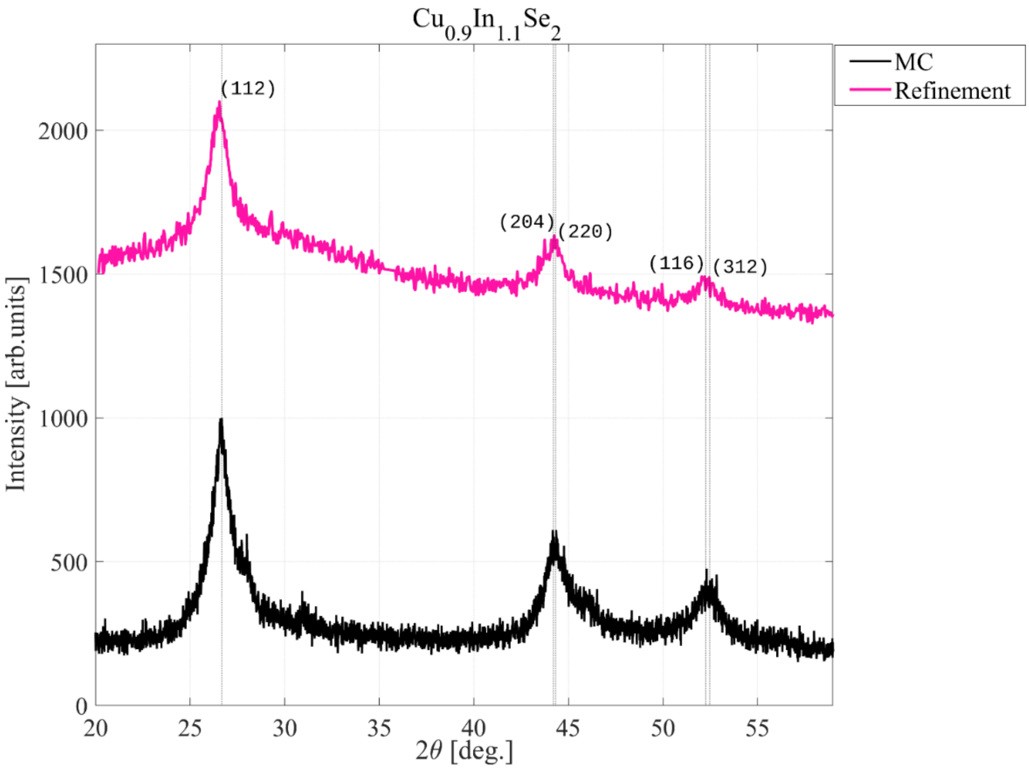

Figure 39: XRD pattern of CISe refined in agate jars at 500 RPM, 24 h, 50 RPM, 5 mm spheres, 4 ml 2-propanol (pink curve) and CISe MC powders (black curve).

Similar results were obtained in the case of CIS. Consistently with the findings from mechanochemical synthesis, sulfur-based products are able to achieve better morphological refinement with a clear reduction of the crystallites size very close to the amorphic state (Figure 40).

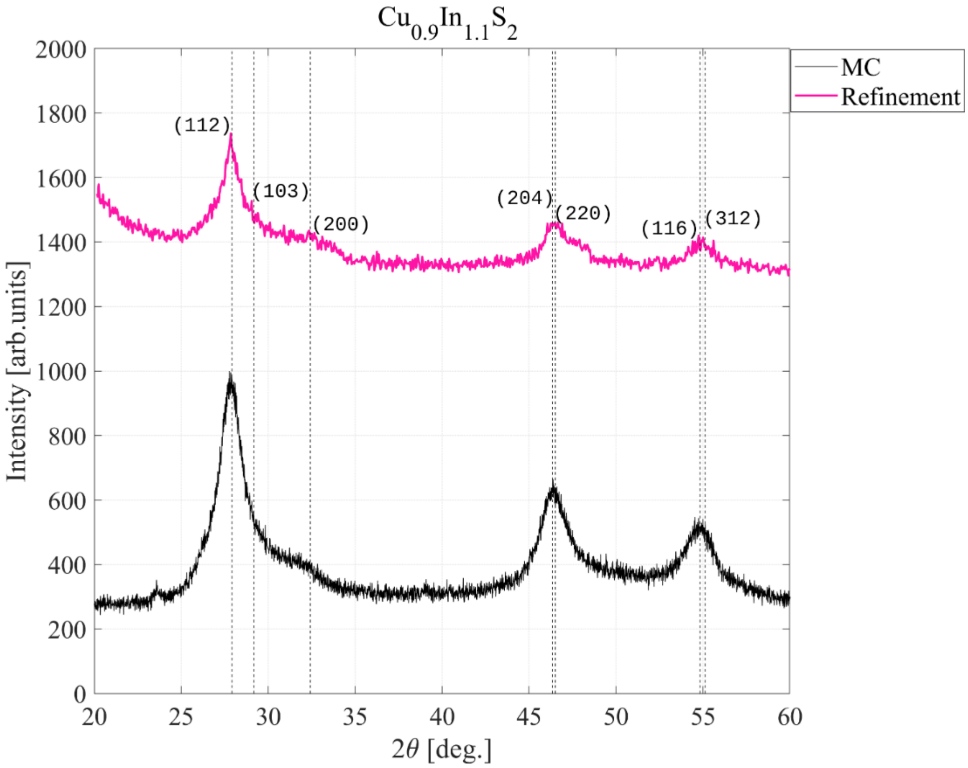

Figure 40: XRD pattern of CIS refined in agate jars at 500 RPM, 24 h, 50 RPM, 5 mm spheres, 4 ml 2-propanol (pink curve) and CIS MC powders (black curve).

The role of the solvent in the CISe refinement, applying the best milling parameters which were established by the previous study was investigated by exploring solvents with different polarity, viscosity, density, and volatility and comparing this with the reference in 2-propanol (IPA) specifically: ethanol (EtOH), methanol (MetOH), cyclohexanone (ChEX), and n-butanol (ButOH) (Table 5). After the refinement the obtained ink are deposited on a glass substrate through a Pasteur pipette and then let dry or in ambient condition or heated on a hot plate to evacuate the less volatile solvents (i.e. n-Butanol and Cyclohexanone).

The solvents that maximize stability (up to weeks when stored in the refrigerator) and allow for the best uniformity of the powders are cyclohexanone and n-butanol, which are the solvents with higher viscosity, density, and higher boiling points, respectively, 155.6°C for cyclohexanone and 117.7°C for n-butanol.

Table 5: Different refinement solvents explored in LAG ball milling conditions fixing 500 RPM, 50 BPR, 24 h as parameters for the treatment.

Refinement	RPM	BPR	Time	Solvent
Refinement IPA	500	50	24h	2-propanol
Refinement EtOH	500	50	24h	Ethanol
Refinement MetOH	500	50	24h	Methanol
Refinement ChEX	500	50	24h	Cyclohexanone
Refinement ButOH	500	50	24h	n-butanol

This is confirmed by the SEM analysis (Figure 41): the image is divided into seven parts, each showing the refined sample for each solvent. In particular, the 2-propanol-refined sample (a) exhibits the most variable grain sizes, with grains ranging from less than 100 nm to over 1 micron. The ethanol-refined sample (b) also shows considerable variability in grain size, and it is not possible to identify a significant difference compared to 2-propanol.

A substantial difference is observed in the case of the methanol-refined sample (c), where the grain size is much more uniform. In this case, just a very little number of grains are extremely large or extremely small compared to the average size and, in addition, a lower shape defectivity of the crystallites. A similar trend is observed for the cyclohexanone-refined sample (d), although the grains are generally smaller than those in the methanol-refined sample and more defective.

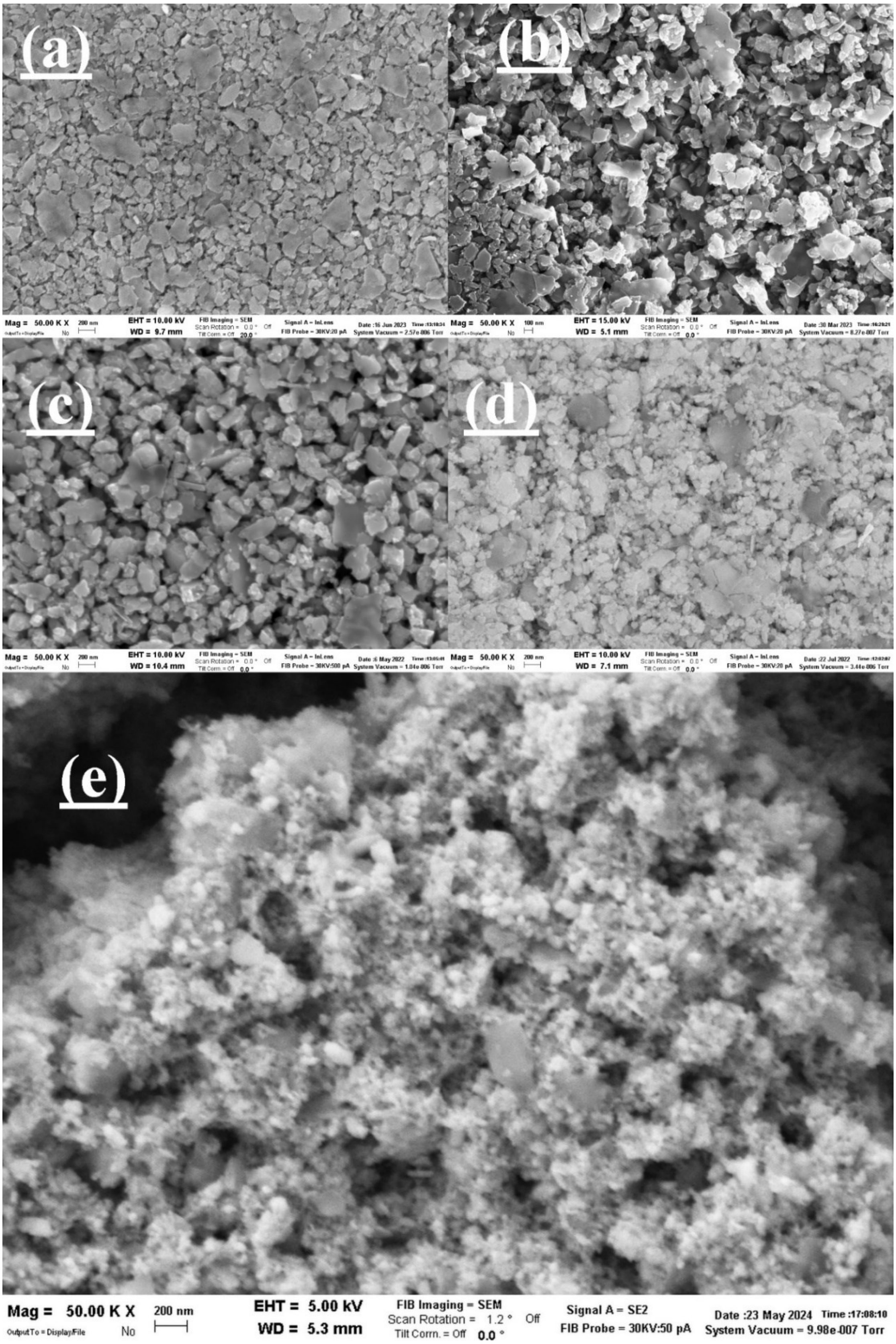

Figure 41: SEM analysis of refined samples at 500 RPM, 50 BPR, 24 hours with (a) 2-propanol, (b) ethanol, (c) methanol, (d) cyclohexanone, (e) n-butanol.

The most significant difference, in our opinion, is observed in the n-butanol-refined sample (e), where the grains are predominantly smaller than 100 nm. This uniformity and smaller grain size indicate that n-butanol is the most effective solvent for achieving a fine and homogeneous grain structure, so enhancing the stability of this suspension. A counter effect is the very high defectivity of the particles and the presence of abundant amorphous populations, represented by the dusty white part upon the larger grains.

However, the EDX analysis reveals the presence of carbon contamination in every sample; however, with a proper annealing treatment at 50°C for 15 min in nitrogen atmosphere, it is possible to partially remove the solvent (thus carbon) which remains trapped within the grains of the powder or weakly bonded to the smaller particles creating agglomerates, although the removal is more effective in films obtained from the most volatile solvents (i.e. 2-propanol, ethanol, methanol). In any case, the impact of residual carbon on the conductivity of the absorber material is not fully understood and still debated so that it requires further investigation to elucidate its role in improving[121] or deteriorating[122] the electrical properties of the devices.

In conclusion, the refinement process performed at low-energy regimes has shown that there is a reduction in the crystalline grain size compared to the powders, regardless of whether the powders were sulfur or selenium-based. However, the energy of the process is not sufficient to achieve a well-controlled nanodistribution of crystallites, meaning that a more energetic process needs to be studied.

The low-energy refinement process also highlights the importance of solvent selection in achieving stable and uniform suspensions. Solvent significantly influences the grain size and uniformity of the refined sample. Isopropanol and ethanol result in variable grain-sized film, while methanol and cyclohexanone produce more uniform grain distributions. The n-butanol-refined sample leads to the most uniform refinement and produces the smallest recorded mean grain size, even though determining the formation of the most defective powder.

This means that the choice of solvent not only affects the stability and uniformity of the suspension but also influences the final properties of the deposited layers. Solvents with higher viscosity and density, such as cyclohexanone and n-butanol, are more effective in maintaining the suspension's stability and preventing the re-aggregation of nanoparticles. This is crucial for applications where a homogeneous and uniform coating is required. However, in the next experimental section, dedicated to liquid phase deposition techniques, the exploration and optimization of various deposition methods required the use of varnishes suspended in solvents with different rheological properties and boiling points. This approach aimed to maximize the achievement of uniform, homogeneous, and continuous films with each technique. Additionally, since there is evidence of carbon contamination, as revealed by EDX analysis, the need for careful control of the annealing process is underscored. However, the annealing process will be examined in depth and discussed in the following chapters.

3.1.2.2 High energy Refinement: Semi-transparent Ink for tandem solar cell applications

The focus shifts from CIS and CISe to CIGS and CGSSe solid solutions, as a high band gap chalcogenide is required for tandem applications. However, our previous study showed that we could not achieve an effective narrow nano-distribution of crystallites in either selenium or sulphur-based compounds. This resulted in an almost completely absorbing black varnish across the solar spectrum of interest, making the previously explored process unsuitable for producing a semi-transparent chalcogenide-based varnish for top cell applications. Therefore, higher-energy milling processes were investigated as reported in subsection (High Energy Ball Milling Mechanosynthesis in controlled atmosphere).

To enhance the energy and the statistics of the impacts in these processes, it was decided to use ZrO_2 jars and 3 mm balls and to abruptly enhance the ball-to-powder ratio (BPR) to 140 but retaining with the amount and type of solvent i.e. 5 ml of 2-propanol. Different RPM of refinement were explored, whilst keeping time at 18 h as reported in Table 6.

Refinement	RPM	BPR	Time	Solvent
Refinement_IPA_HE_1	400	140	18h	2-propanol
Refinement_IPA_HE_2	500	140	18h	2-propanol
Refinement_IPA_HE_3	550	140	18h	2-propanol

Table 6: Refinement of CIGS and CGSSe performed in ZrO_2 jars with a controlled nitrogen atmosphere and the addition of 5 ml of 2-propanol, varying the RPM and Time parameters.

Looking at inks of Figure 43 and Figure 44, the striking difference among these refinement treatments is evident in the transition from 400 to 500 RPM for CIGS and at 550 for CGSSe. After Refinement IPA_HE_2 and 3, respectively, for CIGS and CGSSe, the suspension appears visually brown in color, defining what will henceforth be called brown-chalcogenides varnishes (Figure 42). The hypothesis is that the surface-to-volume ratio of the nanoparticles present in the suspension is so high that it results in completely different optical behavior compared to the previous case and how these chalcogenides usually appear.

When the mean grain dimension becomes so small as to be inferior compared to the wavelength of light, the optical properties of such structures differ from those of the bulk. This process is analytically described by Mie Theory, which explains how scattering and absorption phenomena depend directly on the radius of the particles in suspension.

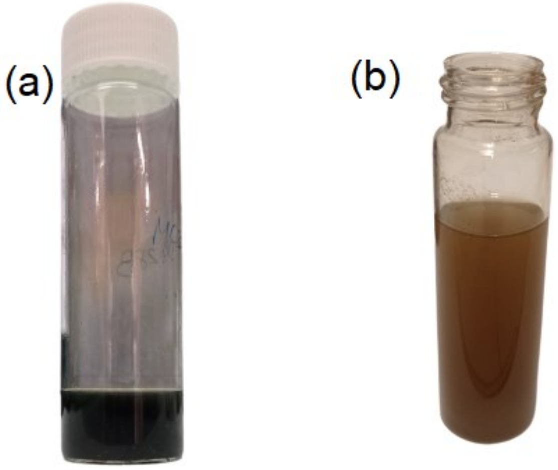

Figure 42: Photograph of black-chalcogenide ink (a) and brown-chalcogenide ink (b).

The transition from black to brown highlights the absorption of visible radiation in the blue region, qualitatively suggesting the optical band-gap value of the materials. The hypothesis that the color variation is due to dimensionality is further confirmed by the aging tests of the paint: after approximately 48 hours, the nanoparticles in suspension begin to re-aggregate due to the high surface energy, leading to a progressive color change from brown to black and an increase in the precipitation rate of the powder.

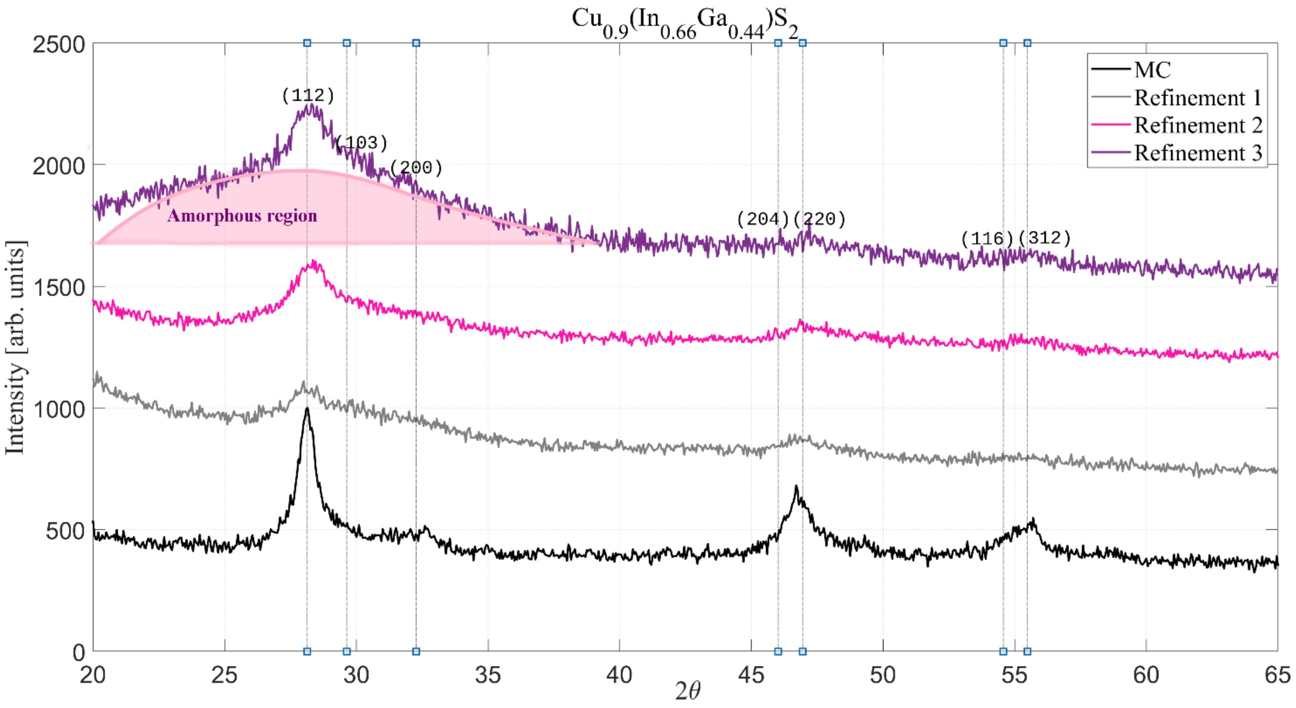

Figure 43: Refinement of CIGS with parameters described in Table 6.

Regarding the structural properties, in the case of CIGS, it is evident from the pattern reported in Figure 43 that the refinement process is very effective under such milling conditions and that the diffractogram deteriorates very rapidly from Refinement_IPA_HE_1, resulting in a brutal reduction in reflection intensities and a consequent increase in FWHM, which can actually be observed only for the main reflection (112). It is also noted that as the RPM parameter increases, the pattern assumes an almost amorphous profile (Figure 43, purple pattern).

The reduction in the crystallinity of CGSSe was far more complex (Figure 44): the refinement process begins to be significant only at 550 RPM, but its effectiveness is still lower than that experienced for CIGS under the same conditions.

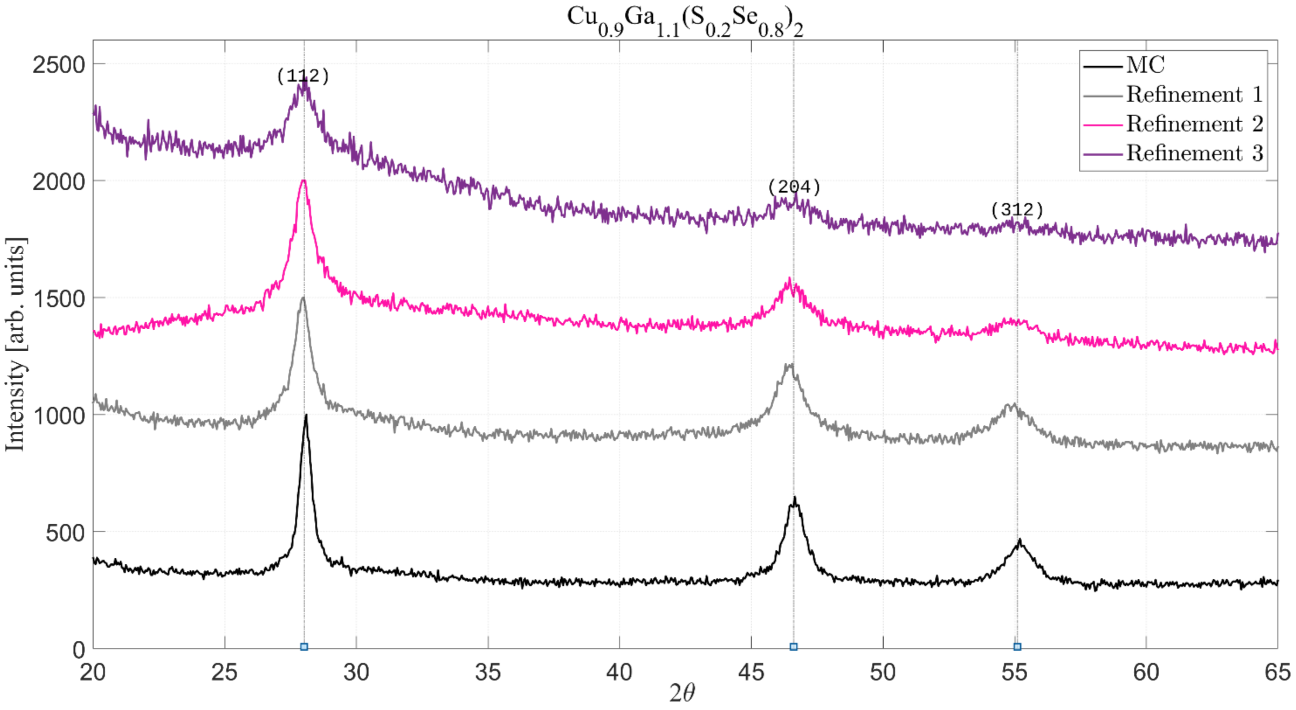

Figure 44: Refinement of CGSSe with parameters described in Table 6.

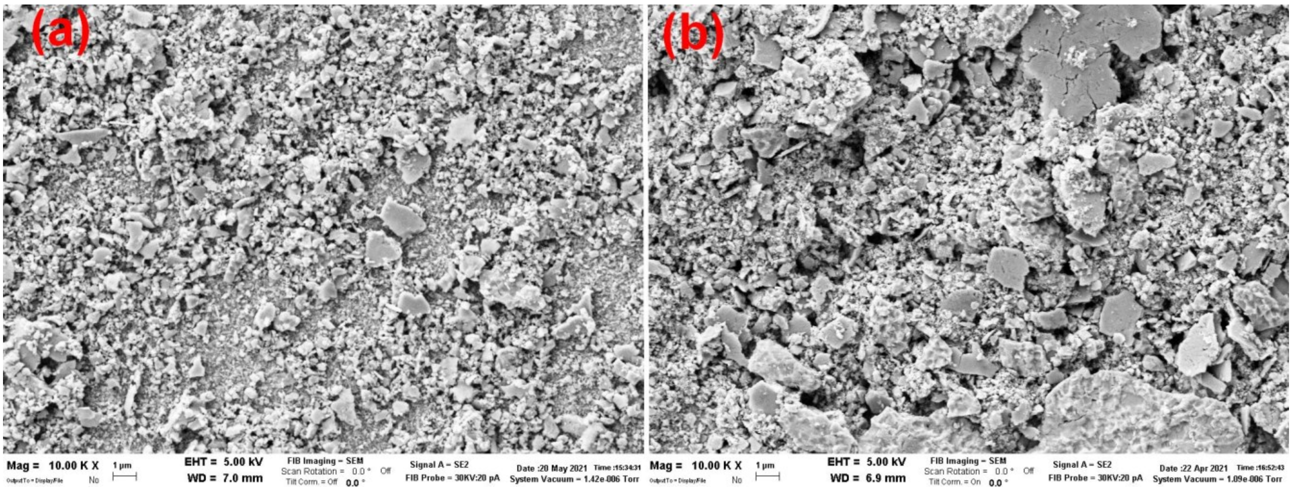

Figure 45: SEM image at 10.00 kX of CIGS paint (a) and CGSSe paint (b).

This difference in quality between the refined CIGS and CGSSe products dried directly from the solution is evident from the SEM analysis , shown in Figure 45(a) and Figure 45(b) respectively: the powders' morphological characteristics for CIGS, obtained after Refinement_IPA_HE_2 (500 RPM, 140 BPR, 18h), and for CGSSe, obtained after Refinement_IPA_HE_3 (550 RPM, 60 BPR, 18h), are highlighted. For CIGS, no agglomerates larger than 1 µm are observed, differently from what emerges from the SEM image of CGSSe, where a significant number of supermicrometric clusters are present, the overall sample is affected by considerable morphological inhomogeneity. Due to this important qualitative difference between the CIGS and CGSSe powders, a substantial macroscopic effect results: the brown-CIGS powder suspended in 2-propanol is stable over time (with a stability time greater than 96 hours), while the brown-CGSSe suspension precipitates almost completely after the first few hours of rest. It is therefore evident that in the case of CIGS, our study has led to the definition of an effective process, while for CGSSe, the high energy refinement needs to be studied independently, extending the range of MC process parameters in the experimental phase. This has implied that the study of the two materials could no longer be conducted in parallel, given the need to substantially differentiate the two treatments. For now, it was decided to discontinue the study on CGSSe at this level (deferring it for future activities) and to dedicate the study and development of the subsequent steps solely for CIGS.

An additional adjustment to the process parameters of CIGS allowed the identification of a median value between 500 and 550 RPM as the best milling energy to obtain a stable, sufficiently homogeneous, and usable liquid suspension, or paint, for the subsequent processes.

For these reasons, the brown-chalcogenide varnish processes were conducted as a standard in ZrO_2 milling media at 520 RPM, 140 BPR for 18h with 5 ml of solvent. However, as explored in the next section, different solvents will be evaluated to best match different liquid-phase deposition techniques.

3.1.3 Liquid Phase Deposition of the absorber layer: study of morphological, electric and opto-electronic properties

In this chapter, I present the results obtained using three different liquid-phase deposition techniques for CIGSSe thin film absorber layer: drop-casting, spin coating, and doctor blading. In this section, by comparing their performance applied to this type of ink, the most suitable technique for the various PV applications discussed within this thesis was identified. This analysis will provide insights into the strengths and limitations of each method, guiding the selection of the optimal deposition technique for every specific requirement.

All processes described in this section were conducted with limited exposure of the material to the ambient atmosphere, where oxygen is present.

3.1.3.1 Drop-Casting

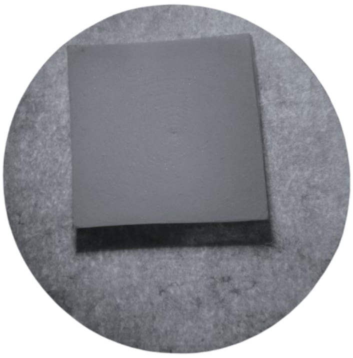

Figure 46: Optical microscope image of the black-chalcogenide dried film, deposited with drop-casting method on a fluorine-doped tin oxide (FTO) substrate of size 1 cm^2, with the varnish stabilized in a solvent with a low boiling point (2-propanol).

The deposition of chalcogenide-based varnishes was initially performed using the drop-casting technique to study the adhesion and morphological properties on various conductive substrates, predominantly fluorine-doped tin oxide (FTO) (see Figure 46) and molybdenum. An organic solvent with a low boiling point (<100 °C), specifically 2-propanol, was chosen as solvent for the varnish. Through drop-casting route, the 2-propanol varnish can be successfully deposited pretty uniform layer to every type of substrate investigated but with several issues. Firstly, adhesion is not optimal, as the film can be completely removed with a Scotch test by placing and then removing a piece of Kapton tape on it. This is due to the lack of chemical interaction between the varnish stabilized in isopropanol and the chosen substrates. To create a chemical interaction, an alternative solvent such as dimethyl sulfoxide (DMSO) or dimethylformamide (DMF) would be required, but these are toxic and have unsuitable boiling points. Moreover, this deposition technique does not allow for optimal control of the amount of material deposited. As a result, obtaining layers with contained and reproducible thicknesses (approximately 1 µm), beside that the deposited layer by drop-casting exhibits good homogeneity and uniformity (Figure 46).

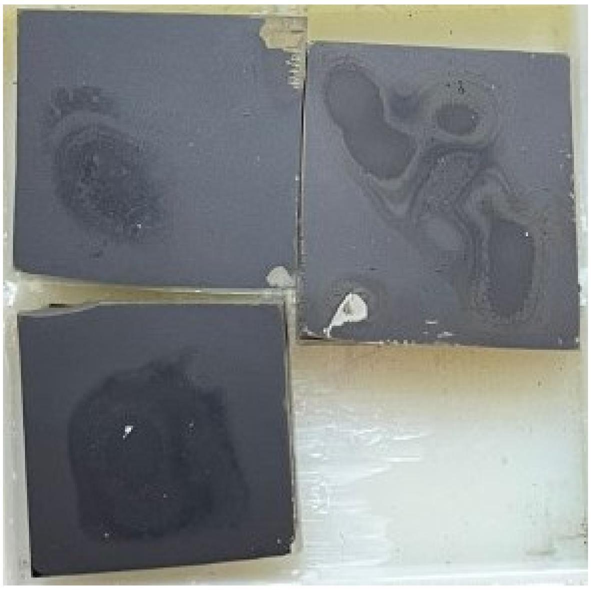

Figure 47: Picture of the black-chalcogenide dried films, deposited with drop-casting method on FTO substrates of size 1 cm^2, with the varnish stabilized in solvent with high boiling point (cyclohexanone).

Otherwise, the use of solvents with a high boiling point (> 100°C) would require the addition of a thermal process carried out on a hot plate for accelerating evaporation . It was found empirically that to achieve a film that fully covers the substrate, a quantity of varnish equal to or greater than 500 µL is required. This causes the varnish to form a convexity on the substrate due to the surface tension of the liquid. Using a hot plate at a temperature below the boiling point of the solvent to gradually evaporate such a large quantity of solvent accelerates the re-aggregation processes inside the convex drop on the surface, leading to the formation of an extremely inhomogeneous film (Figure 47).

However, drop-casting allows for the easy formation of extremely thick bulk films, exploitable in routine characterization of the as-grown structural properties of the particles suspended in the varnishes. It is not possible to perform an optical characterization on these thick films, as they are opaque and absorb the entire spectrum cannot measure any signal, neither in diffuse reflection nor in transmittance configuration.

3.1.3.2 Spin Coating

Spin coating of a suspension of nanoparticles has special requirements compared to the standard spin coating of solutions. Probably the most important aspect to consider is the spin coating method used to dispense the solution—either a static or a dynamic dispense. In a static dispense, the solution is placed upon the substrate while it is stationary, and usually, the entire substrate is covered in the solution before rotation begins. The spin coater is then started and brought up to the required speed as fast as possible. In a dynamic dispense, the substrate is first started spinning to the desired angular speed before the solution is dispensed onto the center of the substrate. The centrifugal force rapidly pulls the solution from the middle of the substrate across the entire area before it dries.

Dynamic dispense spin coating was chosen over static dispense spin coating. In fact, dynamic dispense allows for better control of the deposition and it is generally less dependent on modifications of the utilized substrates, less sensitive to both ramp speed and dispensing time.

This method ensures the solvent does not evaporate until the ink has uniformly and homogeneously covered the substrate. Moreover, varnish consumption is generally lower, although surface wetting properties can influence this.

A schematic representation of the film drying mechanisms during the dynamic spin coating process of a suspension is reported in Figure 48. During this process, through the action of centrifugal force, most of the suspension is initially flung off the substrate, leaving behind a film which gets thin out driven by radial outflow and solvent evaporation. The sub-micrometric particles in suspension are dispensed across the substrate, and as the solvent begins to evaporate, this produces internal fluid-dynamic currents. As the suspension becomes more concentrated, its viscosity rises and then eventually becomes so large that radial outflow effectively ceases (1). The droplet shrinks in size with the internal currents depositing the particles at the receding edges (2). The film continues to thin (3), however, until the solvent has evaporated thoroughly, and a “dried” film of the material is left. By controlling the evaporation rate, it is possible to produce highly uniform films at the edges. However, the coating across the surface can result in unevenness, with the layer thinner in the middle, known as the "coffee staining" effect (4).

Control of this process is critical. From the practical point of view, this means that when these sub-micrometric particles are spin-coated, the uniformity and film thickness do not just depend on the rheology of the solution, but also, and very strongly, on the boiling point of the solvent, the starting density of the varnish, and the particles’ average dimension in suspension.[123]

In this process, as shown in Figure 49, solvents with a boiling point too low (<100°C) like isopropanol and ethanol can evaporate too quickly, preventing the substrate to be uniformly covered so that traces of the evaporation dynamics are observed, typically concentric spirals around where the drop is released, as this evaporates incompletely before the substrate has completed a full rotation.

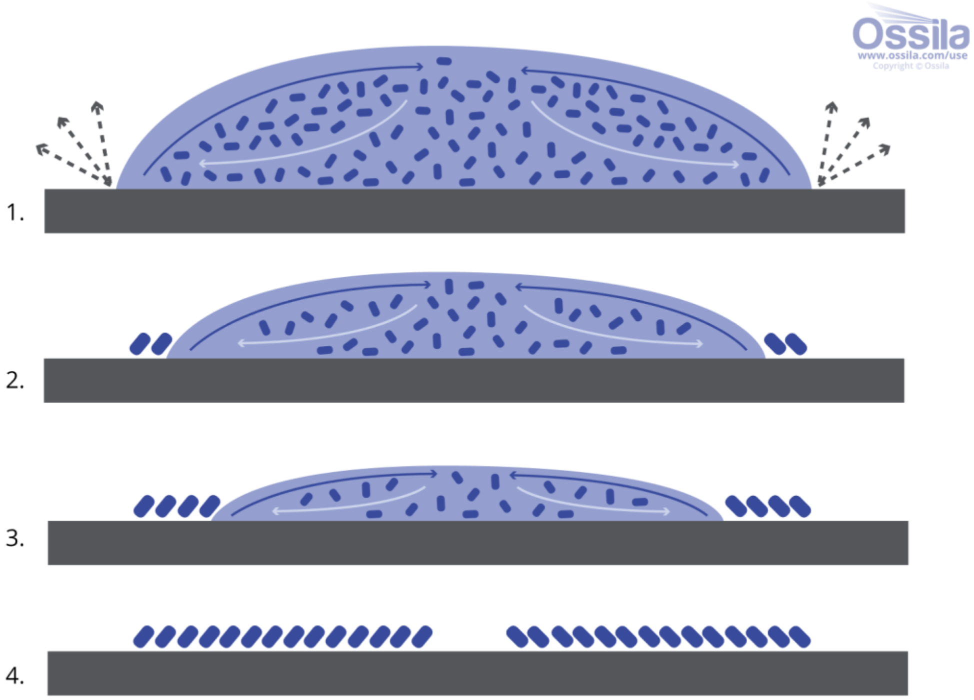

Figure 48: Schematic representation of the film drying mechanism in a spin coating deposition of a nanoparticle's suspension.[124,125]

Figure 49: Picture of the CIGS dried films, deposited with spin coating method on FTO substrates of size 1 cm^2, with the varnish stabilized in 2-propanol.

On the other hand, with high boiling point solvents (>100°C), likely cyclohexanone, even at low speeds (<1000 RPM), the centrifugal force acts more effectively on the particles in suspension, extruding a good quantity from the substrate before the solvent has evaporated, leaving only a thin layer of varnish (Figure 50). To achieve the desired film thickness, it is necessary to apply multiple consecutive layers, waiting for the previous layer to completely dry to avoid material removal from the surface. The use of these solvents at high rotation speeds (>3000 RPM) is detrimental, as all the varnish is immediately flung off the substrate, with no growth of the film.

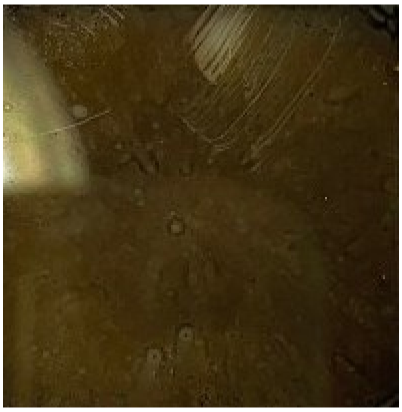

Figure 50: Brown-CIGS film deposited via Spin Coating.

Spin Coating of the black low-bandgap chalcogenides' varnishes

Given these considerations, deposition experiments on FTO/glass and Mo/glass substrates were conducted with the black chalcogenide-based varnishes of CISe and CIS stabilized in cyclohexanone, obtained as described in the section 3.1.2.1.

SEM analysis demonstrates that, regardless of the chosen rotation speed (between 1000 and 3000 RPM), it is not possible to obtain homogeneous, uniform, and continuous films. Additionally, the porosity and rugosity obtained in this case are extremely high, making these films unsuitable for photovoltaic applications. This is due to the size of the grains, which are too large and inhomogeneous (Figure 51).

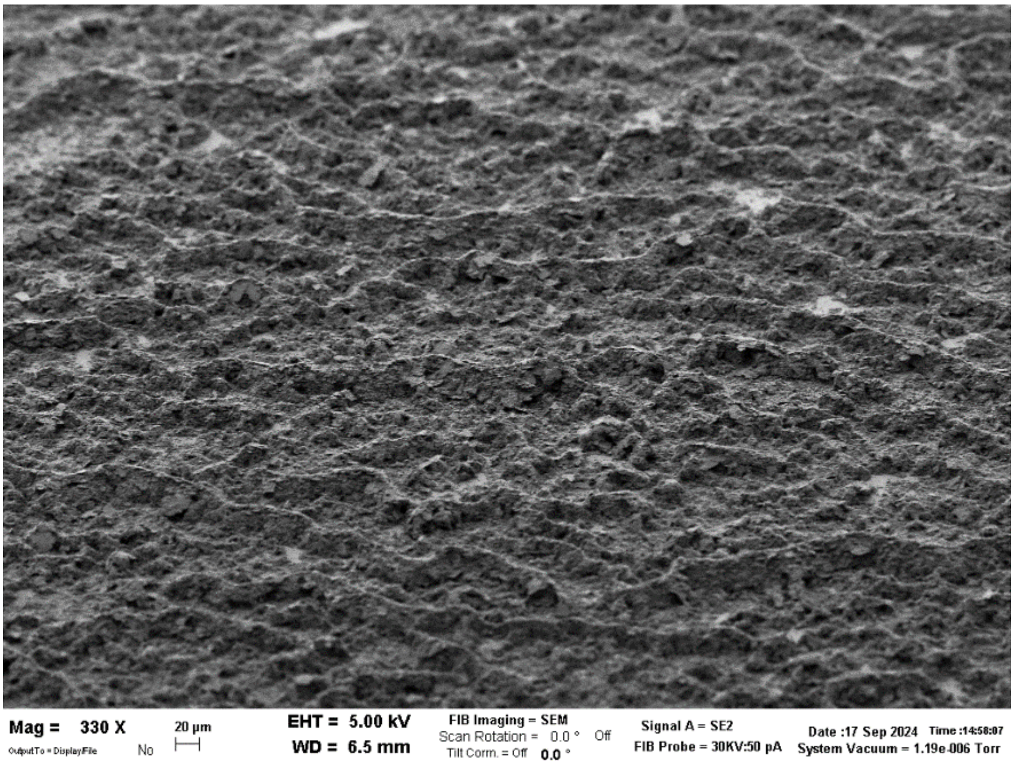

Figure 51: SEM image at 330x of black-CISe dried films, deposited with spin coating method on FTO substrates of size 1 cm^2, with the varnish stabilized cyclohexanone.

Spin coating of brown high-bandgap chalcogenides' varnishes

On the other hand, the same deposition experiments were replicated with the brown-CIGS varnish obtained in cyclohexanone. Due to the reduced particle size, it is possible to obtain a film with much lower porosity compared to the previous case, ensuring greater surface homogeneity (Figure 52). Adhesion tests were performed on glass and glass/FTO substrates: while it is more difficult to obtain a layer adhered to the glass, having extremely reduced roughness, the adhesion of the film to the FTO substrate is optimal, thanks to the sub-micrometric dimensions of the crystallites, which is comparable to the roughness of the substrate.

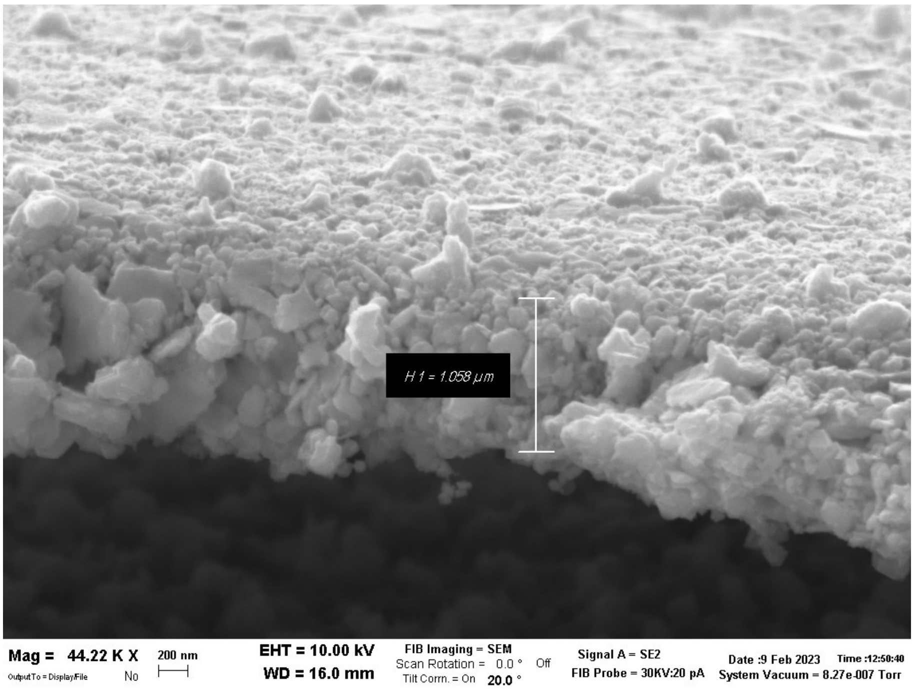

Figure 52: SEM image in cross-section at 44 kX of brown-CISe dried films, deposited with spin coating method on FTO substrates of size 1 cm^2, with the varnish stabilized cyclohexanone. The film is detached from the substrate.

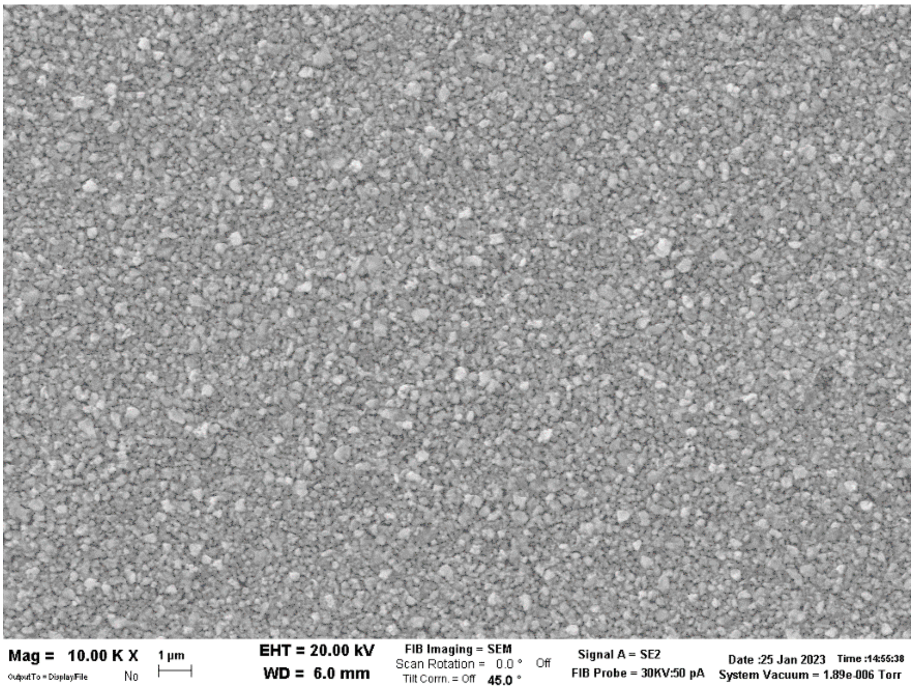

Figure 53: SEM image at 10 kX of CIGS dried films, deposited with spin coating method on FTO substrates of size 1 cm^2, with the varnish stabilized in cyclohexanone, centrifuged at 1800 RPM for 10 minutes before the deposition.

However, the ink required the addition of an extra processing step, namely the addition of a centrifugation step at 1800 RPM for 10 minutes of the varnish itself. This process allowed the separation of smaller particles, useful for deposition, from larger ones that precipitate. The liquid part is then extracted with a pipette and separated from the solid part.

The deposition parameters via spin coating are then optimized for this varnish that has undergone the centrifugation step: in fact, as demonstrated by the SEM analysis reported in Figure 53, to be confronted with Figure 45(a), the dimensional selection of the particles is maximized, resulting in more homogeneous and reduced-size particles. This allows to obtain film with less macroscopic (Figure 54, to be confronted with Figure 50) and microscopic morphological defects.

Figure 54: CIGS film deposited via Spin Coating with the centrifuged varnish. The letter “A” is written on a paper at the bottom of the sample, indicating the transparency of the film

In particular, it is demonstrated that using dynamic spin coating for the deposition of the brown CIGS varnish on a (1’x1’) FTO substrate, with a rotation speed of 2500 RPM, depositing 50 µL per layer for a total of 30 layers, results in a film thickness of a (0.99 ± 0.09) µm, as shown in Figure 55.

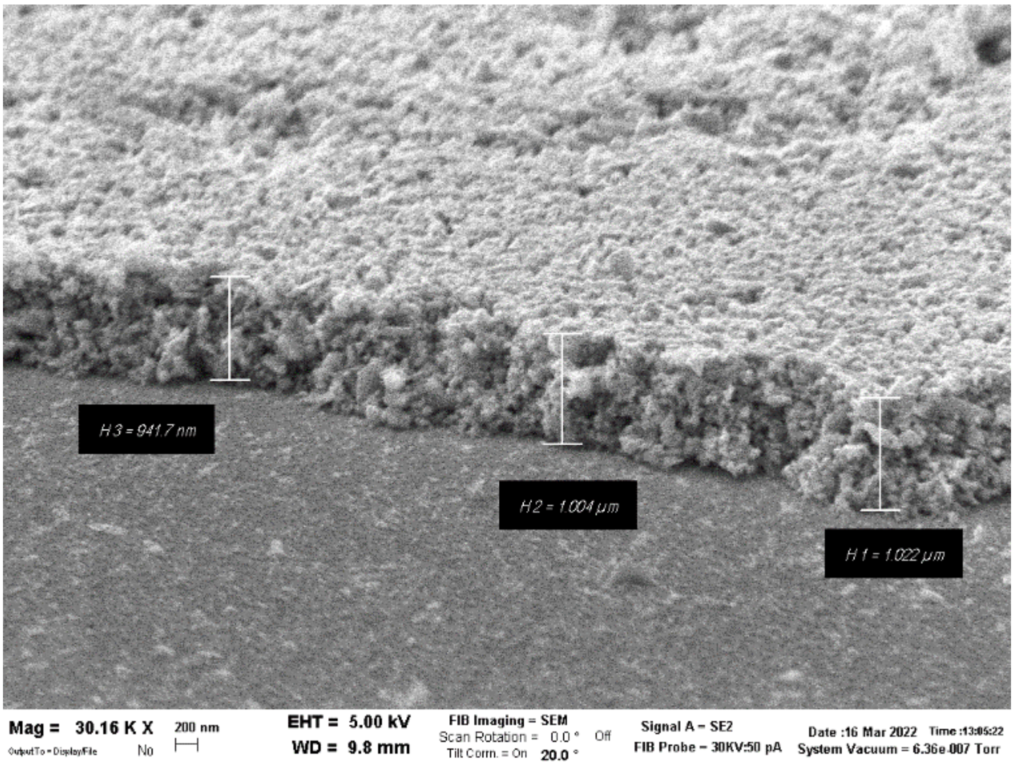

Figure 55: SEM cross-section image at 30.16 kX of brown-CIGS in cyclohexanone varnish dried on a (1'x1') FTO substrate, deposited with a rotation speed of 2500 RPM, 50 µL per layer for a total of 30 layers.

However, the porosity remains far from ideal, with poor grain contact which results in the lack of physical continuity and in perspective this hinders the electrical performance of the absorber. Therefore, a cold pressing treatment was studied on the films, using a manual hydraulic bench press, aiming to reduce the layer's porosity through the action of a single mechanical force.

Figure 56: Experimental setup used for the cold pressing treatments on the samples. On the left, the cylindrical dye inside the manual hydraulic press. On the right, the disassembled cylindrical dye.

Figure 56 shows the optimized experimental setup for this treatment: the sample is located in the center of cylindrical die. The die is then placed under the manual hydraulic press. Noteworthy, a silicon wafer of the same size as the substrate, completely flat and with roughness much smaller than the size of the CIGS grains, is placed in contact with the film. This prevents the detachment of the CIGS layer on the rougher steel surface of the die mechanical medium and prevents contamination with impurities. The system applies a vertical force perpendicular to the film, mechanically compacting the grains together and against the substrate. The maximum force that can be applied with this system is 60 bar of oil pressure, in order to avoid the glass substrate cracking. Beyond 15 minutes of pressing, it is not possible to further reduce the porosity, which reaches a sort of plateau. It is worth noting that mechanical adhesion to the substrate is further improved, making the film resistant to the Scotch test.

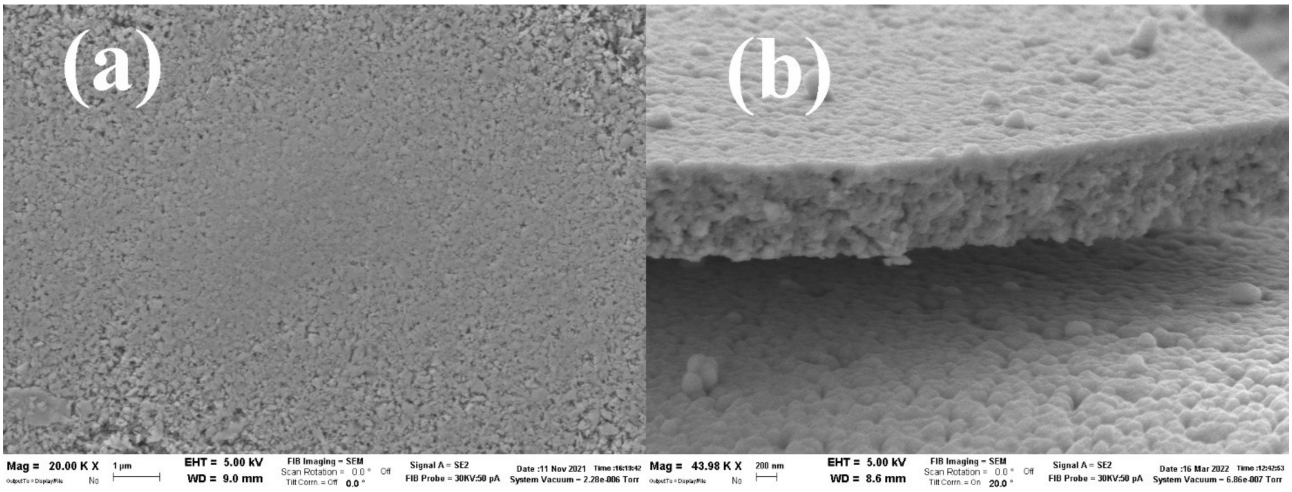

Figure 57: SEM image at 10Kx of CIGS dried films, deposited with spin coating method on FTO substrates of size 1 cm^2, with the varnish stabilized in cyclohexanone, centrifuged at 1800 RPM for 10 minutes before the deposition. The sample underwent to a cold pressing treatment after the deposition.

SEM analysis in plan and cross-section of the samples, shown in Figure 57(a) and (b) respectively, demonstrates that applying this treatment at 60 bar for 15 minutes effectively reduces the film's porosity, approximately halving the thickness of the as-grown film. Surface roughness is also reduced, resulting in a flat, compact, uniform, and homogeneous film.

To achieve a film with this desired compactness and a thickness (i.e. about 1 µm) after the cold pressing treatment, it was decided to deposit 50 drops of 50 µL for each spin coating process.

Electrical properties analysis

The effectiveness of the treatment on morphology and consequently on the electrical properties is confirmed by vertical conductivity measurements of the films that were performed using the setup shown in Figure 58.

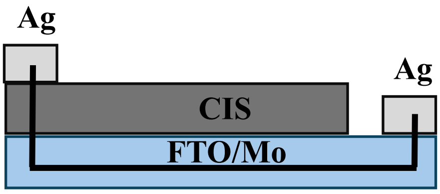

Figure 58: Experimental setup used for vertical conductivity electrical measurements

Assuming that the preferred path of the current is vertical through the film, supposing a higher resistivity of the film with respect to the substrate, the resistance attributable to the material is calculated using the following formula:

$$R_{measured} = R_{CIS} + R_{sub}$$

Equation 29

where $R_{measured}$ is the resistance measured by the multimeter, R_{CIS} is the vertical resistance of the CIS film, and R_{sub} is the resistance measured on an analogous FTO or Mo substrate. From this, we derive:

$$R_{CIS} = R_{measured} - R_{sub}$$

Equation 30

The vertical resistivity is then calculated with the formula:

$$\rho = \frac{S}{l}R$$

Equation 31

Where S is the area of the Ag contact (constant, 0.8 ± 0.2 cm^2), l is the thickness of the film and R the measured vertical resistance.

However, with the current configuration, it is not possible to exclude the contribution of the geometry and the Ag contacts. Therefore, these measurements give only qualitative indication of the electric characteristics of the material, deferring the precise measurement of the material's resistivity with 4-point Van Der Pauw measurements on an insulating substrate. However, the scope of the electrical measurement presented in this section is just to retrieve if there is a qualitative improvement or effects of the films' conductivity after the different post-deposition treatment performed.

The vertical resistivity is compared for two samples deposited with the same spin coating conditions but applying or not the cold pressing treatment. Notably, the vertical resistivity of the as-grown film is $(55.78 \pm 10.62) M\Omega \cdot cm$, while that of the pressed case is $(2.69 \pm 0.51) M\Omega \cdot cm$, being reduced by a factor of 20.

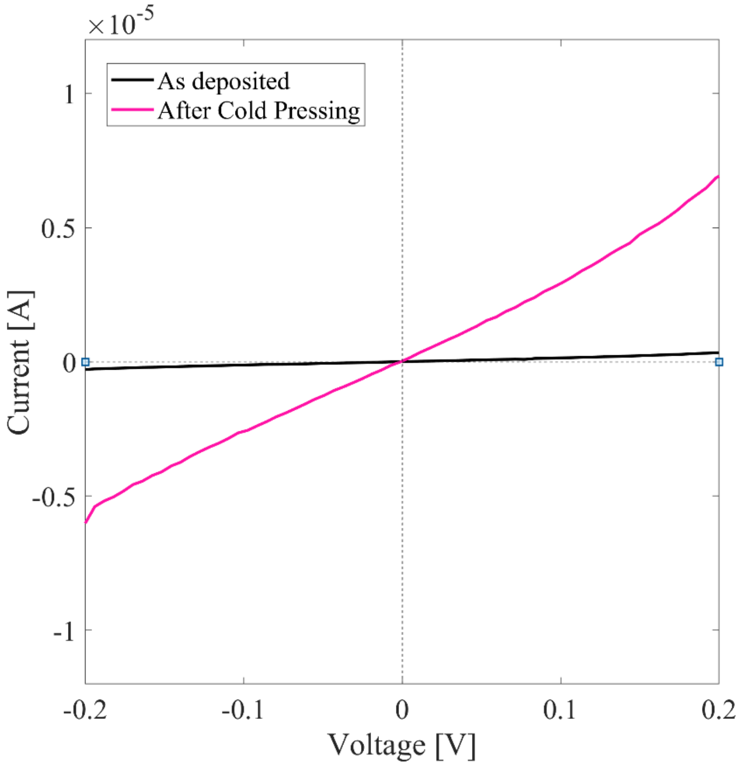

Figure 59: Comparison between the vertical resistance of a cold pressed and a non - cold pressed film.

Optical properties analysis

The optical properties of these films were measured in transmittance using UV-VIS spectrophotometry. The measurement was performed scanning the incident wavelengths of the light between 1300 and 300 nm, a range sufficiently wide to evaluate the absorption in the same region as for Si, which will ideally be the bottom cell of the 4T system. The baseline used was the signal of the FTO substrate, which starts to absorb weakly around 400 nm (Figure 60).

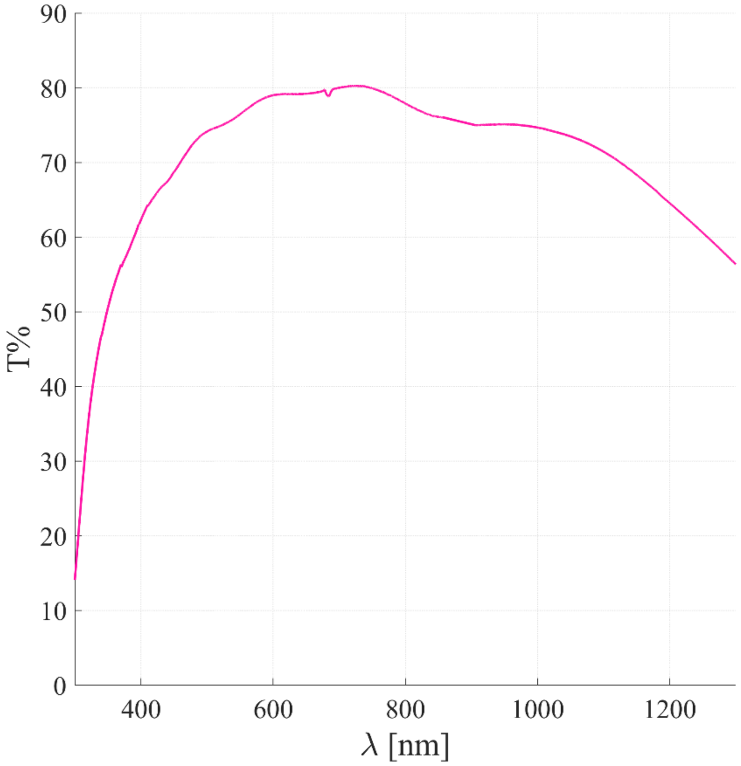

Figure 60: FTO substrate transmittance measured by UV-VIS spectrophotometry.

As reported in Figure 61(a), the transmitted signal is high (up to 73%), and the optical quality of this absorber is immediately evident in its operating region: the incident light is almost completely absorbed for radiation with wavelength lower than 600 nm. Despite the material thickness (about 1 µm), the film is indeed semi-transparent for λ > 800 nm (with transparency between 50 and 70%), in a wide portion of the absorption region of silicon. Remarkably, even though the high absorption coefficient of the bulk material would suggest that for thickness of about 1 µm complete absorption of the probe signal of the spectrophotometer should be expected the film obtained by brown CIGS varnish resulted semi-transparent in the desired region. This behavior relies on the sub-micrometric size of particles which are mechanically compacted but not recrystallized. The low dimensionality modifies the optical properties compared to the bulk case, making it intrinsically semitransparent.

Calculating the bandgap from the UV-VIS measurements as presented in section 2.3.3.3 (Figure 61(b)), reveals another characteristic typical of microstructures, namely the increase in the bandgap compared to the bulk case. In fact, there is a blue/UV shift of the optical absorption edge leading to an increase of the direct optical band-gap value from the theoretical one of 1.8 eV to 2.7 eV.

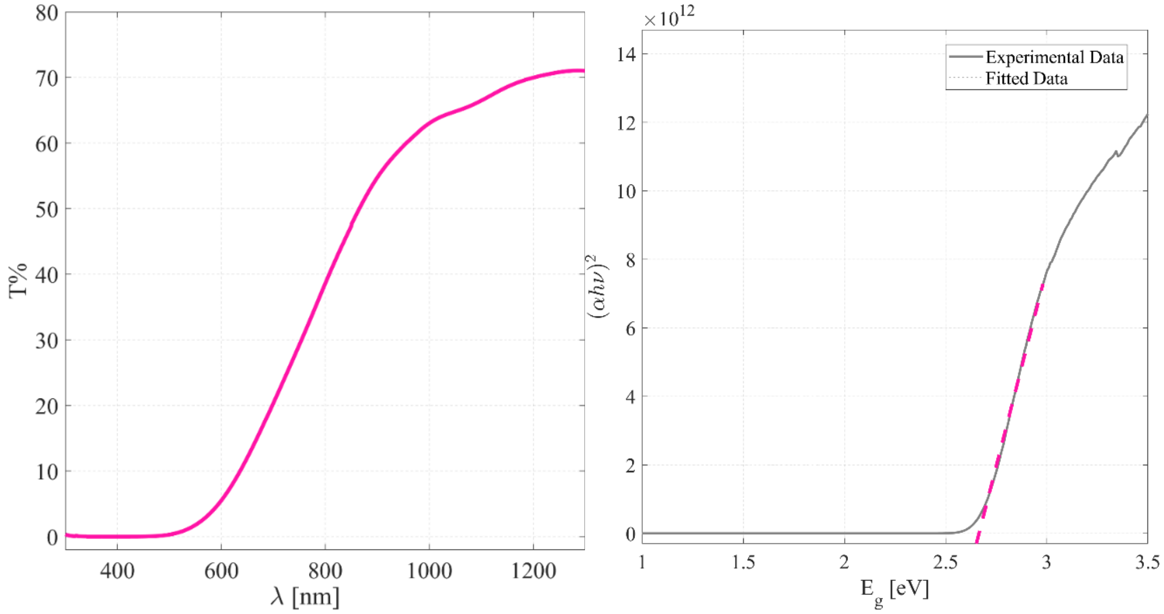

Figure 61: (a) Optical transmittance of the CIGS film with a thickness of 1μm. (b) Bandgap calculation with Kumar Model.

This phenomenon is typically observed in nanostructures due to the quantum confinement effect which usually is observed for systems of critical size lower than 20 nm; however, since the grains here have a larger mean size (about 100 nm), the quantum confinement is less likely to be the primary cause of the observed increase in bandgaps. One possible explanation of this phenomenon is surface effects. The surface of nanoparticles can have a high density of defects or dangling bonds, which can introduce additional energy levels within the bandgap. These surface states can affect the overall electronic structure and increase the effective bandgap.[126] Another factor that can be considered is strain effects: CIGS particles obtained and processed via high-energy ball milling experience lattice strain, as demonstrated from the broad peaks of XRD analysis presented in the previous chapter, due to surface tension or other mechanical stresses, which can alter the electronic structure of the material and lead to changes in the bandgap. Moreover, even if the mean size of the grains present in this film is higher than 10-20 nm, a broad size distribution can include smaller particles that do experience quantum confinement effects, and the overall measured bandgap may be influenced by the presence of these smaller particles.

To summarize, dynamic dispense spin coating was chosen to deposit brown-CIGS varnishes thanks to its superior control and reproducibility on different substrates, ensuring uniform coverage and minimizing solvent evaporation related issues.

Experiments with black-CISe and CIS varnishes stabilized in cyclohexanone showed that achieving homogeneous, uniform, and continuous films was challenging due to large grain sizes and high porosity. In contrast, the brown-CIGS varnish yielded films with lower porosity and greater surface homogeneity. Spin coating was chosen as the preferred method for depositing the CIGS absorber in a 4-T tandem device.

3.1.3.3 Doctor Blading of the black low-bandgap chalcogenides varnishes

Since spin coating has proven unsuitable for the deposition of black-chalcogenides varnishes, I decided to test the doctor blade technique, as it is reported to be a highly efficient technique for creating uniform thin films from colloidal suspensions. One of the key advantages of doctor blade deposition is the minimization of material loss, a significant drawback of spin coating. This is particularly desirable for materials containing expensive elements, like indium and gallium.

One of the main critical factors for a doctor blade process is again the rheology of the varnish, which should mimic a highly dense paste with a viscosity between 1000–10,000 mPa·s.[127] This viscosity range allows the paste to be sufficiently dense to maintain good homogeneity and packing density, but fluid enough to be distributed uniformly by the doctor blade. However, among the studied solvents, the one with the highest viscosity is n-butanol, with a viscosity of 2.573 mPa·s. Even though the viscosity is significantly lower, it proved effective in depositing these varnishes. In fact, a suspension with a low solvent viscosity can still have a higher overall viscosity if it contains a high concentration of solid particles. The solid particles can increase the apparent viscosity of the suspension, making it more suitable for doctor blade deposition. The density of the CISe/CIS varnishes obtained as described in Chapter 3.1.2 ($(125 \pm 25)\frac{mg}{mL}$, calculated by the ratio of powder mass vs. solvent volume in the jars) is indeed very high, making this suitable for deposition via doctor blade.

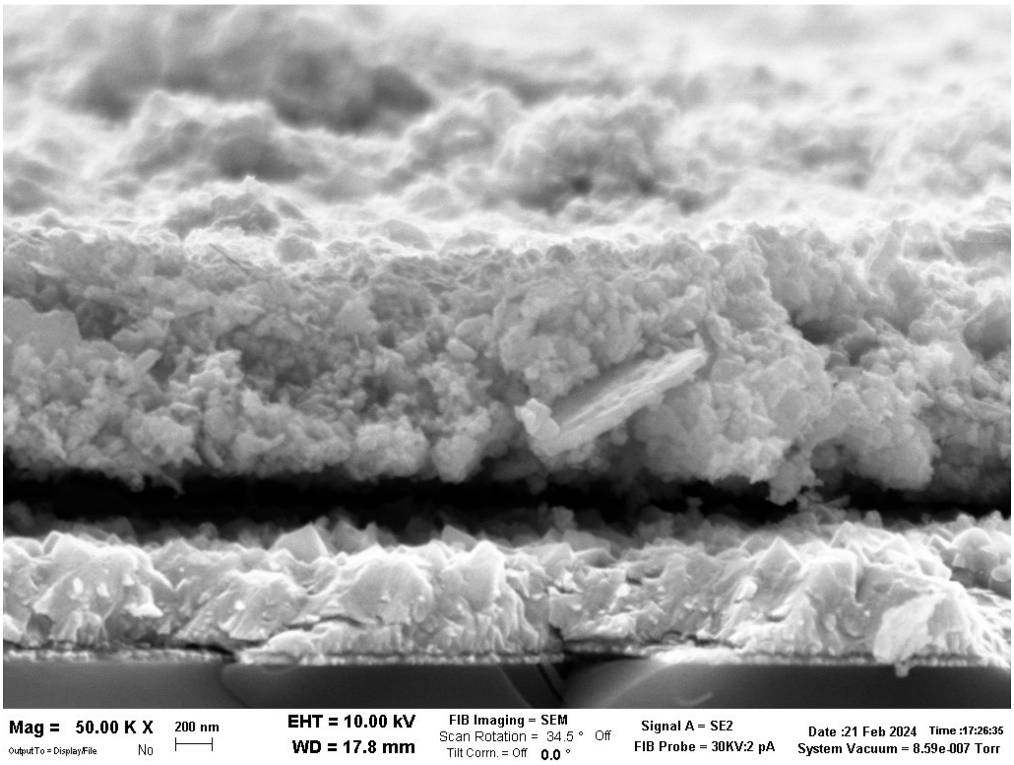

Figure 62: SEM cross section image at 50 kX of a CISe dried films, deposited with doctor blade method on FTO substrates of size 6.25 cm^2, with the varnish stabilized in n-butanol.

Thin films obtained with the doctor blade reach higher packing densities[128] compared to the spin coating technique, as shown in Figure 62 compared to Figure 55.

The denser packing can be attributed to both the compressing action of blade upon the paste during the deposition and the controlled evaporation of the solvent, which is achieved by drying the samples at temperatures lower than the boiling point of the solvent on hot plates ($< 80°C$). This slow evaporation provides particles sufficient time to reaggregate; it results in a more uniform and compact film. This drying mechanism offers a pathway to deposit also flatter layers compared to those obtained via spin coating, with less average peak-to-valley thickness variations.

However, the overall porosity and so the packing efficiency of the film is not negligible yet determining some issues in the transport properties of the material. This is reflected in the measured vertical resistivity of the film, which is $(30.81 \pm 0.53)\ M\Omega \cdot cm$, far from an optimal value for an absorber film in a photovoltaic architecture. Still, a reduction by a factor 2 from the as grown film deposited via spin coating is detected.

It is proven that tailoring rheology by adding additives (thickening agents, binders, or surfactants) significantly influences the final film density and homogeneity. [129]

Through a preliminary qualitative study conducted on various surfactants and binders (mainly propylene glycol, polymethyl meta-acrylate (PMMA), citric acid and monoethanolamine) added to the varnishes in n-butanol during the refinement step, described in section 3.1.2.1, it was noted that only with monoethanolamine (MEA) there is a significant difference in both the macroscopic and microscopic morphological appearance compared to the varnish without additives.

MEA has a higher viscosity than n-butanol, at 23.86 mPa·s, and is soluble in it. Furthermore, MEA acts as a complexing agent for CIS and CISe by forming complexes with the metal ions present in the material, which is crucial for enhancing the solubility and stability of the particles during the refinement process. Specifically, MEA has two active functional groups: an amino group ($-NH_2$) and a hydroxyl group (-OH). These groups can bind to metal ions (Cu^{2+}, In^{3+}) through coordinative bonds. The amino group can donate a lone pair of electrons to the metal ions, forming a coordinative bond, while the hydroxyl group can also participate in complexation, although the amino bond is generally stronger.

MEA forms complexes with copper (Cu^{2+}) and indium (In^{3+}) ions through the amino group, creating structures like $[Cu(NH_2CH_2CH_2OH)_4]^{2+}$ or $[In(NH_2CH_2CH_2OH)_6]^{3+}$, thus acting as a bidentate ligand. The formation of these complexes increases the solubility of the metal ions in the solvent, facilitating the homogeneous mixture of the precursors. Additionally, the complexes formed with MEA are more stable and less prone to precipitation, which is particularly useful for increasing the stability of the suspensions: in fact, these suspensions remain stable if stored in the refrigerator at a temperature of 4°C. The limit of the stability was not found within this thesis, as the first MEA varnish studied still results stable after 6 months from the time of its refinement.

Furthermore, MEA can also act as a passivating agent for grain boundaries by binding to dangling bonds at the surface or grain boundaries of the material, which usually act as trap states and degrade the electrical properties of the film. By binding to these dangling bonds, MEA helps to reduce the density of defect states at the grain boundaries, thereby improving the electrical properties and stability of CISe and CIS. This passivation effect is crucial for enhancing the overall performance and reliability of the film deposited. Moreover, MEA tends to improve adhesion with the molybdenum substrate, chemically binding to it and thus forming a chemical connection between the substrate and the material, making the adhesion optimal. In fact, MEA contains an amino group ($-NH_2$) and a hydroxyl group (-OH), which can act as ligands and form coordination bonds and hydrogen bonds, respectively, with metal atoms on the substrate surface. In some cases, MEA can react with surface hydroxyl groups on the substrate to form covalent bonds. Furthermore, MEA can interact with the substrate through electrostatic interactions, where the protonated amino group in MEA can be attracted to negatively charged surface groups on the Mo substrate. The film can only be removed from the substrate through the chemical action of an acid that acts as an etchant for the chalcogenides, as for example 37% HCl.

A study on the morphological properties of the varnish containing amine was conducted, varying the percentage of amine by volume at 5%, 10%, or 20%. From a qualitative point of view, observing the doctor blade deposition visually, it is seen that with a percentage of amine of 5% and 10% by volume, the films still exhibit inhomogeneities and areas where less material is present, whereas with 20%, the films appear completely covering and uniform, as visible in the photograph reported in Figure 63. For this reason, it was decided to complete the study only in the case of 20%.

Figure 63: Picture of the film obtained with n-butanol+20%vol MEA varnish deposited via doctor blade.

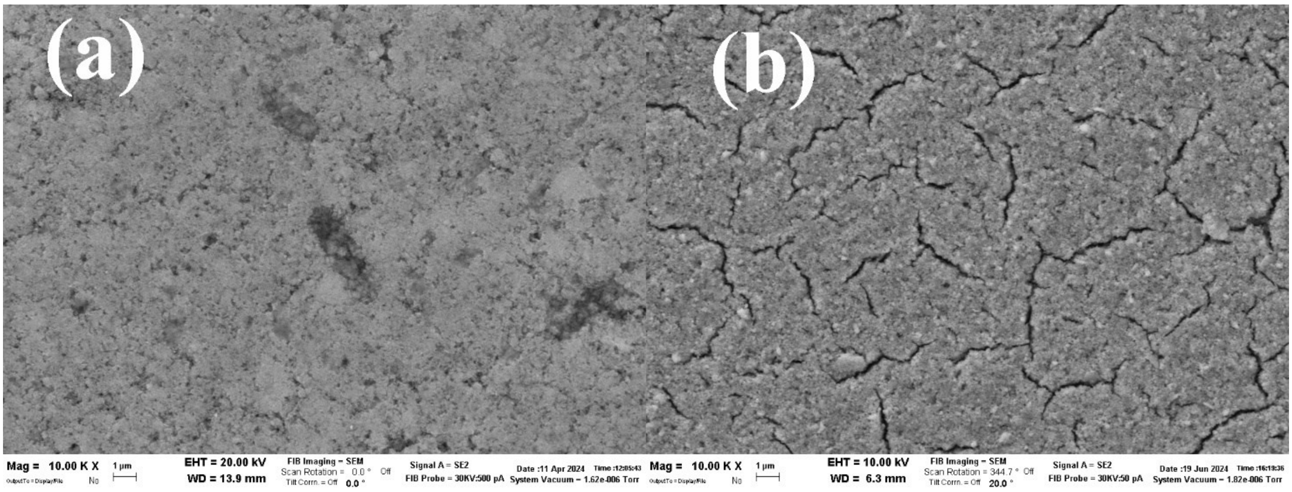

Figure 64: SEM image at 10 kX of the film obtained with n-butanol+20%vol MEA varnish deposited via doctor blade (a) dried with a two-step drying process of 10 minutes at 70°C and 10 minutes at 120°C (b) dried at 150°C.

Films were dried on a hot plate with two different temperature steps: 10 minutes at 70°C to slowly dry n-butanol under its boiling point, and 10 minutes at 120°C to remove MEA, without reaching the boiling point of the solvents, which could damage the films. Additionally, it is observed that with this process, it is possible to limit the formation of cracks in the film, even though at the submicrometric scale they were always observed (Figure 64).

XRD analysis confirms that even with 20%vol MEA added to n-butanol during the refinement process, the structure of the material is not affected, showing no spurious phases that could be attributed to phase dissociation whilst a complete degradation of the crystalline phase towards the amorphous state is detected (Figure 65).

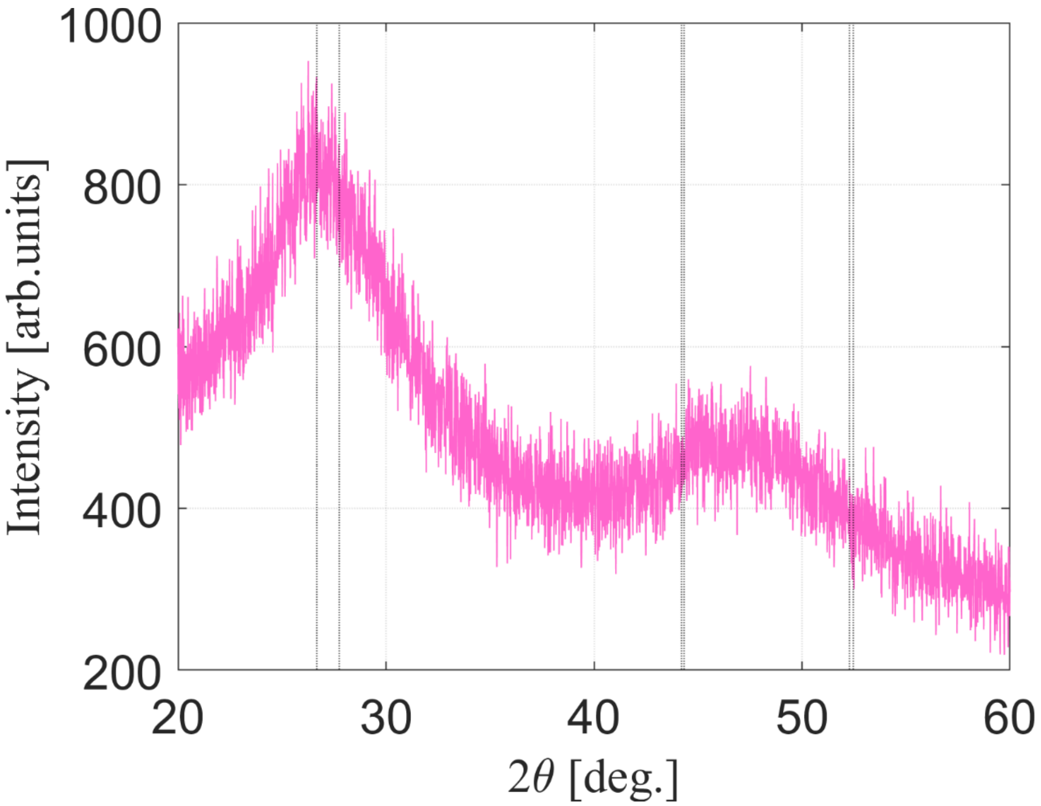

Figure 65: XRD pattern of the film obtained with n-butanol+20%vol MEA varnish deposited via doctor blade.

Moreover, the presence of MEA inside the agate jars during refining performed with standard parameters as described in the 3.1.2.1 chapter, contributes due to its rheological and chemical properties to reducing the particle size in the paste suitable for doctor blade, favoring its amorphization, as visible from the SEM analysis in Figure 66. This SEM analysis also shows that the films containing 20%vol MEA are the densest and most compact, and it is possible to observe that MEA distributes around the grains, contributing keep them together and to passivate. In this SEM image, one can see a sort of slurry that envelops the individual grain and brings it closer to the others, contributing to create a sort of continuum and dense later. Even after removing the MEA with the 2-step drying (Figure 66(b)), the film maintains its compactness, creating an ideal condition for the realization of the film. Still, a small part of carbon residue from the MEA drying can be noted in the part of the film closest to the substrate (pink circles). Even by increasing the time of the drying process(up to 1h), this spurious part cannot be removed solely by applying this treatment.

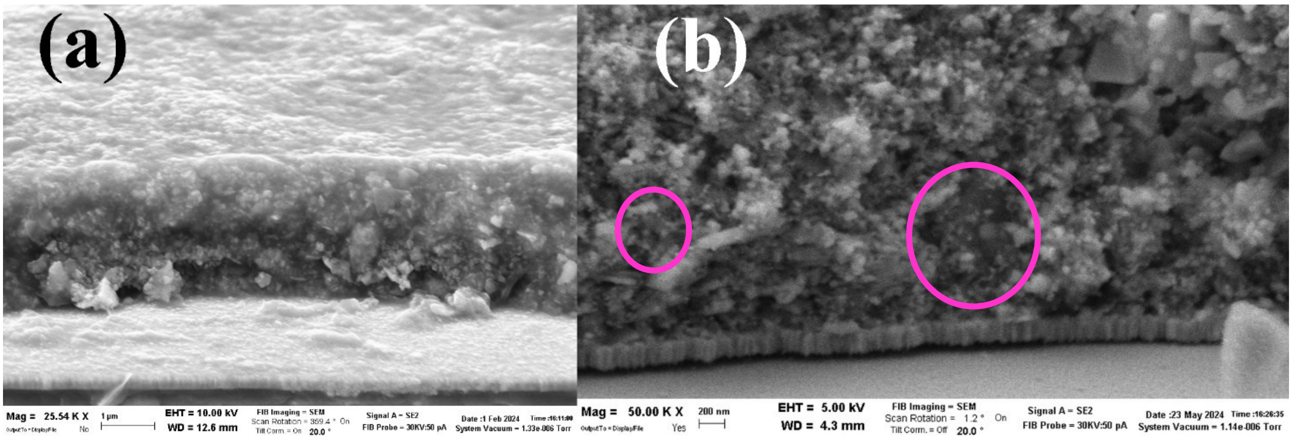

Figure 66: SEM cross-section image of the film obtained with n-butanol+20%vol MEA varnish deposited via doctor blade (a) as deposited at 25.54 kX; (b) with the 2-step hot plate drying at 50 kX; the MEA residuals are circled in pink.

Electrical properties analysis

However, it is not possible to evaluate the role that carbon residuals from MEA have on the electrical properties of the film. In fact, the addition of MEA allows for significantly improving the morphology of the film, drastically lowering its resistivity compared to films without MEA by a factor 10^3, as the measured vertical resistivity results $(11.56 \pm 2.01)\ k\Omega \cdot cm$.

Given this significant improvement primarily attributable to morphology, it is not possible to determine whether in this specific case the carbon residuals are detrimental or beneficial for the electrical properties of the film. To further improve the electrical and morphological properties of the film, the effect of a high-temperature recrystallization treatment of the material was studied. Given the extensiveness of the study and optimization of the parameters performed, the entire subsequent chapter is dedicated to this topic.

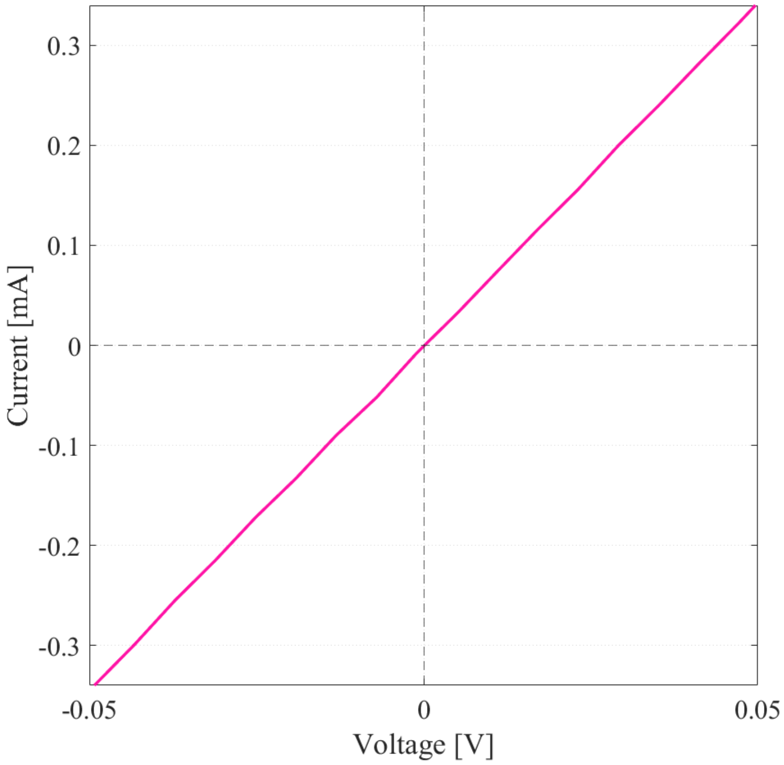

Figure 67: Vertical resistance measurements of a doctor blade-deposited black-chalcogenide varnish with MEA.

Optical properties analysis

The optical properties of these films were measured using UV-VIS spectrophotometry in diffuse reflectivity configuration. As for the previous study, these measurements were performed spanning incident wavelengths between 300 and 1300 nm.

Elaborating the measured reflectivity signal with the Kubelka-Munk function as reported in Chapter 3.1.3.2, the calculated bandgap results (1.16 ± 0.02) eV.

Here, no bandgap shifts were observed, unlike the case of brown-chalcogenides. The explanation can be found in the fact that the black-chalcogenides CIS and CISe are synthesized and processed using lower-energy high energy ball milling treatments in agate mechanical means, which induces less strain in the materials' structures and creates fewer defects and reactive surfaces, thereby reducing the electronic structure alteration of the materials and so the to changes in the bandgap.

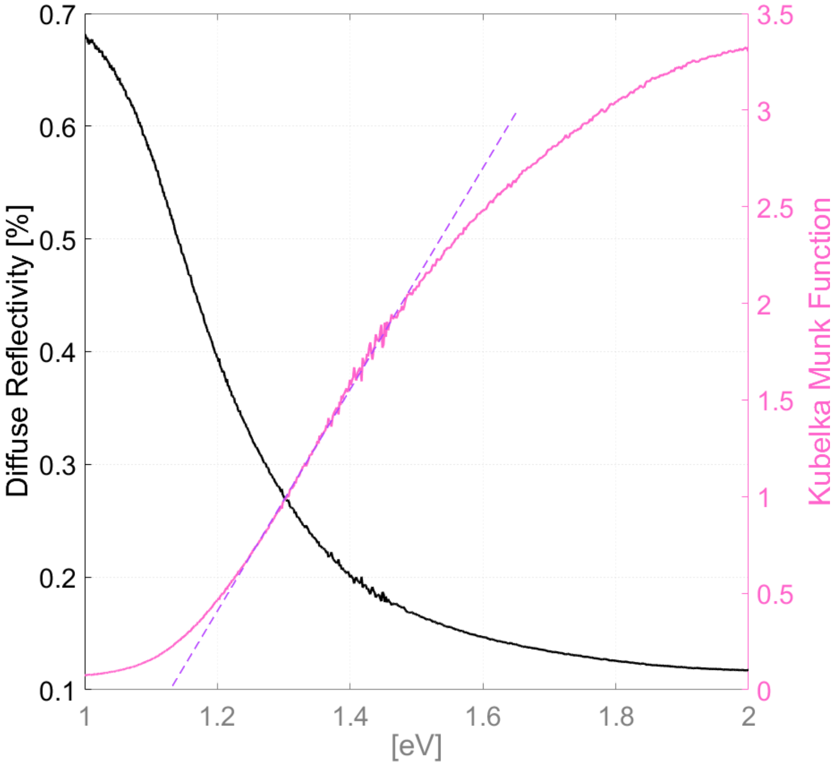

Figure 68: UV-VIS measurement of the film obtained with n-butanol+20%vol MEA varnish deposited via doctor blade. On the left axis is reported the measured diffuse reflectivity. On the right axis the Kubelka Munk calculated function is reported.

3.1.4 A study on the recrystallization of the doctor blade-deposited CIS/CISe films

Literature has shown the beneficial effects of recrystallization treatments on thin films of chalcogenides prepared from nanostructures, typically obtained from solutions. In these systems, recrystallization and grain growth during annealing strongly depend on the chemical composition and structural properties of the precursor, which in this case are significantly different due to the characteristics of the MC products compared to films obtained with nanoparticles synthesized from solutions.[130] Moreover, these processes are highly dependent on the recrystallization conditions. In literature, precursor materials based on crystalline $CuInS_2$, $CuInSe_2$, and CIGS nanoparticles have shown poor recrystallization and grain growth during heat treatment in selenium vapor at moderate temperatures (500–600 °C). This is attributed to the covalent bonding character in CIGS, resulting in low atomic diffusion rates and a relatively high melting point (~1000 °C). Various approaches have been investigated to enhance the sintering and growth of CISe and CIGS nanoparticle precursors, including increasing the selenization temperature, using highly toxic H_2Se gas,[131] incorporating CuSe as a fluxing agent,[132] gas pressure-assisted sintering,[133] and employing selenization processes on metallic Cu–In alloy nanoparticles.[134]

Given the intrinsically different nature of the chalcogenides obtained in this thesis, several recrystallization experiments were conducted to study the recrystallization behavior of this innovatively synthesized/processed materials via high-energy ball milling. An experimental setup was designed consistently with the objectives of this thesis, namely seeking a recrystallization routine for the film which avoids the use of toxic solvents and high-cost techniques. In particular, a heating system for thin films similar to that described by *Zaghi et al.*[130] was created, consisting of three halogen lamps radially positioned around a quartz vial. The quartz vial is equipped with stainless steel ends suitable for high-temperature treatments, allowing the system to be sealed in a closed environment. One end is equipped with an inlet gas valve to allow the introduction of a flux of nitrogen gas, controlled by a flow meter. The system can in principle work in controlled nitrogen atmosphere, either statically or in flow, with a gas exhaust outlet connected to the opposite end of the vial. However, the system is not designed to create a vacuum or withstand static gas pressures above 1 bar. The temperature ramp and annealing time is automatically controlled by a Eurotherm PID, in order to perform controlled heating process.

As a preliminary study, the behavior of CIS and CISe films in a static nitrogen atmosphere (with pressure <1 bar) for a fixed time of 30 minutes was investigated at different temperatures— 300, 400, 500 °C.

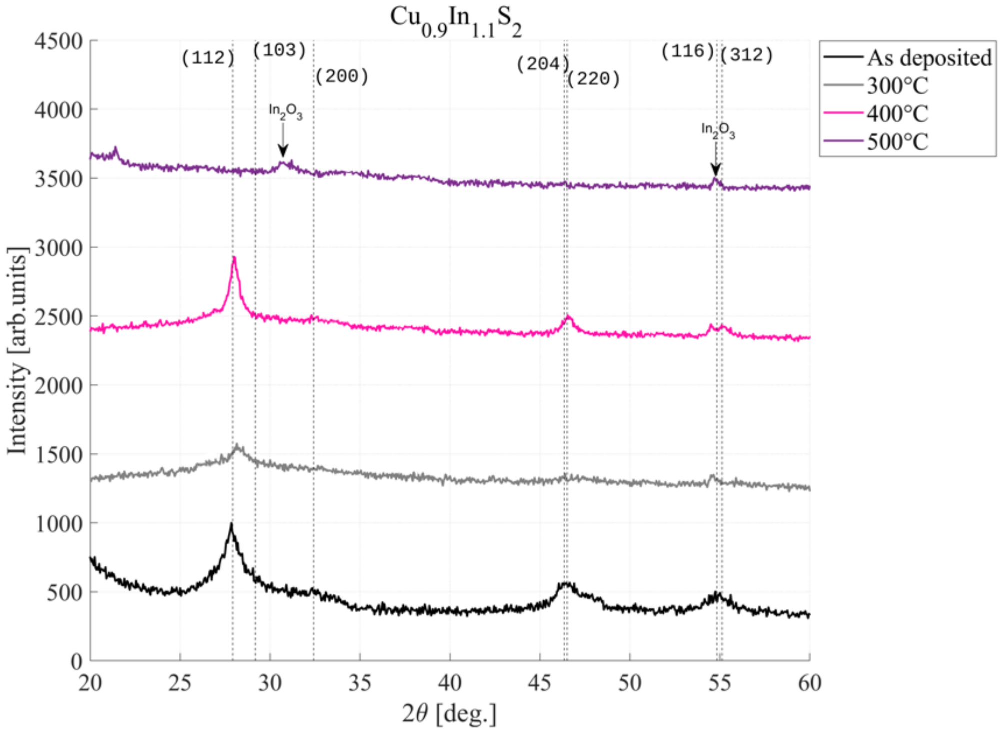

Figure 69: XRD analysis of the CIS film as deposited on a glass/FTO substrate† (black curve) and annealed at 300°C (grey curve), 400°C (pink curve) and 500°C (purple curve) on a FTO substrate.

In the case of CIS, as shown by the comparison between the pattern of the as-deposited ink in Figure 69 (black curve) and the film annealed at a temperature of 300°C (grey pattern), this temperature is insufficient to promote recrystallization as there is no narrowing of the

---

† Since a large number of patterns are compared in this figure, FTO peaks were fitted and subtracted from the measured signal, and the removed data were substituted by extending the blank-Bremsstrahlung signal.

chalcopyrite phase peak. The first noticeable effect occurs at 400°C (pink curve, Figure 69), indicated by the slight reduction of the full width at half maximum (FWHM) together with an increase of intensity of the most intense reflections, namely (112), (204/220), and (116/312). This narrowing suggests an improvement in the crystallinity of the material.

However, as shown by the purple pattern in Figure 69, a further increase of temperature at 500°C does not bring any beneficial effect in the recrystallization process; contrarily, the phase decomposes almost completely before recrystallizing. Specifically, the XRD analysis no longer detects any peaks of the CIS phase, but only the main peak of an indium oxide phase.

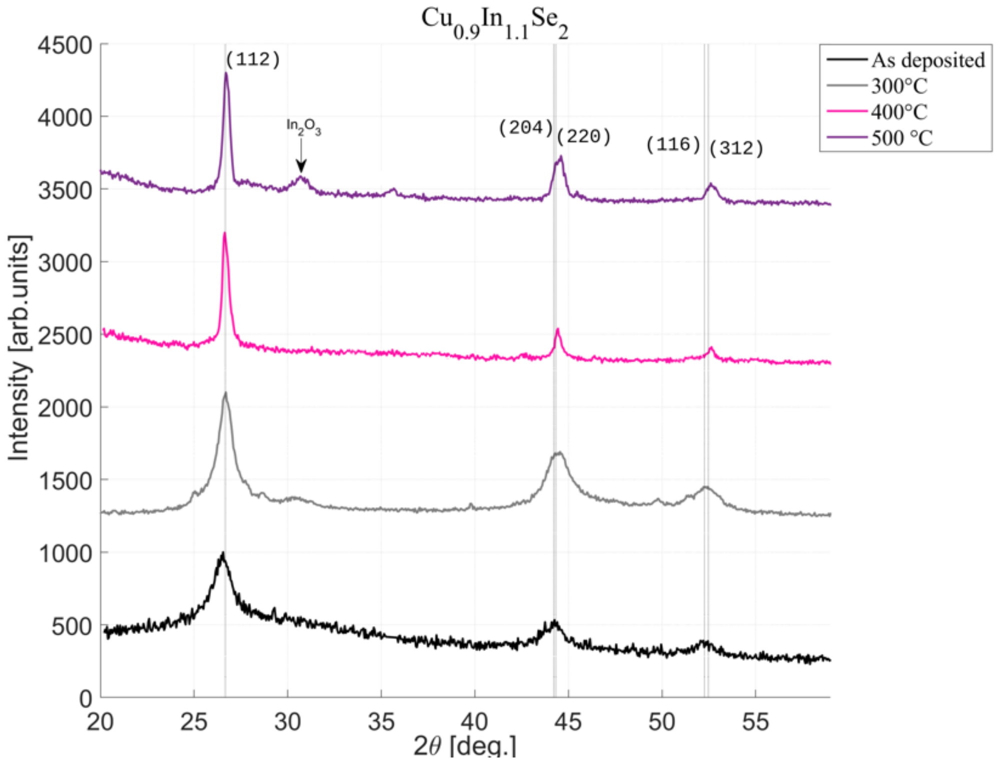

Figure 70: XRD analysis of the CISe film as deposited (black curve) on FTO† and annealed at 300°C (grey curve), 400°C (pink curve) and 500°C (purple curve).

A similar effect is observed in the case of CISe. As shown in Figure 70, 300°C is sufficient to produce a partial recrystallization effect (gray curve), as evidenced by the emergence of the intensities of the two secondary reflections (204/220) and (116/312), and a decrease in FWHM. This indicates that the material is beginning to crystallize, but the effect is not yet complete. At 400°C (pink curve), this effect becomes even more evident, as shown by the further decrease in FWHM. This suggests that the material continues to crystallize and improve its structural order with this increase in temperature. However, CISe treated in this experimental setup also partially decomposes at 500°C, as indicated by the emergence of the main reflection of indium oxide (purple curve).

Both the XRD analysis performed on CIS and CISe show that with our quartz vial heating system working in static atmosphere, it is not possible to prevent oxygen contamination of the material caused by the degradation of the phase with systematic loss of the chalcogen element during the heating process. This happens since a nitrogen overpressure was not created inside the system, which prevents the degradation of the phase. We suppose that presence of indium oxide (In_2O_3), detected after treatment, comes indeed from the uncompensated indium. This oxidation is likely due to the presence of oxygen during the treatment (caused by a loss in the chamber and swallowed up through the sealed ends due to the internal under-pressure) and/or after the removal of the sample and its consequent exposure to the air, which can react with the indium in the material to form indium oxide.

The primary cause of this dissociation, occurring well below the expected temperature for CIS and CISe, is the significant strain induced into the structure by the mechanochemical synthesis process. This strain promotes the formation of defects, particularly at the surface, which in turn reduces thermal stability and facilitates the loss of sulfur and selenium at lower temperatures. This strain is likely due to the high-energy ball milling process used to synthesize the material, which can introduce defects and strain into the crystal structure. Furthermore, the static nitrogen atmosphere was not sufficient to effectively suppress the sublimation of the volatile chalcogens, contributing to the deterioration of the material. This suggests that a more dynamic or controlled atmosphere may be necessary to prevent the loss of sulfur and selenium and improve the recrystallization of the material.

However, another explanation of this anomalous dissociation can be found in the work by *Colombara et al.*[135] This study reveals that single-phase CIGSSe material crosses the phase boundary and forms surface secondary phases upon oxidation, creating anion vacancies. These vacancies and secondary phases are linked to performance losses in CIGSSe-based photovoltaic devices. This suggests that the formation of indium oxide and other secondary phases can degrade the performance of the material and reduce its effectiveness in photovoltaic applications.

In order to absolutely avoid the dissociation of the phases balancing the stoichiometry, and avoid the sublimation of the chalcogens, the system was implemented to allow a selenization/sulfurization of the film, through the intentional sublimation of solid precursors of Se/S put inside a specially designed graphite furnace placed aside the sample, as depicted in Figure 71.

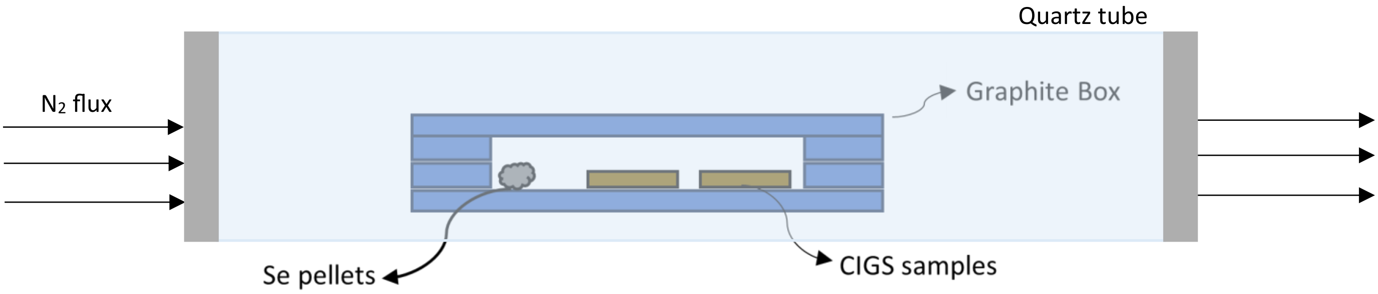

Figure 71: Schematic representation of the annealing system for selenization/sulfurization.

The graphite furnace plays a crucial role during these annealing processes under reactive atmospheres. In fact, graphite's excellent thermal conductivity ensures that the contained samples are heated uniformly, which is essential for achieving a consistent and high-quality reaction. Additionally, graphite is chemically inert, thereby preventing any contamination of the sample. This inertness is particularly important at the temperatures typically used in these annealing processes (up to 550°C). Graphite's ability to withstand this temperature regime without degrading makes it an ideal material for this application.

Moreover, the semi-closed (not sealed) graphite box helps to contain the sulfur and selenium vapor within the samples' zone, ensuring that they are kept fully exposed to the vapor of the sublimated precursors and promoting chemical and physical transformations. In fact, the vapor interacts with the sample, filling selenium/sulfur vacancies which are common defects in the MC material. This interaction helps to stabilize the desired chalcopyrite phase, which is crucial for photovoltaic applications. This can help also to study higher temperatures (up to 550°C) preventing chalcogen ions' losses and, besides, favoring the grains' growth. In order to avoid oxygen contamination, a nitrogen flow is set within the vial; this simultaneously prevents the entry of oxygen from the ends of the vial which, as we demonstrated before, can contaminate the sample and interact also with the vapors of selenium/sulfur This nitrogen flow behaves at the same time as carrier gas of the sublimated precursors allowing the transfer onto the film. The use of the flow during the cooling phase of the system also allows for the evacuation of the S/Se vapor from the system before it can re-condense on the sample and thus reducing the risk to contaminate the surface with spurious phases rich in selenium.

In the case of CISe, the recrystallization of the samples deposited via doctor blade was investigated by varying the main parameters of the system, which are the sample temperature, duration time, and the amount of selenium evaporated in the furnace, which corresponds to a different partial pressure of the chalcogen. Specifically, the following parameter combinations are explored as reported in Table 7.

Sample Temperature [°C]	Time [min]	Selenium precursor [mg]
450	15	80
500	15	80
520	15	80
520	30	80
520	60	80
520	15	160
550	15	80

Table 7: CISe selenization treatment parameters.

Tests were conducted using a three-step temperature ramp: an initial step of 10 minutes at 150°C to facilitate the evaporation of any traces of n-butanol, followed by a step of 10 minutes at 300°C to promote the removal of any moisture or contaminants present in the solid precursor, and then the specific annealing at the target temperature for different durations, as reported in Table 7. Typically, at the selected temperatures, thermalization occurs in approximately 2 minutes due to the characteristics of the graphite furnace.

The first set of tests was performed by fixing the annealing time at 15 minutes and inserting 80 mg using solid elemental selenium into the furnace for selenization process. The 80 mg corresponds to a partial pressure of the chalcogen within the furnace estimated to be around 2 bar at the set-point temperature; however, this is not constant due to the presence of a nitrogen flow. It is possible to use models to predict the variation of pressure on the sample, such as the one reported by Berner,[136] but this goes beyond the scope and preliminary study conducted in this thesis. From empirical evaluations, it was verified that 80 mg is the minimum amount of selenium that must be placed in the system to ensure it remains in the graphite box for the entire duration of the treatment, which is 15 minutes.

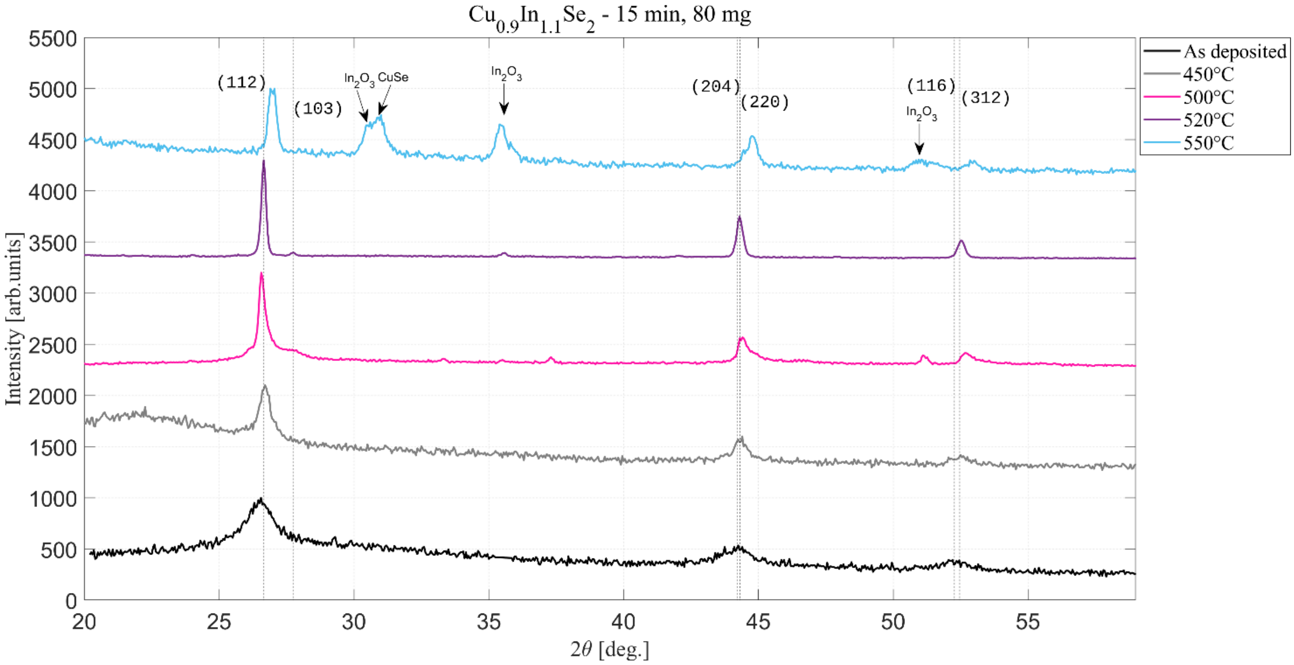

Figure 72: XRD analysis of the CISe film as deposited (black curve) and selenized at 450°C (grey curve), 500°C (pink curve), 520°C (purple curve) and 550°C (light blue curve) for 15 min with 80 mg of solid Se.

From the XRD analysis reported in Figure 72, a significant effect of the treatment is observed starting at 500°C (pink curve): the contribution of the minor reflection (103) of the chalcopyrite phase begins to emerge, and the peaks indicate that recrystallization has occurred. However, the best results were obtained at T = 520°C (purple curve), where the intensity of the reflections is maximized. The temperature of 520°C was set as the maximum temperature achievable with these samples, as at 550°C (light blue curve), the chalcopyrite phase begins to decompose. This is evident from the shift towards higher angles in the typical peaks of CISe, presumably forming CuSe and metallic indium. However, indium subsequently oxidizes to indium oxide upon exposure to air for the XRD characterizations. One of the beneficial effects of a selenium reactive atmosphere is observed when compared to the results previously presented with treatments conducted in a static atmosphere. In fact, compared to that case, decomposition occurs at a higher temperature, indicating that the use of selenium is also beneficial in extending the stability of chalcopyrite.

Fixing the process temperature at 520°C and the amount of selenium at 80 mg, the treatment time of the third step was varied to 30 and 60 minutes. However, no differences in crystallinity were measured compared to the 15-minute case.

In the context of crystal growth and recrystallization processes, thermodynamics usually dictates the final state of the material based on the free energy levels of different phases. In fact, at a given temperature and pressure, the system will tend to move towards the most stable configuration, which in this case is the crystallized chalcopyrite phase. The fact that no significant differences in crystallinity were observed with longer annealing times suggests that the system reaches its most stable state relatively quickly, and further time does not alter this equilibrium.

Kinetics, on the other hand, deals with the rates of chemical reactions and the pathways through which systems reach their equilibrium states. In recrystallization, kinetics would involve the rate at which the material transforms from an amorphous or poorly crystallized state to a well-crystallized state. If the process were kinetically controlled, increasing the annealing time would result in more complete recrystallization and improved crystallinity. However, since no such improvement was observed with longer times, it indicates that the rate of recrystallization is not the limiting factor. Instead, the system reaches its thermodynamic equilibrium quickly, and further time does not drive additional changes.

This indicates that the chosen recrystallization process is guided by the thermodynamics of the process rather than the kinetics.

The rapid achievement of thermodynamic equilibrium in this system can be attributed to several factors. The high temperature of 520°C provides sufficient thermal energy to overcome the activation barriers for recrystallization, allowing the material to quickly reorganize into its most stable crystalline form. Additionally, the diffusion of selenium vapor rapidly permits to fill vacancies and promote the formation of the chalcopyrite phase. The mechanochemically synthesized precursors are likely highly reactive and prone to rapid recrystallization due to their small particle size and high surface area, which facilitate faster reactions. Furthermore, the graphite furnace provides a uniform and efficient heating environment, ensuring that the entire sample reaches the desired temperature evenly, promoting rapid and uniform recrystallization.

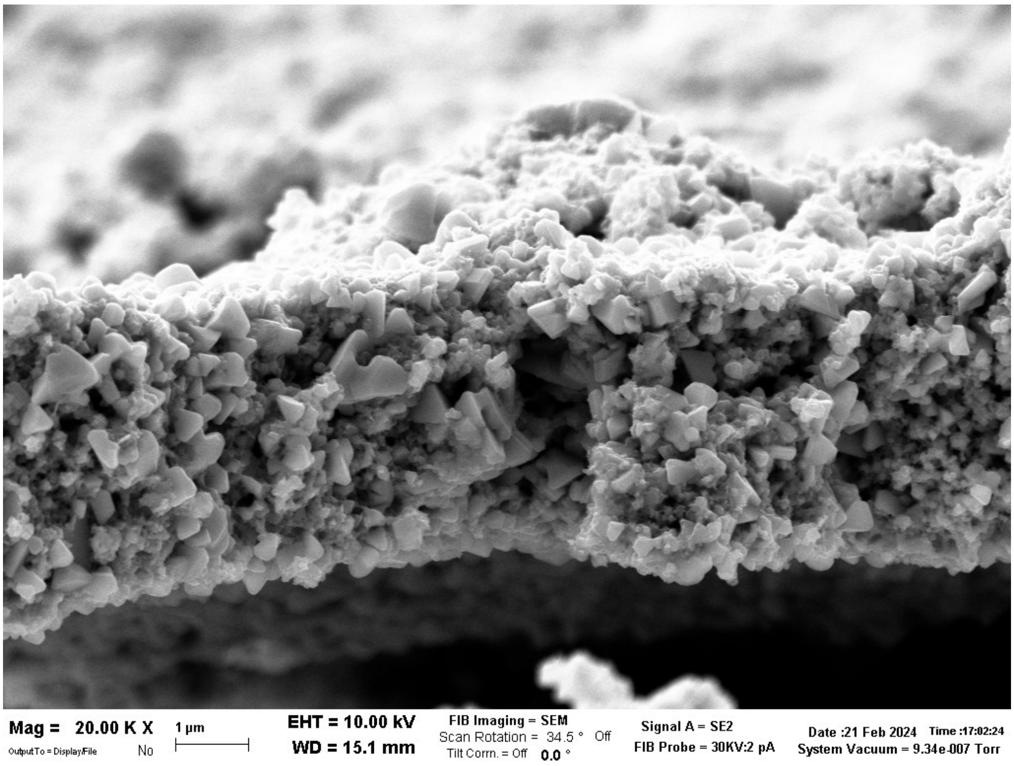

Figure 73: SEM cross-section of the CISe sample selenized for 15 min at 520°C with 80 mg of Se.

SEM morphological analysis was performed on the samples selenized for 15 min at 520°C with 80 mg of Se (Figure 73). It is clear that recrystallization occurs only within individual grains, creating a film that is always formed by a disconnected union of pure CISe microcrystals, rather than by macrograins. This observation indicates that the recrystallization process is localized and does not extend across grain boundaries. The lack of physical contact between the grain boundaries prevents the formation of larger, interconnected crystalline structures, resulting in a film composed of isolated microcrystals.

Secondly, the presence of impurities or secondary phases at the grain boundaries can inhibit the movement of atoms across these boundaries, further hindering the formation of larger crystalline structures. These impurities can act as pinning sites, preventing the grain boundaries from migrating and coalescing into macrograins.

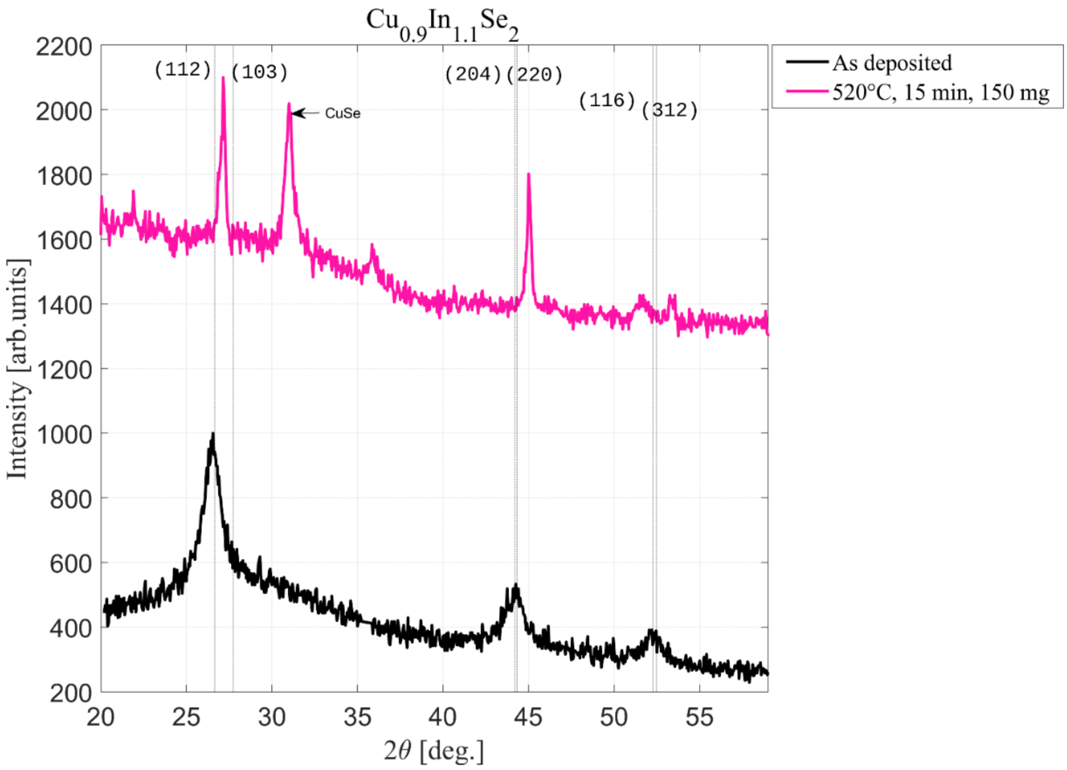

Figure 74: XRD analysis of the CISe film as deposited (black curve) and selenized at 520°C (pink curve) for 15 min with 150 mg of sublimated Se.

The effect of the Se pressure on the recrystallization process was then investigated by increasing the Se content inside the graphite box to 150 mg, which corresponds to a partial pressure of around 4 bar.

Noteworthy, it is observed that the Se overpressure inhibits recrystallization at 520°C with respect to the previous case (Figure 72, purple pattern) while, at the same time, excess Se seems to promote the formation of the large amount of the spurious CuSe phase, as visible in Figure 74. The presence of CuSe is known as detrimental to the electrical properties.[137] The high partial pressure of selenium can hinder the mobility of atoms within the material, making it more difficult for them to rearrange into the desired crystalline structure. This inhibition of atomic movement slows down the recrystallization process, preventing the material from achieving a well-ordered, highly crystalline state.

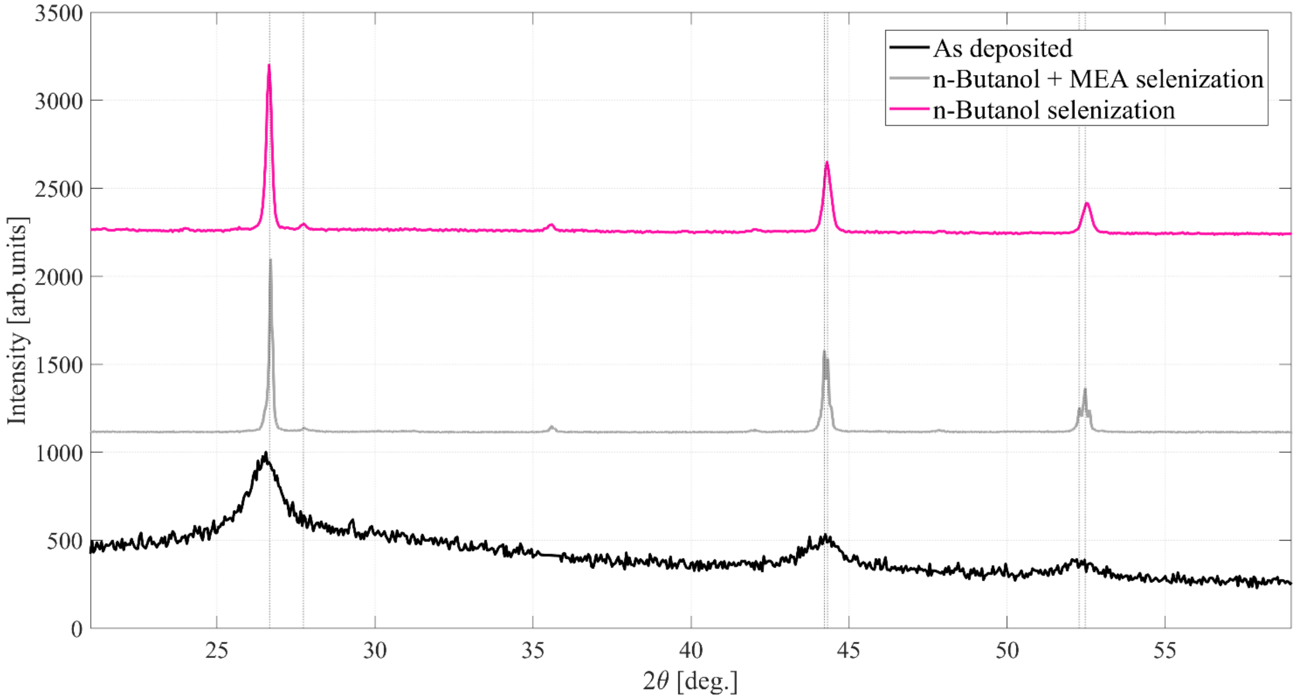

Figure 75: XRD analysis of the CISe film as deposited with MEA (black curve) and after selenization at 520°C for 15 minutes with 80 mg of sublimated Se (gray curve), compared to the film obtained from the ink with only n-butanol and selenized at 520°C for 15 minutes with 80 mg of sublimated Se (pink curve).

To address the issue of not being able to achieve physical continuity within the film and promote the formation of larger, interconnected crystalline structures, the parameters that allowed to achieve the best recrystallization results (15 min of annealing at 520°C with 80 mg of Se) were tested on the samples obtained with the n-butanol/20%vol MEA varnish.

XRD analysis presented in Figure 75 (gray curve) confirms not only the effectiveness of the identified parameters, but also that with a more compact initial morphology, it is even possible to achieve greater crystallinity compared to the case without ethanolamine. Importantly, no spurious crystalline phases are detected. SEM analysis also highlights that the starting morphology of the film is the key factor in obtaining larger crystals. Figure 76 shows that merely by adding MEA, it is possible to achieve a compact and pure crystalline layer of CISe with a thickness of approximately 600 nm, where the grain boundaries are in contact with each other. However, this layer sits above a still non-recrystallized layer.

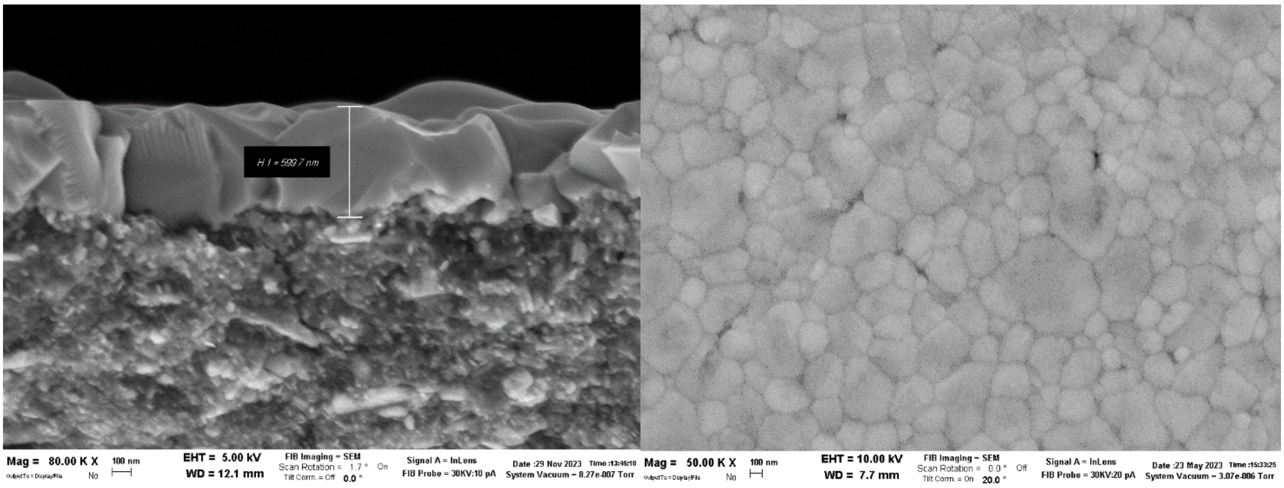

Figure 76: SEM analysis of CISe with MEA sample selenized for 15 min at 520°C with 80 mg of Se (a) in cross-section at 80 kX and (b) in plan at 50 kX.

This result deserves to be highlighted as a significant achievement. In fact, this morphology matches the current state-of-the-art of thin films obtained via solution methods. Typically, these films start from nanograins and are subsequently recrystallized using various methods. The morphology characterized by a layer of nanograins beneath a bulk crystalline layer is precisely what is obtained in this case.[138] However, as demonstrated in this thesis, the morphological and structural properties of the chalcopyrite obtained and processed via high energy ball milling are completely different and characterized by greater defectivity due to the high energy involved in the process. To date, there is no evidence in the literature of such a good result achieved starting from highly defected crystals.

EDX performed on the sample showed a ratio between Cu/In of 1.08, but excess selenium (+4%), which is believed to be located on the surface. This is due to the fact that with this type of treatment, where selenium diffuses from the exposed surface, the surface becomes Se-rich. However, it is possible to remove these impurities with an etching treatment in ammonium sulfide for 10 minutes, as proposed by *M. Buffière et al.*[139] Removing these impurities is fundamental for proceeding with the study on the stand-alone complete cell, ensuring an interface with the minimum number of defects possible between the CISe film and the subsequent CdS layer. Vertical resistivity measurements on the selenized and etched n-butanol/MEA samples (Figure 77) have shown a value of $(307.02 \pm 54.85)\ \Omega \cdot \mathrm{cm}$.

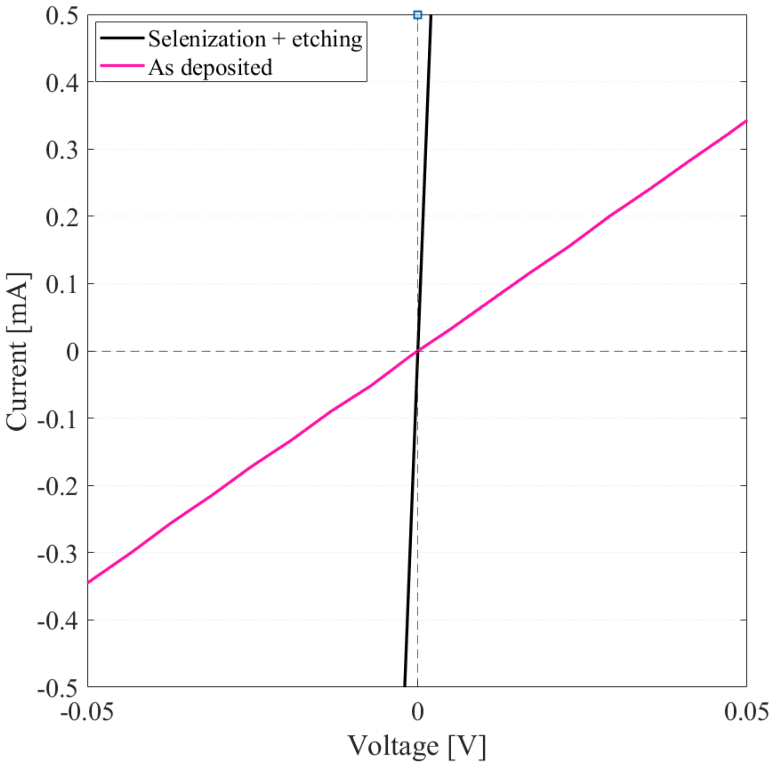

Figure 77: Comparison between the resistance of a film as deposited and a selenized/etched film.

An analogous sample deposited on an insulating substrate was studied using Hall effect measurements, with a probe current of $1 \cdot 10^{-6}$ A and a field of 8 kG (maximum limit of the experimental setup). The measured resistivity of the material is (265.03 ± 0.27) $\Omega \cdot cm$, which is in in agreement not only to what is reported in literature,[25] but also with our qualitative measurements of vertical resistivity.

The chaotic nature of the polycrystalline system, characterized by numerous grain boundaries and inhomogeneities, made it impossible to accurately measure the carrier density and mobility using Hall effect measurements. For comparison, it is estimated that a CISe film grown by Molecular Beam Epitaxy and etched in KCN, with Cu:In ratios of 18.4:23.4:58.2 and a resistivity of $2 \cdot 10^2\ \Omega \cdot cm$, similar to the sample analyzed in this chapter, has a concentration of the majority p-carriers of $3 \cdot 10^{16}\ cm^{-3}$.[140] However, in our case, this cannot be accurately measured. This allows us to demonstrate that, although the film's morphology influences the chaotic nature of the system, making it impossible to measure mobility and carrier density due to their dependence on "localized" and microscopic effects, it is still possible to measure the film's resistivity, which is close to the values reported in the literature. Moreover, these results confirm that it is possible to obtain a CISe phase with excellent electrical properties with this process even though further improvements are still needed in terms of the film's morphology.

The case of CIS is more complex. In fact, it was not possible to achieve any significant crystallization results through sulfurization of the samples using the same experimental setup with graphite boxes and flow conditions employed for the selenization of CISe. Sulfur[141] has a lower vapor pressure at a given temperature compared to selenium,[142] meaning that sulfur requires higher temperatures to achieve sufficient vapor pressure for effective sulfurization. However, it is not possible to exceed a temperature of 550°C due to the deterioration of the substrates.

To demonstrate the primary role of the choice of sulfur as a precursor for crystallization, it was decided to study the selenization of CIS samples in analogy to have been performed for CISe. XRD analysis, shown in Figure 78, indicates that selenization allowed the fast substitution of the sulfur-based chalcogenide into a solid solution with predominantly selenium at the anionic site (i.e. the peaks of the pattern are positioned at an intermediate angle between those of the end members of the solid solution, shifted more towards the theoretical positions of CISe). This occurred volume expansion of the compound and leads to better recrystallization of the system, as evidenced by the narrowing of the peaks of the main phase.

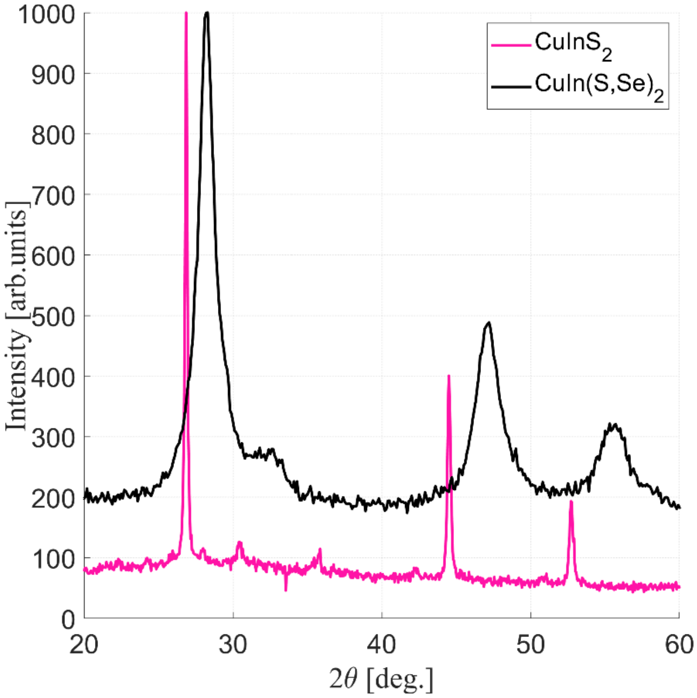

Figure 78: XRD analysis of the CIS film as deposited (black curve) and selenized at 520°C (pink curve) for 15 min with 80 mg of sublimated Se.

However, this achievement and the further study of this compound go beyond the main scope of this thesis. Having not achieved a sufficient degree of crystallinity in the case of the pure CIS phase, it was decided to focus on the more promising results obtained with CISe.

To conclude, this chapter investigated the recrystallization behavior of CIS and CISe films synthesized via high-energy ball milling. A custom heating system was designed to avoid toxic solvents and high-cost techniques, featuring a quartz vial with halogen lamps and a controlled nitrogen atmosphere.

Initial studies in a static nitrogen atmosphere showed that:

- For CIS, recrystallization began at 400°C but decomposed at 500°C, forming indium oxide.
- For CISe, partial recrystallization occurred at 300°C and improved at 400°C, but decomposition was observed at 500°C.

The decomposition was attributed to strain-induced defects from mechanochemical synthesis and oxygen contamination. To mitigate this, a graphite furnace was introduced for selenization/sulfurization, promoting a reactive atmosphere and preventing chalcogen loss. Key findings include: (1) Optimal recrystallization for CISe occurred at 520°C with 80 mg of Se for 15 minutes, showing improved crystallinity and stability. (2) Increasing selenium content inhibited recrystallization and promoted CuSe formation. (3) Adding MEA to the ink enhanced crystallinity and compactness of the CISe film. (4) Resistivity measurements confirmed the electrical properties of the recrystallized CISe films.

However, sulfurization of CIS was unsuccessful due to sulfur's lower vapor pressure. Selenization of CIS showed promise but was not the primary focus. Overall, the recrystallization process was found to be thermodynamically driven, with the graphite furnace playing a crucial role in achieving uniform and efficient heating.

3.1.5 Stand Alone Device

Prototypes of self-standing photovoltaic cells containing a film of $Cu_{0.9}In_{1.1}Se_2$ as the absorber were assembled. Although Hall effect measurements have shown that it is not possible with the current characteristics of the film to verify the carrier density and mobility, the aim of this study was to verify the structural stability, mechanical and chemical resistance of the film to subsequent deposition processes necessary for the final device, and the photoactive behavior of the p-n junction.

The film was prepared using the best parameters identified in Chapter 3.1.4: specifically, it was chosen to (1) deposit via doctor blade the n-butanol-stabilized ink with the addition of 20%vol MEA to obtain a dry film of CISe on a soda-lime glass/molybdenum substrate with a blocking layer of Si_3N_4; (2) perform a selenization treatment on the film at 520°C for 15 minutes with 80 mg of selenium, (3) perform a 10-minute etching in ammonium sulfide to remove superficial contamination of Se. Subsequently, a buffer layer of approximately 100 nm of CdS was deposited via Chemical Bath Deposition, and the cell was completed by sputtering ZnO and Al:ZnO (AZO) layers following the process discussed in Chapter 2.2.2.

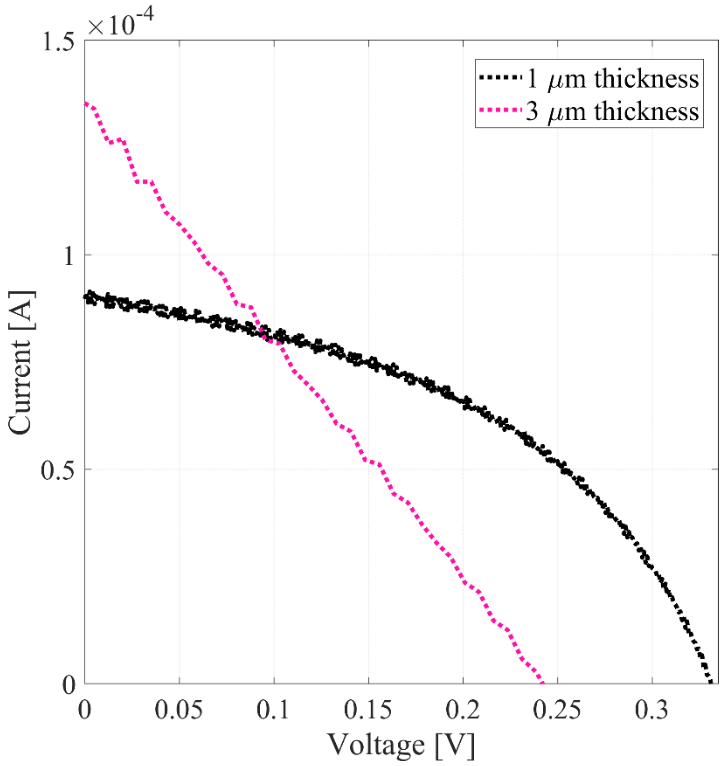

Figure 79: I-V curve of solar cells with 1μm thickness (black curve) and 3μm thickness (pink curve) black-CISe films.

The photovoltaic properties of this cell, prepared with a layer of 1 μm of CISe, shown in Figure 79(pink curve), indicate that it is dominated by the series resistance, which is $40.0\,\Omega \cdot cm$ (Table 8), comparable to values found in literature for CISe NP-based based cells.[143]

	1µm thickness	3µm thickness
Voc (mV)	331	242
Jsc (mA/cm^2)	1.8	1.65
FF	0.46	0.19
R_S ($\Omega \cdot cm$)	40	11
R_{Sh} ($\Omega \cdot cm$)	719	166
Efficiency (%)	0.3	0.1

Table 8: Calculated parameter of the CISe solar cell from curves presented in Figure 79.

However, the value of R_S decreases significantly under illumination, indicating that a photoactive region is present in the junction. This result, although small and not very significant in numerical terms, is fundamental: despite R_{Sh} being low enough to suggest the presence of percolative paths for current along the grain boundaries of the imperfectly sintered CISe films, which cause significant junction losses, it was possible to measure a V_{OC} of 331 mV (compared to an expected V_{OC} of at least 500 mV for such a nanostructured material).[138] This implies that the treatment did not sufficiently increase crystallinity and reduce electron-hole recombination centers; this recombination is a frequent and limiting phenomenon associated with the presence of shallow levels induced by defects, which limit current extraction and hence the J_{SC} which does not exceed 1.8 mA/cm^2 due to the increase in series resistance (a value very low if compared to the mean values of 31 mA/cm^2 present in literature).[143]

However, to verify that the problem is related to the hypothesized reasons, it was chosen to create a film with an increased thickness of approximately 3 microns (Table 8).

When increasing the absorber layer thickness, several key electrical parameters change, reflecting the underlying physical processes in the solar cell. The V_{OC} decreases from 331 mV to 242 mV, indicating that the increased thickness leads to higher recombination rates within the absorber layer. As the thickness increases, the probability of electron-hole pairs recombining before being collected at the contacts increases, thereby reducing the overall voltage generated by the cell.

The J_{SC} slightly decreases from 1.8 mA/cm^2 to 1.65 mA/cm^2, suggesting that while the thicker absorber layer can absorb more light, the mean free path of the photogenerated carriers is not enough to survive to recombination phenomena resulting in a not improved current extraction. .

The FF decreases drastically from 0.46 to 0.19, indicating a significant deterioration in the cell's performance. This is likely due to increased series resistance and higher recombination rates, which is favored by the poor mobility of charge carriers and the high density of defects in the bulk, which reduce the cell's ability to efficiently convert absorbed light into electrical power.

The R_S decreases from 40 $\Omega \cdot cm$ to 11$\Omega \cdot cm$, which might seem counterintuitive, but it could be due to changes in the contact resistance or the bulk resistance of the absorber layer. However, the overall performance of the cell is still negatively impacted by other factors such as increased recombination.

The R_{Sh} decreases from 719 $\Omega \cdot cm$ to 166 $\Omega \cdot cm$, indicating an increase in leakage current paths, which can be attributed to defects and imperfections in the thicker absorber layer and a less effective compactization of the film through the thermal annealing selenization process. Lower shunt resistance leads to higher current leakage, further reducing the cell's efficiency.

In conclusion, the 1 µm thick absorber layer in the photovoltaic cell showed promising results, with a V_{OC} of 331 mV and a J_{SC} of 1.8 mA/cm^2. Despite the low R_{Sh}, which suggested the presence of percolative paths for current along the grain boundaries, it was possible to measure a V_{OC}, although it was lower than expected. This implies that the treatment did not sufficiently increase crystallinity and reduce electron-hole recombination centers, which are frequent and limiting phenomena associated with defects. These defects limit current extraction and hence the J_{SC}. Overall, the results demonstrate the potential of this absorber layer but highlight the need for further optimization to improve crystallinity and reduce recombination mechanisms.

3.1.6 Top Cell – 4T tandem device

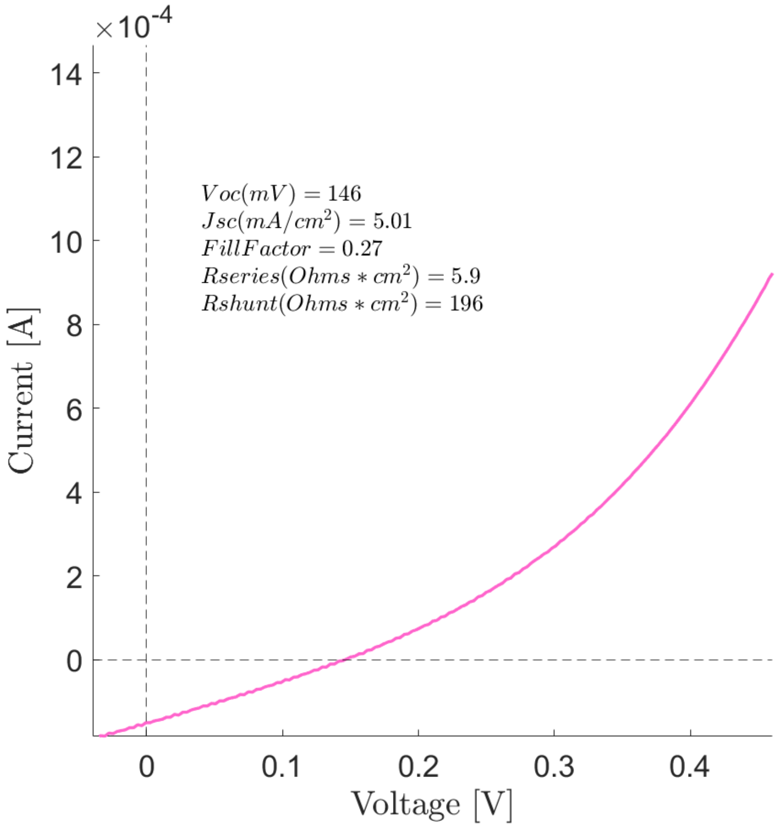

Figure 80: I-V curve of the 1μm thickness brown-CIGS based solar cell.

A prototype self-standing photovoltaic cell containing a semi-transparent layer of brown-CIGS as the absorber layer was created. Specifically, the brown-CIGS film was prepared as described in Chapter 3.1.3.2. Subsequently, a buffer layer of approximately 100 nm of CdS was deposited via Chemical Bath Deposition, and the cell was completed by sputtering ZnO and AZO layers following the process discussed in Chapter 2.2.2.

The photovoltaic properties of this cell primarily evidence that it is dominated by the shunt resistance, which is extremely low. This reflects the presence of percolative paths for current along the grain boundaries of the brown-CIGS, which cause significant junction losses. However, it is still possible to measure the photoactive effect of the p-n junction. In fact, it was possible to measure a V_{OC} of 146 mV and a J_{SC} of 5.01 mA/cm^2.

Compared to the CISe case, this increase in the current and decrease in the V_{OC} could be explained mainly by the fact that this absorber thin film is characterized by smaller grains, whose contact between them is forced mechanically with the cold pressing treatment. No additive is present in these films. So while the overall poorer quality is reflected by a FF of 0.27, the fact that there are no residuals between the grains could contribute to extend the mean free path of the photogenerated carriers, which can be trapped by the presence of defect introduced by the passivating agent (i.e. mainly MEA) at the boundaries resulting in a beneficial effect on the measured J_{SC}. Onn the other hand, the lack of a passivating agent determines an inferior physical continuity of the material and so a reduced density of the film which lead to a lower V_{OC}.

Although negligible, the achievement of a working cell based on our semitransparent chalcogenides acts as a very important starting point and paves the way to possible improvements to overcome the limitations and complexities introduced by this material and these green and ultra low-cost liquid-phase processes, which are highly extremely innovative and pioneristic but very different from established standard PV chalcogenides deposition techniques and devices. Indeed, the utilization of a quasi-amorphous and defective material (like ours) compared to a usually highly crystalline phase introduces a series of intrinsic and extrinsic differences which profoundly affect the principles of transport, doping mechanisms, mobility, and carrier characteristics. These differences will need to be thoroughly analyzed, moving away from what is known and taken for granted from the state of the art and the conventional studies available in literature on these class of compounds for thin film PV applications.

3.2 A study on the application of High Energy Ball Milling Processed Chalcogenides as Hole Transport Layers (HTL) in Carbon-Based Perovskite Solar Cells

The development of perovskite solar cells (PSCs) has garnered significant attention due to their high-power conversion efficiencies and relatively low production costs. One critical aspect of optimizing the performance of these devices is the selection and processing of suitable hole transport materials (HTMs). This chapter focuses on our very preliminary study, in collaboration with *CHOSE* institute[144] in Rome, on the possible application of high energy ball milling processed chalcogenides, specifically $CuInSe_2$, as hole transport layer in carbon-based Formamidinium Lead Iodide (FAPI) hybrid-perovskite solar cells.

However, the process established in the previous chapter as the best one to obtain high quality chalcopyrite thin films, is not suitable for this purpose for several reasons. Firstly, the perovskite solar cells used in this context are fabricated with a superstrate n-i-p architecture (see Figure 24). This implies that the chalcopyrite is deposited as HTL directly onto the perovskite layer before depositing the carbon electrode. Consequently, the use of ethanolamine and n-butanol in the ink for the preparation of CISe films is not feasible, as both solvents instantly degrade the perovskite materials, which are intrinsically very sensitive and unstable.

Moreover, the selenization treatment studied in section 3.1.4 cannot be applied, as the required temperature of 520°C would again destroy the perovskite layer. Therefore, an alternative approach was chosen: CISe is synthesized via MC as described in Chapter "High Energy Ball Milling Mechanosynthesis" and then refined to obtain a homogeneous morphology as described in Chapter "High Energy Ball Milling Refinement", using isopropanol as the organic solvent for the ink. The ink is then extracted from the jars and dried on a hotplate at 50°C until completely dry, resulting in a solid polydisperse powder. However, at this stage, the powders exhibit low crystallinity but high defectivity at the surface which means bad electrical properties so that they are not suitable for the purpose of this study.

To address this, a selenization treatment is performed directly on the powders placed in a graphite furnace system described in section 3.1.4, using the same thermal parameters identified for the films, namely an anneal process at 520°C for 15 minutes, with 80 mg of Se.

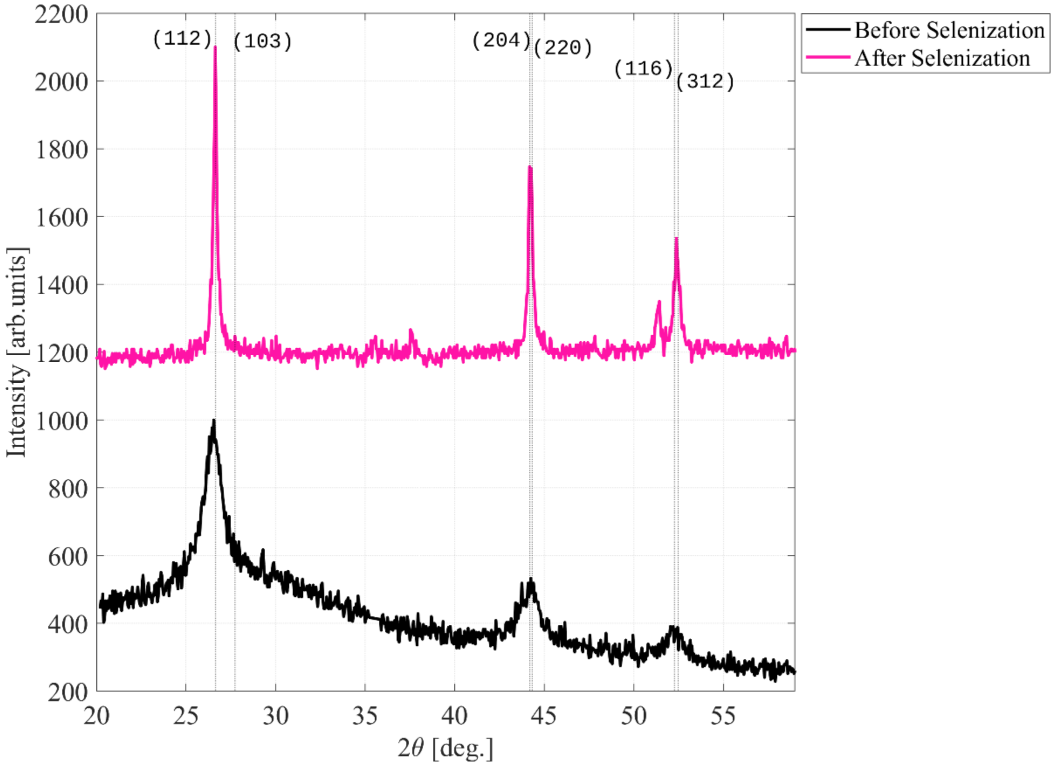

Figure 81: XRD analysis of the CISe powders dried after refinement (black curve) and then after selenization (pink curve) performed at 520°C for 15 mins with 80 mg of sublimated Se.

XRD analysis, shown in Figure 81, confirms the effectiveness of the recrystallization treatment also in the case of the powders.

The powders are then re-dispersed in 2-propanol using an ultrasonic bath at 37 kHz for 1 hour, in an ice/water bath at the equilibrium temperature, i.e. 0°C, to prevent heat-induced reaggregation of the particles. This process yields to an ink which is suitable for thin film doctor blade deposition onto the perovskite layer.

The first objective was then to investigate the alignment of the energy levels between the different layers of the perovskite solar cells, which is essential for inducing charge selectivity, facilitating hole extraction and block electron transfer, critical for achieving efficient charge extraction and minimizing recombination .

To investigate the CISe selenized powders energy bands, we employ a combination of experimental techniques such as ultraviolet photoelectron spectroscopy (UPS) and X-ray photoelectron spectroscopy (XPS) performed on a film deposited via doctor blade of the ink prepared as described above.

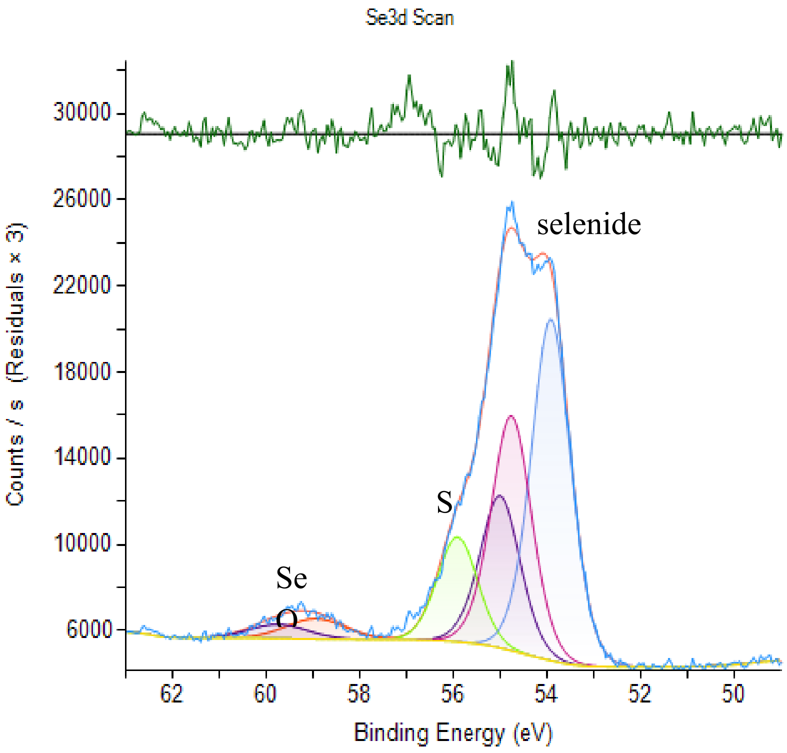

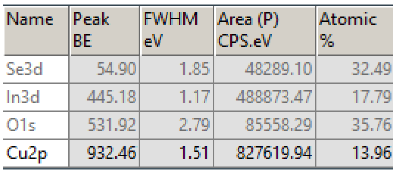

Name	Peak BE	FWHM eV	Area (P) CPS.eV	Atomic %
Se3d	54.90	1.85	48289.10	32.49
In3d	445.18	1.17	488873.47	17.79
O1s	531.92	2.79	85558.29	35.76
Cu2p	932.46	1.51	827619.94	13.96

Figure 82: XPS analysis of the powders after the selenization treatment.

From XPS analysis shown in Figure 82, it comes out that on the surface, the stoichiometry is far from the expected one. C was not possible to quantify due to overlap with Se Auger peaks. Se 3d evidence also the presence of elemental Se(0) and reduced Se(-2), probably, an oxide phase). The Se $3d_{5/2}$ peak at 53.6 eV is more attributable to selenide than $CuInSe_2$. The ratio between Se(-2)and Se(0) is 1:0.45.

On the surface there is also oxygen. As reported in the previous chapter, chalcogenide materials are prone to oxidation upon air exposure. The process can lead to a impure surface where Cu_2Se phases may form, alongside the oxide of the most electropositive cation and excess chalcogen. As a matter of that, in the outermost layers In(3d) bonded with oxygen seems also to be present.

After etching the surface with cluster gun (Ar_n^+ 8000 eV; n = 2000) for 60 s a new stoichiometry was obtained with the proper 1:1 ratio between Cu and In (Figure 69). Likely, Se(0) and oxidized Se disappeared. Moreover, Se $3d_{5/2}$ has the typical Binding Energy (BE) (54.6 eV) of that reported CISe. This means that the degradation observed on the pristine powders is exclusively a surface issue, whilst the core of the grain is constituted by the right composition of the chalcopyrite phase. Oxygen contamination at the surface is coming from the exposure of the sample in ambient conditions, during the transport from our labs to where the XPS/UPS analysis was performed.

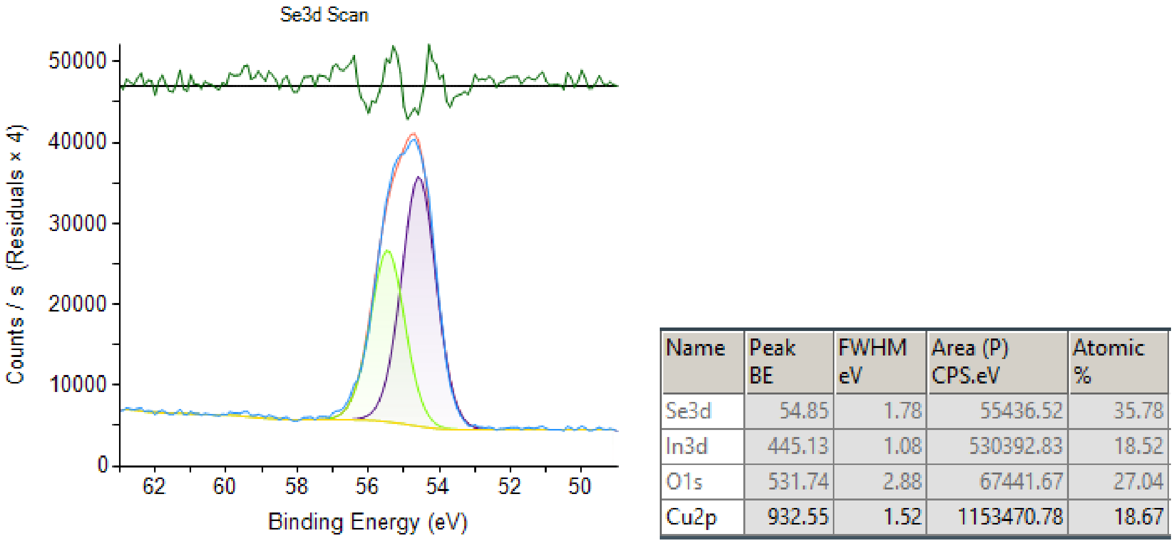

Name	Peak BE	FWHM eV	Area (P) CPS.eV	Atomic %
Se3d	54.85	1.78	55436.52	35.78
In3d	445.13	1.08	530392.83	18.52
O1s	531.74	2.88	67441.67	27.04
Cu2p	932.55	1.52	1153470.78	18.67

Figure 83: XPS analysis of the powders after the selenization treatment, after etching the surface with a cluster gun.

With the UPS measurements were carried out assuming that the optical bandgap of the material is $E_g = 1.14$ eV, returning by UV-VIS spectroscopy characterization performed on the CISe films reported in the chapter 3.1.3.3.

The results are very similar to those reported by *Hoffman et al.*[145] for CISe materials. In particular, from UPS spectroscopy it was obtained the following critical values:

IP = WF+VBM = -5.60 eV

E_A = IP-E_g = -4.46 eV

Where IP is the ionization potential, WF is the work function, VBM is the Maximum energy of the Valence Band and E_A is activation energy which corresponds to the Minimum of the Conduction Band (CBM). From these experimental values, the energy band diagram of the material can be reconstructed as reported in Figure 84.

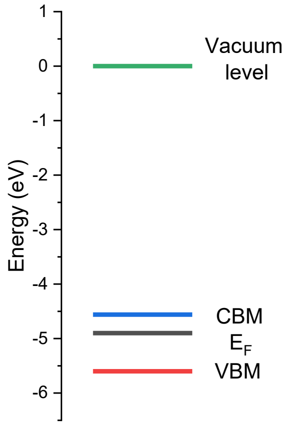

Figure 84: Schematic representation of the CISe selenized powders bands measured with UPS analysis.

Noteworthy, the Fermi Energy of the system (E_F) results closer to the CBM than to the VBM, surprisingly indicating a n-type doping of the material. This is typical of the oxygen-contaminated chalcogenides. To investigate if the nature of the n-type conductivity was due to this oxygen contamination, a qualitative measurement of the Seebeck effect on a film obtain with the same powders not exposed to was performed. Even if very tiny, variation of voltage vs. ΔT was detected, with a sign concordant with a hole mediated transport, resulting in a p-type intrinsic doping character.

Considering the experimental band obtained for the CISe, the energy level diagram of the PSCs can be updated substituting the standard hole transport layer material (i.e. usually SPYRO) with our CISe (Figure 85).

FAPbI3[146] CBM and VBM value and Carbon stripes[147] work function values were evaluated with values found in literature.

The band alignment between the chosen FAPI and CISe is favorable for efficient charge transport in a perovskite solar cell. The CBM of CISe (-4.46 eV) is slightly lower than that of FAPI (-4.3 eV), ensuring effective electron blocking and reducing recombination. Additionally, the VBM of CISe (-5.6 eV) is lower than that of FAPI (-5.4 eV), which promotes hole extraction from the perovskite into the CISe layer. This alignment supports efficient charge separation and transport.

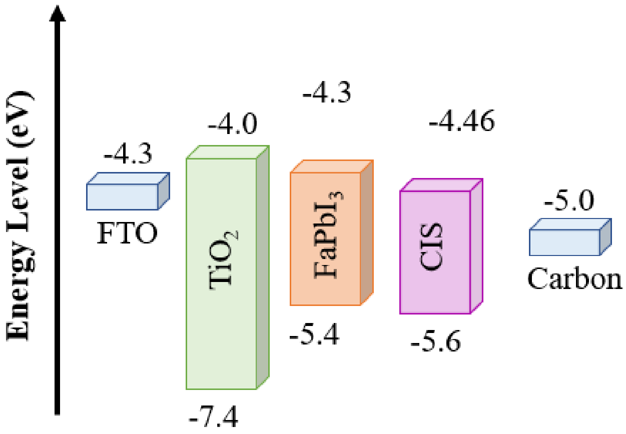

Figure 85: Schematic representation of the energy levels of each layer in the PSCs.

Standing the compatibility between CISe and the other standard layers of this PSCs architecture, the devices were assembled as follows. A compact TiO_2 layer was deposited via spray pyrolysis on a glass/FTO substrate. A layer of porous TiO_2 is then deposited on the top via liquid phase methods. FAPI is then deposited with air assisted-blade coating. CISe ink is deposited on the top studying 3 different cases. Samples (1) are prepared with 3 layers of ink with concentration of 10 mg/mL. Samples (2) are prepared depositing 1 layer of an ink of 10 mg/mL concentration with adding of an amine compatible with perovskite (Methylammonium Iodide, MAI 0.5 mg/mL) which could act as a binder between the CISe-PSK layers.[148] Samples (3) are obtained depositing 2 layers of a more concentrated ink (25 mg/mL).

The number of layers was chosen in order to maintain constant the thickness of the HTL to around 200 nm. On the top of HTL, carbon paste is deposited via blade coating.

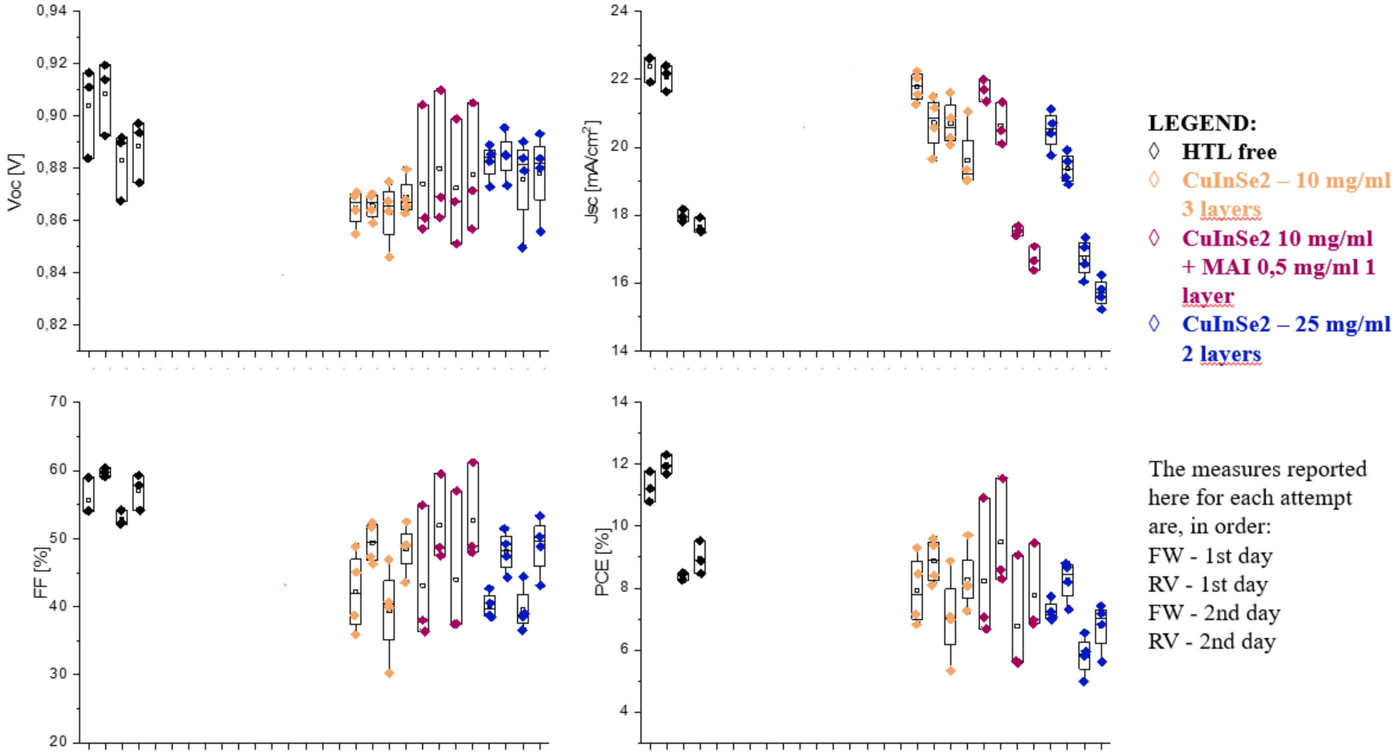

The measures reported here for each attempt are, in order:
FW - 1st day
RV - 1st day
FW - 2nd day
RV - 2nd day

Figure 86: Measured I-V curve of the PSCs without HTL (black), HTL prepared with 10mg/mL CuInSe2 ink (yellow), HTL prepared with 10mg/mL CuInSe2 + 0.5mg/mL MAI ink (purple), HTL prepared with 25mg/mL CuInSe2 ink (blue).

Two sets of measurements were performed (Figure 86):

(a) immediately after the cells were fabricated

(b) after 24 hours.

In fact, typically the PCE of PSCs undergoes a spontaneous enhancement after approximatively 24 hours, which is believed to be based on a reduction in trap-assisted non-radiative recombination possibly due to strain relaxation of the perovskite.[149] All measurements were also done by varying the voltage from a negative value to a positive value (forward scan - FW) and vice versa (reverse scan - RV). For each cell, in order from left to right, these are 1) Forward and 2) Reverse measurements performed immediately after the carbon electrode deposition and 3) Forward and 4) Reverse measurements performed after 24 hours.

Different effects were observed. None of the cells measured just after being realized reached the efficiencies of those used as reference without HTL. In the measurements done after 24 hours, the performance of the reference cells dropped, worsening both Voc and Jsc and thus determining a reduction of the PCE from around 11% to around 9%. A comprehensive comparison is needed, focusing on all the main four parameters of PV, to evaluate the role of CISe in the performance of the PSCs:

- Voc: All the three types of cells made with the CISe as HTL have shown that the mean Voc value remains approximately constant even after 24 hours.

- Jsc decreases drastically in the case of samples (2) and (3). However, in the case of samples (1) this decrease is present but it is very little, making these cells after 24 h the record Jsc of the whole set, notably 10% better than the reference ones.

- FF tends to remain constant in all the analyzed cells, both reference and CISe based, with the difference that the mean value of the latter is around 50, about 5% less than the former. However, as shown in Figure 86, the fact that the FF decreases in the case of CISe compared to the case without is primarily driven by the fact that there is a significant increase in series resistance and a decrease in shunt resistance, probably due to some interaction effect between the perovskite and CIS that leads to the degradation of the perovskite itself, inducing shunt paths and increases in series resistance.

- PCE in all the cells undergoes to a reduction after 24 hours, but the reduction in the CISe case is in percentage lower (1%) than in the case of the reference one (3%).

To sum up, the main difference observed in this preliminary data is that reversely by the reference cell all the CISe based PSCs showed a mean conservation of the efficiency during the 24 h aging even though starting from lower values. Particularly some samples of the Cells set (2) are the most efficient cells after 24 h, surpassing all the reference ones. Furthermore Cells (1) are the unique samples to show the retainment over time of all the four PV parameters, with a special mention for the most critical one for PSCs, the J_{SC}. This study must be extended for higher time to verify this potentially astonishing result is kept over time. An overall evaluation of these first tests (n.b. this study is just at the beginning) suggests that the CISe could have a stabilizing effect on the perovskite cells over time improving the durability and reliability of the system. Noteworthy, stability is the greatest issue which is limiting nowadays this technology to invade the market, so this study paves the way for very interesting and promising developments.

3.3 Antimony sulphoiodide *SbSI*

3.3.1 High Energy Ball Milling Mechanosynthesis

The chalcohalide SbSI investigated in this thesis was again synthesized via MC methods using High Energy Planetary Ball Milling process, starting from elemental reagents according to the following solid-state reaction:

$$2Sb + 2S + I_2 \rightarrow 2SbSI$$

Equation 32

A preliminary study on the synthesis process was carried out to investigate the best operating parameters of the milling machine to obtain the maximum amount possible of final product. It was found that the process can be carried out in an air atmosphere at atmospheric pressure, as the presence of oxygen does not lead to the formation of spurious oxides or undesired oxidation processes. Moreover, during this preliminary study, it was found out that this synthesis requires high rotational energies in order to obtain complete mechanical activation of the less reactive precursor, Sb and avoid the formation of undesired spurious products. For this reason, the largest available grinding media balls (10 mm) made of a very dense material (ZrO_2) were used, setting high rotational energies (≥ 650 RPM) and selecting a high impact statistic with the choice of low BPR 14. Specifically, the optimized parameters are reported in Table 9.

Grinding media material	ZrO_2
Ball diameter (mm)	10
BPR	14
Rotation speed (RPM)	700
Duration	180 min x 6 cycles (5 min pause between each cycle)

Table 9: Optimized operating parameters for the MC synthesis of SbSI.

With this choice of MC parameters, it was possible to obtain up to 5 g of SbSI for each milling process (up to 2.5 g per jar). The powders resulting from the MC process, differently from the greyish precursors, exhibited a bright red color and were initially examined using PXRD. This analysis verified the obtainment of a single-phase polycrystalline product without any detectable impurities above the technique's coherence length, showcasing good crystallinity, especially if the given synthesis technique (i.e. MC) is concerned (Figure 87).

The experimental diffraction pattern aligned closely with the reference pattern for the paraelectric phase of SbSI (space group Pnam), indicating the reaction's complete success. It is important to note that due to the strong similarity in lattice parameters, such as atomic positions and bond distances, between the paraelectric and ferroelectric phases (Pna21), distinguishing these two space groups through a PXRD pattern alone is not feasible.

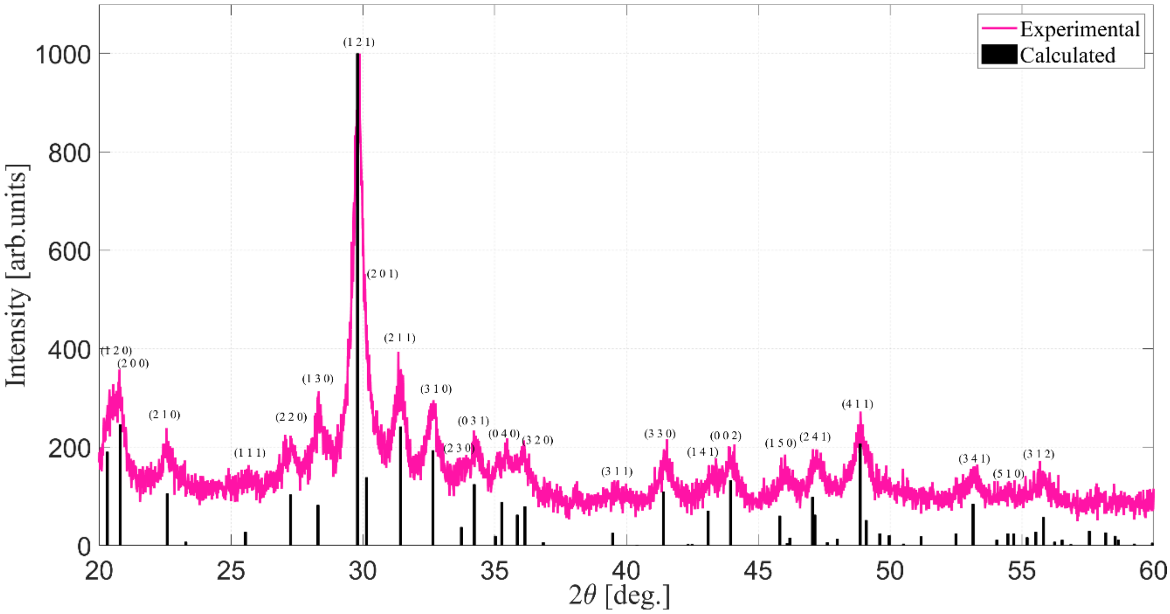

Figure 87: XRD pattern of the MC powders of SbSI (pink curve) and calculated diffraction pattern (black bars).

Further structural investigation was then performed on the powders using Raman spectroscopy. In fact, differently from the PXRD technique, Raman spectroscopy is sensitive to the vibrational modes of a material, which are influenced by the local symmetry and interatomic interactions. The ferroelectric and paraelectric phases of SbSI have distinct crystal symmetries and, consequently, different and well distinguished vibrational modes, that could be investigated with this technique. The measurements were made with a red laser (λ = 633 nm) and power at 0.01% at room temperature (Figure 88), after determining the best conditions to avoid degradation of the phase by the laser.

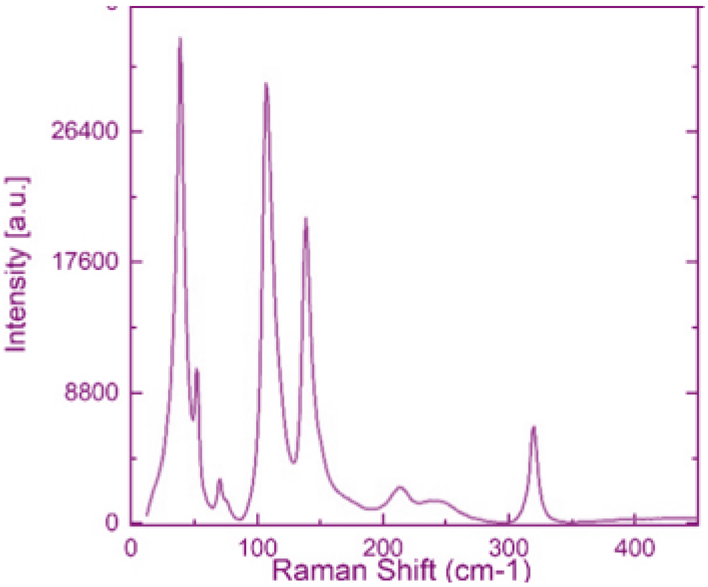

Figure 88: Raman measurement performed with laser with a wavelength of 633 nm and power at 0.01% on the MC powders at 25°C.

It is distinctly shown that the measured Raman shifts are at 39 cm^{-1}, 52 cm^{-1}, 69 cm^{-1}, 105 cm^{-1}, 138 cm^{-1}, 215 cm^{-1}, and 319 cm^{-1}, in the same positions reported in the literature for the paraelectric phase under the same measurement conditions.[150]

Moreover, it was verified that it is possible to thermally induce the structural transition from the paraelectric phase to the ferroelectric phase in the sample. The Raman measurements were repeated with the same parameters by cooling the sample to -150°C (Figure 89).

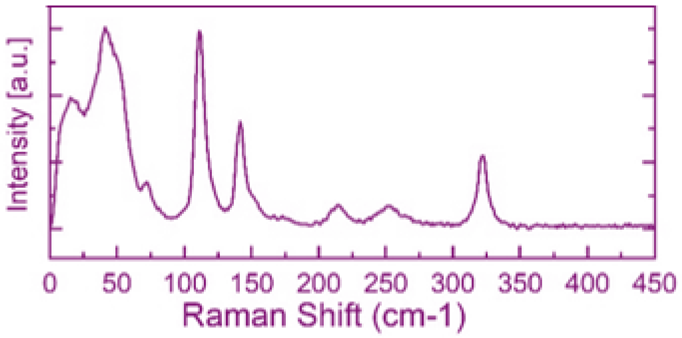

Figure 89: Raman measurement performed with laser with a wavelength of 633 nm and power at 0.01% on the MC powders at -150°C.

Aside from the broadening of lines, an evident change in the Raman spectra can be observed confined to the low-frequency region: $\upsilon < 75$ cm^{-1}. There appear to be several lines which overlap, and the spectrum has the appearance of an asymmetric band. Also, small shifts are detected in the higher frequency region, respectively from 105 to 110 cm^{-1}, from 138 to 140 cm^{-1}, and from 319 to 322 cm^{-1}. Moreover, a distinguished peak at 252 cm^{-1} appears. This is consistent with the ferroelectric phase shifts reported in literature.[150]

The crystalline morphology and chemical composition of the SbSI powders were then assessed using SEM/EDX analysis. This revealed that the particles synthesized via MC were unevenly distributed and predominantly agglomerated, exhibiting a broad size range with average sizes spanning from tens of nanometers to a few micrometers (Figure 90).

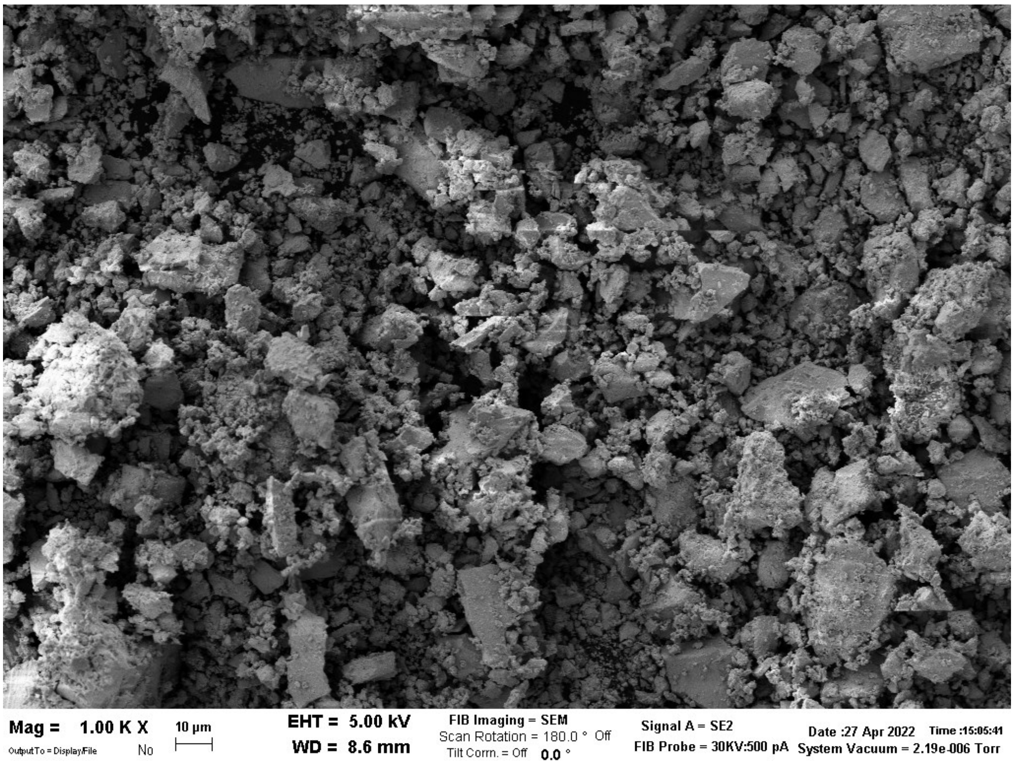

Figure 90: SEM image at 1 kX of the MC SbSI powders.

The EDX analysis, presented in Table 10, confirmed that the elemental composition of the synthesized powders matched the expected stoichiometry (within the error of the instrument) for SbSI, with approx. 1:1:1 ratio of Sb:S:I.

Element	(%)
Sb	33,6%
S	33,2%
I	33,2%

Table 10: EDX measured composition of MC SbSI.

3.3.2 SbSI thin film deposition

In a FE-PV cell, a pivotal role, far more important than in conventional thin film solar cells (as the chalcogenides previously discussed), is played by the orientation of the ferroelectric absorber: precisely the absorber should be oriented pointing its polar axis in one precise direction (possibly the growth direction of the film). In the case of SbSI the polar axis corresponds to the c-axis which is the usual direction along which the needle develops in length. For obtaining a proper film for PV application, we need to find a route to orient these needles in a concordant way during the growth process and/or after, through a proper thermal treatment. In my PhD thesis, I attempted two complementary routes of deposition: via liquid phase deposition; via physical vacuum technique.

Firstly, we succeeded to metastabilize an ink of SbSI which is in principle suitable for liquid phase methods. However, when deposited using the liquid phase methods presented in this thesis, the needles become randomly oriented (inherently polycrystalline) making these films unsuitable for FE-PV application. This process will need to be further optimized to obtain amorphous thin layer which can be subsequently recrystallized, possibly following the way is going to be presented in the next paragraph 3.3.2.3. Standing all these considerations, it was decided to not report any details of this study and focus on the proposed complementary approach in the growth of SbSI thin film, i.e. the physical vacuum technique, precisely exploiting the PED chamber available at IMEM -CNR, which was the one that gave the best results.

3.3.2.1 Target preparation for LT-PED deposition

By using powders derived directly from MC, a dense and compact disc (Figure 91) was produced to act as a target for deposition using the LT-PED vacuum physical technique. Approximately 4g of material is required to create a target with appropriate dimensions and density: we demonstrated that this quantity can be produced with just one milling process adopting the parameters listed in Table 9. The target was formed by placing the powders into a one-inch cylindrical tempered steel die, which was then loaded onto a hydraulic press platform and put under a load of 150 bar for one hour. The resulting target has a calculated density of 3.7g/cm^3. Following this, the target underwent thermal annealing in an N_2 flow at 125°C for 16 hours. The aim of thermal annealing is to reduce internal stress in the material by promoting the coalescence of grain boundaries, thereby increasing the average size of the crystalline grains and enhancing the uniformity of the target material.

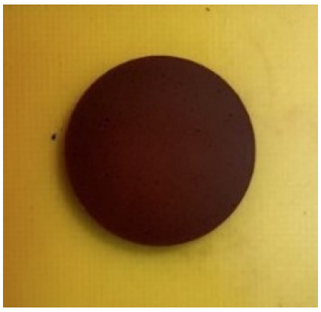

Figure 91: LT-PED target of SbSI made from MC powders.

XRD structural analysis performed on the target is presented in Figure 92. A significant reduction in the FWHM of the peaks (pink curve) is observed, indicating the formation of a more crystalline phase whose minor intensity peaks can also be resolved, as seen by the clear presence of the resolved peaks (120)/(200), (121)/(201), (040)/(320), and (002)/(150), which could have not been observed in the powders' pattern (black curve).

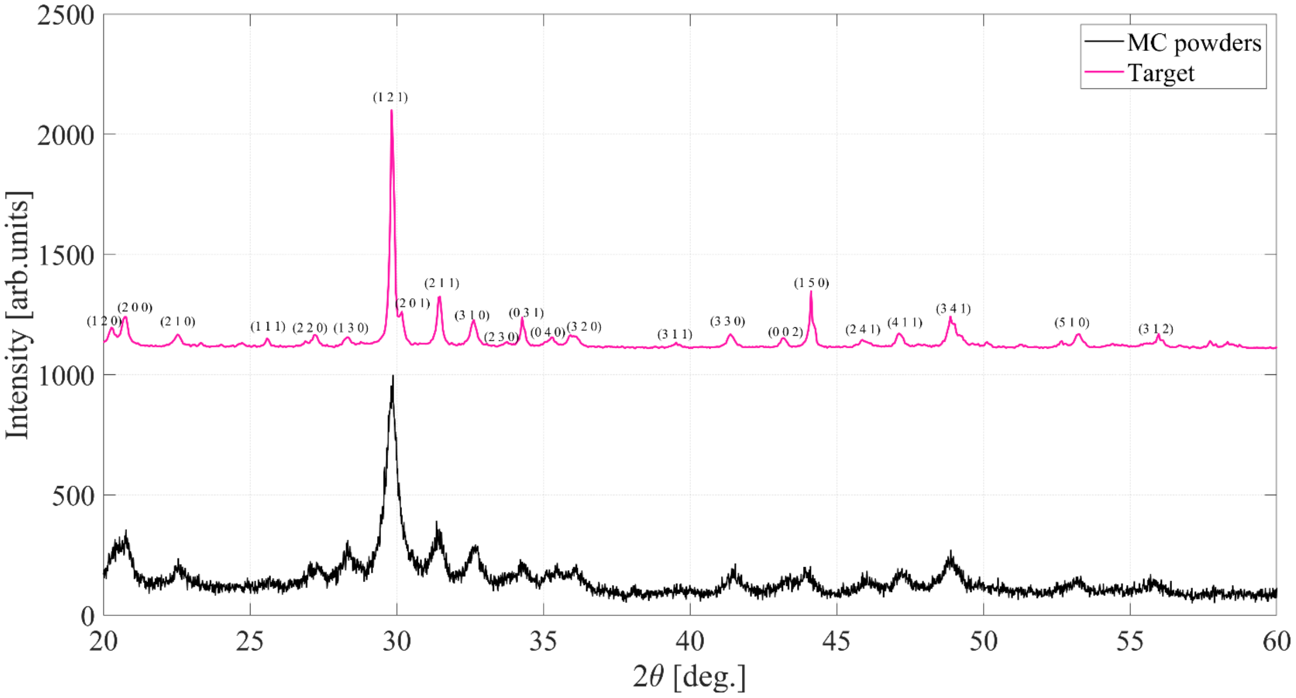

Figure 92: XRD of the SbSI MC powder (black curve) and of the sintered target (pink curve).

Also, the SEM analysis confirmed the suitability of the target for the PED deposition: surface is extremely regular, uniform, and dense (Figure 93(a)), except for certain areas where material has detached, likely during the extraction from the mold (Figure 93(b)). In some parts, micrometric chips of material have lifted, revealing the characteristic microstructure of its crystallites with needle-shaped structures typical of SbSI[104] (Figure 93 (c)).

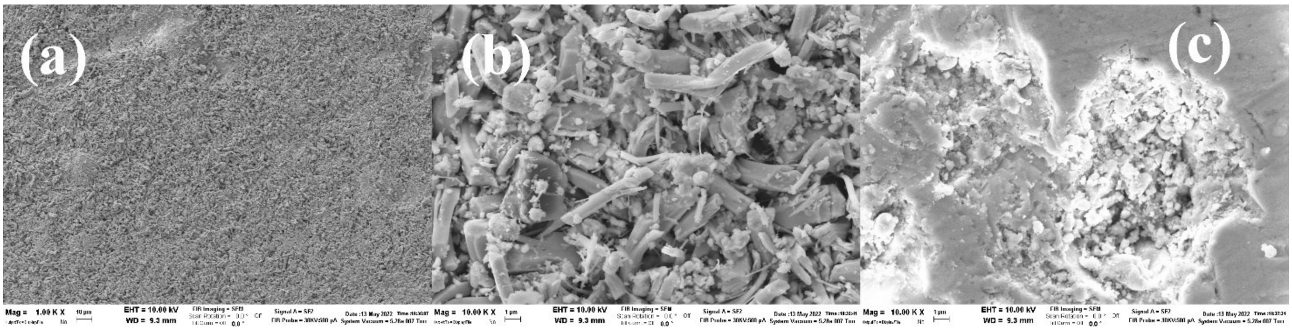

Figure 93: SEM images of the surface of the annealed MC target. (a) Planar surface at 1 kX. (b) Microstructure of the material constituting the surface at 10 kX. (c) Exfoliated surface portions at 10 kX.

3.3.2.2 LT-PED SbSI thin film deposition

Deposition tests via LT-PED were initially performed starting by the MC target optimized as described in the previous paragraph by setting the substrate temperature to 300°C to force the crystallization of the film during the deposition process, using a FTO/glass substrate. However, this high operating temperature caused the complete sublimation of iodine and partial sublimation of sulfur, reducing the material to highly crystalline metallic Sb and Sb_2S_3 (Figure 94).

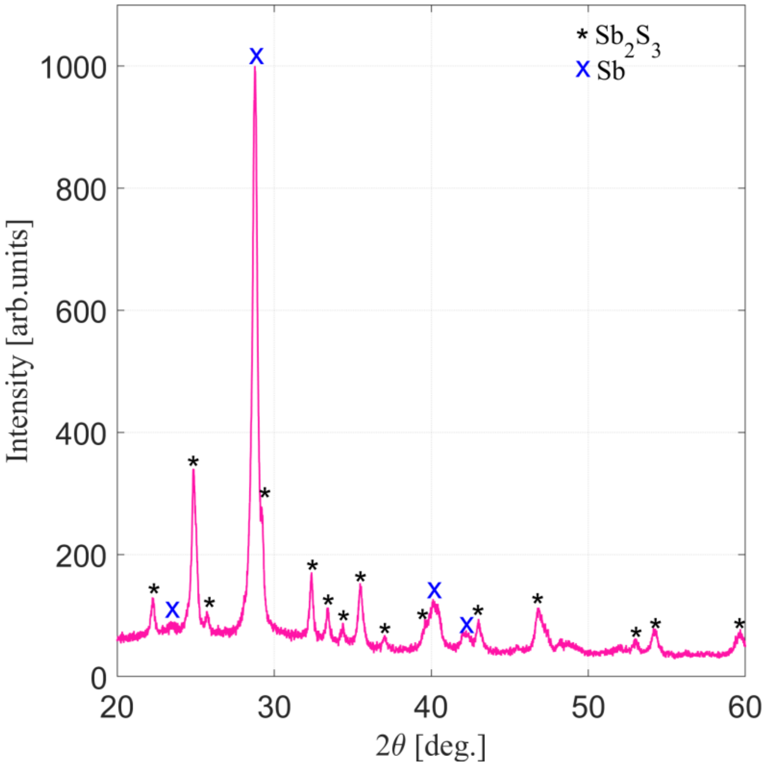

Figure 94: XRD of the film deposited via PED heating the substrate at 300°C during the deposition.

Consequently, it was decided to use lower deposition substrate temperatures, specifically working at room temperature, to minimize the potential evaporation of iodine and sulfur from the sample. The deposition at RT inevitably led to the formation of an amorphous phase of SbSI in the film, as demonstrated by various subsequent attempts. RT-PED parameters were optimized to obtain reproducible amorphous films, with a tunable thickness between 600÷1000 nm (Table 11), by varying the number of pulses.

Parameter	Value
Substrate	FTO/Glass
Deposition Temperature	RT
Voltage	14 kV
Target-Substrate Distance	8 cm
Number of Pulses	15000÷25000 (variable)
Chamber Gas Flow	Ar

Table 11: PED parameters for the SbSI film RT-deposition.

The elemental composition of the target was maintained. Therefore, an attempt was made to induce recrystallization of this amorphous phase through a thermal annealing treatment directly in the PED chamber following the deposition phase, at 90°C in the presence of Ar for 20 minutes. Preliminary annealing tests have indeed shown that the annealing parameters in this setup have an extremely narrow range, as temperatures ≥ 100°C and times ≥ 25 minutes cause the sublimation of sulfur and iodine from the substrate, degrading the SbSI phase.

RT-PED SbSI thin film XRD characterization

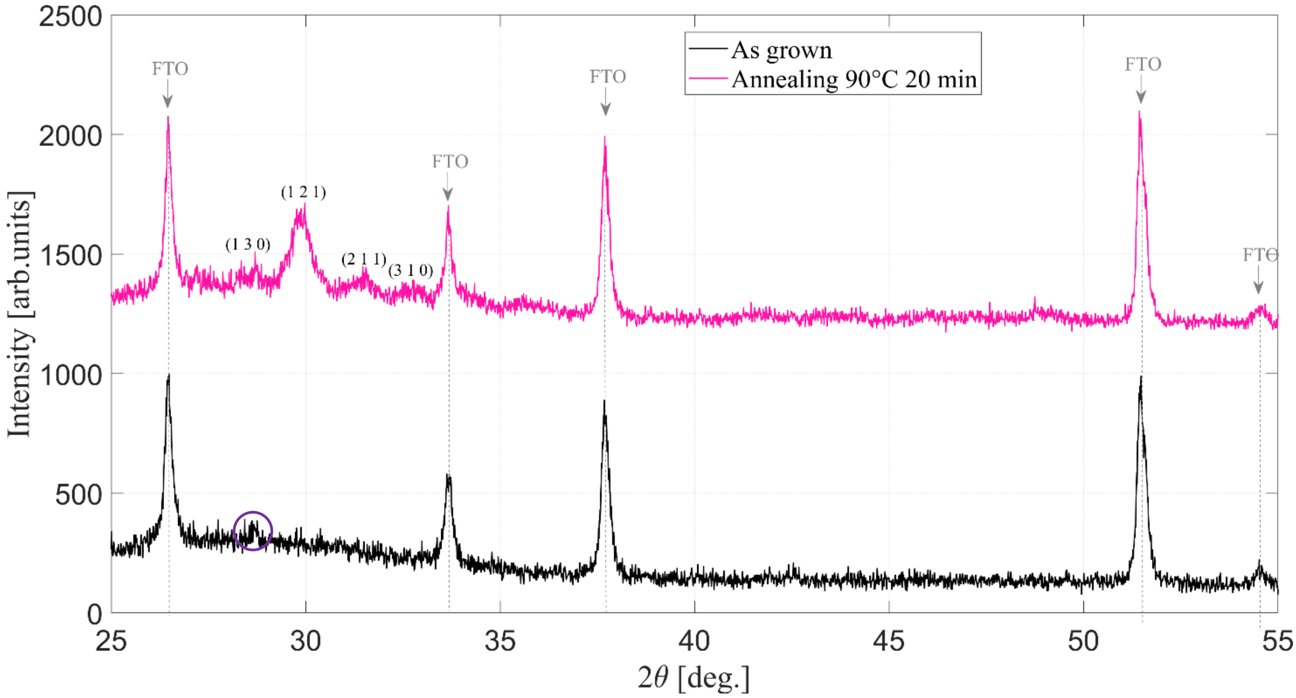

Figure 95: XRD pattern of thin SbSI films produced via LT-PED at RT on FTO/glass, non-annealed (black curve) and annealed in the PED chamber at 90°C for 20 minutes (pink curve).

The deposition of thin films using LT-PED led to the formation of an amorphous phase of SbSI on FTO/glass (Figure 95, black curve); however, a weak peak of another crystalline phase is detected at 28.7° (. Even if it is not possible to identify a phase with certainty by detecting only one reflection, it is hypothesized that this could be associated with the (012) reflection of metallic Sb, the most intense, due to a slight sub-stoichiometry of the PED plume probably emerging by the bad ablation of the volatile iodine and sulfur as a result of the high-energy electronic pulses of the process hitting the target during the process.

As mentioned earlier, the amorphous films underwent post-thermal treatment inside the PED chamber. Specifically, at 90°C in the presence of Ar for 20 minutes. This process resulted in the formation of an SbSI phase with weak crystallinity, indicated by the appearance of a weak peak at approximately 30°, associated with the main reflection of SbSI, the (121)

(Figure 95, pink curve). Other minor reflections can be detected, such as (130), (211) and (310).

RT-PED SbSI thin film SEM/EDX characterization

Films deposited on FTO glass, both as grown and annealed in the PED chamber, were observed through SEM analysis. The images show a particulate-like structure of the material, which does not correspond to SbSI crystallites' peculiar morphology, indicating an amorphous or quasi-amorphous state of SbSI (Figure 96(a)). The thickness of the film, evaluated in cross-section, is approximately TOT PM nm (Figure 96(b)). The annealing treatment in the PED chamber at 90°C for 20 minutes, as indirectly observed from the respective XRD spectra, although seemed to XD to have promoted partial recovering of a ordered structure, does not cause any visible change in the shape of crystallites of SbSI (Figure 97).

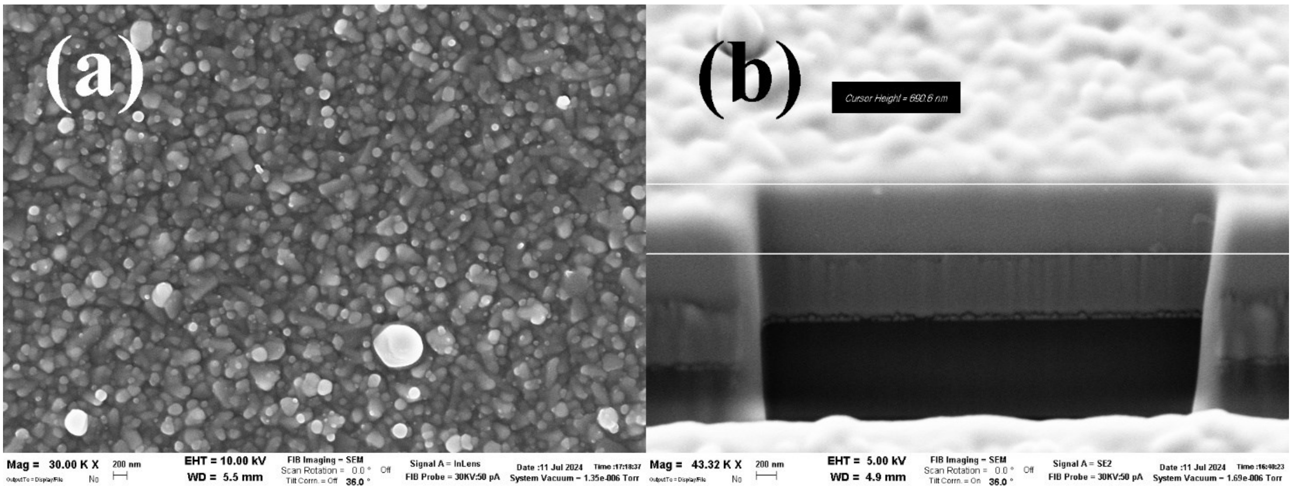

Figure 96: SEM images of the SbSI thin film produced via LT-PED at RT, non-annealed: (a) plan view at Mag 30 kX, and (b) cross-section made using FIB at Mag 43.32 kX.

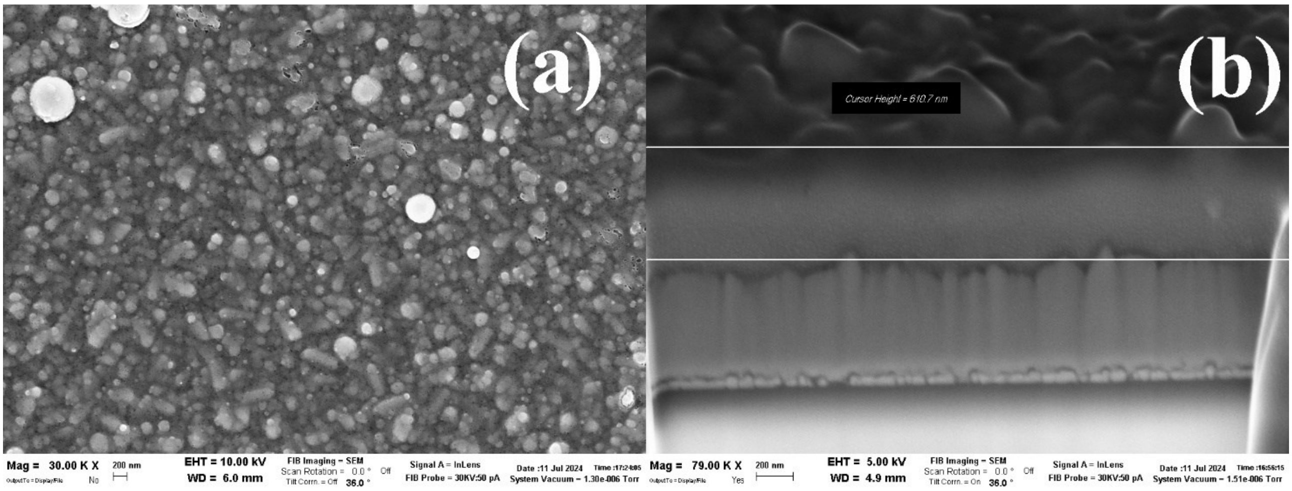

Figure 97: SEM images of the SbSI thin film produced via LT-PED at RT, annealed in the chamber at 90°C for 20 minutes: (a) plan view at 30 kX, and (b) cross-section made using FIB at 79 kX.

In the case of thin films produced via LT-PED, EDX analysis cannot be considered reliable due to the particularly reduced thickness of the films, which results in the detection of high concentrations of tin from the FTO, making it impossible to distinguish its contribution from that of sulfur. Nevertheless, the produced films qualitatively appeared to be sub-stoichiometric both in sulfur and iodine.

RT-PED SbSI thin film optical characterization

The optical properties and the optical bandgap of SbSI film deposited via PED were investigated using UV-VIS spectrophotometry.

The predicted electronic band structure of SbSI is characterized by an indirect forbidden band gap $E_{gIf} = 1.862$ eV,[104] referred to the transition from the Γ point to the S point of the reciprocal lattice. Standing the various mechanisms of absorption of electromagnetic radiation in semiconductors, which can coexist within the same spectral range, *Nowak et al.*[151] proposed a method for fitting the spectral dependence of the Kubelka-Munk function. In this method, the least square function has been minimized as follows:

$$\chi^2 = \sum_{i=1}^{n} \left[F_{KM}(h\nu_i) - B \sum_{j} \alpha_j (h\nu_i) \right]^2$$

Equation 33

In this context, ***i*** is a counting integer which discriminates photons of different energies, while ***j*** describes various mechanisms of light absorption, and ***B*** is the proportionality factor. Three out of the 32 known mechanisms of absorption in semiconductors have been considered, each one defining a particular value of the α parameter, specifically:

1. Statistical mediated excitons and phonons absorption, expressible as:

$$\alpha_1 = A_{60}\left(h\nu - E_{gIf}\right)^3 for\ h\nu \geq E_{gIF}$$

Equation 34

where E_{gIf} represents the indirect forbidden energy gap and A_{60} is a constant amplitude parameter.

2. Urbach-ruled absorption, defined by the equation:

$$\alpha_2 = A_U\, e^{\left[\frac{h\nu}{E_U}\right]}$$

Equation 35

Where E_U is the Urbach energy and A_U is a constant amplitude parameter.

3. An optical absorption term, related to the complex part of the refractive index of the material k, which can be written as:

$$\alpha_3 = A_0$$

Equation 36

where constant absorption term A_0 is an attenuation coefficient that is considered as the sum of scattering and absorption independent on $h\nu$, near the absorption edge.

Figure 98 (pink curve) illustrates the Kubelka-Munk plot of the investigated SbSI thin films deposited via PED, calculated from the diffuse reflectance UV-VIS measured spectrum, and the least square fitted theoretical dependence (black curve), which is appropriate for the sum of indirect forbidden absorption without excitons and phonon statistics (α_1), Urbach-ruled absorption (α_2), and a constant absorption term (α_3).

With this method, the fitted band gap values for the as grown films deposited via RT-PED were obtained with high confidence $(R^2 = 0.9996)$. An energy band ap value of $(1.89 \pm 0.01)eV$ returned by this interpolation is fully in line with expectation. The other fitting parameters are reported in Table 12.

Analogous results were obtained in the case of the annealed film at 90°C for 20 min, consistently with the unvaried morphology and crystallinity detected with XRD and SEM analysis.

Parameter	Value	95% Confidence Bounds
A_{60}	192.7	(190.2, 195.2)
E_g	1.888	(1.887, 1.889)
Au	6.832e-05	(5.203e-05, 8.461e-05)
Eu	0.2557	(0.2475, 0.264)
A_0	0.06531	(0.06444, 0.06618)

Table 12: Least square fitted parameters for Kubelka-Munk SbSI function.

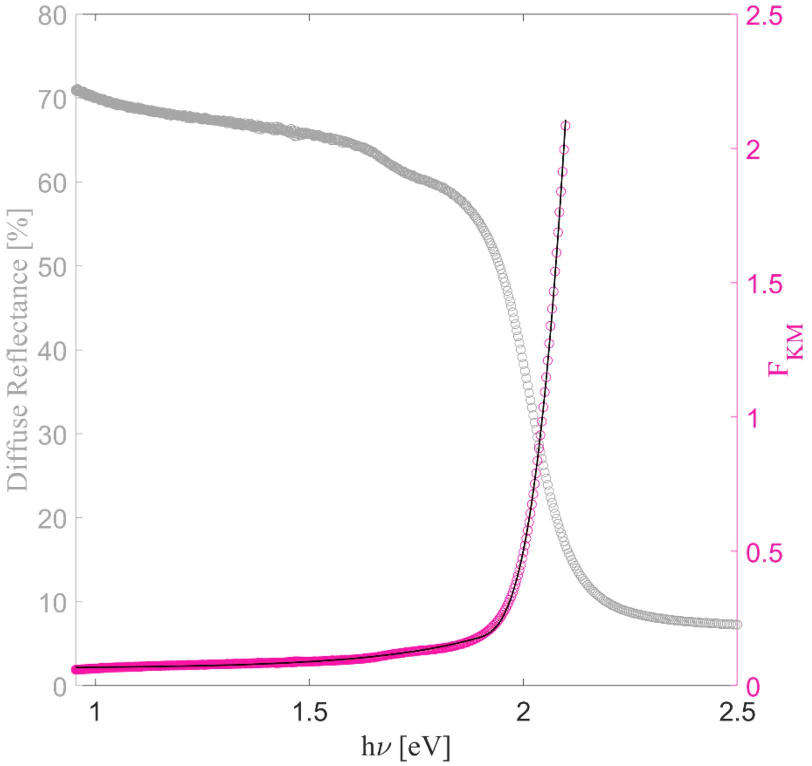

Figure 98: (Left axis, in grey) Measured UV-VIS Diffuse Reflectance of SbSI film deposited via RT-PED and (right axis, pink) the calculated Kubelka-Munk function in pink with the fitting function in black.

3.3.2.3 Preliminary results: Post-deposition treatment under high pressure gas conditions

Given the interlocutory results on the reported thermal treatments on the amorphous SbSI films deposited via PED, a collaboration was recently initiated with a research group from the *Universitat Politècnica de Catalunya*, in Barcelona, using an annealing system that allows working in a vial at high pressures of inert gas (Ar), up to 5 bar. The idea is that this high partial pressure in the heating chamber could prevent the sublimation of sulfur and iodine and aid in the crystallization of the material, imparting a specific preferential orientation, hopefully the one defined by the polar axis of the material.

Figure 99: High-pressure furnace used for the annealing treatment of our RT-PED deposited thin films of SbSI at Universitat Politècnica de Catalunya.

In more detail, SbSI films were deposited with the PED parameters reported in Table 11. However, the gas flow was increased during the deposition to reduce the thickness of the samples to around 700 nm, in order to verify if it was possible to achieve top-to-bottom recrystallization of the entire sample. A high-pressure furnace (Figure 99) equipped with gas flow was used to carry out the experiments. The samples were placed in a borosilicate petri dish and placed in the furnace. Once the system was purged to ensure the inertness of the atmosphere, 9N Argon was introduced until the chosen pressure was reached at room temperature. Finally, the furnace was ramped up to the process temperature at a rate of 10°C/min. The process time started counting at the end of the thermal ramp when the temperature setpoint was reached. After the process was finished, the sample was slowly cooled down to room temperature. Preliminary tests showed that: (1) high temperature ($>$ 250°C) degrade the film to Sb_2S_3 and metallic Sb; (2) short times ($<$ 1h) don't induce any significant recrystallization in the samples; (3) high pressures (> 4 bar) prevent completely the recrystallization.

For these reasons, only the annealing studies at temperatures of 200 and 250°C were further investigated, setting the annealing time to 1h and the pressure to 2 bar.

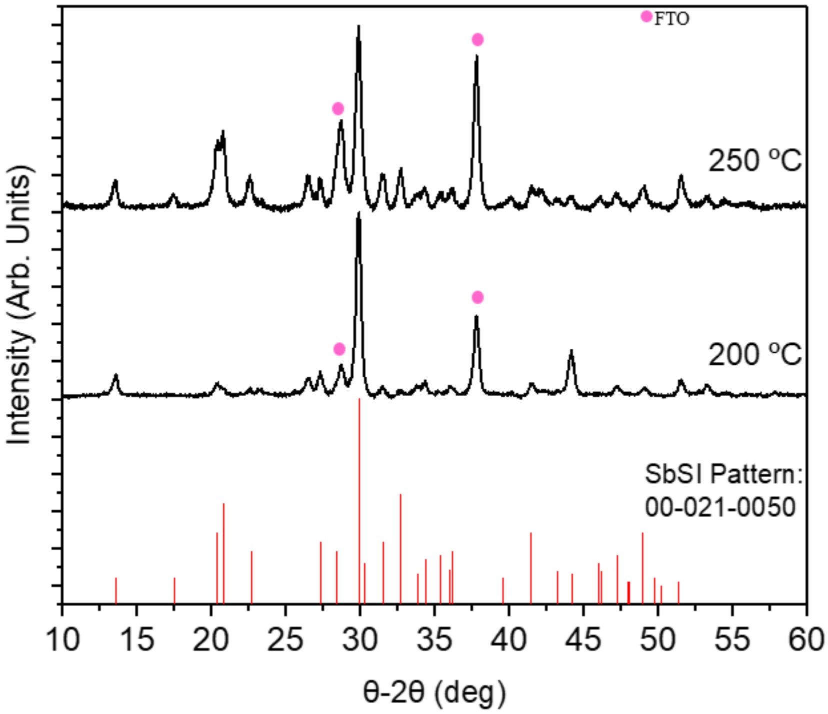

Figure 100: XRD pattern of the (bottom) calculated SbSI phase, (middle) PED SbSI film annealed at 200°C, 2 bar, 1h and (top) PED SbSI film annealed at 250°C, 2 bar, 1h.

XRD analysis on the annealed films showed in both cases a notable recrystallization compared to the initially completely amorphous film and also compared to the results obtained performing the annealing ramp into the PED chamber as described in the previous paragraph. In the case at 200°C, on the other hand, some peaks have a lower intensity than expected from the theoretical pattern, indicating a preferential orientation of the crystallites within the film and no evidence of spurious phase is detected. At higher temperature of treatment, at 250°C, some additional reflections appear compared to the case at 200°C, such as those around 17.5°, 21°, and 43°. Moreover, some reflections appear to have higher relative intensity with respect to expected for a polycristalline sample, for instance the one at 28.4° and 30.3°.

This is confirmed by the SEM analysis in cross-section performed on the samples, reported in Figure 101(a) for the sample at 200°C and in Figure 101(b) for the sample at 250°C.

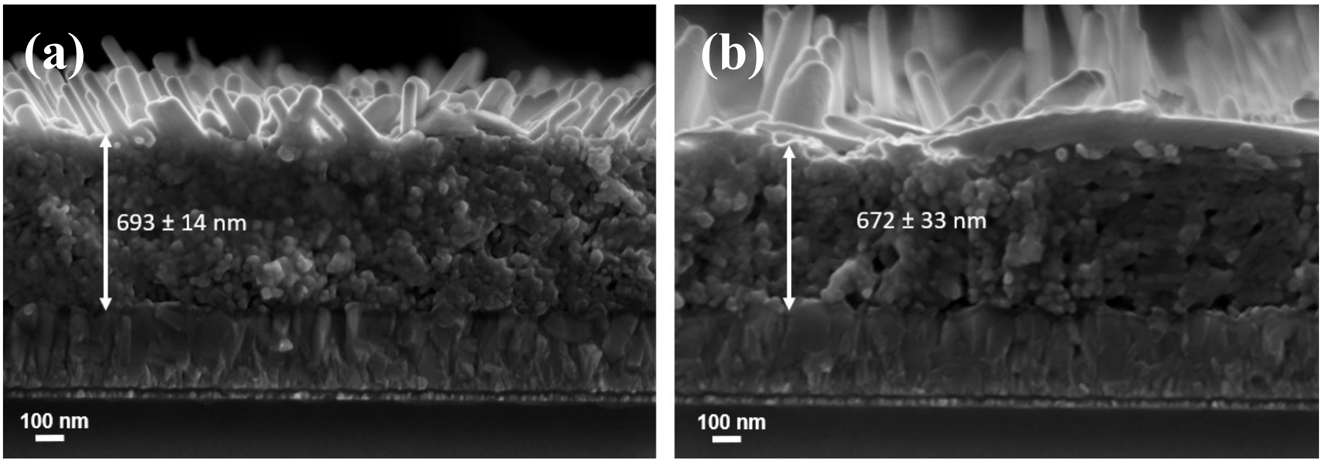

Figure 101: SEM cross-section of (a) PED SbSI film annealed at 200°C, 2 bar, 1h and (b) PED SbSI film annealed at 250°C, 2 bar, 1h.

In both cases, it is evident that there is a mixed amorphous/nanocrystalline layer above which partial recrystallization of the SbSI needles occurs, whose growth orientation is influenced by the temperature and by the Ar gas pressure. At 200°C, the needles grow in a very homogeneous mosaic pattern, more or less of the same length, and with an angle that is on average 45° or thereabouts in one direction or the other relative to the normal. However, at 250°C, they grow either horizontally or at 90° to the surface, which would be suitable for FE-PV applications because the polar axis is precisely along the length of the needle. They are also larger and more heterogeneous in size.

EDX analysis was used to preliminarily investigate the composition of the films, only as a qualitative reference; in fact, excess antimony is always detected, but it cannot be determined whether this is entirely due to the sublimation of sulfur and iodine or to the overlap of the Sb signal with the Sn signal (from the FTO substrate).

Element	(%)
S	30,1 ± 0,8
Sb	40,2 ± 0,9
I	29,7 ± 1,7

Table 13: EDX analysis of the PED film annealed at 250°C, 2 bar, 1h.

Element	Concentration %
S	27,0 ± 0,8
Sb	39,1 ± 3,5
I	33,9 ± 3,3

Table 14: EDX analysis of the PED film annealed at 200°C, 2 bar, 1h.

However, despite the excess of antimony, it is important to note that the S/I ratio for both studied temperatures is close to 1. In the case of the annealed film at 250°C (Table 13), a smaller percentage of iodine is detected with respect to the case studied at 200°C, indicating that it is possibly the first species to be sensitive to the enhancement of the temperature (Table 14). However, further study with different techniques will be needed to investigate the exact composition of the films.

The findings presented in this chapter represent a significant milestone in the development of a functional SbSI FE-PV device prototype, particularly through the collaborative efforts with the research group from the *Universitat Politècnica de Catalunya*. The use of a high-pressure furnace for annealing SbSI films has yielded promising results, addressing critical challenges such as the sublimation of sulfur and iodine and promoting the crystallization of the material with a specific preferential orientation. This has not only advanced the understanding of the material's behavior under different annealing conditions but has also provided valuable insights into optimizing the performance of SbSI-based FE-PV devices.

4 CONCLUSIONS

To foster resilience beyond the solar sector, a comprehensive, economy-wide approach is essential, focusing on areas where Europe and Western Countries can realistically develop their own economic advantages and support firms which are not overly reliant on subsidies. Pursuing China's dominance in the mass-produced, oversupplied silicon technology markets is unlikely to yield success. By diversifying their focus and investing in innovative photovoltaic (PV) technologies and applications (like building/product integrated PV and tandem cells), the dependence on Chinese supply cand be reduced and they can carve out a niche in the global solar market. This strategic shift could not only enhance Europe's competitiveness but also drive significant advancements in the renewable energy sector. In this framework there is substantial scope for new products, materials, and technologies.

In this PhD thesis work, I have conducted an in-depth study on the green, simple and cheap synthesis and deposition of two distinct classes of PV materials, i.e. traditional chalcogenides (Cu In Ga based) and explorative chalcohalides (antimony based) for the production of low-cost and scalable thin film solar cells which can match the overmentioned challenges of PV renovation and readaptation in our contemporaneity.

Specifically, chalcogenides of the series $Cu(In_{1-x}\,Ga_x\,)(S_y\,Se_{1-y}\,)_2$ (CIGSSe) are well-known p-type semiconductors used as absorbers in thin-film solar cells. These materials are perfect because it is possible to reduce the amount of material used, given their high absorption coefficient ($> 10^4\ cm^{-1}$). The great advantage of films made from these copper-based solid solutions is that the optical bandgap, typically direct, can be modulated by varying the cationic ratio In/Ga (x) and the anionic ratio S/Se (y), ranging from 1.04 eV (CISe) to 2.5 eV (CGS). However, they are typically synthesized using costly vacuum techniques, methods that require toxic reagents, and usually non-scalable processes. To address this, a bottom-top process was developed to produce low bandgap chalcogenides, namely $CuInS_2$ and $CuInSe_2$, starting from two innovative and cheap synthesis methods. The aim was to make these materials viable alternatives to silicon in the industrial landscape, reducing manufacturing and production costs, and utilizing high energy ball milling induced mechanochemical reaction as the primary method for synthesis and processing. This approach avoids the use of toxic solvents, making it an environmentally friendly option. Then, the objective was to find the conditions for stabilizing a PV ink which could be deposited with simple liquid-phase techniques on appropriate substrates and then sintered and made usable as a core element of different PV cell technologies. Moreover, a parallel process was developed to modify the high absorption of two high bandgap chalcogenides, $CuInGaS_2$ and $CuGaSSe_2$, such as an absorber in the top cell in tandem with a commercial bottom Si cell where intrinsic semi-transparency of the chalcogenide is needed.

In the case of the two low bandgap chalcogenides, it was demonstrated that MC starting from the binary sulfides and selenides is an effective technique; in particular, these materials require a low-energy mechanochemical regime conducted in agate grinding media. However, the presence of a different chalcogen ion strongly influences the process: while it is possible to work with the same BPR (17) and time (180 min), different rotational speeds are needed for sulfides (650 RPM) and selenides (550 RPM). The products are obtained in pure form and with the expected chalcopyrite structure and the proper stoichiometry; particularly, XRD analysis highlighted the typical characteristics of MC products, such as very broad reflections due to high strain and defects induced to the powders by this technique. By studying the materials as the MC parameters are varied, it emerged that this first step is not sufficient to reduce the particle size and obtain narrow distribution of the grains' dimension, which is fundamental for stabilizing a stable suspension for liquid-phase. The particle size of both compounds is indeed extremely inhomogeneous so that, a liquid-assisted refinement treatment (LAG) was investigated to further reduce the size, to metastabilize a suspension of CIS and CISe ink. The optimization of the refinement parameters allowed to obtain deep black chalcogenides' varnish with different types of organic solvents: however, the most suitable solvent for doctor blade deposition methods resulted to be n-butanol. The deposited layer immediately demonstrated good adhesion to various substrates (mainly FTO and Mo); however, SEM/EDX analysis of these films did not show adequate properties for photovoltaic application, namely a physical discontinuity between a large number of grain boundaries, which is reflected in the very high resistivity ($M\Omega \cdot cm$). Therefore, a specific sintering treatment at high temperature (520°C, 15 min) was studied by placing the sample in a graphite box in a quartz vial with a controlled nitrogen flow and a reactive atmosphere of the corresponding chalcogen element inside the same box. While in the case of CIS it was not possible to obtain a significant effects, in the case of CISe, sublimating 80 mg of Se created a sufficiently reactive atmosphere to cure the defected surfaces, improving the crystallinity and conductivity of the film, but without reaching a level suitable for PV; in fact, recrystallization was confined at the local scale, promoting only the single grain's growth without leading to coalescence between the cured crystallites. The addition of a complexing agent, namely ethanolamine added at 20% in volume during the refinement process, drastically improved these issues. The same selenization treatment allowed the reduction of CISe resistivity to the order of $k\Omega \cdot cm$. Indeed, SEM analysis shows that the selenized films present a layer of nanograins above which there is a layer of about 700 nm completely coalesced and crystalline. The same morphology and resistivity values are typically observed in the literature for the same chalcogenides obtained from solution methods. A photovoltaic cell based on these thin films was fabricated by depositing standard top structures for CISe (i.e. CdS as buffer layer and ZnO+Al:ZnO as windows layer and top contact). The PV performances were tested demonstrated interlocutory results: V_{OC} of 331 mV; J_{SC} of 1.8 mA/cm^2. In particular, very low R_{Sh} are detected indicating the presence of percolative paths for current along the grain boundaries and suggesting that the identified treatment did not adequately enhance crystallinity or reduce electron-hole recombination centers, which are common and limiting phenomena associated with defects. These defects impede current extraction and consequently thus lower the J_{SC}. Overall, the results underscore the potential of this absorber layer but emphasize the necessity for further optimization to improve crystallinity and mitigate recombination mechanisms.

In the case of the high bandgap chalcogenides CIGS and CGSSe, chosen for semitransparent solar cells realizations a high energy ball milling solid state reaction conducted with higher energetic MC conditions using harder mechanical media (i.e. ZrO_2) demonstrated that it is possible to obtain a pure phase of also of these more complex solid solutions. Beside this, by applying a refinement treatment on the products with a high BPR (140) using cyclohexanone as solvent, the final color of the suspension surprisingly changes from black to brown, indicating a modification of the powder structure at the microscale and a significant reduction in the average diameter of the crystallites: the first ever reported brown-CIGS and brown-CGSSe paints were thus obtained, whose optical properties are compatible with the set objective. While the refinement conditions explored allowed for fine control of the particle size of CIGS (with particles not exceeding 500 nm and the paint remaining in suspension for several days), it was not possible to identify the refinement regime suitable for significantly reducing the size of CGSSe particles similarly to the CIGS ones, which naturally tend to re-agglomerate and precipitate within a few hours; therefore it was decided to continue the study only on CIGS. After a centrifuge of the suspension, with the removal of the precipitated material, it was possible to deposit controlled and reproducible layers of approx. 1 µm which showed semi-transparency of over 70% in the spectral region between 750 and 1300 nm, effectively being transparent to the radiation necessary for the operation of a bottom Si cell. However, the film obtained with this method showed high resistivity ($M\Omega \cdot cm$). Through a cold-pressing densification process the layer was significantly compacted and became shinier, but with scarce grain coalescence yet. Under these conditions, the crystallographic phase does not undergo variations, and the optical properties of the films are not deeply modified, while the resistivity is reduced by a factor of 20. A prototype device on a transparent FTO substrate was then assembled with the standard thin film architecture. Although the performance was negligible, the achievement of a working cell based on semi-transparent chalcogenides, considering all the morphological, structural, and physical criticalities described, represents a good starting point to continue the study

As a side activity, our chalcogenides-based inks were preliminarily applied as a hole transport layer (HTL) in carbon-based Formamidinium Lead Iodide (FAPI) hybrid-perovskite solar cells (PSCs) was explored, in collaboration with CHOSE Lab in Rome. The above detailed processes for CISe synthesis and deposition are unsuitable due to solvent incompatibility and high-temperature requirements with respect to the standard PSCs fabrication process. Here the MC powders were directly dried and selenized at the same thermal conditions of the thin films and re-dispersed in a suitable solvent, 2-propanol. Devices were assembled with different solution concentrations and number of deposited layers starting from the readapted CISe ink. Preliminary PV measurements showed that while reference cells show initial larger performances than the ones with CISe as HTL, after just 24 hours their solar cells parameters drop of about 3% while CISe PSCs almost retained their starting efficiencies. Notably, some CISe-based cells outperformed reference cells after aging, suggesting a stabilizing effect on perovskite cells. This preliminary study seems to forecast the potential of CISe to enhance the durability and reliability of PSCs, addressing what is considered the major issue in perovskite technology.

A relevant part of this thesis experimental activity was parallelly focused on the MC synthesis and the deposition of thin film of the antimony chalcohalide, SbSI. Specifically, SbSI is one of the most intriguing members of the ferrophotovoltaics (FE-PV) family, materials characterized by the RT superposition between ferroelectric and semiconductive behavior. This combination theoretically simplifies the architecture of thin-film PV devices, as a single phase intimately acts like a p-n junction and allows photogenerated charge separation due to the presence of a residual polarization field along the polar axis of its crystalline structure. SbSI, composed of abundant and non-critical materials, crystallizes in a stable orthorhombic polar symmetry with a FE-Curie temperature near room temperature (298K). Its good electrical conductivity, high tolerance to substitutional defects, and high saturation polarization (25 $\mu C/cm^2$), along with other interesting optoelectronic properties, make it an ideal candidate for FE-PV devices. Traditionally, SbSI is produced through hydrothermal synthesis, sonochemical methods, and multi-step processes involving liquid or vapor phase reactions of antimony chalcogenide and halide.

The solid-state reaction of the FE-PV compound SbSI was successfully carried out for the first time using mechanochemical synthesis from its constituent elements (Sb, S, and I) in a high-energy planetary ball mill with 10 mm balls and 45 ml ZrO_2 jars. The reaction was optimized for direct production of up to 5 g of material in a single dry milling process conducted in air and without any solvents. The optimal mechanochemical (MC) parameters were identified as 700 rpm primary rotation speed, a Ball-to-Powder Ratio (BPR) of 15, and a process duration of 180 minutes over 6 cycles. The resulting product was a single-phase SbSI with good crystallinity but an inhomogeneous morphology, with grain sizes ranging from hundreds of nanometers to tens of microns. Starting from the MC product, a target of

SbSI with appropriate density, thickness, and crystallinity was produced by optimizing a two-step sintering process: about 4 g of MC-SbSI powder was manually ground and placed in a cylindrical mold, treated at 150 bar for 1 hour; the obtained 3-4 mm thick compact pellet was then subjected to thermal treatment in a quartz vial at 125°C for 16 hours. The physical-morphological and structural characterization revealed a widespread successful sintering of the crystalline grains. This target was then used in the Pulsed Electron Deposition system (PED) as a source material. The optimal growth and stoichiometric transfer conditions of the target onto the substrate by elemental ablation involved a process at room temperature (RT), where the target was not preheated to induce recrystallization. The resulting thin film grew amorphously with thickness of about 700 nm and excellent surface uniformity.

It has been recently activated a collaboration with the Universitat Politècnica de Catalunya, Barcelona, to study recrystallization thermal treatment using a high-pressure furnace set-up with inert gas (Ar) pressures up to 5 bar. The aim was to prevent sulfur and iodine sublimation and aid in material crystallization with a preferential orientation along the polar axis. XRD analysis revealed notable recrystallization at both temperatures, with a preferential orientation of crystallites which is observed for temperature $>$ 200 °C. SEM analysis confirmed these findings, showing a bimodal growth of the crystals with a component lying with the polar axis along the surface and the other orienting the polar axis normal to the surface: especially the latter is likely suitable for FE-PV applications. These results, coming out just at the beginning of this new collaboration, represent a significant milestone which shed hopes in the development of working SbSI FE-PV prototypes.

5 ON MY PHD SCIENTIFIC PRODUCTION

The work on chalcogenides presented in this thesis was carried out within the framework of the industrial project named “Fourier”, which is a RdS (Ricerca di Sistema) Type B project funded by the Italian Government CSEA/MITE; the industrial partner required to exploit the scientific results of this research by creating a patent within the end of this year (2024), which covers all the processing of the syntheses and ink production presented along the thesis. Consequently, despite the significant amount of innovative results, it has not yet been possible to publish any scientific articles on this subject and this is the reason why this thesis will be embargoed for 1 year.

However, leveraging the skills I developed during my traineeship, I contributed to the realization of two scientific publications outside the research topic of this thesis, one of which as the first author, as evidenced in this chapter.

5.1 High-Pressure Bulk Synthesis of InN by Solid-State Reaction of Binary Oxide in a Multi-Anvil Apparatus

Authors: *Elena Del Canale, Lorenzo Fornari, Chiara Coppi, Giulia Spaggiari, Francesco Mezzadri, Giovanna Trevisi, Patrizia Ferro, Edmondo Gilioli, Massimo Mazzer, Davide Delmonte*

DOI: https://doi.org/10.1021/acs.inorgchem.3c00231

Abstract: We present a new method to synthesize bulk indium nitride by means of a simple solid-state chemical reaction carried out under hydrostatic high-pressure/high-temperature conditions in a multi-anvil apparatus, not involving gases or solvents during the process. The reaction occurs between the binary oxide In_2O_3 and the highly reactive Li_3N as the nitrogen source, in the powder form. The formation of the hexagonal phase of InN, occurring at 350 °C and $P \geq 3$ GPa, was successfully confirmed by powder X-ray diffraction, with the presence of Li_2O as a unique byproduct. A simple washing process in weak acidic solution followed by centrifugation allowed us to obtain pure InN polycrystalline powders as a precipitate. With an analogous procedure, it was possible to obtain pure bulk GaN, from Ga_2O_3 and Li_3N at T ≥ 600 °C and $P \geq 2.5$ GPa. These results point out, particularly for InN, a clean, and innovative way to produce significant quantities of one of the most promising nitrides in the field of electronics and energy technologies.

My contribution: In this paper, where I was the first author and corresponding author, I was responsible for drafting and writing the article and managing the correspondence, coordinating the other authors, and handling the corrections and review of the work. Moreover, I contributed by studying the solid-state synthesis via high energy ball milling of gallium nitride and indium nitride, which was used as a preliminary study for investigating the high-pressure synthesis of these materials.

5.2 Cu-Doped Sb_2Se_3 Thin-Film Solar Cells Based on Hybrid Pulsed Electron Deposition/Radio Frequency Magnetron Sputtering Growth Techniques

Authors: *Roberto Jakomin, Stefano Rampino, Giulia Spaggiari, Michele Casappa, Giovanna Trevisi, Elena Del Canale, Enos Gombia, Matteo Bronzoni, Kodjo Kekeli Sossoe, Francesco Mezzadri, Francesco Pattini*

DOI: https://doi.org/10.3390/solar4010004

Abstract: In recent years, research attention has increasingly focused on thin-film photovoltaics utilizing Sb_2Se_3 as an ideal absorber layer. This compound is favored due to its abundance, non-toxic nature, long-term stability, and the potential to employ various cost-effective and scalable vapor deposition (PVD) routes. On the other hand, improving passivation, surface treatment and p-type carrier concentration is essential for developing high-performance and commercially viable Sb_2Se_3 solar cells. In this study, Cu-doped Sb_2Se_3 solar devices were fabricated using two distinct PVD techniques, pulsed electron

deposition (PED) and radio frequency magnetron sputtering (RFMS). Furthermore, 5%Cu:Sb_2Se_3 films grown via PED exhibited high open-circuit voltages (V_{OC}) of around 400 mV but very low short-circuit current densities (J_{SC}). Conversely, RFMS-grown Sb_2Se_3 films resulted in low V_{OC} values of around 300 mV and higher J_{SC}. To enhance the photocurrent, we employed strategies involving a thin NaF layer to introduce controlled local doping at the back interface and a bilayer p-doped region grown sequentially using PED and RFMS. The optimized Sb_2Se_3 bilayer solar cell achieved a maximum efficiency of 5.25%.

My contribution: In this paper I contributed by performing and optimizing the deposition of all the cadmium sulfide buffer layers onto the Sb_2Se_3 absorbers, grown by PED technique, which are key constituents of the final architecture of these thin films solar cells.

6 REFERENCES

[1] © European Union 2023, European Commission, Joint Research Centre (JRC), EDGAR (Emissions Database for Global Atmospheric Research) Community GHG database, comprising IEA-EDGAR CO_2, EDGAR CH_4, EDGAR N_2O and EDGAR F-gases version 8.0 (2023)

[2] IPCC, 2022: Summary for Policymakers [H.-O. Pörtner, D.C. Roberts, E.S. Poloczanska, K. Mintenbeck, M. Tignor, A. Alegría, M. Craig, S. Langsdorf, S. Löschke, V. Möller, A. Okem (eds.)]. In: *Climate Change 2022: Impacts, Adaptation, and Vulnerability.* Contribution of Working Group II to the Sixth Assessment Report of the Intergovernmental Panel on Climate Change [H.-O. Pörtner, D.C. Roberts, M. Tignor, E.S. Poloczanska, K. Mintenbeck, A. Alegría, M. Craig, S. Langsdorf, S. Löschke, V. Möller, A. Okem, B. Rama (eds.)]. Cambridge University Press, Cambridge, UK and New York, NY, USA, pp. 3-33

[3] *Global Warming of 1.5°C. An IPCC Special Report on the impacts of global warming of 1.5°C above preindustrial levels and related global greenhouse gas emission pathways, in the context of strengthening the global response to the threat of climate change, sustainable development, and efforts to eradicate poverty* [Masson-Delmotte, V., P. Zhai, H.-O. Pörtner, D. Roberts, J. Skea, P.R. Shukla, A. Pirani, W. Moufouma-Okia, C. Péan, R. Pidcock, S. Connors, J.B.R. Matthews, Y. Chen, X. Zhou, M.I. Gomis, E. Lonnoy, T. Maycock, M. Tignor, and T. Waterfield (eds.)]. Cambridge University Press, Cambridge, UK and New York, NY, USA, pp. 3-24

[4] © Energy Institute - Statistical Review of World Energy 2024

[5] SolarPower Europe (2023): Global Market Outlook for Solar Power 2023-2027

[6] Wood Mackenzie | Data & analytics solutions: https://www.woodmac.com/

[7] Source: IRENA (2024), Renewable Capacity Statistics 2024, The International Renewable Energy Agency, Abu Dhabi.

[8] China Photovoltaic Industry Association: http://www.chinapv.org.cn/index.html

---

[9] © 2024 | Climate Energy Finance, https://climateenergyfinance.org/wp-content/uploads/2024/08/MONTHLY-CHINA-ENERGY-UPDATE-_-China-Reached-2030-Energy-Targets-6-Years-Ahead-of-Time-while-Slowing-Down-New-Coal-Power-Permits.pdf

[10] Fraunhofer Institute for Solar Energy Systems ISE, Photovoltaics Report 2024, https://www.ise.fraunhofer.de/content/dam/ise/de/documents/publications/studies/Photovoltaics-Report.pdf

[11] i Cabarrocas, P. Roca. "Plasma enhanced chemical vapor deposition of amorphous, polymorphous and microcrystalline silicon films." *Journal of non-crystalline solids* 266 (2000): 31-37

[12] Rubaiee, S., & Fazal, M. A. (2022). The Influence of Various Solar Radiations on the Efficiency of a Photovoltaic Solar Module Integrated with a Passive Cooling System. *Energies*, *15*(24), 9584

[13] https://www.firstsolar.com/en/Technology/CadTel

[14] https://iallpowers.eu/products/allpowers-sf100-flexible-solar-panel-100w

[15] Hoppe, Harald, and Niyazi Serdar Sariciftci. "Organic solar cells: An overview." *Journal of materials research* 19.7 (2004): 1924-1945

[16] Li, Yang, et al. "A review on morphology engineering for highly efficient and stable hybrid perovskite solar cells." Journal of Materials Chemistry A 6.27 (2018): 12842-12875

[17] Yamaguchi, Masafumi, et al. "Multi-junction III–V solar cells: current status and future potential." *Solar Energy* 79.1 (2005): 78-85

[18] https://www.nrel.gov/pv/interactive-cell-efficiency.html

[19] https://www.spectrolab.com/support.html#datasheets

[20] Chichibu, S., et al. "Band gap energies of bulk, thin-film, and epitaxial layers of $CuInSe_2$ and $CuGaSe_2$." *Journal of Applied Physics* 83.7 (1998): 3678-3689

[21] Krunks, Malle, et al. "Structural and optical properties of sprayed $CuInS_2$ films." Thin solid films 338.1-2 (1999): 125-130

---

[22] Siebentritt, Susanne. "Wide gap chalcopyrites: material properties and solar cells." *Thin Solid Films* 403 (2002): 1-8

[23] Delmonte, Davide, et al. "Metastable (CuAu-type) CuInS$_2$ phase: high-pressure synthesis and structure determination." *Inorganic Chemistry* 59.16 (2020): 11670-11675

[24] Stanbery, Billy J.. (2002). *Copper Indium Selenides and Related Materials for Photovoltaic Devices., 27(2), 73–117*

[25] Kodigala, Subba Ramaiah. *Cu(In$_{1-x}$Ga$_x$)Se$_2$ Based thin film solar cells.* Academic Press, 2011

[26] Coutts, T. J., & Osterwald, C. R. (1987). The quantum efficiency of CdS/CuIne solar cells. *Solar cells*, *22*(3), 195-209

[27] J.A.M. AbuShama, S. Johnston, T. Moriarty, G. Teeter, K. Ramanathan, R. Noufl, Prog. Photovolt. Res. Appl.12 (1) (2004) 39-45

[28] K. Rui, Y. Takeshi, A. Shunsuke, H. Atsushi, F.T. Kong, K. Takuya, S. Hiroki, in: Proceedings of the 2016 IEEE43th Photovolt. Spec. Conference PVSC 2016 Portland(OR) USA, June 2016., pp. 3-7, 2016

[29] S. Ishizuka, A. Yamada, P.J. Fons, H. Shibata, S. Niki, Appl. Phys.Lett. 103 (14) (2013) 3(8)

[30] K. Siemer, J. Klaer, I. Luck, J. Bruns, R. Klenk, D. Braunig, Sol. Energy Mater. Sol. Cells 67 (1-4) (2001), 159-166

[31] H. Hiroi, Y. Iwata, S. Adachi, H. Sugimoto, A. Yamada, New World Record Effciency for Pure Sulfide Cu (In,Ga) S2 Thin-Film Solar Cell With Cd-Free Buffer Layer via KCN-Free Process, pp. 1-4, 2016

[32] K. Tanaka, K. Ishii, S. Matsuda, Y. Hasegawa, K. Sato, Jpn. J. Appl. Phys. 28 (1) (1989) 12-15

[33] Wada, Takahiro, Satoshi Nakamura, and Tsuyoshi Maeda. "Ternary and multinary Cu-chalcogenide photovoltaic materials from CuInSe$_2$ to Cu$_2$ZnSnS$_4$ and other compounds." *Progress in Photovoltaics: Research and Applications* 20.5 (2012): 520-525

[34] Wada, Takahiro. "CuInSe$_2$ and related I–III–VI2 chalcopyrite compounds for photovoltaic application." *Japanese Journal of Applied Physics* 60.8 (2021): 080101

---

[35] Suresh, Sunil, et al. "Extrinsic Doping of Ink-Based Cu(In, Ga)(S, Se)2-Absorbers for Photovoltaic Applications." *Advanced Energy Materials* 12.18 (2022): 2103961

[36] Huang, C. H., Chuang, W. J., Lin, C. P., Jan, Y. L., & Shih, Y. C. (2018). Deposition technologies of high-efficiency CIGS solar cells: development of two-step and co-evaporation processes. *Crystals*, *8*(7), 296

[37] Jung, S., Ahn, S., Yun, J. H., Gwak, J., Kim, D., & Yoon, K. (2010). Effects of Ga contents on properties of CIGS thin films and solar cells fabricated by co-evaporation technique. *Current Applied Physics*, *10*(4), 990-996

[38] Wang, H., Zhang, Y., Kou, X. L., Cai, Y. A., Liu, W., Yu, T., ... & Sun, Y. (2010). Effect of substrate temperature on the structural and electrical properties of CIGS films based on the one-stage co-evaporation process. *Semiconductor science and technology*, *25*(5), 055007

[39] Park, S. U., Sharma, R., Ashok, K., Kang, S., Sim, J. K., & Lee, C. R. (2012). A study on composition, structure and optical properties of copper-poor CIGS thin film deposited by sequential sputtering of CuGa/In and In/(CuGa+ In) precursors. *Journal of Crystal Growth*, *359*, 1-10

[40] Kang, S., Sharma, R., Sim, J. K., & Lee, C. R. (2013). Band gap engineering of tandem structured CIGS compound absorption layer fabricated by sputtering and selenization. *Journal of alloys and compounds*, *563*, 207-215

[41] Nakada, T., & Kunioka, A. (1998). Sequential sputtering/selenization technique for the growth of CuInSe2 thin films. *Japanese journal of applied physics*, *37*(9A), L1065

[42] Nicolaou, C., Zacharia, A., Delimitis, A., Itskos, G., & Giapintzakis, J. (2020). Single-step growth of high quality CIGS/CdS heterojunctions using pulsed laser deposition. *Applied Surface Science*, *511*, 145547

[43] Chen, C. C., Qi, X., Chang, W. C., Tsai, M. G., Chen, I. G., Lin, C. Y.,& Chang, K. P. (2015). The effects of pulse repetition rate on the structural, optical, and electrical properties of CIGS films grown by pulsed laser deposition. *Applied Surface Science*, *351*, 772-778

[44] Chen, S. C., Hsieh, D. H., Jiang, H., Liao, Y. K., Lai, F. I., Chen, C. H., ... & Kuo, H. C. (2014). Growth and characterization of Cu (In, Ga) Se 2 thin films by nanosecond and femtosecond pulsed laser deposition. *Nanoscale research letters*, *9*, 1-7

---

[45] Rampino, S., Bissoli, F., Gilioli, E., & Pattini, F. (2013). Growth of Cu (In, Ga) Se2 thin films by a novel single-stage route based on pulsed electron deposition. *Progress in Photovoltaics: Research and Applications*, *21*(4), 588-594

[46] Bronzoni, M., Stefancich, M., & Rampino, S. (2012). Role of substrate temperature on the structural, morphological and optical properties of CuGaSe2 thin films grown by Pulsed Electron Deposition technique. *Thin Solid Films*, *520*(24), 7054-7061

[47] Delmonte, D., Manfredi, R., Calestani, D., Mezzadri, F., Righi, L., Mazzer, M., ... & Gilioli, E. (2020). An affordable method to produce CuInS2 ‘mechano-targets’ for film deposition. *Semiconductor Science and Technology*, *35*(4), 045026

[48] Neendoor Mohan, R. (2016). Mechanochemical synthesis of Cu (In, Ga) Se2: Deposition, selenization and characterization of films. Síntesis mecanoquímica de Cu (In, Ga) Se2: Depósito, selenización y caracterización de películas.

[49] Ramanujam, J., & Singh, U. P. (2017). Copper indium gallium selenide based solar cells–a review. *Energy & Environmental Science*, *10*(6), 1306-1319

[50] Suresh, S., & Uhl, A. R. (2021). Present status of solution-processing routes for Cu (In, Ga)(S, Se) 2 solar cell absorbers. *Advanced Energy Materials*, *11*(14), 2003743

[51] Mitzi, D. B., Yuan, M., Liu, W., Kellock, A. J., Chey, S. J., Gignac, L., & Schrott, A. G. (2009). Hydrazine-based deposition route for device-quality CIGS films. *Thin Solid Films*, *517*(7), 2158-2162

[52] Aguiar, I., Mombrú, M., Barthaburu, M. P., Pereira, H. B., & Fornaro, L. (2016). Influence of solvothermal synthesis conditions in BiSI nanostructures for application in ionizing radiation detectors. *Materials Research Express*, *3*(2), 025012

[53] Song, L., Zhang, S., & Wei, Q. (2012). Porous BiOI sonocatalysts: hydrothermal synthesis, characterization, sonocatalytic, and kinetic properties. *Industrial & engineering chemistry research*, *51*(3), 1193-1197

[54] Kijima, N., Matano, K., Saito, M., Oikawa, T., Konishi, T., Yasuda, H., ... & Yoshimura, Y. (2001). Oxidative catalytic cracking of n-butane to lower alkenes over layered BiOCl catalyst. *Applied Catalysis A: General*, *206*(2), 237-244

---

[55] Li, X. H., Shi, Z. H., Yang, M., Liu, W., & Guo, S. P. (2022). Sn7Br10S2: The First Ternary Halogen-Rich Chalcohalide Exhibiting a Chiral Structure and Pronounced Nonlinear Optical Properties. *Angewandte Chemie*, *134*(9), e202115871

[56] Fong, C. Y., & Wooten, F. Experimental and Theoretical Study of the Feasibility of the Gunn Effect in BiSCl. *BiSBr, BiSI, BiSeI, BiSeBr and BiSeC (Dept of Applied Science, California University, Davis, 1981)*

[57] Audzijonis, A., Sereika, R., & Žaltauskas, R. (2008). Antiferroelectric phase transition in SbSI and SbSeI crystals. *Solid state communications*, *147*(3-4), 88-89

[58] Fatuzzo, E., Harbeke, G., Merz, W. J., Nitsche, R., Roetschi, H., & Ruppel, W. (1962). Ferroelectricity in SbSI. *Physical review*, *127*(6), 2036

[59] Grigas, J., Microwave Dielectric Spectroscopy of Ferroelectrics and related Materials, (Gordon and Breach Publ. Inc. Amsterdam, 1996), p. 336

[60] Audzijonis, A., Grigas, J., Kajokas, A., Kvedaravičius, S., & Paulikas, V. (1998). Origin of ferroelectricity in SbSI. *Ferroelectrics*, *219*(1), 37–45.

[61] Nie, R., Yun, H. S., Paik, M. J., Mehta, A., Park, B. W., Choi, Y. C., & Seok, S. I. (2018). Efficient solar cells based on light-harvesting antimony sulfoiodide. *Advanced Energy Materials*, *8*(7), 1701901

[62] Chen, G., Li, W., Yu, Y., & Yang, Q. (2015). Fast and low-temperature synthesis of one-dimensional (1D) single-crystalline SbSI microrod for high performance photodetector. *RSC Advances*, *5*(28), 21859-21864

[63] Varghese, J., Whatmore, R. W., & Holmes, J. D. (2013). Ferroelectric nanoparticles, wires and tubes: synthesis, characterisation and applications. *Journal of Materials Chemistry C*, *1*(15), 2618-2638

[64] Han, X., Ji, Y., & Yang, Y. (2022). Ferroelectric photovoltaic materials and devices. *Advanced Functional Materials*, *32*(14), 2109625

[65] Fatuzzo, E., Harbeke, G., Merz, W. J., Nitsche, R., Roetschi, H., & Ruppel, W. (1962). Ferroelectricity in SbSI. *Physical review*, *127*(6), 2036

[66] Wang, Y., Hu, Y., Chen, Z., Guo, Y., Wang, D., Wertz, E. A., & Shi, J. (2018). Effect of strain on the Curie temperature and band structure of low-dimensional SbSI. *Applied Physics Letters*, *112*(18)

---

[67] Mistewicz, Krystian, Marian Nowak, and Danuta Stróż. "A ferroelectric-photovoltaic effect in SbSI nanowires." Nanomaterials 9.4 (2019): 580

[68] R. Kern, J. Phys. Chem. Solids 1962, 23, 249

[69] A. Ibanez, J. C. Jumas, J. O. Fourcade, E. Philippot, M. Maurin, J. Solid State Chem. 1983, 48, 272

[70] C. R. Wang, K. B. Tang, Q. Yang, B. Hai, G. Z. Shen, C. H. An, W. C. Yu, Y. T. Qian, Inorg. Chem. Commun. 2001, 4, 339

[71] Dubey, Harish K., et al. "A study of the electrical properties of SbSI synthesized using CVD techniques." QScience Connect 2013.1 (2013): 40

[72] Szperlich, Piotr, et al. "Growth of large SbSI crystals." Materials Science-Poland 32.4 (2014): 669-675

[73] Dong-Kyun Seo, Roald Hoffmann,“Direct and indirect band gap types in onedimensional conjugatedor stacked organic materials”, Theor Chem Acc (1999)

[74] 7. Goetzberger, A., Hoffmann, V.U., 2005. Photovoltaic Solar Energy Generation. Berlin-Heidelberg: Springer

[75] Kitai, A., 2011. Principles of Solar Cells, LEDs and Diodes. The Role of the PN Junction. Chichester: John Wiley Sons

[76] Handbook of Photovoltaic Science and Engineering, edited by A. Luque and S. Hegedus Wiley, West Sussex, 200

[77] William Shockley and Hans J. Queisser, Journal of Applied Physics 32, 510-519 (1961)

[78] A. Parisi, R. Pernice, A. C. Busacca, ”Graded Carrier Concentration Absorber Profile for High Efficiency CIGS Solar Cells”, International Journal of Photoenergy, vol. 2015, Article ID 410549, 9 pages, 2015. https://doi.org/10.1155/2015/410549

[79] Li, Z., Yu-Ming, X., Chuan-Ming, X., Qing, H., Fang, L. F., Chang-Jian, L., & Yun, S. (2012). Microstructural characterization of Cu-poor Cu (In, Ga) Se2 surface layer. *Thin Solid Films*, *520*(7), 2873-2877

---

[80] Rampino, S., Armani, N., Bissoli, F., Bronzoni, M., Calestani, D., Calicchio, M., ... & Mazzer, M. (2012). 15% efficient Cu (In, Ga) Se2 solar cells obtained by low-temperature pulsed electron deposition. *Applied Physics Letters*, *101*(13)

[81] Touafek, N., & Mahamdi, R. (2014). Excess defects at the CdS/CIGS interface solar cells. *Chalcogenide Letters*, *11*(11), 589-596

[82] Yastrebova, N. V. (2007). High-efficiency multi-junction solar cells: Current status and future potential. *Centre for Research in Photonics, University of Ottawa*, 17

[83] cessed at http://www.ise.fraunhofer.de/en/press-and-media/ press-releases/pressreleases-2014/new-world-recordfor-solarcell-efficiencyat-46-percent on 7 December 2014, 201

[84] Green, M.A., 2001. Third Generation Photovoltaics: Ultra-high Conversion Efficiency at Low Cost. Prog. Photovolt: Res. Appl., 9, 123–135

[85] Semonin, O. E., Luther, J. M., & Beard, M. C. (2012). Quantum dots for next-generation photovoltaics. *Materials today*, *15*(11), 508-515

[86] E. D. Jackson, "Areas for improvement of the semiconductor solar energy converter," in Trans. Intern. Con$ Use of Solar Energy--The Scientific Basis, vol. V, p. 122, 1955

[87] Todorov, T., Gunawan, O., & Guha, S. (2016). A road towards 25% efficiency and beyond: perovskite tandem solar cells. *Molecular Systems Design & Engineering*, *1*(4), 370-376

[88] Werner, J., Weng, C. H., Walter, A., Fesquet, L., Seif, J. P., De Wolf, S., ... & Ballif, C. (2016). Efficient monolithic perovskite/silicon tandem solar cell with cell area> 1 cm2. *The journal of physical chemistry letters*, *7*(1), 161-166

[89] Tress, W. (2017). Perovskite solar cells on the way to their radiative efficiency limit–insights into a success story of high open-circuit voltage and low recombination. *Advanced Energy Materials*, *7*(14), 1602358

[90] Salim, K. M., Masi, S., Gualdrón-Reyes, A. F., Sánchez, R. S., Barea, E. M., Kreĉmarová, M., ... & Mora-Seró, I. (2021). Boosting long-term stability of pure formamidinium perovskite solar cells by ambient air additive assisted fabrication. *ACS Energy Letters*, *6*(10), 3511-3521

---

[91] Gok, E. C., Yildirim, M. O., Haris, M. P., Eren, E., Pegu, M., Hemasiri, N. H., ... & Ahmad, S. (2022). Predicting perovskite bandgap and solar cell performance with machine learning. *Solar RRL*, *6*(2), 2100927

[92] Jiang, CS., Yang, M., Zhou, Y. *et al.* Carrier separation and transport in perovskite solar cells studied by nanometre-scale profiling of electrical potential. *Nat Commun* 6, 8397 (2015).

[93] Gonzalez-Pedro, V., Juarez-Perez, E. J., Arsyad, W. S., Barea, E. M., Fabregat-Santiago, F., Mora-Sero, I., & Bisquert, J. (2014). General working principles of CH3NH3PbX3 perovskite solar cells. *Nano letters*, *14*(2), 888-893.

[94] Ren, G., Han, W., Deng, Y., Wu, W., Li, Z., Guo, J., ... & Guo, W. (2021). Strategies of modifying spiro-OMeTAD materials for perovskite solar cells: a review. *Journal of Materials Chemistry A*, *9*(8), 4589-4625

[95] Lin, F., Luo, J., Zhang, Y., Zhu, J., Malik, H. A., Wan, Z., & Jia, C. (2023). Perovskite solar cells: Li–TFSI and t-BP-based chemical dopant engineering in spiro-OMeTAD. *Journal of Materials Chemistry A*, *11*(6), 2544-2567

[96] Xu, L., Deng, L. L., Cao, J., Wang, X., Chen, W. Y., & Jiang, Z. (2017). Solution-processed Cu (In, Ga)(S, Se) 2 nanocrystal as inorganic hole-transporting material for efficient and stable perovskite solar cells. *Nanoscale research letters*, *12*, 1-8

[97] Lv M, Zhu J, Huang Y, Li Y, Shao Z, Xu Y, Dai S (2015) Colloidal CuInS2 quantum dots as inorganic hole-transporting material in perovskite solar cells. ACS Appl Mater Interfaces 7:17482–17488

[98] Lopez-Varo, P., Bertoluzzi, L., Bisquert, J., Alexe, M., Coll, M., Huang, J., ... & Yuan, Y. (2016). Physical aspects of ferroelectric semiconductors for photovoltaic solar energy conversion. *Physics Reports*, *653*, 1-40

[99] Liu, H., Chen, J., Ren, Y., Zhang, L., Pan, Z., Fan, L., & Xing, X. (2015). Large Photovoltage and Controllable Photovoltaic Effect in PbTiO3-Bi (Ni2/3+ xNb1/3–x) O3–δ Ferroelectrics. *Advanced Electronic Materials*, *1*(4), 1400051

[100] Bai, Z., Zhang, Y., Guo, H., & Jiang, A. (2017). The Influence of Conductive Nanodomain Walls on the Photovoltaic Effect of BiFeO3 Thin Films. *Crystals*, *7*(3), 81

---

[101] He, H., He, Z., Jiang, Z., Wang, J., Liu, T., & Wang, N. (2017). A controllable photoresponse and photovoltaic performance in Bi4Ti3O12 ferroelectric thin films. *Journal of Alloys and Compounds*, *694*, 998-1003

[102] Kooriyattil, S., Katiyar, R. K., Pavunny, S. P., Morell, G., & Katiyar, R. S. (2014). Photovoltaic properties of Aurivillius phase Bi5FeTi3O15 thin films grown by pulsed laser deposition. *Applied Physics Letters*, *105*(7)

[103] Jalaja, M. A., & Dutta, S. (2015). Ferroelectrics and multiferroics for next generation photovoltaics. *Adv. Mater. Lett*, *6*(7), 568-584

[104] Mistewicz, K., Nowak, M., & Stróż, D. (2019). A ferroelectric-photovoltaic effect in SbSI nanowires. *Nanomaterials*, *9*(4), 580

[105] Yuan, Y., Xiao, Z., Yang, B., & Huang, J. (2014). Arising applications of ferroelectric materials in photovoltaic devices. *Journal of Materials chemistry A*, *2*(17), 6027-6041

[106] Bowden, F. and Yo_e, A. Initiation and Growth of Explosion in Liquids and Solids, 1952,104

[107] S. L. James, C. J. Adams, D.C. Waddel Chem. Soc. Rev, 41(2012),415

[108] Thiessen, K.P. Physikalische Chemie,260,(1979),403-409

[109] P. A. Thiessen, K. Meyer and G. Heinicke, Grundlagen der Tribochemie, Akademie-Verlag, Berlin, 1967

[110] Baláž, P., Achimovičová, M., Baláž, M., Billik, P., Cherkezova-Zheleva, Z., Criado, J. M., ... & Wieczorek-Ciurowa, K. (2013). Hallmarks of mechanochemistry: from nanoparticles to technology. *Chemical Society Reviews*, *42*(18), 7571-7637

[111] Avvakumov, E., Senna, M., & Kosova, N. (2001). Some theoretical aspects of mechanochemical reactions. *Soft Mechanochemical Synthesis: A Basics for New Chemical Technologies*, 39-58

[112] Lyakhov, N. Z. Proceedings of the Ist International Conference on Mechanochemistry Cambridge Interscience Publishing, Cambridge,1,(1993),59-65

[113] Scriven, L. E. (1988). Physics and applications of dip coating and spin coating. *MRS Online Proceedings Library*, *121*(1), 717-729

---

[114] Vig, J. R. (1985). UV/ozone cleaning of surfaces. *Journal of Vacuum Science & Technology A: Vacuum, Surfaces, and Films*, *3*(3), 1027-1034

[115] Contreras, M. A., Romero, M. J., To, B., Hasoon, F., Noufi, R., Ward, S., & Ramanathan, K. (2002). Optimization of CBD CdS process in high-efficiency Cu (In, Ga) Se2-based solar cells. *Thin Solid Films*, *403*, 204-211

[116] https://www.crystalimpact.com/match/

[117] Li Yang and Bjorn Kruse, "Revised Kubelka{Munk theory. I. Theory and application," J. Opt. Soc. Am. A 21, 1933-1941 (2004)

[118] M. Bar, W. Bohne, Ch.-H. Fischer, Hahn-Meitner-Institut Berlin, Glienicker Strasse 100, 14109 Berlin, Germany T. P. Niesen and F. Karg Shell Solar GmbH, Otto-Hahn-Ring 6, 81739 Munich, Germany, J. Appl. Phys. 96, 3857-3860 (2004)

[119]https://www.fritsch-italy.it/preparazione-dei-campioni/macinazione/mulini-planetari/details/product/pulverisette-7-premium-line/accessories/

[120] Arnaud Gerthoffer, Christophe Poulain, Frederic Roux, Fabrice Emieux, Louis Grenet, Simon Perraud, CIGS solar cells on ultra-thin glass substrates: Determination of mechanical properties by nanoindentation and application to bending-induced strain calculation, Solar Energy Materials and Solar Cells, Volume 166, 2017, Pages 254-261, ISSN 0927-0248

[121] M. Ben Rabeh, M. Kanzari, B. Rezig, Role of oxygen in enhancing N-type conductivity of CuInS2 thin films, Thin Solid Films, Volume 515, Issue 15, 2007, Pages 5943-5948, ISSN 0040-6090

[122] Bekaert, J., Saniz, R., Partoens, B., & Lamoen, D. (2015). First-principles study of carbon impurities in CuInSe2 and CuGaSe2, present in non-vacuum synthesis methods. *Journal of Applied Physics*, *117*(1)

[123] Rehg, T. J., & Higgins, G. (1992). Spin coating of colloidal suspensions. *AIChE journal*, *38*(4), 489-501

[124] Pichumani, M., Bagheri, P., Poduska, K. M., González-Viñas, W., & Yethiraj, A. (2013). Dynamics, crystallization and structures in colloid spin coating. *Soft Matter*, *9*(12), 3220-3229

[125] https://www.ossila.com/pages/spin-coating

[126] Onyia, A. I., Ikeri, H. I., & Chima, A. I. (2020). Surface and quantum effects in nanosized semiconductor. *American Journal of Nano Research and Applications*, *8*(3), 35-41

[127] Cherrington, R., & Liang, J. (2016). Materials and deposition processes for multifunctionality. *Design and Manufacture of Plastic Components for Multifunctionality: Structural Composites, Injection Molding, and 3D Printing*, 19-21

[128] C. Eberspacher, K. Pauls and J. Serra, "Non-vacuum processing of CIGS solar cells," *Conference Record of the Twenty-Ninth IEEE Photovoltaic Specialists Conference, 2002.*, New Orleans, LA, USA, 2002, pp. 684-687

[129] Kapur, V.K., Basol, B.M., TSENG, E.S., 1987. Low-cost methods for the production of semiconductor-films for CuInSe2/CdS solar cells. Solar Cells 21, 65–72

[130] Zaghi, A. E., Buffière, M., Koo, J., Brammertz, G., Batuk, M., Verbist, C., ... & Vleugels, J. (2015). Effect of selenium content of CuInSex alloy nanopowder precursors on recrystallization of printed CuInSe2 absorber layers during selenization heat treatment. *Thin solid films*, *582*, 11-17

[131] Guillen, C., & Herrero, J. (1996). Improved selenization procedure to obtain CulnSe2 thin films from sequentially electrodeposited precursors. *Journal of The Electrochemical Society*, *143*(2), 493

[132] Kim, B., & Min, B. K. (2018). Strategies toward highly efficient CIGSe thin-film solar cells fabricated by sequential process. *Sustainable Energy & Fuels*, *2*(8), 1671-1685

[133] Wu, Y. C., Yang, C. T., Sun, M., & Hsiang, H. I. (2019). Gas-pressure assisted sintering of copper indium gallium selenide thin films. *Journal of the American Ceramic Society*, *102*(4), 1548-1552

[134] Kaelin, M., Rudmann, D., Kurdesau, F., Meyer, T., Zogg, H., & Tiwari, A. N. (2003). CIS and CIGS layers from selenized nanoparticle precursors. *Thin Solid Films*, *431*, 58-62

[135] Colombara, D., Elanzeery, H., Nicoara, N., Sharma, D., Claro, M., Schwarz, T., ... & Siebentritt, S. (2020). Chemical instability at chalcogenide surfaces impacts chalcopyrite devices well beyond the surface. *Nature communications*, *11*(1), 3634

[136] Berner, U. M. (2015). Formation of Cu (In, Ga) Se2 from solution processed sodium containing metal precursors

---

[137] Caballero, R., & Guillen, C. (2005). CuInSe2 Formation by selenization of sequentially evaporated metallic layers. *Solar Energy Materials and Solar Cells*, *86*(1), 1-10

[138] Park, Sang-Wook, et al. "Solid-state selenization of printed Cu (In, Ga) S2 nanocrystal layer and its impact on solar cell performance." Solar energy materials and solar cells 125 (2014): 66-71

[139] Buffière, M., Mel, A. A. E., Lenaers, N., Brammertz, G., Zaghi, A. E., Meuris, M., & Poortmans, J. (2015). Surface cleaning and passivation using (NH4) 2S treatment for Cu (In, Ga) Se2 solar cells: a safe alternative to KCN. *Advanced Energy Materials*, *5*(6), 1401689

[140] Philip, R. R., Pradeep, B., Okram, G. S., & Ganesan, V. (2004). Investigations of the electrical properties in CuInSe2 and the related ordered vacancy compounds. Semiconductor science and technology, 19(7), 798

[141] Rau, H., Kutty, T. R. N., & De Carvalho, J. G. (1973). High temperature saturated vapour pressure of sulphur and the estimation of its critical quantities. *The Journal of Chemical Thermodynamics*, *5*(2), 291-302

[142] Hoshino, H., Schmutzler, R. W., & Hensel, F. (1976). The high temperature vapour pressure curve and the critical point of liquid selenium. *Berichte der Bunsengesellschaft für physikalische Chemie*, *80*(1), 27-31

[143] Ehemba, A. K., Dieng, M., DIALLO, D., SOCE, M., & WADE, D. (2015). al., Influence of CuInSe2 and Cu (In, Ga) Se2 thin layer thickness on the electric parameters on the solar cell. *Current Trends in Technology and Science*, *4*(03)

[144] http://www.chose.uniroma2.it/

[145] Hofmann, A., & Pettenkofer, C. (2011). Surface orientation dependent band alignment for CuInSe2–ZnSe–ZnO. *Applied Physics Letters*, *98*(11)

[146] Zhang, H., Zhang, S., Ji, X., He, J., Guo, H., Wang, S., ... & Wu, Y. (2024). Formamidinium Lead Iodide-Based Inverted Perovskite Solar Cells with Efficiency over 25% Enabled by An Amphiphilic Molecular Hole-Transporter. *Angewandte Chemie*, *136*(16), e20240126

[147] Bu, F., He, B., Ding, Y., Li, X., Sun, X., Duan, J., ... & Tang, Q. (2020). Enhanced energy level alignment and hole extraction of carbon electrode for air-stable hole-transporting material-free CsPbBr3 perovskite solar cells. *Solar energy materials and solar cells*, *205*, 110267

---

[148] Zhu, T., Zheng, D., Rager, M. N., & Pauporté, T. (2020). The stabilization of formamidinium lead tri-iodide perovskite through a methylammonium-based additive for high-efficiency solar cells. *Solar RRL*, *4*(11), 2000348

[149] Moghadamzadeh, S., Hossain, I. M., Jakoby, M., Nejand, B. A., Rueda-Delgado, D., Schwenzer, J. A., ... & Paetzold, U. W. (2020). Spontaneous enhancement of the stable power conversion efficiency in perovskite solar cells. *Journal of Materials Chemistry A*, *8*(2), 670-682

[150] M. Balkanski; M. K. Teng; S. M. Shapiro; M. K. Ziolkiewicz. (1971). *Lattice modes and phase transition in SbSi. , 44(1), 355–368*

[151] Nowak, M., Kauch, B., & Szperlich, P. (2009). *Determination of energy band gap of nanocrystalline SbSI using diffuse reflectance spectroscopy. Review of Scientific Instruments, 80(4), 046107.*

Acknowledgments

I would like to express my deepest gratitude to all those who have contributed to the successful completion of this work. First, I am indebted to Professor Enrico Dalcanale for his guidance and support as my doctoral program coordinator.

I would also like to extend my sincere thanks to all the internal and external to IMEM-CNR collaborators, who generously contributed their expertise, significantly enriching the content of my research. In particular, I am deeply indebted to Dr. Enos Gombia for his unparalleled expertise, which he unselfishly dedicated to this thesis. His contributions to electrical measurements, coupled with his ability to foster a stimulating intellectual environment, have greatly enriched these three years of research. I would also like to thank Dr. Giovanna Trevisi for her meticulous SEM investigations, Dr. Giulia Spaggiari for her Raman Measurements, Dr. Marzio Rancan for his insightful XPS/UPS analyses, Dr. Francesco Mezzadri for his expertise in XRD measurements, and Dr. Antonella Parisini and Salvatore Vantaggio for their precise Hall effect measurements and their unwavering support throughout the project. Their care and attention made a significant difference in my research.

I would like to thank Professor Aldo di Carlo for giving me the opportunity to collaborate with the CHOSE Institute in Rome, where I had the chance to gain firsthand knowledge and learn more about the promising field of perovskites. Beyond that, I would like to express my gratitude to Dr. Luigi Vesce's group, a remarkable team of highly competent, dedicated, professional, and skilled individuals. I have learned so much from you, both academically and personally.

I would like to thank personally Elena Iannibelli, the PhD student who has been by my side throughout this period. By sharing meaningful moments, a strong bond has formed. I wish you the best for your great academic journey, you deserve it.

I would also like to thank Professor Saucedo's group, in particular Alejandro Navarro, for the collaboration and research conducted together on antimony sulphoiodide. This newly established collaboration holds great promise, and I am confident that it will lead to significant advancements.

I would like to thank all the Camlin and Henesis group collaborators, particularly Dr. Konstantin Koshmak for his valuable support. Also, I would like to thank Dr. Roman Sajapin and Dr. Andrea Stefani, two friends always present, tireless workers, and the best lab partners one could wish for.

I extend my sincere gratitude to Dr. Andrea Zappettini, Director of IMEM-CNR, for providing me with the opportunity to pursue my doctoral thesis at the institute. Finally, I would like to thank the entire Green Energy Group. I would like to express my particular gratitude to Dr. Edmondo Gilioli and Dr. Massimo Mazzer for

their exceptional work in guiding this group on a daily basis, consistently supporting our endeavors, and always striving to create a serene and collaborative working environment. Their support and guidance have been invaluable. A special thanks is for Dr. Stefano Rampino and Dr. Francesco Pattini, who have created an environment where even the most challenging work can be approached with a smile. They have always been willing to lend me a hand, believing in my ideas and making me feel valued. I am grateful to have had the opportunity to share my journey with people of such great experience, expertise, and compassion.

Also, I would like to thank Dr. Michele Casappa, a really reliable and supportive lab partner with a great artistic sense. I really like your drawings.

I would like to express my gratitude to Dr. Davide Calestani for his immense patience and willingness to share his extensive knowledge with the group.

A special thanks goes to Dr. Giulia Spaggiari, not only for conducting the Raman measurements for this thesis but also for being an invaluable companion throughout this journey. Her support and friendship have made all the difference.

I would also like to express my deepest gratitude to Dr. Matteo Bronzoni, who not only conducted the electrical measurements for this thesis but also provided invaluable emotional support, listening attentively to my reflections and actively participating in discussions. His constant presence and encouragement, as well as his reminder that there is a fulfilling life beyond research, gave me the strength to persevere.

I would like to thank my co-supervisor Davide Delmonte for always being by my side and never abandoning me in times of difficulty from the very first day I set foot in IMEM. These have been three intense and meaningful years, during which I have grown both as a person and as a professional.

Forever grateful,

Elena